

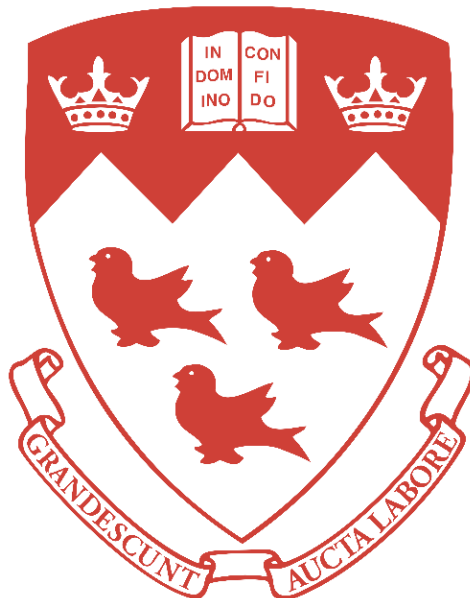
Laser Powder Bed Fusion Additive Manufacturing of Molybdenum and Titanium- Zirconium-Molybdenum alloy

Tejas Ramakrishnan

Department of Mining and Materials Engineering
McGill University
Montreal, Quebec, CANADA

November 2023

First published on 01st November 2024



A thesis submitted to McGill University in partial fulfillment of the requirements of the degree
of Doctor of Philosophy.

© Tejas Ramakrishnan, 2023

All rights reserved.

Table of Contents

Table of Contents	i
Abstract	vi
Résumé.....	viii
List of Figures	xi
List of Tables	xv
List of Abbreviations	xvi
Acknowledgements.....	xix
Contributions to Original Knowledge.....	xxi
Contributions of Authors	xxii
Chapter 1 – Introduction	1
1.1 Background	1
1.2 Research objectives	2
1.3 Thesis layout	3
1.4 References	3
Chapter 2 – Literature Review	6
2.1 Refractory metals	6
2.2 Mo metal and TZM alloy	7
2.3 Limitations in the application and processing of Mo and TZM.....	9
2.3.1 Grain boundary cracking	9
2.3.2 Oxidation of Mo and TZM	18
2.3.3 Refractory nature of Mo and TZM	19
2.4 Conventional processing of Mo and TZM	19

2.4.1 Mo metal production.....	19
2.4.2 Powder metallurgy	20
2.5 Future applications for Mo and TZM.....	20
2.6 Powder Bed Fusion	22
2.7 Laser Powder Bed Fusion Additive Manufacturing.....	24
2.7.1 Overview of the LPBF process	24
2.7.2 Key process parameters	26
2.7.3 Powder feedstock and substrate	29
2.7.4 Build atmosphere	32
2.7.5 Defects in LPBF processed parts	34
2.8 LPBF-AM of Mo and TZM	37
2.8.1 Progress in LPBF AM of Mo and TZM	37
2.8.2 Key challenge in LPBF AM of Mo and TZM	47
2.9 References	48
Chapter 3 – Methods	62
3.1 Sample fabrication.....	62
3.1.1 Powder feedstock and its characterization.....	62
3.1.2 LPBF AM	63
3.1.3 Build atmosphere	64
3.2 Characterization	64
3.2.1 Sample preparation	64
3.2.2 Optical microscopy	64
3.2.3 Electron microscopy	65
3.2.4 X-ray diffraction	65
3.2.5 Inert gas fusion.....	66

3.2.6 Dilatometry	66
3.2.7 Vickers microhardness.....	66
3.2.8 Laser flash analysis.....	66
3.3 Phase diagram and paraequilibrium diagram calculations	69
3.4 First-principles atomistic modelling and calculations.....	69
3.4.1 Schrödinger equation	69
3.4.2 Density functional theory.....	70
3.4.3 Generalized-gradient approximation	71
3.4.4 Atomistic modelling using Quantum Espresso.....	72
3.5 Finite element analysis	73
3.5.1 Governing Equations	73
3.5.2 FEM using ABAQUS	74
3.6 References	74
Chapter 4 – Laser powder bed fusion additive manufacturing of molybdenum using a nitrogen build atmosphere.....	77
4.1 Abstract	78
4.2 Introduction	78
4.3 Experimental methods.....	81
4.4 Computational methods.....	82
4.5 Results and Discussion.....	83
4.5.1 Powder Characterization.....	83
4.5.2 Sample Characterization	84
4.5.3 DFT calculations.....	94
4.5.4 Effect of nitrogen.....	95
4.6 Conclusion.....	96

4.7 Supplementary Material	96
4.8 Acknowledgement.....	98
4.9 References	99
Chapter 5 – Laser powder bed fusion of molybdenum under various Ar-N ₂ mixture build atmospheres.....	106
5.1 Abstract	107
5.2 Introduction	107
5.3 Experimental methods.....	109
5.4 Results and Discussion.....	111
5.4.1 Powder Characterization.....	111
5.4.2 Sample Characterization	112
5.5 Conclusion.....	125
5.6 Acknowledgement.....	126
5.7 References	126
Chapter 6 – Laser powder bed fusion additive manufacturing of Mo and TZM exoskeleton with Cu infiltration for new heat sinks configuration	133
6.1 Abstract	134
6.2 Introduction	134
6.3 Material and methods	137
6.3.1 LPBF fabrication of HCS	137
6.3.2 Cu infiltration into HCS.....	138
6.3.3 Sample preparation and characterization	139
6.3.4 Thermal diffusivity setup and measurements	141
6.3.5 FEM simulation of Cu-Mo-Cu vs Mo-HCS	142
6.4 Results and Discussion.....	144

6.4.1 Fabrication and characterization of Mo-HCS	144
6.4.2 Cu-infiltrated Mo-HCS	146
6.4.3 TZM vs Mo as exoskeleton in HCS.....	150
6.4.4 Thermal diffusivity measurements	153
6.4.5 FEM simulation of Cu-Mo-Cu vs Mo/TZM-HCS.....	154
6.5 Conclusion.....	155
6.6 Supplementary Material	156
6.6.1 CTE calculations from simple and modified rules of mixtures	156
6.6.2. In-house custom-made laser flash analysis equipment and measurements	157
6.6.3 FEM simulations.....	162
6.7 Acknowledgement.....	163
6.8 References	163
Chapter 7 – Discussion	170
7.1 Introduction	170
7.2 Mo and TZM powders for LPBF	171
7.3 Crack-free Mo via LPBF.....	172
7.4 Influence of N ₂ on LPBF-processed Mo	173
7.5 Microstructure of Mo and TZM parts with thin wall features	175
7.6 Cu infiltrated Mo and TZM structures with tailored CTE	176
7.7 References	178
Chapter 8 – Conclusion.....	181

Abstract

Molybdenum (Mo) and TZM alloy provide promising mechanical and thermal properties, making them ideal candidate materials for a wide variety of industrial applications. The refractory nature of these materials restricts their formability to parts with simple geometries using the powder metallurgy route. The laser powder bed fusion (LPBF) additive manufacturing (AM) process is a modern manufacturing technique that can fabricate near-net shape parts with complex geometries and internal features. The few studies in the literature report limited success with LPBF processing of Mo due to the grain boundary embrittlement and cracking in the fabricated parts. Alloying and substrate heating proved to be the only means to resolve the cracking issue, but those solutions present limitations to the LPBF process. This study investigates the LPBF processing of Mo and TZM in an N₂ build atmosphere without the need for alloying or substrate heating. The study documents the fabrication of a replacement for a commercial laminate Mo-Cu heat sink for power electronics application, using Mo and TZM parts fabricated through the LPBF process, with thin walls and honeycomb cavity structures.

Mo samples were fabricated through the LPBF process using a conventional Ar atmosphere and N₂ build atmosphere. Microstructural characterization and electron back-scattered diffraction (EBSD) analysis were used to understand the influence of the build atmosphere on the microstructure and cracking tendency of the fabricated samples. Fabrication under the Ar atmosphere led to long columnar grains aligned along the build direction in the samples (Mo-Ar), which evidenced GB cracking. Samples fabricated under the N₂ atmosphere (Mo-N) showed a smaller and more irregular grain structure with no evidence of cracking. Fracture surface (FS) investigations were performed to understand the FS makeup. Inert-gas fusion technique was employed to quantify the interstitial element content in the samples and their role in the cracking behaviour. The presence of N around ~600 ppm in the Mo-N samples resulted in a crack-free microstructure, despite similar O content in both sets of samples. Atomistic modelling was used to describe the interactions between N and O interstitials in the Mo lattice. The results revealed that the diffusion barrier energy for O in the presence of N in the Mo lattice is higher than that for O in the pure Mo lattice.

Gas mixtures of varying Ar-N₂ compositions were then used as build atmosphere to study the influence of N₂ partial pressure on the N content, microstructure and cracking behaviour of LPBF-processed Mo. Inert gas fusion tests showed an increasing trend of N content with N₂ partial pressure. EBSD analysis was performed to characterize the microstructure. The microstructure was observed to evolve from a columnar grain structure with a high aspect ratio to grains with a lower aspect ratio and increasing irregularity in morphology with the increase in N content. Crack lengths were measured and found to decrease with the change in grain structure, suggesting that disruptions in the columnar grain structure hinder crack growth. Fracture surface investigations were performed, which revealed the influence of N on the extent of GB oxide segregation. Microhardness measurements revealed a generally increasing trend of hardness with N content. The study identified a threshold N content in Mo required to prevent O segregation to GB and suppress cracking tendency.

Finally, with the knowledge gained, Mo and TZM parts with thin walls and honeycomb cavity structures (Mo-HCS) were fabricated using the LPBF process. Microstructural studies were performed, which revealed that the thin walls retained the characteristic microstructural form required to limit GB cracking. Copper infiltration was performed into the parts to create composite structures that match the Mo/Cu content ratio of commercial laminate Cu-Mo-Cu heat sinks. Microstructural analysis showed that excellent wetting was achieved between Cu and Mo structures. Coefficient of thermal expansion (CTE) measurements revealed that Mo-HCS with Cu offered a lower and closely matched CTE to power electronics semiconductors when compared to the laminate heat sinks. The results of the laser flash analysis study showed that the thermal diffusivity of the fabricated parts matched the laminate heat sinks. FEM simulations showed that Mo-HCS structures showed similar conduction resistance, leading to lower thermal stresses and reduced delamination risk.

Résumé

Le molybdène (Mo) et l'alliage TZM présentent des propriétés mécaniques et thermiques prometteuses, ce qui en font des matériaux candidats idéaux pour une grande variété d'applications industrielles. La nature réfractaire de ces matériaux limite leur formabilité à des pièces de géométrie simple par la voie de la métallurgie des poudres. Le processus de fabrication additive (AM, en anglais) par fusion laser sur lit de poudre (LPBF, en anglais) est une technique de fabrication moderne qui permet de fabriquer des pièces de forme presque nette avec des géométries et des caractéristiques internes complexes. Quelques études dans la littérature font état d'un succès limité du traitement LPBF du Mo en raison de la fragilisation des joints des grains (GB, en anglais) et de la fissuration des pièces fabriquées. L'alliage et le chauffage du substrat se sont avérés être les seuls moyens de résoudre le problème de la fissuration, mais ces solutions présentent des limites au processus LPBF. Cette étude examine le traitement LPBF du Mo et du TZM dans une atmosphère de construction de N₂ sans qu'il soit nécessaire d'allier ou de chauffer le substrat. L'étude documente la fabrication d'un remplacement pour un dissipateur thermique commercial en Mo-Cu laminé pour une application d'électronique de puissance, en utilisant des pièces en Mo et TZM fabriquées par le procédé LPBF, avec des parois minces et des structures de cavité en nid d'abeille.

Des échantillons de Mo ont été fabriqués par le biais du processus LPBF en utilisant une atmosphère conventionnelle d'Ar et une atmosphère de construction de N₂. La caractérisation microstructurale et l'analyse par diffraction électronique rétrodiffusée (EBSD, en anglais) ont été utilisées pour comprendre l'influence de l'atmosphère de fabrication sur la microstructure et la tendance à la fissuration des échantillons fabriqués. La fabrication sous atmosphère d'Ar a donné lieu à de longs grains colonnaires alignés le long de la direction de construction dans les échantillons (Mo-Ar), ce qui a mis en évidence la fissuration GB. Les échantillons fabriqués sous atmosphère N₂ (Mo-N) présentaient une structure de grain plus petite et plus irrégulière, sans aucun signe de fissuration. Des études de la surface de rupture ont été réalisées pour comprendre la composition de la surface de rupture. La technique de fusion sous gaz inerte a été employée pour quantifier la teneur en éléments interstitiels dans les échantillons et leur rôle dans le comportement de fissuration. La présence d'environ 600 ppm de N dans les échantillons de Mo-N a permis

d'obtenir une microstructure sans fissure, malgré une teneur en O similaire dans les deux séries d'échantillons. La modélisation atomistique a été utilisée pour décrire les interactions entre les interstitiels N et O dans le réseau Mo. Les résultats ont révélé que l'énergie de la barrière de diffusion pour O en présence de N dans le réseau de Mo est plus élevée que pour O dans le réseau de Mo pur.

Des mélanges de gaz de compositions variables Ar-N₂ ont ensuite été utilisés comme atmosphère de construction pour étudier l'influence de la pression partielle de N₂ sur la teneur en N, la microstructure et le comportement à la fissuration du Mo traité par LPBF. Les essais de fusion sous gaz inerte ont montré une tendance à l'augmentation de la teneur en azote avec la pression partielle de N₂. Une analyse EBSD a été réalisée pour caractériser la microstructure. On a observé que la microstructure évoluait d'une structure de grain colonnaire avec un rapport d'aspect élevé vers des grains avec un rapport d'aspect plus faible et une irrégularité croissante dans la morphologie avec l'augmentation de la teneur en azote. Les longueurs des fissures ont été mesurées et on a constaté qu'elles diminuaient avec le changement de la structure des grains, ce qui suggère que les perturbations de la structure des grains colonnaires entravent la croissance des fissures. Des études de la surface de rupture ont été réalisées et ont révélé l'influence de l'azote sur l'étendue de la ségrégation des oxydes aux joints de grains. Les mesures de microdureté ont révélé une tendance générale à l'augmentation de la dureté avec la teneur en azote. L'étude a identifié un seuil de teneur en N dans le Mo nécessaire pour empêcher la ségrégation de l'O aux joints des grains et supprimer la tendance à la fissuration.

Enfin, grâce aux connaissances acquises, des pièces en Mo et TZM avec des parois minces et des structures de cavité en nid d'abeille (Mo-HCS) ont été fabriquées à l'aide du procédé LPBF. Une étude microstructurale a été réalisée, qui a révélé que les parois minces conservaient la forme microstructurale caractéristique requise pour limiter la fissuration aux joints des grains. Une infiltration de cuivre a été réalisée dans les pièces pour créer des structures composites qui correspondent au rapport Mo/Cu des dissipateurs thermiques laminés Cu-Mo-Cu du commerce. L'analyse microstructurale a montré qu'un excellent mouillage a été obtenu entre les structures de Cu et de Mo. Les mesures du coefficient de dilatation thermique (CTE, en anglais) ont révélé que le Mo-HCS avec Cu offrait un CTE inférieur et étroitement adapté aux semi-conducteurs de

l'électronique de puissance par rapport aux dissipateurs thermiques stratifiés. L'analyse par flash laser a montré que la diffusivité thermique des pièces fabriquées correspondait à celle des dissipateurs thermiques stratifiés. Les simulations par la méthode des éléments finis ont montré que les structures Mo-HCS présentaient une résistance à la conduction similaire, ce qui a permis de réduire les contraintes thermiques et le risque de délamination.

List of Figures

Figure 2.1. Periodic Table of Elements.	6
Figure 2.2. (a) R value for Mo vs other bcc metals, and (b) W_{SEP} showing inherent GB brittleness in Mo (Adapted from [27])	12
Figure 2.3. DBTT for low carbon arc cast Mo in (a) stress-relieved and (b) recrystallized conditions (Adapted from [34])	13
Figure 2.4. Solubility of N and O in Mo vs temperature (Adapted from [36-38])	14
Figure 2.5. (a) Diffusion barrier energy for O and C in Mo, and (b) diffusion coefficient of O vs inverse temperature in Mo at different C content [43]	16
Figure 2.6. Fracture surface in Mo (a) before, and (b) after addition of C. (c) Critical stress vs C content for Mo. (d, e) Effect of selected elements on GB cohesion in Mo (Adapted from [44, 45, 48]).....	17
Figure 2.7. Weight change vs temperature for TZM in O and air [53].....	18
Figure 2.8. Example images of (a) as-reduced Mo powders [57] and (b) SEM micrograph of commercially available Mo powders.	20
Figure 2.9. (a) Ultimate tensile strength vs temperature, and (b) CTE for various materials, including refractory metals (Adapted from [63, 64]).....	21
Figure 2.10. Schematic of an EB-PBF system (Adapted from [75])	23
Figure 2.11. Schematic of an LPBF system (Adapted from [89])	25
Figure 2.12. List of major parameters influencing LPBF processed part.	26
Figure 2.13. Visualization of the processing parameters in LPBF (Adapted from [95, 96]).....	27
Figure 2.14. Typical laser scanning strategies in the LPBF process. (Adapted from [101, 102])	29
Figure 2.15. (a) Some key attributes of powder studied in LPBF, and (b-d) SEM micrographs of some metal powders. (Adapted from [105, 107]).	30
Figure 2.16. (a) Absorptance as a function of bed packing density ([109]), and (b) Thermal conductivity as a function of temperature for various metal powders [110].	31
Figure 2.17. Stresses in the LPBF process from the (a) heating and (b) cooling cycles (Adapted from [112]). Distribution of residual stresses in substrate and part after (c) 2 layers and (d) part is produced (Adapted from [113])	32

Figure 2.18. (a) Typical LPBF process emissions, and (b) gas flow used for removal of process emissions (Adapted from [115])	33
Figure 2.19. (a) LPBF process emissions under Ar vs He [119], and (b) UTS vs ED for Al-12Si under various build atmospheres in LPBF [117].	33
Figure 2.20. Balling defect in the LPBF process [120]	35
Figure 2.21. (a) Delamination defect, (b) high surface roughness defect, and (c) ideal surface roughness in LPBF-AM (Adapted from [121, 122])	35
Figure 2.22. (a) Lack-of-fusion pores, gas-trapped pores [101], and (b) keyhole pores [124].....	36
Figure 2.23. Representative images and microstructure from the study by Faidel et al. [126]	38
Figure 2.24. Cracking behaviour of LPBF Mo [105]	39
Figure 2.25. Influence of laser scan rotation (a) 0°, (b) 90°, and (c) 67° on grain structure in LPBF Mo. (d-f) GB and stress representations for the three conditions. [105]	40
Figure 2.26. (a) Use of support structures and crack-free microstructures for Mo in (b-c) top surface and (d) along build direction. [105]	41
Figure 2.27. (a-b) Mo powders used in the study, and (c) microstructure and (d) IPF map from EBSD analysis. [129].....	42
Figure 2.28. Oxides in LPBF processed Mo [129]	43
Figure 2.29. Microstructure of LPBF processed parts: (a, d) pure Mo with the substrate at 800 °C, (b, e) Mo-0.45 wt.%C at 800 °C, (c, f) Mo-0.45 wt.%C at 500 °C [130].....	44
Figure 2.30. Influence of ED and scan speed on crystallographic texture in LPBF processed Mo [131].....	45
Figure 2.31. Microstructure showing cracks for LPBF processed (a) Mo and (b) Mo-47.5wt.%Re [132].....	46
Figure 2.32. (a) Microstructure, and (b) EBSD map of LPBF processed TZM [134].....	47
Figure 3.1 SEM micrographs of (a-b) Mo and (c-d) TZM powders used in this study	62
Figure 3.2. (a) Renishaw AM400 LPBF machine [3], and (b) Example image of a build layout on RBV from this study.	63
Figure 3.3. Schematic of the custom-made laser flash analysis equipment with the different components	68
Figure 4.1 (a,b) SEM images of Mo powders showing size and morphology of the particles. (c) Particle size distribution, and (d) cohesiveness index wrt rotation speed, for Mo powder.	84

Figure 4.2 (a) Optical, and (b) EBSD micrograph of Mo-Ar sample. BD indicates the build direction of the samples. (c) Optimization results showing part density against volumetric energy density with average crack length of the samples.....	85
Figure 4.3 (a) Optical, and (b) EBSD micrograph of a representative crack-free Mo-N sample. (c) Optimization results showing part density against volumetric energy density with average crack length of the samples	87
Figure 4.4 (a, b) BSE micrograph of Mo-N grains showing precipitates	88
Figure 4.5 (a, b) High magnification STEM showing the precipitates, and (c) EDS line scan analysis of the precipitates as shown in Figure 4.5b.....	89
Figure 4.6 SEM micrographs showing oxide particles in (a) Mo-Ar, and (b) Mo-N.....	90
Figure 4.7 Calculated paraequilibrium line in Mo-N phase diagram.	91
Figure 4.8 SEM fractographs (a, b) Mo-Ar, and (c, d) Mo-N, showing oxide particles.	93
Figure 4.9 Diffusion barrier for (a) O in bcc Mo, and (b) O in bcc Mo with N interstitial	95
Figure 4.10 Convergence tests (a) Brillouin-zone sampling, (b) Work function cut-off energy, and (c) No. of atoms in supercell.....	98
Figure 5.1 (a) Design layout of the build plate, (b) Representative image of a build plate.....	110
Figure 5.2 (a, b) SEM micrographs showing morphology of the Mo powders.....	111
Figure 5.3 (a-f) Optical micrographs of samples MoAr, Mo10N, Mo60N, Mo90N, Mo95N, and MoN, respectively.....	113
Figure 5.4 Average crack length, and porosity, vs N ₂ gas content in the build atmosphere, respectively.	114
Figure 5.5 IPF maps from EBSD analysis of (a) MoAr, (b) Mo10N, (c) Mo60N, (d) Mo90N, (e) Mo95N, and (f) Mo-N sample.....	116
Figure 5.6 (a) Representative grain boundaries with high misorientation angles in MoN, (b-d) misorientation angle plots for 3 locations in Figure 5.6a, and (e) within grain misorientation for MoAr and MoN.....	118
Figure 5.7 Fracture surface micrographs showing oxide particles in (a) MoAr, (b) Mo10N, (c) Mo60N, (d) Mo90N, (e) Mo95N, and (f) MoN.....	120
Figure 5.8 N content in Mo vs N ₂ partial pressure.	122
Figure 5.9 XRD analysis plots for the samples.....	124

Figure 5.10 Microhardness and N content in samples vs N ₂ partial pressure in the build atmosphere	125
Figure 6.1 (a) Model view of the HCS with dimensions and (b) view of the section prepared for CTE and microstructural analysis.	138
Figure 6.2 Temperature profile of the Cu infiltration process.	139
Figure 6.3 Location of EDS map (marked in red) and those for microhardness analysis (marked in blue) performed on the HCS sample.	141
Figure 6.4 Three-dimensional models of (a) GaAs-Mo-HCS+Cu and (b) GaAs-CuMoCu, respectively.	143
Figure 6.5 (a) LPBF-AM of a Mo-HCS sample with honeycomb structure, (b, c) SEM micrographs detailing the thin walls and cavity features, (d) optical micrograph, and (e) EBSD micrograph of a thin wall.	145
Figure 6.6 Mo and Cu regions shown in (a, b) optical micrographs, and (c, d) EDS maps; (e) XRD spectrum showing Mo and Cu phases.	147
Figure 6.7 (a) (a) Recrystallization fraction analysis from EBSD for Mo and representative maps for (b) AB, (c) 1073 K, and (d) 1373 K conditions.	149
Figure 6.8 (a) Optical micrograph and (b) IPF map from EBSD analysis of a wall in TZM-HCS.	151
Figure 6.9 (a) Recrystallization fraction analysis from EBSD for TZM and representative maps for (b) AB, (c) 1073 K, and (d) 1373 K conditions.	152
Figure 6.10 Microhardness values of AB Mo-HCS and AB TZM-HCS along with the microhardness profile across the breadth of Mo-HCS+Cu and TZM-HCS+Cu.	153
Figure 6.11 (a) Temperature profile along the depth of the heat sink. Stress maps for (b) GaAs- CuMoCu and (c) GaAs-Mo-HCS+Cu setups, respectively.	155
Figure 6.12 (a) Schematic of the custom-made laser flash analysis equipment with the different components; (b) view of the sample stage with integrated IR detectors; (c) the sample stage inside the chamber seen through the glass window with the laser optics above it.	158
Figure 6.13 Representative response signals from (a) Netzsch LFA 427 and (b) custom-made laser flash analysis equipment.	159
Figure 6.14 Coupled temperature-displacement thermo-mechanical models and mesh structure for the heat sinks of (a, c) GaAs-CuMoCu and (b, d) GaAs-MoHCS+Cu, respectively.	163

List of Tables

Table 2.1. Selected properties of refractory metals [6, 7].....	7
Table 2.2. Commercial specification for PM-Mo (Type 361) and PM-TZM (Type 364) feedstock	8
Table 2.3. Solubility of interstitial elements (values in ppm) in Mo and other refractory metals at room temperature [39]	14
Table 3.1. Chemical composition (as per certificate of conformity) of powders used in this study.	63
Table 3.2. Details of various gas combinations used in build atmosphere in this study.	64
Table 4.1 Composition of Mo powders used in this study as per the certificate of conformity ...	81
Table 4.2. N and O content in Mo powder, Mo-Ar and Mo-N samples (values in ppm).....	94
Table 4.3 Interstitial incorporation energies for O and N in Mo.	95
Table 5.1 Chemical composition of Mo powders used as per the certificate of conformity	109
Table 5.2 Build atmospheres used for the LPBF process, with sample IDs	110
Table 5.3. N and O content in the samples (values in ppm)	121
Table 5.4. Lattice parameters for different samples estimated from XRD analysis	124
Table 6.1 Thermal properties of power electronics semiconductors and possible heat sink materials.....	135
Table 6.2 Selected thermomechanical properties used for FEM simulations.....	143
Table 6.3 Thermal diffusivity and thermal conductivity at 298 K (25 °C) for the samples.	154
Table 6.4 Calculations of CTE (in 10^{-6} K^{-1}) using simple and modified rules of mixtures.....	157
Table 6.5 Thermal diffusivity and thermal conductivity at 25 °C of the samples.....	160
Table 6.6 Collected measurements and calculated values from LFA for control samples.	162
Table 6.7 Collected measurements and calculated values from LFA for Mo and TZM-HCS+Cu.	162

List of Abbreviations

AB	As-built
AM	Additive Manufacturing
ASM	American Society of Metals
ASTM	American Society for Testing of Materials
BCC	Body centred cubic
BD	Build direction
BO	Born-Oppenheimer
BSE	Back-scattered electron
C3D4T	Coupled temperature displacement tetragonal
CAE	Computer aided engineering
COD	Crystallography Open Database
CTE	Coefficient of thermal expansion
DBT	Ductile to brittle transition
DBTT	Ductile to brittle transition temperature
DFT	Density functional theory
EB-PBF	Electron beam powder bed fusion
EBSD	Electron back-scattered diffraction
ED	Energy density
EDS	Energy dispersive spectroscopy
FCC	Face centred cubic
FEA	Finite element analysis
FEM	Finite element method
FE-SEM	Field emission scanning electron microscope
FS	Fracture surface
GB	Grain boundary
GGA	Generalized gradient approximation
HAGB	High angle grain boundary

HCP	Hexagonal close-packing
HCS	Honeycomb cavity structure
HIP	Hot isostatic pressing
HP	High purity
HV	Hardness Vickers
ID	Identification notes
IPF	Inverse pole figures
IR	Infra-red
ISO	International Organization for Standards
LBPF	Laser powder bed fusion
LT	Layer thickness
MIM	Metal injection molding
MMC	Metal matrix composite
MP	Melting point
NEB	Nudged elastic band
OFHC	Oxygen free high conductivity
PBE	Perdew-Burke-Ernzerhof
PD	Point distance
PDF	Powder diffraction file
PLA	Polylactic acid
PM	Powder metallurgy
PSD	Particle size distribution
RT	Room temperature
SE	Strength of embrittlement
SEM	Scanning electron microscope
SI	International System
TD	Theoretical density
TEM	Transmission electron microscope
TZM	Titanium-Zirconium-Molybdenum
UTS	Ultimate tensile strength

xc	Exchange-correlation
XRD	X-ray diffraction
Nd.YAG	Neodymium-doped Yttrium Aluminium Garnet

Acknowledgements

This work has been made possible only due to the support and love of countless great minds and hearts I have had the privilege of associating with and engaging with. Many of them deserve dedicated paragraphs below, but concision demands otherwise.

Firstly, I would like to express my sincerest and deepest gratitude to my supervisor Prof. Mathieu Brochu for his unwavering support, guidance, and mentorship. This endeavour would not have been possible without his persistent vision, continued participation, deep trust in my ability, and unwavering support in the directions I took in this study. I would like to thank the members of my supervisory committee Prof. Mainul Hasan, Prof. Raynald Gauvin, and Prof. Roderick I. L. Guthrie for their valuable comments throughout this journey. I would also like to express my sincerest gratitude to Prof. Sivaprasad Katakam, my supervisor during my Masters' study for his guidance and support, for inspiring me to study and learn more, and for motivating me to take the journey that I am on right now. I thank Dr. Gowri Subrahmanyam, Dr. Projjal Basu and Shri. Nadimuthu Srinivasan from my time at SNAM Alloys Pvt. Ltd., for their support in my journey towards a Ph.D. study. I would like to acknowledge the late Shri. Prabhakaran, my mathematics tutor, for telling me that I could do better than good. I would also like to express my sincere thanks to Smt. Ajitha A. M, my chemistry teacher, for sealing my friendship with 118 strangers around a peculiar table. Her contagious love for materials and their chemistry set the path for me in my career.

Secondly, I would like to sincerely thank the Department of Mining and Materials Engineering staff for their diligent support. Thanks to Dr. Florence Paray for her support through MMC and her guidance during the TAships that I undertook, to Dr. Sriraman K Rajagopalan for his support with XRD facilities, to Nicolas Brodusch and Stéphanie Bessette for their support with electron microscopy, and special thanks to Barbara Hanley, Leslie Bernier, and June Persaud for their constant support and assistance.

Thirdly, I would like to thank my friends and colleagues from the P²AM² (Powder Processing and Additive Manufacturing of Advanced Materials) group for their friendship and support. As I write this, I fondly remember and acknowledge Abhi, Amit, Amy, An, Ani, Anne, Anubhav, Ashutosh, Beto (Jose), Edem, Eileen, Emilio, Fatih, Ivonne, Jaskaranpal, Kevin (Kuanhe), Mauro, Mohammad, Mohsen, Murali, Oscar, Pierre, Qi, Satish, Sila, Tiffany, Xianglong and Zhen.

I would also like to express my sincere thanks to the Natural Sciences and Engineering Research Council (NSERC) of Canada and the McGill Engineering Doctoral Award (MEDA) for the financial support provided to me so that I could undertake this Ph.D.

Finally, I want to acknowledge my family, without whom I wouldn't be here today. My parents Shri. Ramakrishnan and Smt. Jayasree for providing me with the ability, encouraging me with love and support, to achieve everything I have. My wife Sruthi for her unwavering love, support and dedication to our life, family and success. My son Krishang for making me want to do better and be better at everything I do. My daughter Amaya for making the last few weeks' work on this manuscript easy. And my sister Srilakshmi for making me human and keeping me grounded. I would have been amiss if I didn't mention my in-laws' support at the right time, especially my father-in-law Shri. Sreedharan for his interest in my field of study, who often, through short discussions, re-ignited my focus.

Contributions to Original Knowledge

The contributions to original knowledge achieved through this study are highlighted in the following list:

1. This study demonstrated the successful fabrication of crack-free Mo samples via LPBF processing without the need for pre-alloying or substrate heating.
2. This study investigated the use of N₂ gas and Ar+N₂ gas mixtures as build atmosphere for LPBF processing and reported on the influence of build atmosphere on the microstructure of samples fabricated.
3. This study demonstrated a threshold N content and characteristic microstructure to ensure the fabrication of crack-free Mo samples through LPBF AM.
4. This study demonstrated in-situ nitriding capability in LPBF-processed AM samples with a nitrogen content ranging from 100 to 600 ppm through the use of different partial pressure inside the build chamber.
5. This study successfully fabricated Mo and TZM parts with thin walls and honeycomb cavity structures and demonstrated the successful Cu infiltration of such structures for creating heat sink components with tailored coefficient of thermal expansion.

Contributions of Authors

This thesis has been organized in a manuscript-based style following the guidelines¹ provided by the Graduate and Postdoctoral Studies (GPS) of McGill University. The thesis contains three manuscripts, which have been submitted for publication. Chapters 4, 5, and 6 consist of each individual manuscript. The contributions of the authors of each manuscript are summarized below.

Chapter 4: T. Ramakrishnan, E. R. L. Espiritu, S. Kwon, M. K. Keshavarz, J. A. Muñiz-Lerma, R. Gauvin, and M. Brochu, *Laser powder bed fusion additive manufacturing of molybdenum using a nitrogen build atmosphere*.

Chapter 5: T. Ramakrishnan, S. Kwon, M. Brochu, *Laser powder bed fusion of molybdenum under various Ar-N₂ mixture build atmospheres*.

Chapter 6: T. Ramakrishnan, A. Kumar, P. Hudon, M. Brochu, *Laser powder bed fusion additive manufacturing of Mo and Mo-alloy heat sinks with a tailored coefficient of thermal expansion*.

As the first author of the above-indicated manuscripts, I devised the main idea, conceived the plan, and performed the execution of the research, prepared most of the samples, carried out most of the materials characterization, and performed the data analysis and writing of the manuscripts.

Dr. Eileen R. L. Espiritu provided support with powder characterization using a laser particle size analyzer and electron microscopy for study in Chapter 4.

Dr. Sunyong Kwon provided support with phase diagram modelling for the study in Chapter 4 and helped with the discussion and review of the manuscript in Chapter 5.

Dr. Mohsen K. Keshavarz provided support in electron microscopy and discussions in the study in Chapter 4.

¹ McGill GPS Thesis Guidelines - <https://www.mcgill.ca/gps/thesis/thesis-guidelines>

Dr. Jose A. Muñoz-Lerma provided support in sample fabrication with Renishaw™ AM400 system in the study in Chapter 4.

Mr. Amit Kumar provided support with FEM modelling of the two structures using ABAQUS™ system in the study in Chapter 6.

Dr. Pierre Hudon provided training and support with dilatometry and review for study in Chapter 6.

Prof. Raynald Gauvin provided guidance and access to high-resolution electron microscopy for the study in Chapter 4.

Prof. Mathieu Brochu supervised the project providing technical and scientific advice, arranged funding, and performed proofreading and correction for all chapters.

Chapter 1 – Introduction

1.1 Background

Refractory metals are typically defined as those which are highly resistant to heat and wear. These have a melting point higher than 2477 K (2204 °C) and include molybdenum (Mo), niobium (Nb), rhenium (Re), tantalum (Ta), and tungsten (W) [1]. Mo is one of the most commonly used refractory metals due to its lower cost, excellent specific strength, high thermal conductivity, hardness, high melting point, and corrosion resistance [1, 2]. Mo finds significant use as an alloying element in stainless and high-strength steels to increase wear-resistance, hardness and strength, and in the production of superalloys, due to its ability to provide corrosion resistance and extreme temperature resistance to creep damage [3]. While it is extensively used as an alloyant with other metals, pure and lightly alloyed Mo also find numerous applications in the industry [4]. Mo metal and its TZM (Titanium-Zirconium-Molybdenum) alloy are valuable resources in various applications in aerospace, automotive and medical industries. However, the very nature of their resistance to heat and wear that make them valuable leads to challenges in their processing [5]. Powder metallurgy (PM) is the conventional processing method for Mo and TZM, and this presents limitations in the part shapes and size [6, 7]. Hence, there is a need for the development of new processing routes to fully exploit the benefits of Mo and TZM [8].

Laser powder bed fusion (LPBF) additive manufacturing (AM) is a manufacturing process that offers great design freedom and enables the fabrication of parts with near-net complex forms with intricate features [9]. The LPBF process starts with processing a digital 3D file of the part, slicing it into layers, and generating a sliced model, which is then transferred to the printer [10, 11]. In the printer, a laser beam selectively melts and fuses regions in a bed of metal powders spread on a substrate under an inert atmosphere [12]. Once a layer of powder bed is processed, a new layer is raked over it, and the laser melting process continues. In this layer-by-layer manner the part is fabricated. The process enables the fabrication of parts in short lead times without the need for tooling, unlike most conventional processes. Still, the fabricated parts can be affected by defects such as porosity and cracking [13, 14]. LPBF has been successfully applied to a variety of materials, including aluminum [15], stainless and high-strength steels [16], titanium [17], and

superalloys [18], and crack-free near fully dense parts can be fabricated from many of these materials today.

Leveraging the LPBF process can enable the fabrication of complex parts using Mo and TZM beyond the limitations of the PM route. If successfully applied, it opens the possibility of manufacturing parts such as turbine blades, nozzle shrouds, combustion chambers, heat sinks and heat exchangers that can replace superalloys [4]. Researchers have studied the LPBF processing of Mo and TZM materials and documented the challenges and successes [19-21]. Porosity and cracking continue to be significant impediments in Mo and TZM parts produced by LPBF [20]. Alloying continues to be a major avenue to reduce the grain boundary (GB) embrittlement factor for cracking, but this can lead to changes in material property and present issues in terms of meeting material or standard specifications [21]. Substrate heating has been applied to eliminate cracking by reducing the cooling rate through the ductile-to-brittle transition region, but this can complicate the manufacturing process and limit the design freedom provided by LPBF [19]. It is thus clear that there is a need for a LPBF processing strategy for Mo and TZM that does not have any of these limitations and enables the crack-free fabrication of parts with intricate features.

1.2 Research objectives

The general objective of this research was to investigate the LPBF processing of samples and parts from pure Mo and TZM alloy. The sub-objectives are detailed below:

1. To develop a protocol to fabricate crack-free parts of Mo using the LPBF AM process.
2. To study the influence of an N₂ build atmosphere on the LPBF processing of Mo, prepare samples through such a process, and characterize them through various techniques to evaluate the potential of eliminating cracks.
3. To study the influence of the build atmosphere containing various Ar-N₂ gas mixtures and characterize the samples fabricated to understand the influence of N₂ partial pressure on the N dissolution, the cracking behaviour and the properties of the samples fabricated.
4. To create Mo and TZM alloy samples using the LPBF process and demonstrate the ability of LPBF to fabricate complex parts with honeycomb (HC) cavities.
5. To fabricate Cu-infused Mo and TZM structures with tailored coefficients of thermal expansion (CTE) to investigate their properties and performance in heat sink applications.

1.3 Thesis layout

The main body of this thesis is presented under 8 Chapters. Chapter 1 provides an introduction to the thesis and background information along with the study's main objectives. Chapter 2 extensively reviews the current state of the literature on the topic, starting with refractory metal Mo and TZM alloy. It continues through a study of their conventional processing and their applications. The chapter then reviews the challenges in the conventional processing of Mo and TZM and, evaluates the LPBF process as an alternate processing method. The chapter ends by discussing the current state of AM processing of Mo and TZM. Chapter 3 describes the experimental methods used in this study. Chapter 4 discusses using nitrogen build atmosphere instead of argon in LPBF processing of Mo and investigates the properties of the fabricated crack-free samples. Chapter 5 explores the use of nitrogen-argon gas mixtures as build atmospheres and their influences on the LPBF processing of Mo parts. Using the new insights gained, Chapter 6 describes the fabrication of complex parts from Mo and TZM. Mo/TZM heat sinks with Cu infiltration are then benchmarked as an alternative to commercial Mo-Cu laminated heat sinks. Chapter 7 presents a general discussion of the work presented throughout the thesis, and Chapter 8 is the conclusion of the thesis.

1.4 References

- [1] E. Pink and R. Eck, "Refractory Metals and Their Alloys," in *Materials Science and Engineering*: Wiley-VCH Verlag GmbH, 2006, ch. 10.
- [2] J. A. Shields, "Applications of Molybdenum Metal and its Alloys," International Molybdenum Association, 2013.
- [3] M. Bauccio, *ASM Metals Reference Book*. ASM International, 2003.
- [4] R. W. Burman, "Molybdenum - a super superalloy," *Journal of Metals*, vol. 29, pp. 12-17, 1977, doi: 10.1007/BF03354338.
- [5] C. L. Briant, "Refractory Metals and Alloys," in *Encyclopedia of Materials: Science and Technology*, K. H. J. Buschow, R. W. Cahn, M. C. Flemings, E. J. Kramer, B. Ilschner, S. Mahajan, and P. Veyssi re Eds.: Elsevier Science Ltd, 2001, pp. 8088-8095.

- [6] D. Li, H. Hou, Z. Tan, and K. Lee, "Metal injection molding of pure molybdenum," *Advanced Powder Technology*, vol. 20, no. 5, pp. 480-487, 2009, doi: 10.1016/j.appt.2009.05.005.
- [7] J. L. Johnson, "Sintering of refractory metals," in *Sintering of Advanced Materials*, 2010, pp. 356-388.
- [8] C. L. Briant, "New Applications and Novel Processing of Refractory Metal Alloys," presented at the 15th International Plansee Seminar, Reutte, 2001.
- [9] S. Chowdhury, N. Yadaiah, C. Prakash, S. Ramakrishna, S. Dixit, L. R. Gupta, and D. Buddhi, "Laser powder bed fusion: a state-of-the-art review of the technology, materials, properties & defects, and numerical modelling," *Journal of Materials Research and Technology*, vol. 20, pp. 2109-2172, 2022, doi: 10.1016/j.jmrt.2022.07.121.
- [10] M. McMillan, M. Leary, and M. Brandt, "Computationally efficient finite difference method for metal additive manufacturing: A reduced-order DFAM tool applied to SLM," *Materials & Design*, vol. 132, pp. 226-243, 2017, doi: 10.1016/j.matdes.2017.06.058.
- [11] I. Yadroitsev, I. Yadroitsava, and A. Du Plessis, "Basics of laser powder bed fusion," in *Fundamentals of Laser Powder Bed Fusion of Metals*: Elsevier, 2021, ch. 2, pp. 15-38.
- [12] H. Lee, C. H. J. Lim, M. J. Low, N. Tham, V. M. Murukeshan, and Y.-J. Kim, "Lasers in additive manufacturing: A review," *International Journal of Precision Engineering and Manufacturing-Green Technology*, vol. 4, no. 3, pp. 307-322, 2017, doi: 10.1007/s40684-017-0037-7.
- [13] A. Du Plessis, E. MacDonald, J. M. Waller, and F. Berto, "Non-destructive testing of parts produced by laser powder bed fusion," in *Fundamentals of Laser Powder Bed Fusion of Metals*, 2021, pp. 277-300.
- [14] M. Leary, "Economic feasibility and cost-benefit analysis," in *Fundamentals of Laser Powder Bed Fusion of Metals*, 2021, pp. 597-620.
- [15] J. H. Martin, B. D. Yahata, J. M. Hundley, J. A. Mayer, T. A. Schaedler, and T. M. Pollock, "3D printing of high-strength aluminium alloys," *Nature*, vol. 549, no. 7672, pp. 365-369, Sep 20 2017, doi: 10.1038/nature23894.
- [16] J. Suryawanshi, K. G. Prashanth, and U. Ramamurty, "Mechanical behavior of selective laser melted 316L stainless steel," *Materials Science and Engineering: A*, vol. 696, pp. 113-121, 2017, doi: 10.1016/j.msea.2017.04.058.

- [17] L. C. Zhang, H. Attar, M. Calin, and J. Eckert, "Review on manufacture by selective laser melting and properties of titanium based materials for biomedical applications," *Materials Technology*, vol. 31, no. 2, pp. 66-76, 2016, doi: 10.1179/1753555715y.00000000076.
- [18] J.-P. Choi, G.-H. Shin, S. Yang, D.-Y. Yang, J.-S. Lee, M. Brochu, and J.-H. Yu, "Densification and microstructural investigation of Inconel 718 parts fabricated by selective laser melting," *Powder Technology*, vol. 310, pp. 60-66, 2017, doi: 10.1016/j.powtec.2017.01.030.
- [19] D. Wang, C. Yu, J. Ma, W. Liu, and Z. Shen, "Densification and crack suppression in selective laser melting of pure molybdenum," *Materials & Design*, vol. 129, pp. 44-52, 2017, doi: 10.1016/j.matdes.2017.04.094.
- [20] J. Braun *et al.*, "Molybdenum and tungsten manufactured by selective laser melting: Analysis of defect structure and solidification mechanisms," *International Journal of Refractory Metals and Hard Materials*, vol. 84, 2019, doi: 10.1016/j.ijrmhm.2019.104999.
- [21] L. Kaserer *et al.*, "Fully dense and crack free molybdenum manufactured by Selective Laser Melting through alloying with carbon," *International Journal of Refractory Metals and Hard Materials*, vol. 84, 2019, doi: 10.1016/j.ijrmhm.2019.105000.

Chapter 2 – Literature Review

2.1 Refractory metals

Refractory metals are defined as those metals which have a high melting point, and a very high resistance to heat and wear. While this attribute may describe a wider range of metals as highlighted in Figure 2.1, the naming in particular is used for metals with a melting point above 2477 K (2204 °C) [1, 2]. In Figure 2.1 among the highlighted elements, refractory metals are those marked in grey and include molybdenum (Mo), niobium (Nb), rhenium (Re), tantalum (Ta), and tungsten (W). Those marked in blue show melting points slightly below the cut-off value used for this definition. Technetium (Tc) and Rutherfordium (Rf) marked in yellow in Figure 2.1, also fall under these definitions but are not relevant since they are practically inexistent in nature [3, 4].

H																		He
Li	Be											B	C	N	O	F	Ne	
Na	Mg											Al	Si	P	S	Cl	Ar	
K	Ca	Sc	Ti	V	Cr	Mn	Fe	Co	Ni	Cu	Zn	Ga	Ge	As	Se	Br	Kr	
Rb	Sr	Y	Zr	Nb	Mo	Tc	Ru	Rh	Pd	Ag	Cd	In	Sn	Sb	Te	I	Xe	
Cs	Ba	*	Lu	Hf	Ta	W	Re	Os	Ir	Pt	Au	Hg	Tl	Pb	Bi	Po	At	Rn
Fr	Ra	**	Lr	Rf	Db	Sg	Bh	Hs	Mt	Ds	Rg	Cn	Nh	Fl	Mc	Lv	Ts	Og
		*	La	Ce	Pr	Nd	Pm	Sm	Eu	Gd	Tb	Dy	Ho	Er	Tm	Yb		
		**	Ac	Th	Pa	U	Np	Pu	Am	Cm	Bk	Cf	Es	Fm	Md	No		

Figure 2.1. Periodic Table of Elements.

In addition to the high melting point, refractory metals have good resistance to electrochemical corrosion, excellent high-temperature strength, excellent thermal conductivity, and low coefficient of thermal expansion (CTE) [5]. Table 2.1 lists the selected properties of the refractory metals [6, 7]. Among these, Nb and Ta find widespread use due to the relative ease of their processing, and W/Re finds specific applications where high density and extreme hardness are required, while Mo is desired for its higher specific strength and availability [8, 9].

Table 2.1. Selected properties of refractory metals [6, 7]

Element	Unit	Mo	Nb	Re	Ta	W
Melting point	K	2896	2750	3459	3290	3695
	°C	2623	2477	3186	3017	3422
Thermal Conductivity	$\text{W}\cdot\text{m}^{-1}\cdot\text{K}^{-1}$	138	54	71	55	178
CTE	$\times 10^{-6} \text{K}^{-1}$	5.0	7.3	6.7	6.5	4.5
Density	$\text{kg}\cdot\text{m}^{-3}$	10280	8570	21020	16690	19250
Young's modulus	GPa	329	105	463	186	411
Vickers hardness	MPa	1530	1320	2450	873	3430
Recrystallization temperature	K	1173	1073	1623	1073	1773
	°C	900	800	1350	800	1500

2.2 Mo metal and TZM alloy

Mo is a metal with the atomic number 42 and has a body-centred cubic (BCC) crystal structure. In addition to its excellent strength (across a range of temperatures), high thermal conductivity, hardness, and high melting point, it is also known for its resistance against chemical attacks from certain acids and other corrosive agents [10]. As an alloying element, Mo is used in stainless steels, high-strength steels, and superalloys for its contribution to wear resistance, corrosion resistance, and strength [11]. Beyond these uses, pure and lightly alloyed Mo finds various applications in aerospace, automotive and industrial components due to its high-temperature resistance and excellent thermal conductivity [12]. Due to its high wear resistance and high melting point, it is used in industrial components like extrusion dies, valves and pumps. Its high thermal conductivity, good electrical conductivity and chemical inertness to molten glass enable its use as an electrical heater in continuous glass-making operations [13]. The high thermal conductivity, melting point and low vapour pressure at high temperatures make it ideal for cold, low vacuum and inert atmosphere furnaces. In addition, Mo is also widely used in the medical field due to its corrosion resistance, where it is used to make implants, screws, and surgical instruments [14]. It is also used in radiation shielding, as its high atomic weight and density help to absorb radiation. Due to its

similarity to tungsten (W) in various properties, Mo is also increasingly used to replace W metal, where weight-saving and the relative ease of processing would be beneficial [15].

TZM is an alloy of Mo, which contains small additions of titanium (Ti), zirconium (Zr), and carbon (C). TZM finds similar applications to Mo in structural furnace components and tool/die inserts. While more expensive than pure Mo due to the alloying additions, TZM offers improved strength at elevated temperatures and has a higher recrystallization temperature [16]. Some of the strengthening is attributed to the solid solution strengthening of the Mo matrix by dissolved Ti, while most of the strengthening and recrystallization resistance comes from the precipitates [16]. Simple carbides of Mo and Ti, and ternary carbides of Mo-Ti, observed at the grain boundaries, and oxides of Zr and Ti found at the sub-grain boundaries, are reported to hinder the migration of sub-grain and grain boundaries leading to the strengthening of TZM [17]. For long-duration and high-temperature exposure applications like isothermal forging dies and piercing plugs for pierced stainless steel tubing manufacture, TZM parts find preference over Mo due to their increased resistance to recrystallization [18]. It finds additional use in rocket nozzles and as electrodes, stirrers and shields for extreme-temperature furnaces.

Table 2.2 lists the general commercial specifications for powder metallurgy (PM) Mo and TZM feedstock. These specifications are covered under Type 361 and Type 364 sub-sections in American Society for Testing and Materials (ASTM) International standards B386/B386M-19e1 and B387-18 [19, 20]. Comparing the tensile strength vs temperature for Mo and TZM, it can be observed that even at temperatures above 1373 K (1100 °C) they retain usable strength [21]. Most of the commercial materials, including steel and superalloys lose strength beyond 1373 K (1100 °C) [9].

Table 2.2. Commercial specification for PM-Mo (Type 361) and PM-TZM (Type 364) feedstock

Material	Mo	Ti	Zr	C	Others
Mo	99.98	< 0.01	< 0.01	< 0.005	< 0.01
TZM	99.38	0.40 to 0.55	0.06 to 0.12	0.01 to 0.04	< 0.01

2.3 Limitations in the application and processing of Mo and TZM

The excellent physical properties of Mo and TZM deem them suitable for various applications. Still, the limitations in their application from the challenges in their processing to desired shapes and parts hinder a greater adoption. Some of the limitations and challenges are the susceptibility to grain boundary (GB) cracking, poor oxidation resistance at temperatures above 873 K (600 °C), and finally, their refractory nature [22].

2.3.1 Grain boundary cracking

2.3.1.1 GB energy and cohesion

In engineering, most materials are polycrystalline in nature, meaning they consist of regions of uniform lattice (or single crystal) called grains that are misoriented to each other. In these materials, the grains meet each other at grain boundaries (GBs) [23]. GBs are considered defects in the materials; they strongly affect various material properties and can act as sinks and transport pathways for point defects (vacancies, interstitials, etc.) [24]. Extended defects like GB and free surfaces in crystal structure have interfacial energy because of the disruption in the atomic periodicity and the broken bonds across the interface. The interfacial energy of a GB is generally lower than that of a free surface since the atoms in a GB are surrounded on all sides by other atoms and have only a few broken or distorted bonds [25].

The GB energy is usually denoted by the energy difference between a crystal with and without the defect. For GBs and other extended defects, the energy is normalized to the area of the defect. Equation (2.1) gives the relation for GB energy (γ_{GB}) as per the above definition; here, E_{GB} is the energy of a system with a GB defect, E_{BULK} is the energy of a system without GB, and A is the total GB area.

$$\gamma_{GB} = \frac{E_{GB} - E_{Bulk}}{A} \quad (2.1)$$

Now, the energy of a free surface is the energy needed to generate the surface by the breaking of bonds. Equation (2.2) represents the free surface energy as a relationship, where E_{FS} is the energy of a system with two free surfaces with area A .

$$\gamma_{FS} = \frac{E_{FS} - E_{Bulk}}{2A} \quad (2.2)$$

The work of separation is the amount of reversible work required to separate an interface and is an indicator of the cohesion of the interface [26]. For a bulk crystal, this work (W_{SEP}) to separate or cleave at a distinct crystal plane is equated to the energy of the free surfaces created, as indicated in equation (2.3). The work is equal to $2\gamma_{FS}$ when two identical surfaces are created, or $\gamma_{FS,1} + \gamma_{FS,2}$ otherwise. When a GB is separated, the thermodynamic threshold energy for GB fracture, again depicted as W_{SEP} , is the difference between the surface energy and GB energy [27]. This is indicated in equation (2.4), where $E_{FS'}$ is the total energy of a system containing the two new surfaces.

$$W_{SEP} = \begin{cases} 2\gamma_{FS} \\ \gamma_{FS,1} + \gamma_{FS,2} \end{cases} \quad (2.3)$$

$$W_{SEP_GB} = \gamma_{FS,1} + \gamma_{FS,2} - \gamma_{GB} = \frac{E_{FS'} - E_{GB}}{A} \quad (2.4)$$

According to the Griffith-Orowan theory, fracture stress is linked to the amount of work associated with the fracture process. In the case of GB fracture, the relationship is depicted as shown in equation (2.5). Here, σ_f^2 is the fracture stress, while γ_p is the plastic work which accompanies the initial stage of brittle crack extension on the microscale [28]. Jokl et al. [29] and McMahon and Vitek [30] have shown that the plastic work is directly proportional to the grain boundary energy and work of separation, and therefore the fracture stress relation can be equated as in equation (2.6). Further, this establishes that the misorientation dependence of fracture stress directly reflects the misorientation dependence of GB energy [28]. D. Scheiber et al. [27] computed GB properties for Mo and other bcc transition metals and reported that Mo and W exhibit intergranular cleavage or GB fracture.

$$\sigma_f^2 \propto W_{SEP_GB} + \gamma_P \quad (2.5)$$

$$\sigma_f^2 \propto \gamma_{GB} \quad (2.6)$$

2.3.1.2 Intrinsic brittleness and ductile-to-brittle transition

Various simulation and experimental studies have shown that Mo is particularly prone to intergranular fracture at or above room temperature (RT) [27, 31-33]. The simulation studies stipulate either from the viewpoint of a lower GB energy or a lower ratio of GB cohesion to bulk cohesion, while experimental studies observe the fracture mode across temperatures and arrive at the ductile to brittle transition temperature (DBTT), below which the material fails via brittle fracture. Sutton and Balluffi discussed about the ratio of work of separation to the free surface energy of the preferred cleavage plane as an indicator of the fracture mode in metals, as depicted by equation (2.7) [31]. Here, γ_{FS}^{PCP} is the free surface energy for the preferred cleavage plane. For bcc metals like Mo, this is mainly the (100) plane.

$$R = \frac{W_{SEP}}{2\gamma_{FS}^{PCP}} \quad (2.7)$$

If the value of R is close to 1, the fracture is transgranular, and for lower values intergranular fracture is expected. Figure 2.2a shows the R value (the arithmetic mean of R for all GBs) for various bcc metals as computed by atomistic methods by D. Scheiber et al. [27]. In Mo, the value is observed to be ~0.75, indicating that the mode of fracture is intergranular. From the same study, Figure 2.2b depicts the W_{SEP} (indicative of GB cohesion) computed for different GBs in Mo, showing inherent GB brittleness [27]. These results from DFT calculations corroborate well with previously reported experimental observations. For example, Brosse et al. [33] studied highly purified Mo samples and reported that there is intrinsic intergranular brittleness in Mo which is not due to any precipitates or segregation. Similarly, Pokluda and Santera [32] studied the intrinsic

ductile vs brittle response of ideal crystals containing cracks for different materials and reported that Mo showed inherent brittleness.

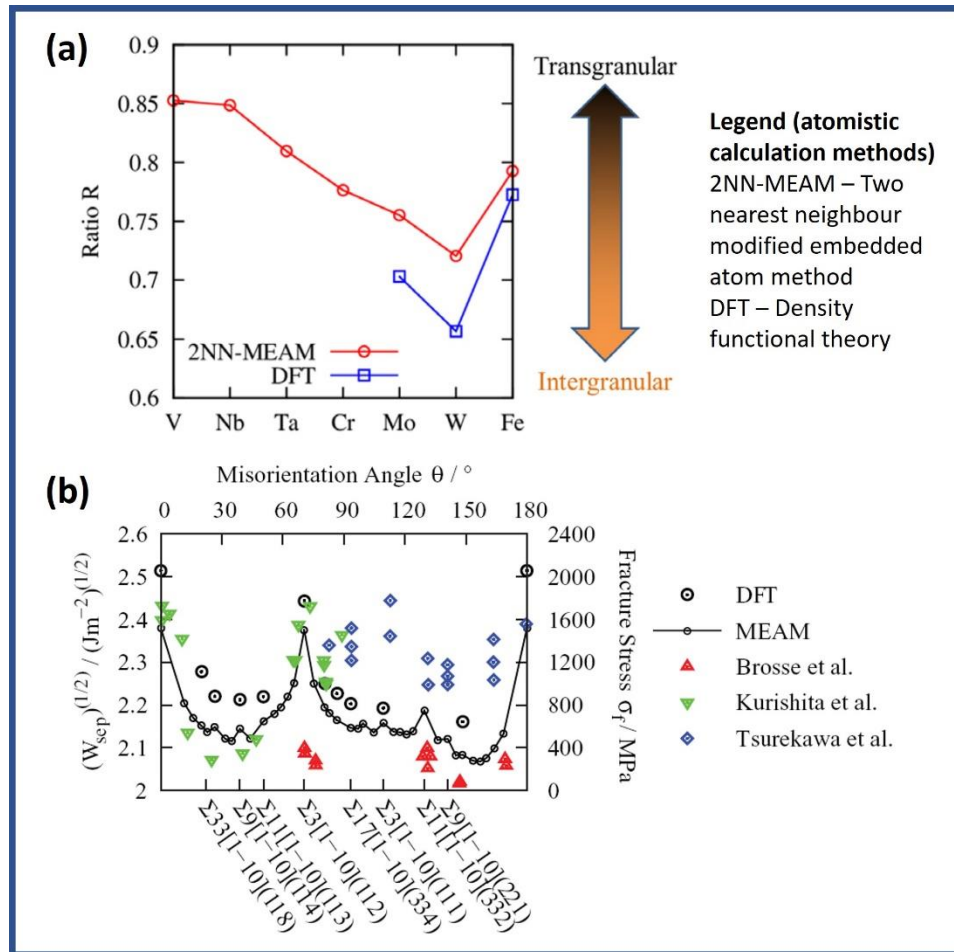


Figure 2.2. (a) R value for Mo vs other bcc metals, and (b) W_{SEP} showing inherent GB brittleness in Mo (Adapted from [27])

The brittleness of Mo is also highly influenced by the material condition – grain size, internal strain energy, and impurity content. The temperature and the rate of loading determine the fracture mode. Hence, Mo exhibits a ductile to brittle transition behaviour in fracture mode and is described by a ductile to brittle transition temperature. Cockeram et al. [34] showed that high-purity arc-cast Mo exhibited a DBTT of $\sim 533\text{K}$ (260°C). Hiraoka et al. [35] showed that pure Mo exhibited a DBTT of $\sim 373\text{K}$ (100°C) under impact loading and a DBTT of 200K (-73°C) under static loading. The difference in the DBTT values reported in the literature arises from the difference in the condition of the Mo material. Figure 2.3 shows the change in impact energy vs temperature for low carbon

arc-cast Mo in stress-relieved and recrystallized conditions [34]. The presence of certain interstitial impurity elements worsens this GB embrittlement.

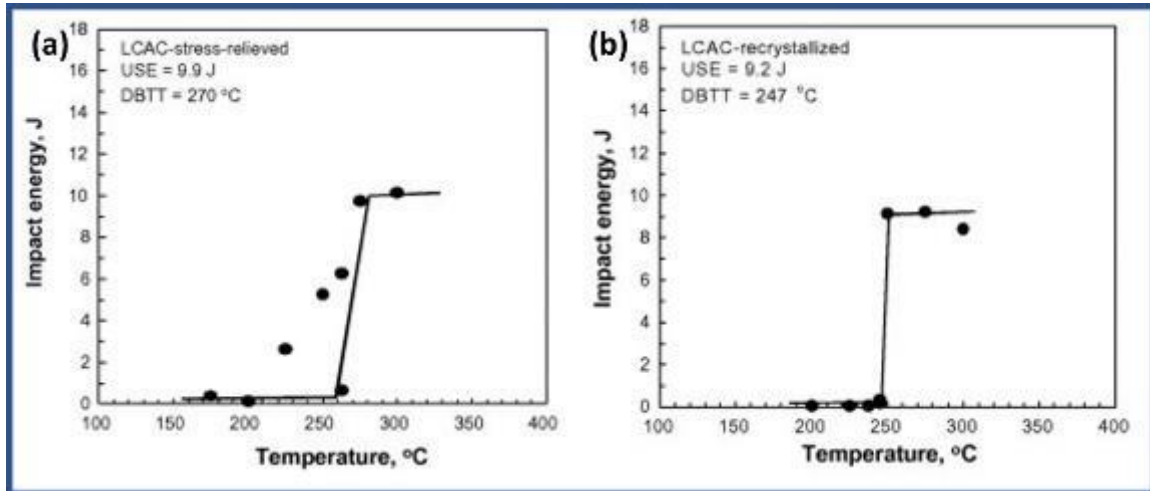


Figure 2.3. DBTT for low carbon arc cast Mo in (a) stress-relieved and (b) recrystallized conditions (Adapted from [34])

2.3.1.4 GB embrittlement

Engineering materials are plagued by the impurity concentration. In the case of Mo and TZM, the presence of hydrogen (H), carbon (C), nitrogen (N), oxygen (O), or impurity elements can be present as interstitial content. During processing at higher temperatures, the solubility of interstitials in Mo is high, as indicated in Figure 2.4 [36-38]. Table 2.3 gives the RT solubility of selected interstitials in Nb, Mo and W. At RT, the solubility of the interstitial content in Mo is very low, especially when compared to Nb and other metals, with only W having lower solubility for these interstitials [39]. Inevitably, the interstitial atoms trapped in Mo at high temperatures during processing reach concentrations beyond the solid solubility limit as Mo cools and segregate to the GBs or free surfaces.

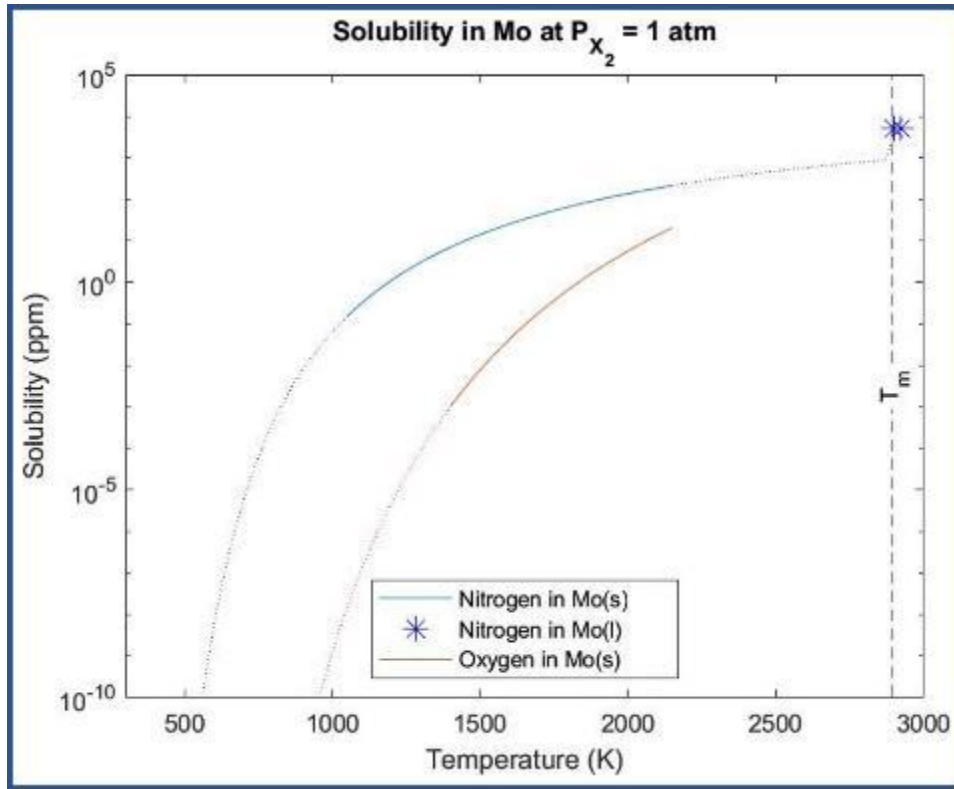


Figure 2.4. Solubility of N and O in Mo vs temperature (Adapted from [36-38])

Table 2.3. Solubility of interstitial elements (values in ppm) in Mo and other refractory metals at room temperature [39]

Material	Nitrogen	Oxygen
Niobium	0.3×10^3	1.0×10^3
Molybdenum	1.0	1.0
Tungsten	$\ll 0.1$	1.0

Segregation is the enrichment of solute atoms at preferred sites (usually GBs, free surfaces or dislocations) in a material. The segregation in a binary system can be described simplistically, using McLean isotherm, as depicted in equation (2.8) [40, 41]. Here, X_{GB} is the concentration of the interstitial at GB, X_0 is the concentration in bulk, G_{seg} is the segregation energy, K_B is Boltzmann's constant, and T is the temperature. If the segregation energy of a solute to the GB is negative, segregation is favoured. Segregation lowers the energy of the system and lowers the GB energy. This impacts the work of separation following equation (2.4). Considering segregation

energies, the new work of separation W'_{SEP_GB} can be defined as indicated in equation (2.9), where ΔW_{SEP_GB} is the difference in work of separation.

$$\frac{X_{GB}}{1-X_{GB}} = \frac{X_0}{1-X_0} e^{\left(-\frac{G_{seg}}{k_B T}\right)} \text{ where } G_{seg} = \frac{\partial G}{\partial X_{GB}} - \frac{\partial G}{\partial X_0} \quad (2.8)$$

$$W'_{SEP_GB} = \frac{(E_{FS} + E_{seg}^{FS}) - (E_{GB} + E_{seg}^{GB})}{A} = W_{SEP_GB} + \Delta W_{SEP_GB} \quad (2.9)$$

Re-arranging for W_{SEP_GB} from equation (2.4) in (2.9), we get the relation for ΔW_{SEP_GB} as in equation (2.10). Here, SE is the strength of embrittlement and is the difference of segregation energies. Interstitial solutes that lead to a negative value for SE lead to an increase in GB cohesion, while a positive value of SE leads to an increase in GB embrittlement [41].

$$\Delta W_{SEP_GB} = \frac{E_{seg}^{FS} - E_{seg}^{GB}}{A} = \frac{-SE}{A} \quad (2.10)$$

Researchers have studied the segregation and influence of interstitial elements on the mechanical properties of Mo and TZM. Kumar and Eyre [41] studied the influence of C and O in arc-cast and zone-refined Mo and reported that O readily segregates to GBs in Mo and promotes brittle GB fracture. They also observed that the applied GB fracture stress is inversely related to the segregated O level. In addition, they suggested that if C is present at a higher bulk concentration than O, it suppresses the segregation tendency of O and replaces O at GB. They also reported that a reduction in GB O level from 0.47 to 0.11 wt.% increased the work of fracture by ~60%, clearly showing the GB embrittling effect of O. Drachinskiy et al. [42] determined the segregation energies for C and O in Mo at -0.72 eV and -1.23 eV respectively, indicating that segregation tendency of O is higher than that of C. But they reported a reduction in GB cohesion in Mo due to both O and C, in contrast to Kumar and Eyre [41]. Z. -Q. Wang et al. [43] used atomistic modelling

to quantify the diffusion barrier energy for C and O in Mo and reported that O has a higher segregation tendency than C. Additionally, they reported that in the presence of C, the diffusion coefficient of O in Mo decreased drastically with increase C content. Figure 2.5a shows the diffusion barrier energy for O and C in Mo, while Figure 2.5b shows the diffusion coefficient of O in Mo for different C content with inverse temperature.

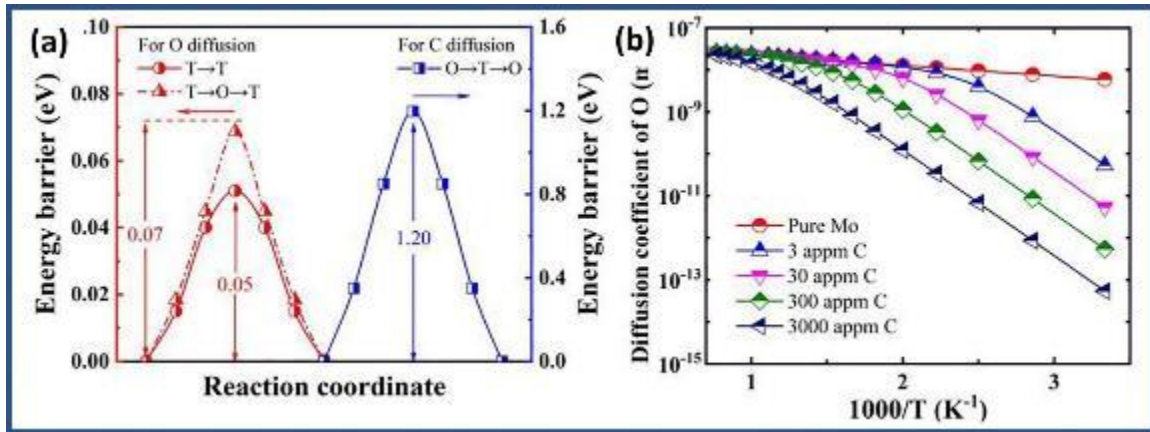


Figure 2.5. (a) Diffusion barrier energy for O and C in Mo, and (b) diffusion coefficient of O vs inverse temperature in Mo at different C content [43]

Hiroaka et al. [44] reported that even small additions of C improved Mo ductility even without forming any precipitates, suggesting that C improved the GB cohesion. Kadokura et al. [45] reported that the DBTT for Mo decreases with C additions, indicating a positive effect on GB cohesion. They observed a change in the fracture mode from intergranular to trans-granular. Figure 2.6a-b shows the change in fracture mode from intergranular to trans-granular with the addition of C, while Figure 2.6c shows the variation in critical stress with C addition [44, 45]. Miller and Kurishita [46] observed through atom probe analyses that O does not segregate to GBs in locations where C is present and vice versa, suggesting that C has a beneficial effect of displacing O from GBs. They also observed N segregation to GBs. In another study, Miller et al. [47] showed that there was no significant segregation of O to any of the GBs in the Mo alloy containing Zr, B and C through atom probe tomography. A change in fracture mode from intergranular to trans-granular was observed as well. D. Scheiber et al. [48] computed the influence of s- and p-elements on GB cohesion in Mo using DFT study and reported that O and H have a negative effect on GB cohesion

in Mo, while other interstitial elements C, N, and B had a positive effect. Figure 2.6d shows the summary of this result.

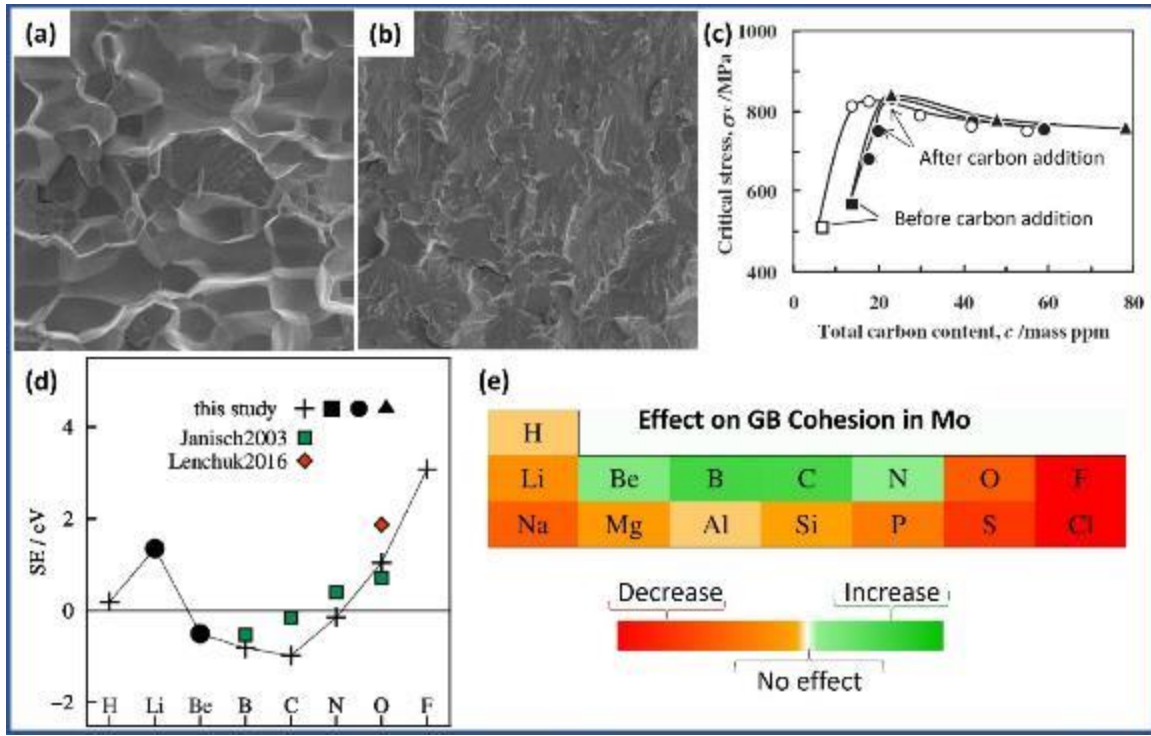


Figure 2.6. Fracture surface in Mo (a) before, and (b) after addition of C. (c) Critical stress vs C content for Mo. (d, e) Effect of selected elements on GB cohesion in Mo (Adapted from [44, 45, 48]).

Krajnikov et al. [49] observed that C increases the ductility of Mo by increasing GB cohesion and suppressing O segregation, whereas O decreases GB cohesion and leads to increased brittleness. They suggested that alloying by chemical elements with a high affinity for O (Ti, Zr, etc., as in TZM are examples), accompanied by the precipitation of complex oxy-carbides, usually improved the properties of as-annealed alloys within the temperature range of stability of these precipitates. Literature unequivocally confirms that oxygen remains the single-most embrittling factor for Mo. The mechanical properties and manufacturability of Mo and its alloys, conventionally and in LPBF, are also significantly affected by the amount of oxygen present. High oxygen concentrations at the GBs can cause brittleness and hot cracks and increase the DBTT. In addition to this embrittlement effect, O presents another challenge to Mo and TZM – oxidation.

2.3.2 Oxidation of Mo and TZM

Researchers have investigated the oxidation resistance of Mo and TZM. While the presence of Ti and Zr in TZM stabilizes internal oxides, their contribution to oxidation resistance is practically non-existent. Mo and TZM are similarly susceptible to oxidation in air. Gulbransen et al. [50] investigated the oxidation behaviour of Mo at temperatures ranging from 823 to 1973 K (550 to 1700 °C) and reported that above 923 K (650 °C), the formation and vaporization of MoO_3 was rapid, leading to mass loss. Mo readily reacts with O to form the highly volatile tri-oxide species, and the fresh surface was continuously re-exposed to O. Smolik et al. [51] observed similar results and reported a sharp reduction in the fraction of oxide volatilized when the temperature was below 923 K (650 °C). Additionally, they described evidence of a molten layer on the samples tested at 1073 K (800 °C). Yang et al. [52] reported that the oxidation tendency of TZM alloys is low below 400 °C, but that changes when the temperature reaches between 673 and 923 K (400 and 650 °C). A mass gain was measured from the formation of MoO_x (where x ; $2 \leq x < 3$) oxide layers. At temperatures above 923 K (650 °C), the oxide layer formed turns into MoO_3 , which volatilizes with increasing temperature, causing a sharp mass loss. Chakraborty et al. [53] reported similar results with TZM oxidation under O atmosphere and in air, as shown in Figure 2.7.

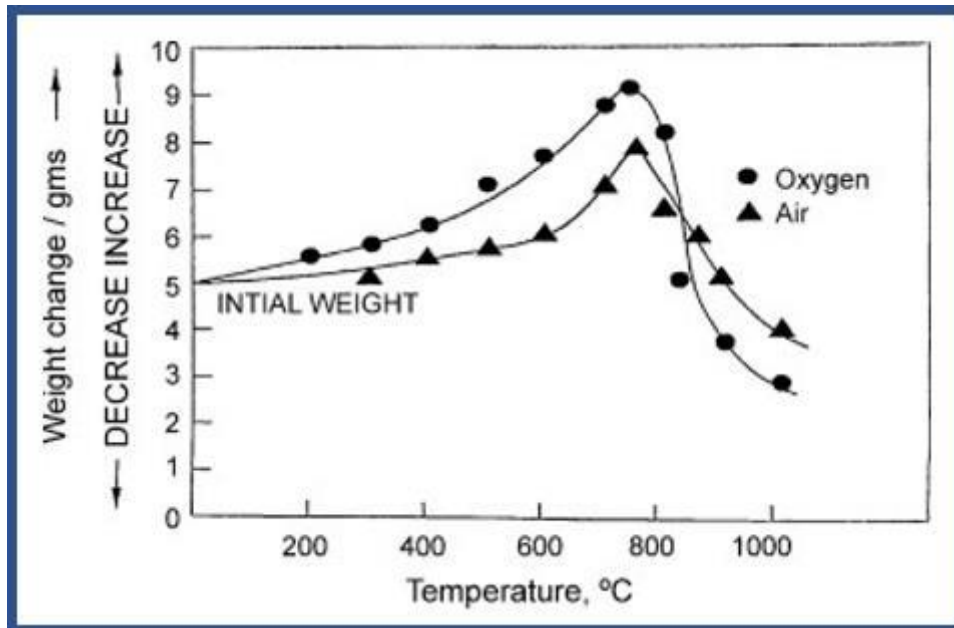


Figure 2.7. Weight change vs temperature for TZM in O and air [53]

2.3.3 Refractory nature of Mo and TZM

The refractory nature and properties of Mo and its alloys present significant challenges in its processing. One factor among this is the melting point, and Mo has one of the highest melting points of all metals, at around 2,896 K (2,623 °C) [54]. This makes it challenging to form Mo or TZM into shapes or conventionally cast into various products. Typical commercially available high-temperature induction furnaces that are used to melt steel, superalloys or even titanium use Mo heating elements and coils inside [9]. Naturally, these furnaces are limited to temperatures below the melting point of Mo. In order to process Mo effectively, very high-temperature furnaces and specialized techniques are often required. Electric arc furnaces are typically employed to process Mo in this manner [22].

Another aspect of this is the high strength and hardness of Mo. Its tensile strength is higher than that of most grades of steel and its hardness is comparable to most grades of tool steel. Tools and dies made of Mo and TZM are quite frequently used in forming operations performed on high-strength steels and superalloys. This level of strength makes the machining and shaping of Mo and its alloys a costly and cumbersome process compared to steel or superalloy machining [10]. Unlike most metals, Mo and TZM retain their strength at higher temperatures, presenting challenges in high-temperature processing [55].

2.4 Conventional processing of Mo and TZM

2.4.1 Mo metal production

From its ores, Mo is most often extracted through a series of steps that include crushing of the ore, its grinding, and flotation, followed by leaching and preparation of molybdenite (MoS_2) concentrate. Roasting of MoS_2 concentrate produces Mo oxides which are turned into Mo powders following a three-stage hydrogen reduction process [56]. The bulk of industrial Mo metal production in the world is done in this manner, with the output in the form of powder. Further processing of the reduced powders by spheroidization gives high-quality spherical Mo powders with good flowability. Figure 2.8 shows as-reduced Mo powders [57] and micrographs from scanning electron microscope (SEM) of commercially available Mo powders.

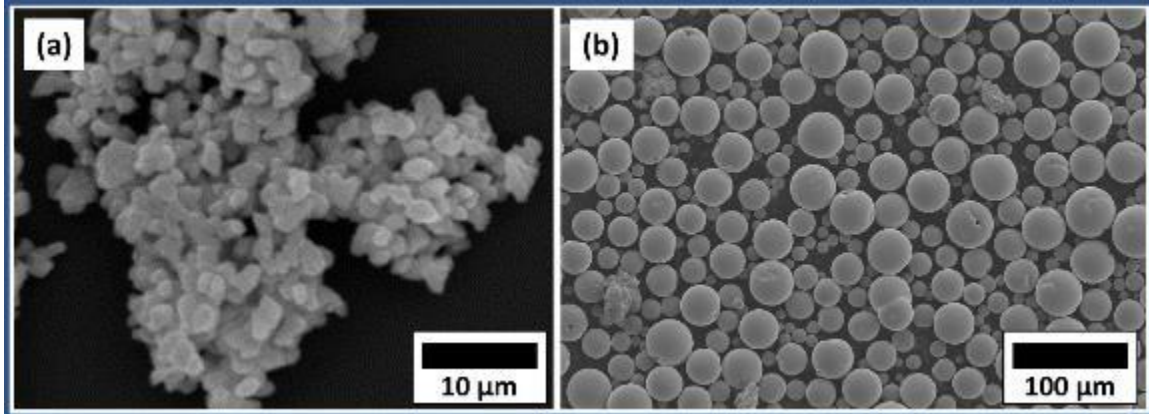


Figure 2.8. Example images of (a) as-reduced Mo powders [57] and (b) SEM micrograph of commercially available Mo powders.

2.4.2 Powder metallurgy

Conventional processing of Mo and TZM, like other refractory metals and alloys, is done via powder metallurgy (PM), in stark contrast to the ingot metallurgy route used for most other engineering metallic materials [10, 54]. Due to the refractory nature of Mo, powder remains the starting feedstock for almost all the products and parts made from them. In PM, the powder is pressed to form green compacts, which are sintered into pellets or other simple shapes and formed into parts [58]. Mo powder is also processed into different forms based on demand; for example, it can be pressed and sintered into mill product forms like sheets, plates, foils, rods or bars as needed [59]. PM processing route and its variants like metal injection moulding (MIM) remain a crucial forming technique for Mo and other refractory metals. The prevalence of PM in their processing is due to the fact that it reduces and often eliminates the need for secondary operations [60], like machining and grinding that are time-consuming and expensive. Hence near-net shaping processes have a distinct cost advantage for these materials.

2.5 Future applications for Mo and TZM

Aerospace applications like advanced and efficient turbojets and scramjets capable of sustained supersonic or hypersonic flights will need materials with improved temperature resistance and load-bearing capabilities [61]. The current state-of-the-art superalloy materials have an operational ceiling temperature of 1350 K (1077 °C), and there has been a long demand from designers for

materials which can perform in the range of 1400 to 2300 K (1127 to 2027 °C) [61, 62]. Figure 2.9a shows the ultimate tensile strength with temperature for a variety of materials, including superalloys and refractory metals (Adapted from [63]). Similarly, increasing demand for electrical energy, the propensity of electric vehicles and push for renewables necessitate power electronics semiconductors that can perform longer and at higher loads. A major limitation currently is the packaging of these materials, which necessitate increased cooling performance, resistance to thermal cycling by close matching of CTE, and reliability at higher junction temperatures. Figure 2.9b shows the CTE for various materials and how they compare to that of power electronics semiconductors (Adapted from [64]).

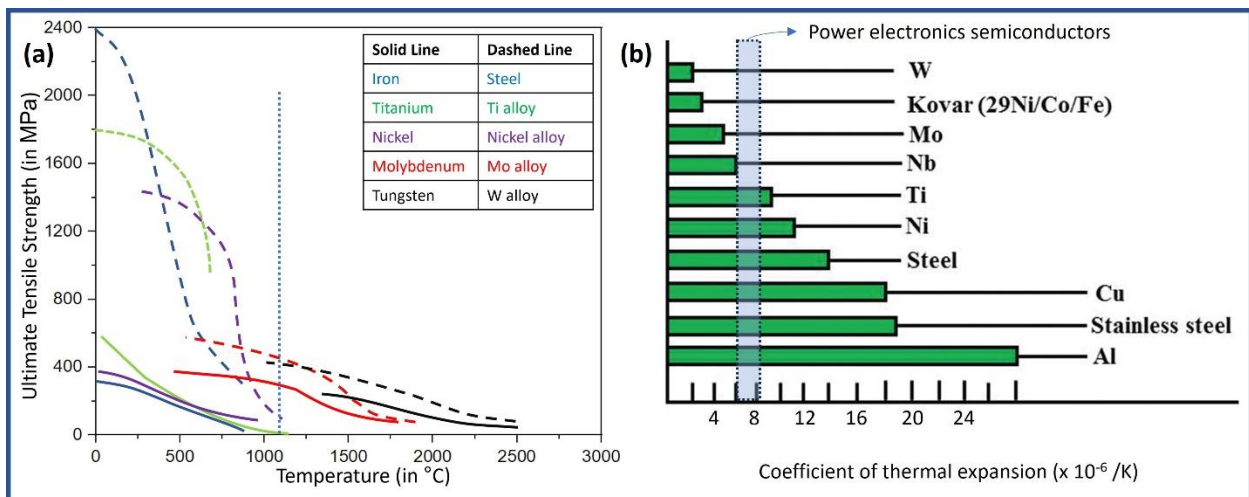


Figure 2.9. (a) Ultimate tensile strength vs temperature, and (b) CTE for various materials, including refractory metals (Adapted from [63, 64]).

Ceramics and composites have met some of the needs of the aerospace industry. Still, materials with good thermal conductivity which do not require intense cooling are ideal for applications like the hot sections of turbines. These turbine blades are presently manufactured out of superalloys [65]. For power electronics semiconductor cooling applications, conventional Cu or Mo-Cu laminate heat sinks do not offer suitable CTE matching and often larger systems with forced air or liquid cooling is necessary [66]. Refractory metals would be ideal for such applications if the grain-boundary embrittlement and high-temperature oxidation issues can be mitigated and a suitable processing technique is developed for these materials [67]. Powder bed fusion additive

manufacturing has been proposed as an alternate processing technique in this aspect, with more than one benefit.

2.6 Powder Bed Fusion

Powder bed fusion (PBF) is one of the key categories of additive manufacturing (AM) processes defined under ISO/ASTM 52900:2015 as a “process in which thermal energy selectively fuses regions of a powder bed” [68]. The PBF process has been studied for various materials due to the ability to fabricate parts without the need for tooling, despite the higher cost of powder feedstock [69-73]. PBF processes are highly desirable for Mo since there is no additional material cost disadvantage in the powder processing of these materials due to the prevalence of powder feedstock in their conventional processing. PBF processes can be mainly categorized into two based on the source of the “thermal energy” used to fuse the material: (i) Electron-beam powder bed fusion (EB-PBF) and (ii) Laser powder bed fusion (LPBF).

In EB-PBF, as the name indicates, the thermal energy source is a high-energy electron beam (~3000 W) [74]. Figure 2.10 shows the schematic of an EB-PBF system with its different elements [75]. A heated filament acting as a cathode emits electrons in such a system, and an anode accelerates these. The accelerating voltage is usually between 50 kV to 400 kV. Using magnetic lenses/coils, the electron beam is focused and scanned, as necessary, onto the powder bed. The energy of the electron beam is transferred to the powder bed (which is usually pre-heated and sintered in place by the beam at a higher scan speed) to cause the powders to melt and fuse with the substrate. The entire chamber is evacuated (often to $\sim 10^{-4}$ torr) to allow for free travel of electrons and avoid diffusing the EB. Some systems use Helium gas (at $\sim 10^{-2}$ torr) for dissipating electrical charges in the powder and for the thermal stability of the system [76].

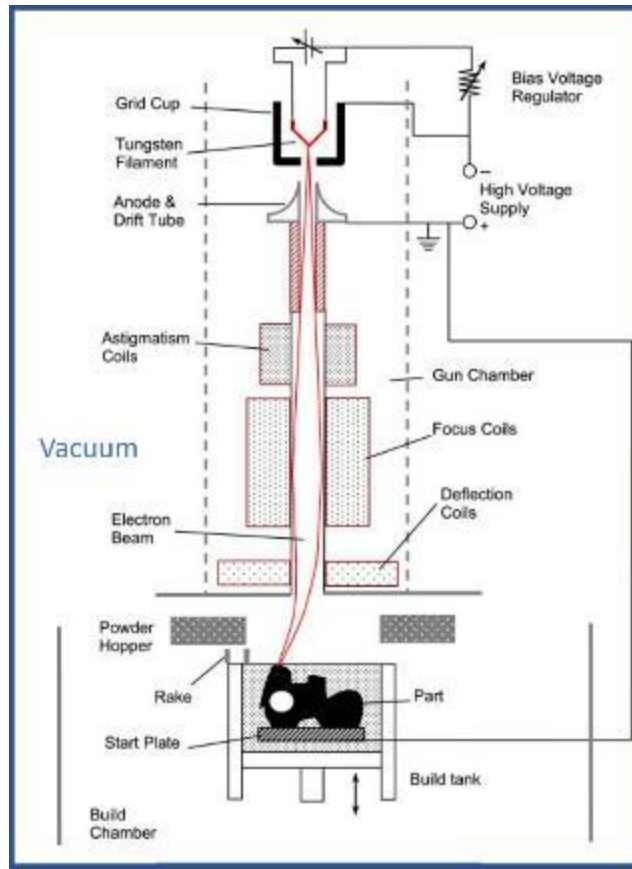


Figure 2.10. Schematic of an EB-PBF system (Adapted from [75])

Due to the nature of this process, it is highly suited for reactive metals like titanium and magnesium [73]. The use of a vacuum atmosphere favours lower cooling rates and allows for reduced residual stresses [77]. But the process suffers from poorer dimensional accuracy and surface roughness from the large melt pool ($\sim 600 \mu\text{m}$) created in the process [78].

LPBF system uses a laser with a power of 100 to 400 W typically (1000 W available in some systems) as the source of thermal energy instead of an electron beam. Nd:YAG lasers with a wavelength λ of $\sim 1064 \text{ nm}$ are most commonly used [75]. A lower energy tighter laser beam allows for smaller melt pools of size $\sim 200 \mu\text{m}$, depending on the material. Smaller melt pools permit the creation of parts with finer features, intricate geometries, and higher dimensional accuracy using the LPBF process [79]. Unlike EB-PBF, the LPBF process is carried out under an inert atmosphere

[3]. The LPBF process, which will be the focus of this thesis, is discussed in greater detail in the next section.

2.7 Laser Powder Bed Fusion Additive Manufacturing

2.7.1 Overview of the LPBF process

LPBF AM is a manufacturing process that has gained significant attention in recent years due to its potential to fabricate complex three-dimensional (3D) geometries with high accuracy and precision for various materials [80-83]. LPBF is a 3D printing technology that utilizes a high-energy laser beam to selectively melt layers of metallic, ceramic, or polymeric powders to build a 3D object layer-by-layer. For metals, as “metal 3D printing”, LPBF is particularly popular as it allows for tight tolerances and high surface finishes, making it an ideal solution to produce components that require a high degree of precision, such as medical implants and aerospace parts [84]. For Mo, the LPBF process is highly desirable since there is no additional material cost disadvantage in the powder processing of these materials due to the prevalence of powder feedstock in their conventional processing. LPBF enables the creation of channels within a part or other internal features, which can be used for cooling or fluid transport in aerospace and medical applications [85]. Additionally, LPBF can produce parts with intricate lattice structures that offer high strength-to-weight ratios, making them ideal for lightweight components and specialty applications in aerospace and automotive applications [86, 87].

Figure 2.11 shows a simplistic schematic of the LPBF process. Before the process starts in the LPBF machine, a 3D model of the file is processed using dedicated software, which prepares layer information via a step called slicing. This information gets transferred into the machine for the LPBF process. The process starts by preparing a thin layer of metal powder onto a substrate placed on the build platform, where it selectively melts the powders using a high-energy laser. The selective melting is performed based on the layer information prepared from the digital file via slicing. Once a layer is processed, the build platform lowers, and a recoater spreads a new layer of powder on top of the previous layer. The process is repeated layer by layer, fusing each subsequent layer onto the last layer until the final part is complete [88]. The process is performed in a controlled environment, typically in a chamber filled with an inert gas to prevent the oxidation of the metal powder [89].

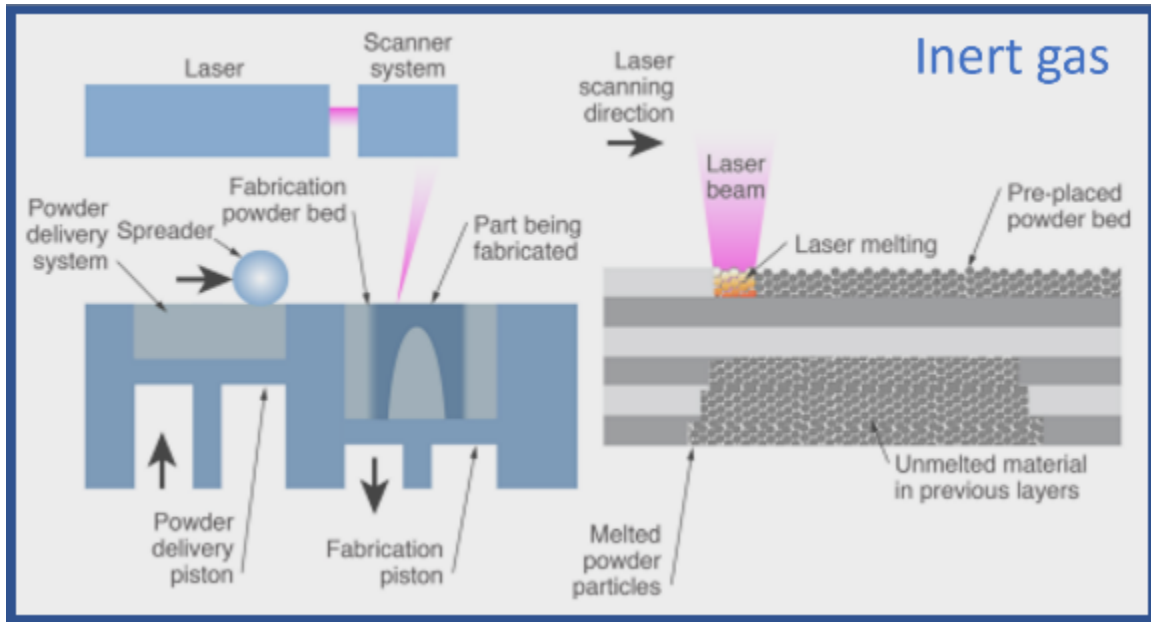


Figure 2.11. Schematic of an LPBF system (Adapted from [89])

The properties of the parts produced using the LPBF process depend upon many process parameters, including the laser power, powder layer thickness, scanning speed, powder bed temperature, and the size and distribution of the powder particles [90]. The optimization of the LPBF process for a part involves the control of these and other process parameters along with a laser scan strategy, to achieve better mechanical properties, such as tensile strength, fatigue resistance, and ductility, as well as improving the surface finish and dimensional accuracy of the parts [91, 92]. Figure 2.12 lists the major parameters influencing the quality and properties of the LPBF-processed parts.

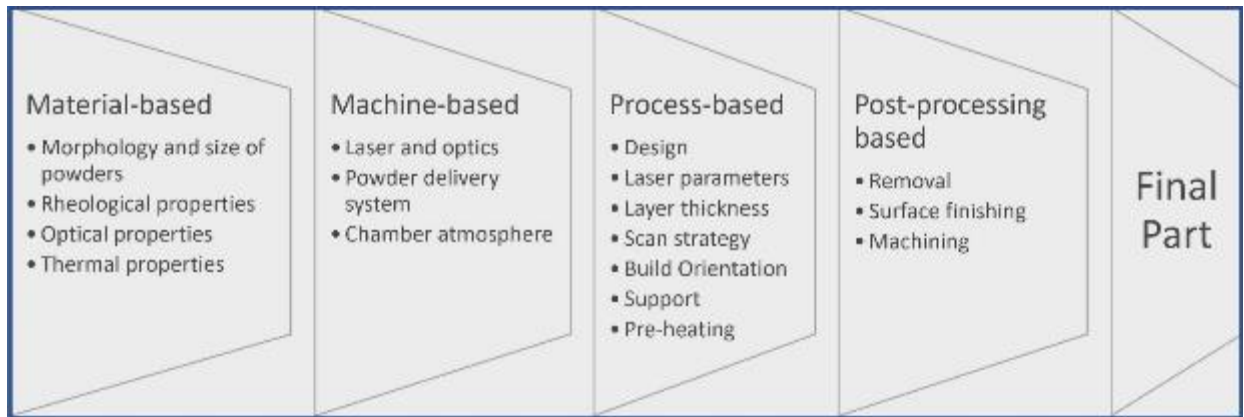


Figure 2.12. List of major parameters influencing LPBF processed part.

2.7.2 Key process parameters

The LPBF process has numerous parameters, as indicated in the earlier section. Rehme and Emmelmann [93] indicated that more than 130 parameters could affect the LPBF process. While many of these are pre-defined with the choice of the machine and the powder feedstock, numerous process parameters are still available for optimizing the process. The key process parameters for LPBF include layer thickness (LT, in μm), laser power (P, in Watts), hatch distance (HD, in μm), point distance (PD, in μm) and exposure time (ET, in μs) [94]. In this context, the terminology is defined as follows: layer thickness is the set thickness of the powder layer, hatch distance is the distance between two adjoining tracks of molten pools, point distance is the distance between two positions where laser power shines, and exposure time is the time for which the laser is incident at a position.

Figure 2.13 visually represents the process parameters in the LPBF process. The interaction of the laser beam with the powder material causes the powders to melt locally and create a molten pool. The laser moves to a different position after the exposure time. The process essentially links molten pools into tracks. The LPBF process is a track-by-track layer formation and a layer-by-layer part fabrication process, where the individual melt pools are building blocks. Equation (2.11) highlights the relationship of the parameters as an expression for the input energy density (ED, in J/mm^3) into the powder bed. The process parameters are interconnected and often linked to the material used or limited by the machine used [83]. For example, choosing a powder feedstock material will

govern the layer thickness, the requisite laser power to melt and fuse such a layer, and the nature of the protective atmosphere required. The layer thickness affects the dimensional accuracy and surface roughness of the part produced [79].

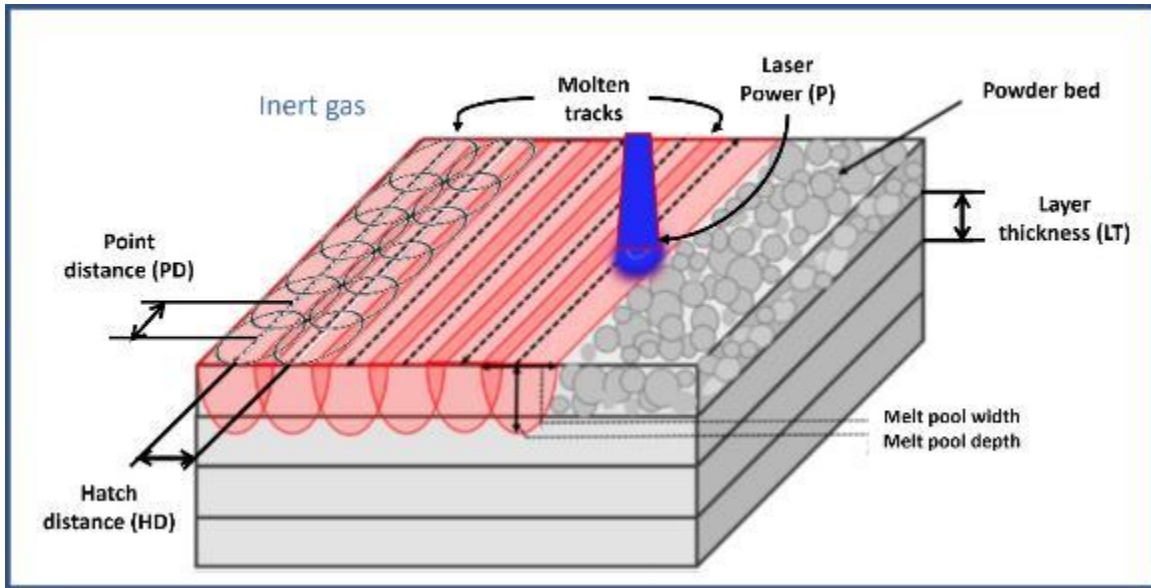


Figure 2.13. Visualization of the processing parameters in LPBF (Adapted from [95, 96]).

$$ED = \frac{P \cdot ET}{PD \cdot HD \cdot LT} \quad (2.11)$$

The melt pool, which is the building block of the LPBF process, has various characteristics dependent upon these parameters. The melt pool temperature increases with increased laser power or ED [97]. The temperature gradient rises linearly with increasing laser power and is generally more pronounced with low thermal conductivity materials [98]. Melt pool lifetime, which is the duration from the melting of the powders to the solidification of the molten pool, increases with laser power [99]. Melt pool dimensions, the width and depth increase with ED. In addition, the stability of the melt pool, which is a function of the ED and the material properties, can lead to defects in the LPBF processed part [100].

The laser scan strategy is an additional control to optimize the LPBF process. Figure 2.14 lists some typical laser scanning strategies used in the LPBF process: (a) uni-directional, (b) bi-directional, (c) island strategy, (d) spot strategy, or (e-f) combinations of such strategies [101]. Researchers have optimized scan strategies to achieve optimum processing conditions for various materials under LPBF and discussed the advantages of key scanning strategies [101-103]. The scanning strategy, which dictates the travel of the energy (and thereby, heat) source during the process, affects the direction of heat flow. For example, long uni-directional scans have been linked to increased residual stress, which can cause defects in the parts produced [101]. Spot or island strategies can mitigate this risk. In addition to these per-layer strategies, the start positions of the tracks can be shifted through rotation of the track layout for the next layer to reduce the residual stresses. Figure 2.14(g-i) represents the three common layer-wise rotation strategies used in LPBF [102]. The 67° rotation, for example, gives a large number of layers before the realignment of the scan start-positions and tracks occur. This results in the resulting samples having randomly oriented grain structures due to the varying orientations of the melt pool boundaries, which disrupt the epitaxial columnar growth [103].

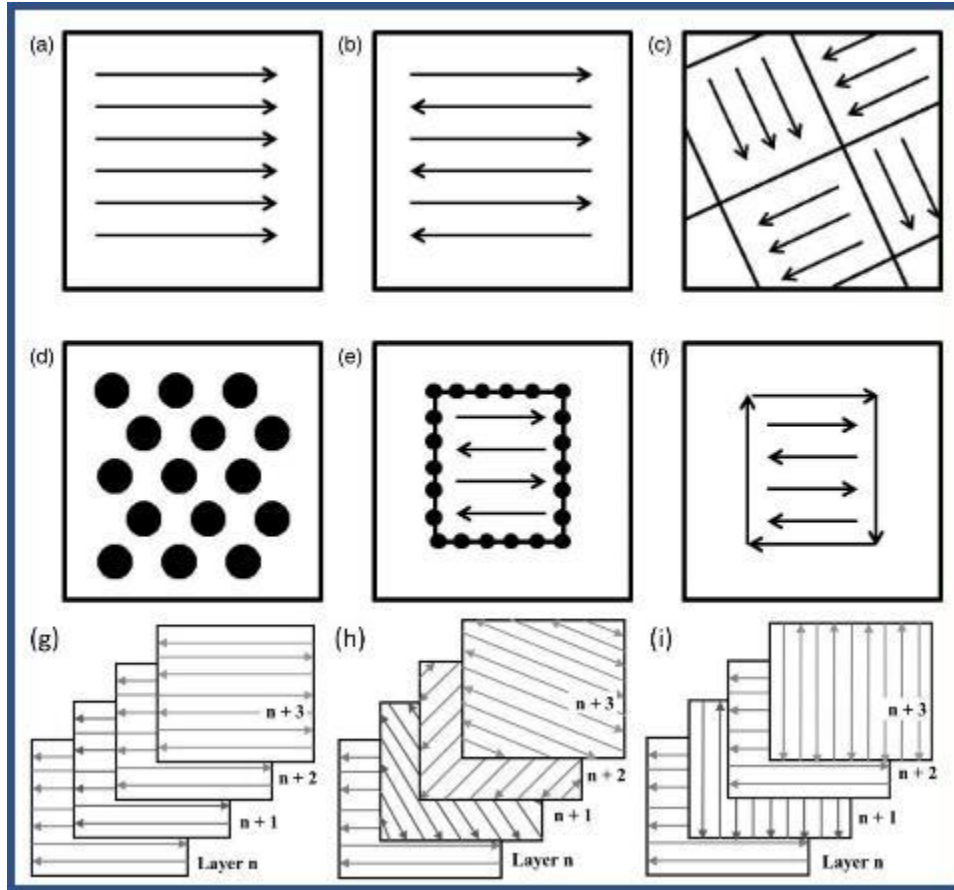


Figure 2.14. Typical laser scanning strategies in the LPBF process. (Adapted from [101, 102])

2.7.3 Powder feedstock and substrate

Powder feedstock is one of the most important components in the LPBF process. The size, morphology, chemical composition, mechanical and metallurgical properties, and thermal, optical and rheological characteristics play a key role in the LPBF process [104]. Figure 2.15a details some of the powder properties studied in LPBF and the critical attributes of the powder bed quantified as part of the preparation for the LPBF process. Figure 2.15b-d show SEM micrographs of Mo metal powders [105]. Powder with spherical particles of size between 15 to 45 μm is typically favoured due to its flowability and ease in packing them into the bed of layer thickness suitable for LPBF [106]. The maximum powder particle diameter in relation to the layer thickness can also lead to issues in the powder bed density [107]. Non-spherical powders tend to interlock mechanically, present flow challenges, and result in uneven powder beds or poor bed density. This

can create uneven layers upon melting, which affects the subsequent layer, cascading into part quality issues with defects like unmelted powders and porosity [108].

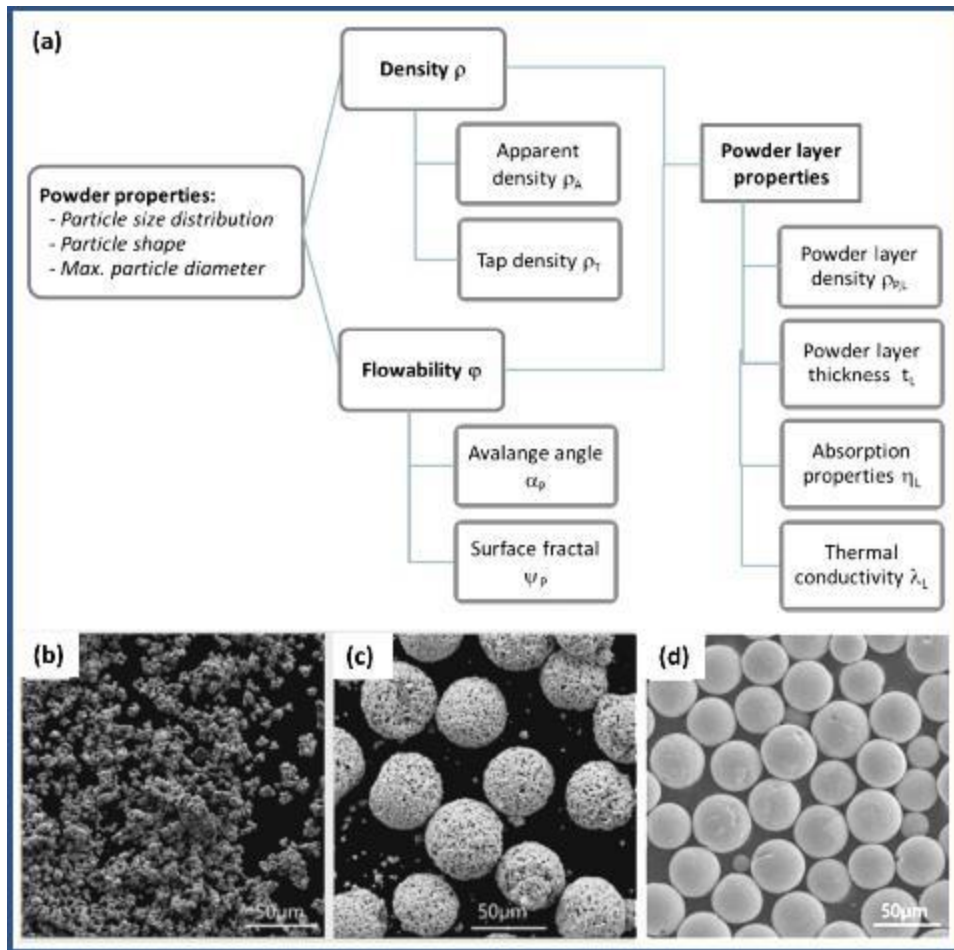


Figure 2.15. (a) Some key attributes of powder studied in LPBF, and (b-d) SEM micrographs of some metal powders. (Adapted from [105, 107]).

Due to their high surface area to volume ratio, metal powders are prone to oxidation and other contamination by gas or moisture adsorption. Oxidation and other surface contaminants can affect the laser absorptivity and lead to the lack of fusion defect. Figure 2.16a provides the laser effective absorptance vs bed packing density for Fe and Cu powders, while Figure 2.16b shows the variation of thermal conductivity with respect to temperature and that in the presence of a gas for various alloy powders used in LPBF [109, 110]. These can also cause poor powder bed quality and lead to the degradation of part quality. In addition, as discussed in Section 2.2.2, O contamination can cause GB embrittlement for Mo, leading to defects in LPBF processed parts.

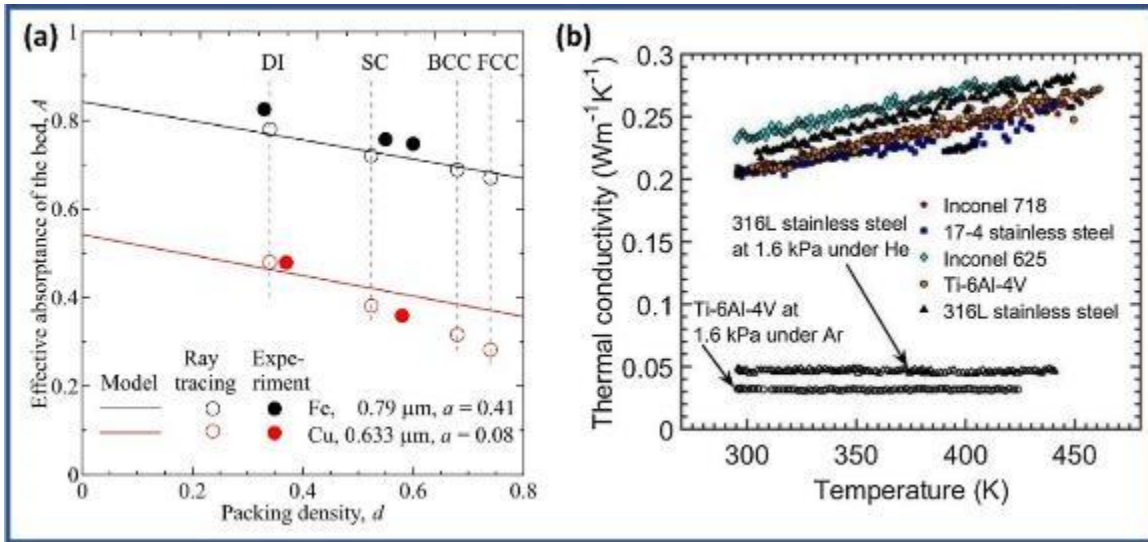


Figure 2.16. (a) Absorptance as a function of bed packing density ([109]), and (b) Thermal conductivity as a function of temperature for various metal powders [110].

Like powder feedstock, the substrate (also called baseplate) forms a critical building block of parts manufactured using the LPBF process. The surface of the substrate needs to be flat and free from oxidation or any other contamination to ensure sufficient adhesion and achieve ideal powder bed density [111]. In addition, the substrate works to constraint the part during the process and hence needs to be able to resist deformation. The heating and cooling involved in the LPBF process cause expansion and contraction of the part and the substrate upon which it is built. The heating and cooling cycles imposed on the part lead to residual stresses. Figure 2.17 shows a representation of the sources of the stress in the LPBF process and the distribution along the substrate and part [112, 113]. The same material as the powder, or material with a closely matching coefficient of thermal expansion (CTE), is often desired for the LPBF process to reduce differential expansion and stresses and limit part delamination and other issues. Some systems allow substrate heating to temperatures as high as 1273 K (1000 °C) during LPBF, followed by controlled cooling, in an effort to reduce the cooling rate and eliminate issues related to it [114].

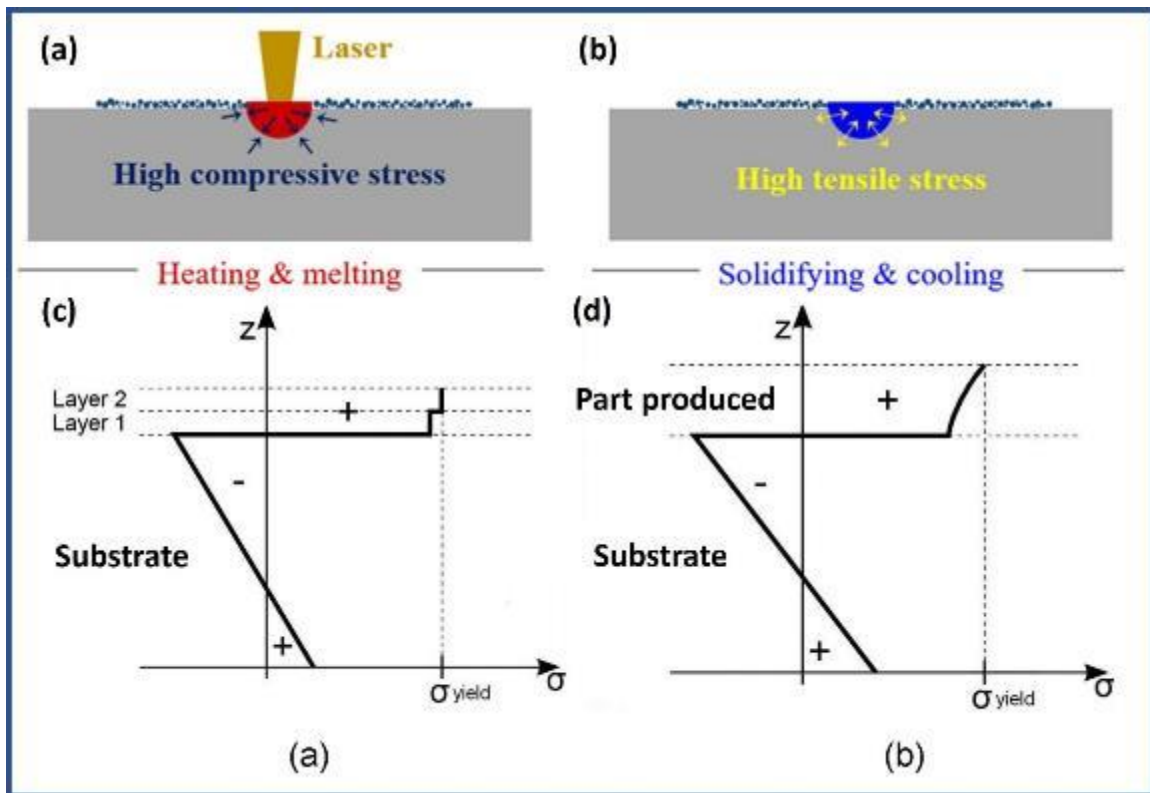


Figure 2.17. Stresses in the LPBF process from the (a) heating and (b) cooling cycles (Adapted from [112]). Distribution of residual stresses in substrate and part after (c) 2 layers and (d) part is produced (Adapted from [113])

2.7.4 Build atmosphere

In the LPBF process, the build atmosphere is another parameter to consider. The LPBF process is typically conducted under an inert gas atmosphere, usually of argon (Ar), nitrogen (N₂), helium (He), etc., unlike the EB-PBF process, which is conducted under a vacuum. Like in welding, the main purpose of the inert gas is to shield the process from the ambient atmosphere and prevent oxidation. Additionally, with the shielding gas flow, the added benefit of removing process emissions (spatter, etc.) keeps the build area and build chamber clean, as shown in Figure 2.18a-b [115]. The selection of the gas and its purity significantly impact the quality and properties of parts fabricated through LPBF. Ar is the most commonly used inert noble gas for filling the build chamber [116]. While N₂ is more economical and typically unreactive, certain materials containing elements such as Ti, Nb, and V can react with the printed material during melting.

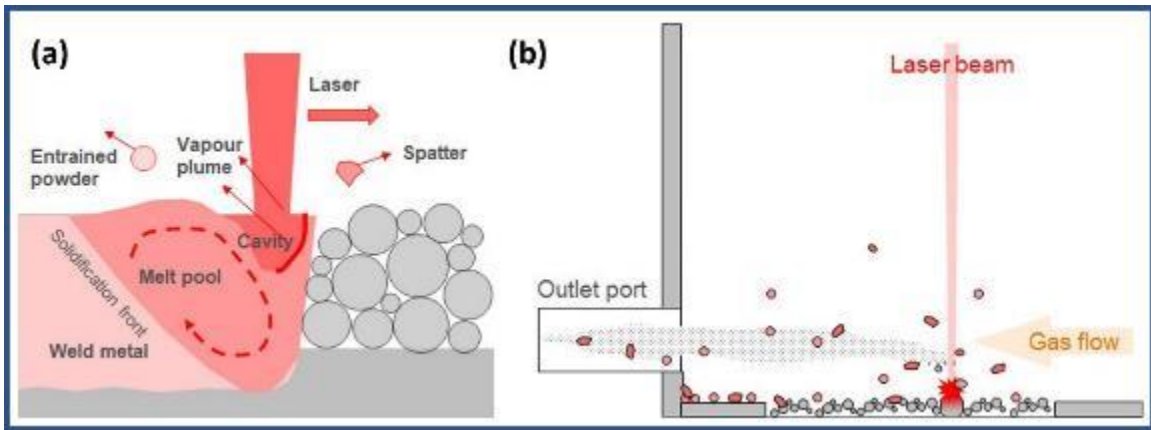


Figure 2.18. (a) Typical LPBF process emissions, and (b) gas flow used for removal of process emissions (Adapted from [115])

Traore et al. [117] quantified the difference in process emissions under Ar and He for LPBF processing of nickel and reported that high denudation but lower emission was observed under He, as indicated in Figure 2.19a. Wang et al. [118] studied the effect of Ar, N₂, and He build atmospheres on LPBF-processed Al-12Si parts. Figure 2.19b shows the results of the study with the mechanical properties of the parts versus ED for different atmospheres. They reported that higher pore content was observed in parts built under helium atmosphere at higher ED compared to the other atmospheres, leading to a loss in ultimate tensile strength (UTS) and ductility.

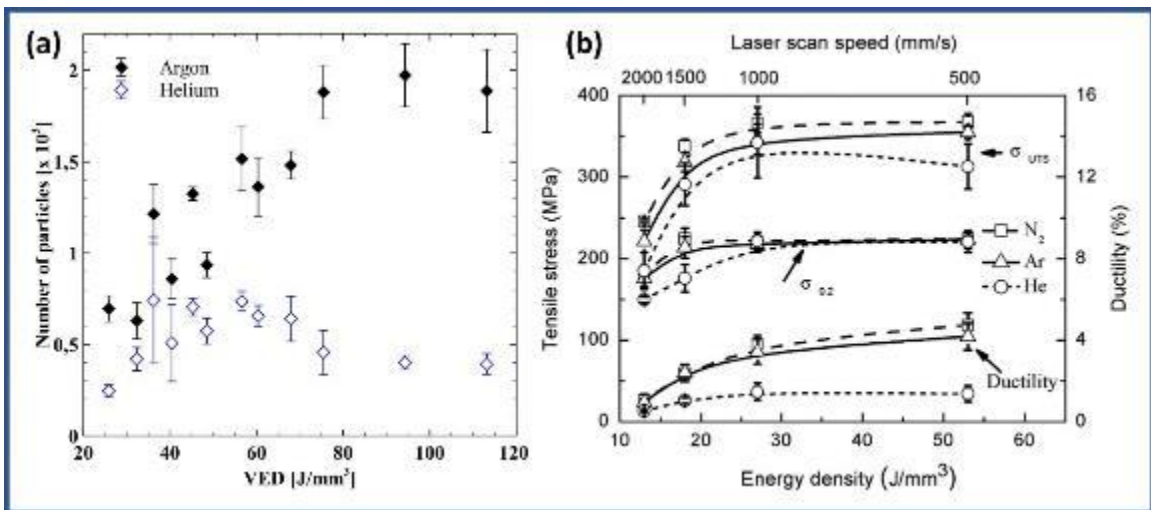


Figure 2.19. (a) LPBF process emissions under Ar vs He [119], and (b) UTS vs ED for Al-12Si under various build atmospheres in LPBF [117].

In addition, research has also explored the effects of using gas mixtures on the microstructure and properties of parts manufactured using stainless steel alloys. S. Roy et al. [119] reported that the use of the He+Ar+CO₂ gas mixture achieved the closest dimensional stability, while the Ar+N₂ gas mixture resulted in the highest hardness and UTS in the study. Although most system manufacturers recommend using Ar gas during fabrication, the possibility of using different gas atmospheres exists within LPBF.

2.7.5 Defects in LPBF processed parts

As discussed in earlier sections, AM processes, including the LPBF process, are modern manufacturing methods with numerous advantages. Still, the process comes with certain setbacks. The outcome of the LPBF process depends on the numerous parameter combinations, making it challenging to optimize them for a particular combination of material, machine, and design/part. The main defects encountered in the LPBF process are balling, delamination, deformation, high surface roughness, porosity, and cracking [84].

2.7.5.1 Balling defect

Balling is the presence of small spherical ball-like particles or surface irregularities formed on the melt tracks, as seen in Figure 2.20 [120]. Balling affects the quality of a processed layer/surface and the surface finish. It can also impede recoater movement, cause damage and lead to a cascade of other defects in the part [75]. Among the process parameters, laser power, exposure time, layer thickness, powder compositions, etc., are critical to balling phenomena. The use of a higher laser power and exposure time or reducing the layer thickness usually resolves balling [75, 120].

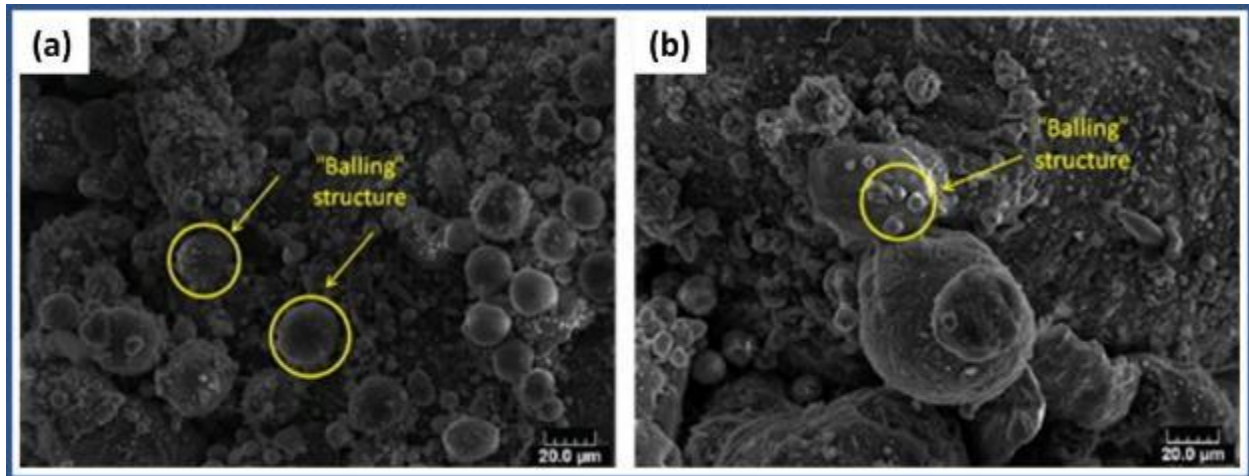


Figure 2.20. Balling defect in the LPBF process [120]

2.7.5.2 Delamination, deformation and high surface roughness

Delamination is another defect in LPBF parts where printed layers are not fully attached due to a lack of fusion or become separated due to high residual stresses. Substrate heating has been reported as beneficial for materials prone to delamination from high residual stresses [121]. These stresses can also cause warping or deformation of parts. Dimensional accuracy and near-net-shape forming is the main selling point for LPBF. High surface roughness, a defect related to laser scanning and the powder bed, has been widely studied on up-facing surfaces of finished parts [52]. Roughness can also arise on down-facing surfaces when printing overhangs over unmelted powder rather than previously solidified material. Figure 2.21 shows images of some of these defects in LPBF-processed samples.

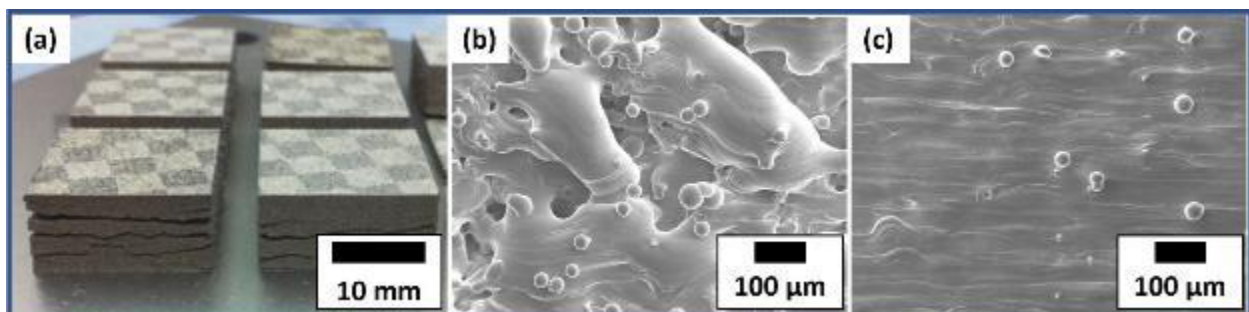


Figure 2.21. (a) Delamination defect, (b) high surface roughness defect, and (c) ideal surface roughness in LPBF-AM (Adapted from [121, 122])

2.7.5.3 Porosity defect

Porosity, a major defect in LPBF-processed parts, is essentially a discontinuity in the material makeup of the part and can be of different forms. Lack-of-fusion pores are formed either from the lateral spacing of the melt pools (from the hatch and point distances) or when the overlap depth between melt pools of adjacent layers is less than the layer thickness [101]. Laser power, exposure time, and hatch spacing can influence melt pool size and their stitching together, leading to this defect. Processing windows identified through trials for the combinations of these parameters can eliminate lack-of-fusion porosity [123]. Another type of porosity is gas-induced porosity. It originates from gas trapped within the powder particles during its manufacturing. During the LPBF process, melt pool lifetimes are short (in microseconds), and the time for the gas to escape from the melt pool is very short, leading to their trapping within the solidifying region [124]. Keyhole porosity is another type of porosity defect in LPBF-processed parts. In keyhole mode LPBF where high laser powers are used, the instability near the bottom of the melt pool from the high temperatures and vaporization of metal can lead to defects called keyhole pores [125]. Figure 2.22 depicts the different porosity defects reported in the literature [101, 124].

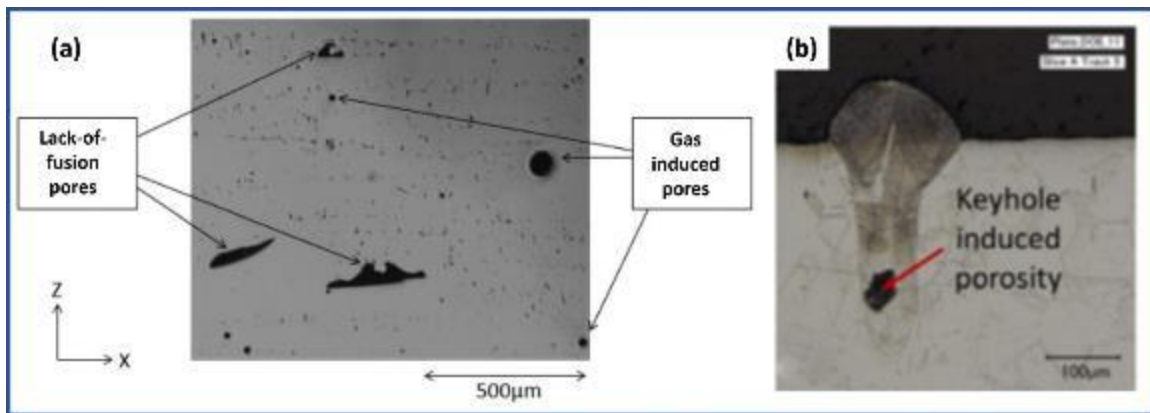


Figure 2.22. (a) Lack-of-fusion pores, gas-trapped pores [101], and (b) keyhole pores [124].

2.7.5.4 Cracking defect

Cracking is another major defect in LPBF-processed parts. There are two types of cracks: hot cracks and cold cracks. Hot cracks occur during solidification and are also called solidification cracks. These occur due to insufficient strength in the melt pool structure to withstand contraction during solidification [124]. Cold cracks are caused by the residual stresses generated during the

LPBF process and are more common in LPBF. The high cooling rates and thermal gradients cause residual stresses in conjunction with cyclical heating and cooling. When the residual stress is higher than the yield stress, the part is forced to relieve the stress either via deformation or cracking [84, 124]. Materials with an inability to deform (brittle materials) inevitably crack to relieve residual stress. Cold cracking is a major issue in LPBF-processed Mo samples and is discussed in detail in the next section. The study to eliminate cracking in LPBF Mo is the basis of this thesis.

2.8 LPBF-AM of Mo and TZM

2.8.1 Progress in LPBF AM of Mo and TZM

Faidel et al. [126] performed one of the pioneering studies on LPBF AM of Mo. They used a preliminary comparative study of melt pools using laser welding on stainless steel and TZM sheets to identify the suitable processing window for Mo from known LPBF parameters for stainless steel. They performed experiments using a laser power of 200 W at various ED values by adapting the layer thickness and melt pool overlap (hatch distance). Spherical atomized Mo powder with a 10-45 μm size range was used, with N_2 as the shielding gas. They observed an improvement in part density with a reduction in layer thickness and reported that at 20% overlap, the prepared surfaces were smooth. Maximum densities of 82.5% were reported. An increase in overlap to 40% and 60% lead to a decrease in surface quality, including defects like lack of fusion and delamination. This was attributed to the increased energy input into the layers, which caused thermal strains and deformed the part. Figure 2.23 shows representative results from the study.

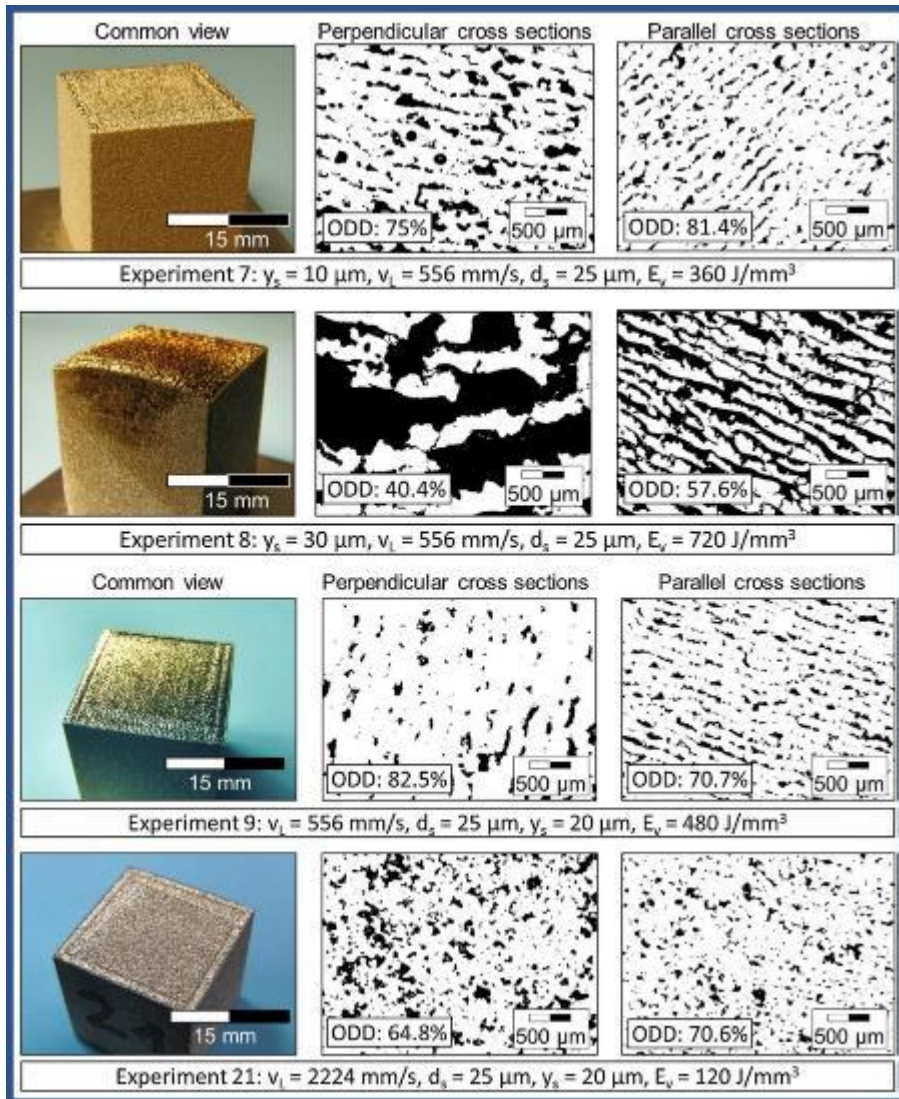


Figure 2.23. Representative images and microstructure from the study by Faidel et al. [126]

Leitz et al. [127, 128] used simulations and single-track experimental verifications to investigate the impact of powder bed properties on the LPBF processing of Mo. They found that Mo's high melting point results in the formation of small melt pools, which can be problematic for achieving high density through overlap control strategies due to the sensitivity of the process to the powder bed's morphological features. The study observed that an increase in laser power and ED contributed to an increase in melt pool width but not depth. No additional information on microstructure or defects was provided in the study.

Wang et al. [105] performed one of the most extensive early studies on the LPBF processing of Mo in the literature. Using plasma spheroidized powder and high laser power of 400 W under an Ar atmosphere, they reported maximum densities of 99.1% in the parts produced. Cracks were observed and characterized by the researchers. They observed that cracks created a network with distances corresponding to the hatch distance perpendicular to the building direction. These cracks then propagated along the grain boundaries of the columnar grains in the build direction. The study did not provide any quantitative discussion on cracking. However, using the provided literature micrographs (see Figure 2.24), a crack density of 7 cracks per mm² and a crack length of 550 ± 80 μm could be approximated.

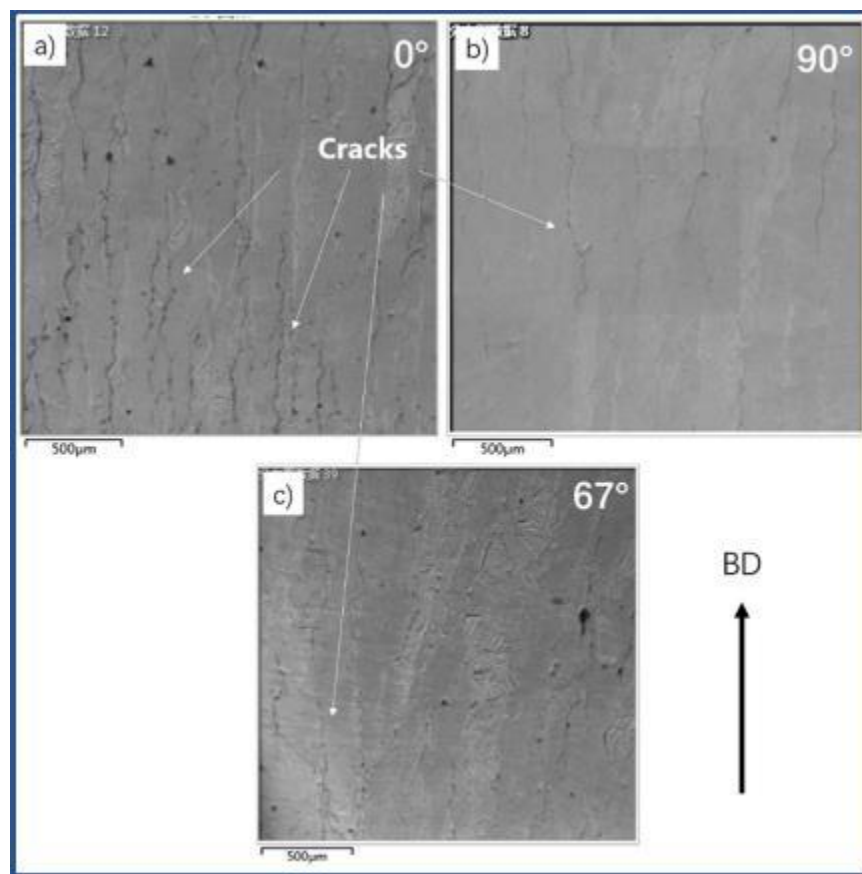


Figure 2.24. Cracking behaviour of LPBF Mo [105]

The study by Wang et al. [105] also investigated the influence of laser scan rotation strategies (0°, 90°, and 67°) and showed that rotating the scanning direction (0° to 90° strategy) layer by layer

could reduce the length of the longitudinal cracks, with no significant change to transverse cracks. The crack length could be further reduced by adding an offset between the starting points of the scan vectors to minimize stacking overlap and influence the thermal gradient. Rotating the scanning direction by 67° from layer to layer eliminated longitudinal cracks (Figure 2.24). The laser scan rotation by 67° leads to intertwined grain boundaries, which enhances crack growth resistance due to a better-distorted heat gradient, better interlocking of grain boundaries, and reduced match between metallographic preferred directions and heat gradients for epitaxial grain growth. Figure 2.25 details the results of the laser scan rotation strategy on the grain structure in LPBF Mo.

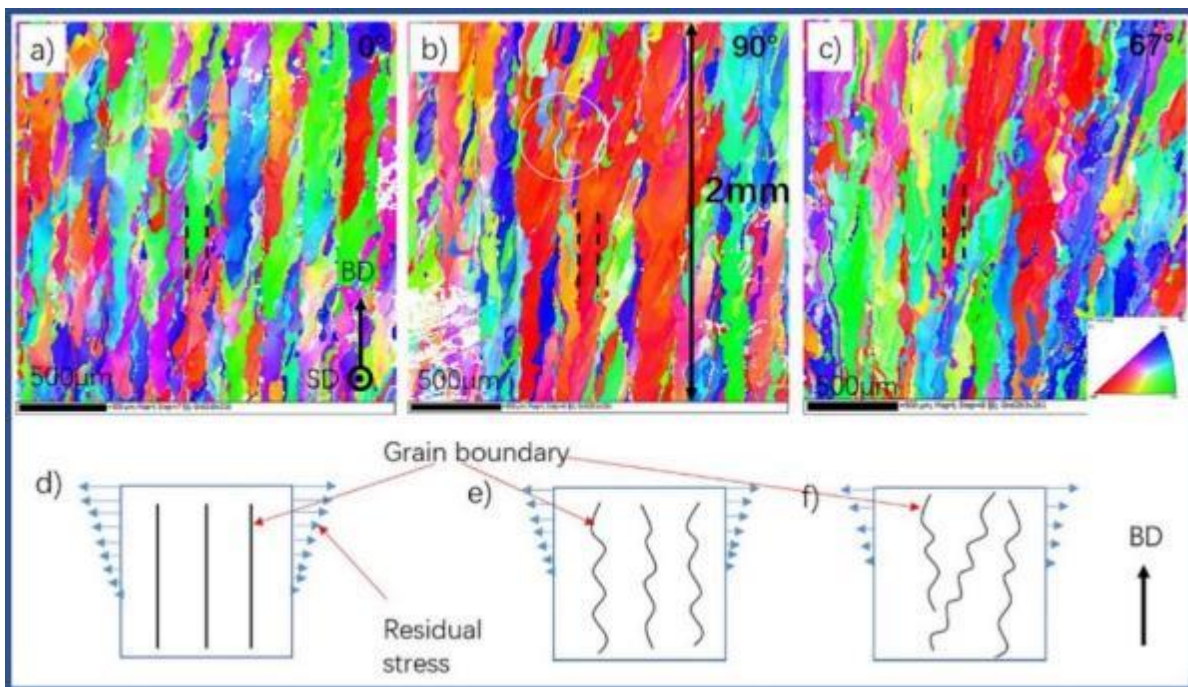


Figure 2.25. Influence of laser scan rotation (a) 0° , (b) 90° , and (c) 67° on grain structure in LPBF Mo. (d-f) GB and stress representations for the three conditions. [105]

They optimized the ED to reduce thermal stresses and developed a supporting structure to compensate for shrinkage and further decrease thermal stresses. The use of a support structure creates an envelope of low thermal conductivity powders surrounding the sample. Figure 2.26 shows the crack-free microstructure of the samples when support structures were used.

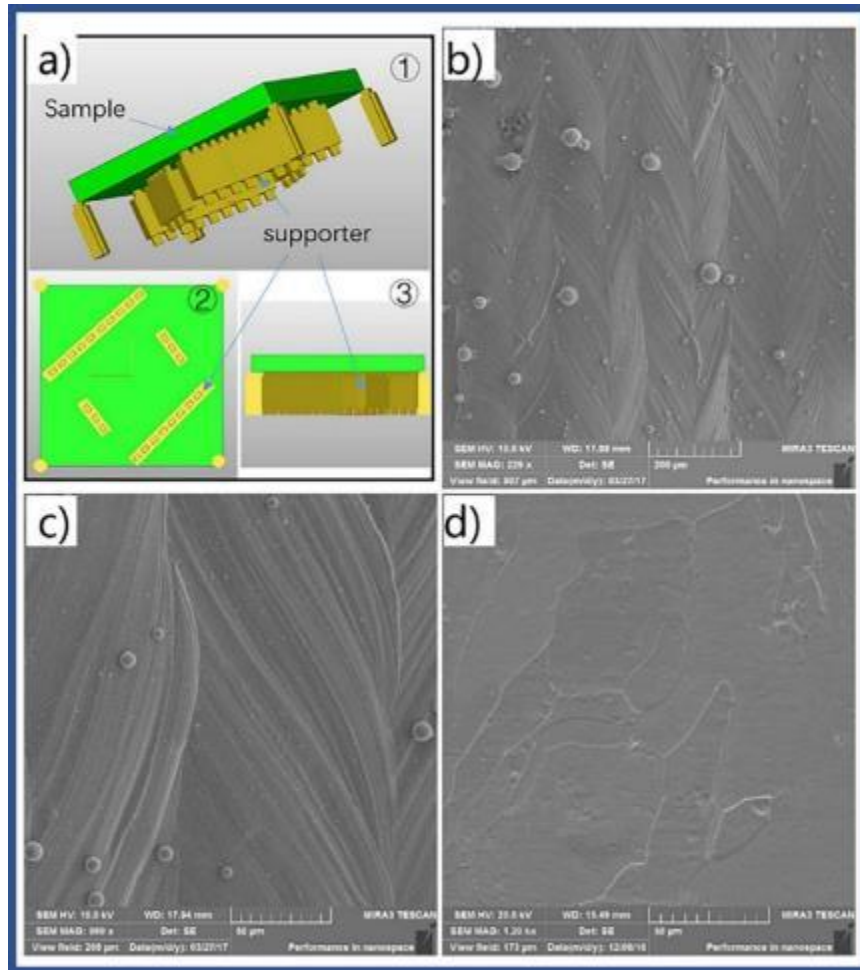


Figure 2.26. (a) Use of support structures and crack-free microstructures for Mo in (b-c) top surface and (d) along build direction. [105]

Braun et al. [129] studied the influence of oxygen on the defect structure in LPBF-processed Mo under an Ar atmosphere. Figure 2.27a-b shows the morphology of the powders used in the study. Using as-spheroidized and stored (for six months) Mo powders which had O content of 535 $\mu\text{g/g}$ and 1216 $\mu\text{g/g}$, respectively, they reported densities of 96.0 % and extensive cracking along the build direction. No quantification of cracking was provided, but a crack density of 16 cracks per mm^2 and average crack lengths of $870 \pm 70 \mu\text{m}$ could be estimated from the available micrographs. The cracks were observed to be located at the border of the molten track, and through an EBSD study, this was identified to coincide with the GBs (as seen in Figure 2.27c-d). They observed that the cracked GBs were high-angle GBs prone to cracking in Mo.

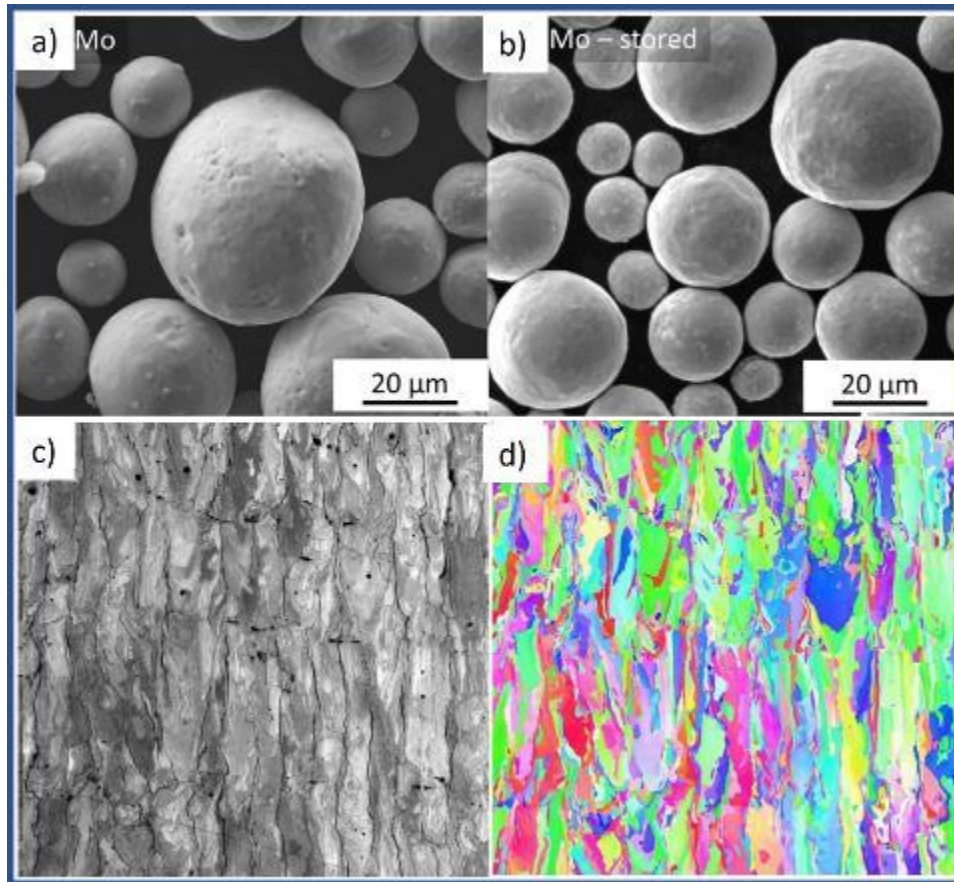


Figure 2.27. (a-b) Mo powders used in the study, and (c) microstructure and (d) IPF map from EBSD analysis. [129]

In the study, the LPBF part prepared using the stored Mo powder (1216 μg/g) showed an O content of 1150 μg/g, indicating that most of the O were retained in the built part. The parts showed similar cracking behaviour as the Mo sample prepared with as-spheroidized Mo powder. An investigation of fracture surfaces and GB surfaces showed large oxide particles, as verified by EDS and TEM analyses. Figure 2.28a shows the surface of a pore, while Figure 2.28b-c shows the fracture surface within the LPBF processed Mo part. Oxide particles, and in the case of higher oxygen content, an oxide film is visible at the GBs and fracture surfaces.

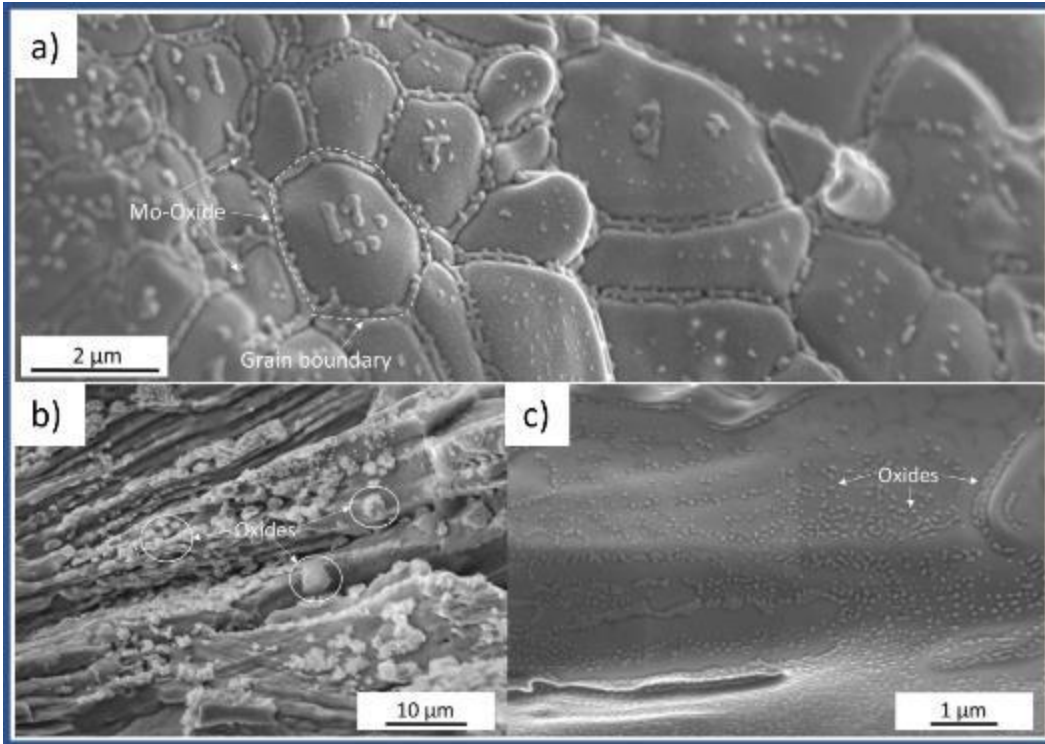


Figure 2.28. Oxides in LPBF processed Mo [129]

Kaserer et al. [130] reported a study on LPBF processing of Mo with C alloying (0.45 wt.%) and substrate heating at 773 K and 1073 K (500 and 800 °C) under an Ar atmosphere. The study reported the fabrication of crack-free samples through the alloying with C and substrate heating (Figure 2.29). They suggested that the addition of C changed the solidification mode from planar to cellular due to constitutional supercooling and that the cells are organized in colonies where a closed network of Mo_2C surrounds the alpha Mo phase. The study reported that the fracture mode changed from the typical intergranular mode for pure Mo to a mostly transgranular mode in Mo-0.45 wt.%C samples. A substrate temperature of 1073 K (800 °C) was deemed necessary to eliminate cracking and densify up to 99.7%. The study also indicated that about 50% of the O content and 12% of the C content in the powder feedstock was outgassed during the process at 1073 K (800 °C), resulting in a final O content of $\sim 76 \mu\text{g/g}$.

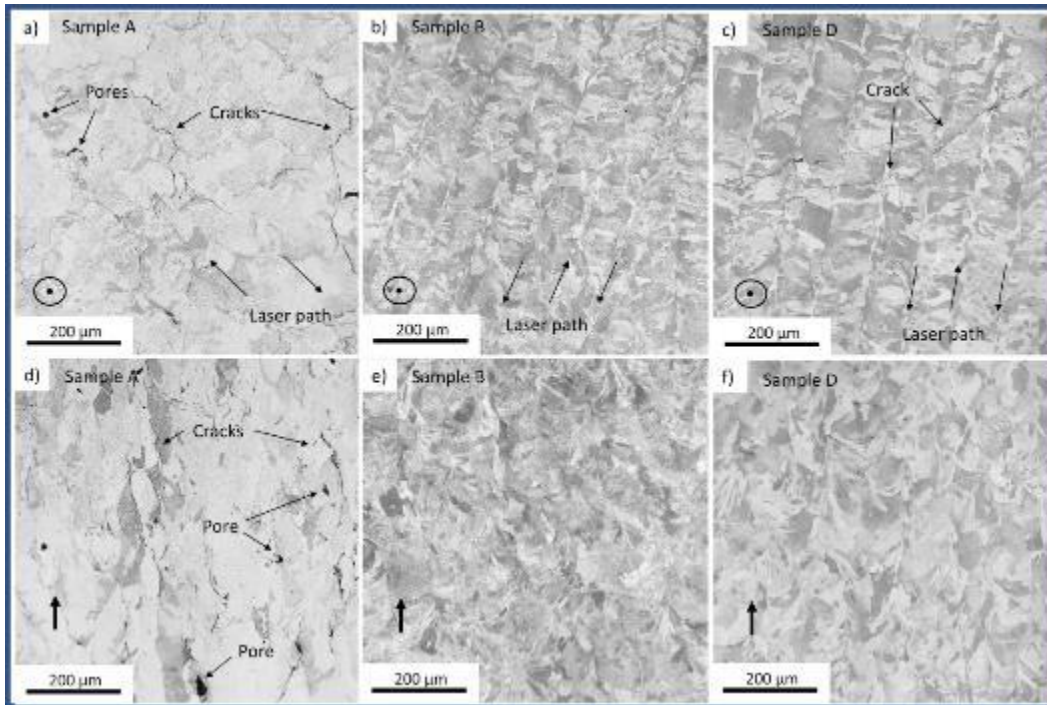


Figure 2.29. Microstructure of LPBF processed parts: (a, d) pure Mo with the substrate at 800 °C, (b, e) Mo-0.45 wt.%C at 800 °C, (c, f) Mo-0.45 wt.%C at 500 °C [130]

Higashi and Ozaki [131] studied the influence of LPBF process parameters on microstructure and crystallographic texture in Mo. They reported the fabrication of dense samples with low porosity and showed that porosity decreased with an increase in the ED and that an ED value above 150 J/mm³ was needed to achieve a porosity of <1%. They also observed that keyhole pores were always formed regardless of process parameters and attributed this to the oxidation behaviour of Mo. The study investigated the relationship between the process parameters and the resulting crystallographic texture (represented in Figure 2.30); a strong <110> fiber texture was observed at low scan speeds, while <001> texture was observed in samples processed at 800 mm/s. This was attributed to a change in grain growth direction within the melt pool. Additionally, a decrease in the ED at a low scan speed range resulted in a weak <111> texture formation. Information regarding cracking, although indicated, was not provided in the study.

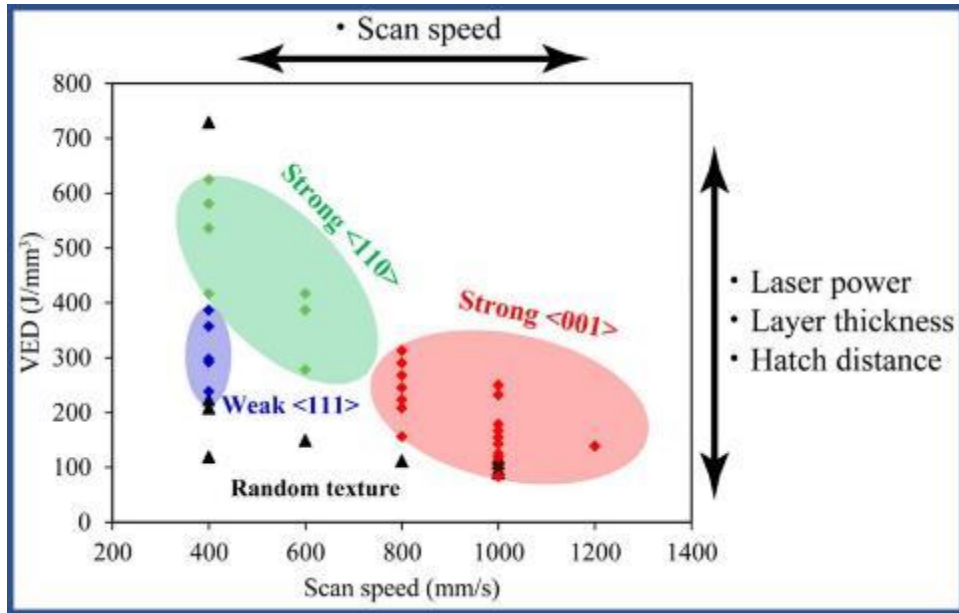


Figure 2.30. Influence of ED and scan speed on crystallographic texture in LPBF processed Mo [131]

Oehlerking et al. [132] studied the LPBF processing of pure Mo and alloyed Mo and reported that the fabricated parts exhibited cracking issues. Samples of density values of 98.5% for pure Mo and 99.4% for alloyed Mo were reported in their study. Alloying with rhenium (Re), even at 47.5 wt.%, did not suppress the cracking, and this was attributed to the presence of O, which is detrimental to LPBF-processed Mo. From the micrographs, a crack density of 9 cracks per mm² and average crack lengths of 360 ± 80 μm could be estimated for Mo, and the alloyed sample showed similar cracking. Figure 2.31 shows the microstructure of the LPBF processed Mo and Mo-47.5wt.%Re samples.

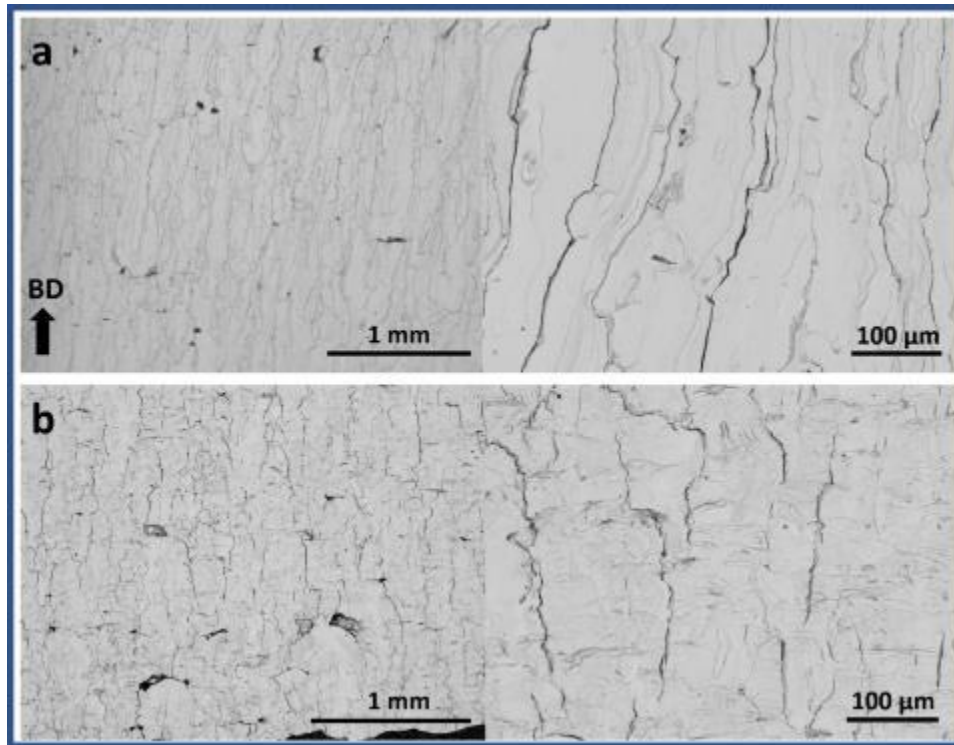


Figure 2.31. Microstructure showing cracks for LPBF processed (a) Mo and (b) Mo-47.5wt.%Re [132]

Guan et al. [133] reported the fabrication of pure Mo samples and Mo dosed with La_2O_3 . They reported a reduction in cracking in Mo-0.9wt. % La_2O_3 which was attributed to decreased residual stresses due to the additive. They indicated that samples with densities of 99.7% were fabricated. Crack number density at the surface was reported, and a decrease from 208 / mm^2 to 96 / mm^2 was claimed. For large samples where porosity was observed to be higher than 1%, the study performed hot isostatic pressing (HIP) treatment and indicated that densities of 99.6% could be obtained.

Kaserer et al. [134] reported the first study on the LPBF processing of TZM under an Ar atmosphere in literature. Using substrate heating at 1073 K (800 °C), they reported the fabrication of crack-free samples with a density of 99.7 %. They reported that due to the presence of oxygen-gettering elements like Zr and Ti, fracture surface or GB surfaces did not evidence any O and that the GBs were effectively purified. Through the use of EDS and TEM analysis, they suggested that O impurities were observed to be bound as ZrO_2 and in ternary molybdenum-titanium carbide $((\text{Mo,Ti})_x\text{C}_y)$ precipitates within the grains. They postulated that $((\text{Mo,Ti})_x\text{C}_y)$ precipitates have the

ability to dissolve O within. Grains elongated along the BD were reported, with a weak $\langle 111 \rangle$ fiber texture parallel to BD. The fracture mode was reported to be trans-granular, indicating that GB embrittlement did not occur. Figure 2.32 shows the microstructure and results of EBSD analysis for the LPBF-processed TZM sample.

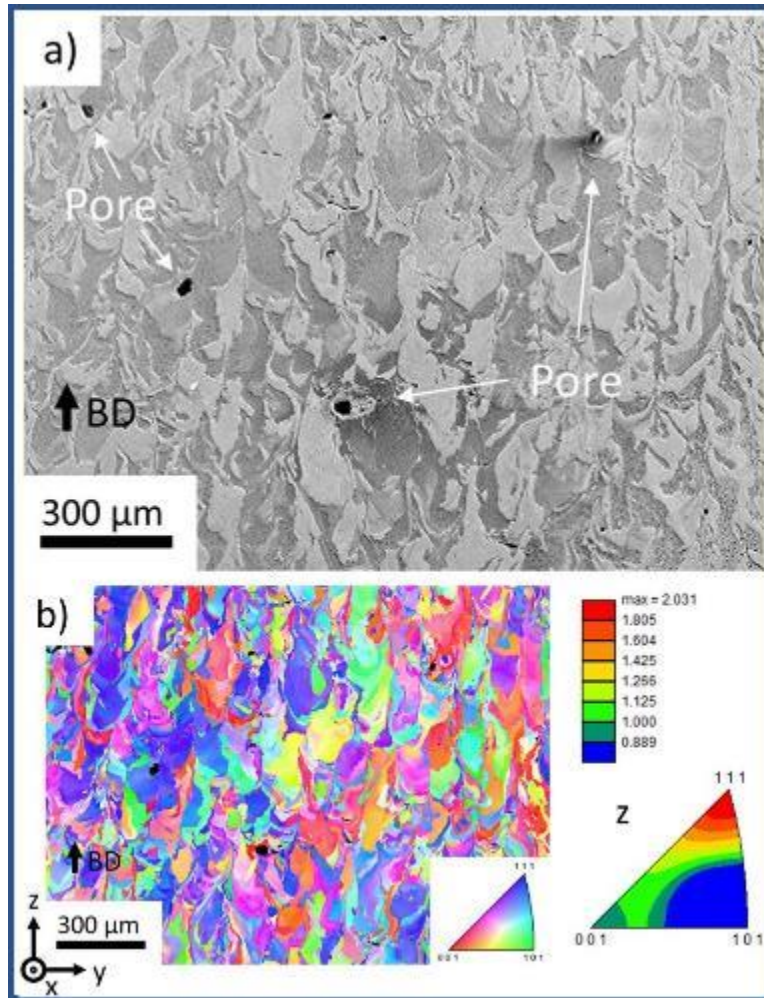


Figure 2.32. (a) Microstructure, and (b) EBSD map of LPBF processed TZM [134]

2.8.2 Key challenge in LPBF AM of Mo and TZM

The LPBF process provides the opportunity to fabricate complex structures out of Mo, but the cracking of LPBF-processed Mo is a key challenge that has to be overcome. As discussed in the previous section, the literature shows that cracking remains a major issue. The cracking of Mo occurs as the fabricated part cools, and the material is unable to relieve the residual stresses by deformation due to a lack of ductility. In LPBF-processed Mo, O enters the material from the

powder feedstock or the chamber atmosphere. This O is inevitably introduced into the melt pool, where it dissolves in larger amounts than the solid solubility. The cooling and solidification of the melt pool force the O out of the Mo lattice, and O segregates to the free surfaces and GBs. When the part cools further, the inherent brittleness of Mo GBs and the worsening of the GB cohesion due to the presence of O leads to the relieving of stresses via GB cracking. The use of support structures and substrate heating presents limitations in the design freedom offered by LPBF; hence an alternate protocol is needed to eliminate cracking.

2.9 References

- [1] E. Pink and R. Eck, "Refractory Metals and Their Alloys," in *Materials Science and Engineering*: Wiley-VCH Verlag GmbH, 2006, ch. 10.
- [2] ScienceDirect. "International Journal of Refractory Metals and Hard Materials - Aims and Scope." Elsevier B.V. <https://www.sciencedirect.com/journal/international-journal-of-refractory-metals-and-hard-materials> (accessed 03-April-2023).
- [3] C. Ren, Z. Z. Fang, M. Koopman, B. Butler, J. Paramore, and S. Middlemas, "Methods for improving ductility of tungsten - A review," *International Journal of Refractory Metals and Hard Materials*, vol. 75, pp. 170-183, 2018, doi: 10.1016/j.ijrmhm.2018.04.012.
- [4] K. Schwochau, *Technetium: Chemistry and radiopharmaceutical applications*. Germany: Wiley-VCH, 2000.
- [5] G. M. Ault, "NASA Technical Memorandum X-52135 - A decade of progress in refractory metals," 68th Annual Meeting of the American Society for Testing Materials, Lafayette, Indiana, 1965.
- [6] A. S. M. H. Committee, *Properties and Selection: Nonferrous Alloys and Special-Purpose Materials*: ASM International, 1990. [Online]. Available: <https://doi.org/10.31399/asm.hb.v02.9781627081627>.
- [7] "Proceedings of a Symposium on Metallurgy and Technology of Refractory Metals," in *Symposium on Metallurgy and Technology of Refractory Metals*, Washington, D.C., R. T. B. I. Machlin, E. D. Weisert, Ed., April 25–26, 1968 1968: Springer New York, NY, doi: 10.1007/978-1-4684-9120-3.
- [8] R. W. Burman, "Molybdenum - a super superalloy," *Journal of Metals*, vol. 29, pp. 12-17, 1977, doi: 10.1007/BF03354338.

- [9] J. A. Shields, "Applications of Molybdenum Metal and its Alloys," International Molybdenum Association, 2013.
- [10] A. I. H. Committee, *ASM Handbook - Volume 20 - Materials Selection and Design*. Metals Park, Ohio: ASM International, 1997, p. 2005.
- [11] R. E. Smallwood, A. S. f. Testing, Materials, A. C. B.-o. Reactive, R. Metals, and Alloys, *Refractory Metals and Their Industrial Applications: A Symposium*. ASTM, 1984.
- [12] C. L. Briant, "Refractory Metals and Alloys," in *Encyclopedia of Materials: Science and Technology*, K. H. J. Buschow, R. W. Cahn, M. C. Flemings, E. J. Kramer, B. Ilschner, S. Mahajan, and P. Veyssi re Eds.: Elsevier Science Ltd, 2001, pp. 8088-8095.
- [13] W. Liu, "Optimization of Molybdenum Electrodes for Glass Melting," Ph.D., Worcester Polytechnic Institute, Worcester, Massachusetts, 2015.
- [14] C. L. Briant, "New Applications and Novel Processing of Refractory Metal Alloys," presented at the 15th International Plansee Seminar, Reutte, 2001.
- [15] Plansee. "Molybdenum." Plansee SE. <https://www.plansee.com/en/materials/molybdenum.html> (accessed 31-March-2023).
- [16] M. A. Harimon, N. A. Hidayati, Y. Miyashita, Y. Otsuka, Y. Mutoh, S. Yamamoto, and H. Aoyama, "High temperature fracture toughness of TZM alloys with different kinds of grain boundary particles," *International Journal of Refractory Metals and Hard Materials*, vol. 66, pp. 52-56, 2017, doi: 10.1016/j.ijrmhm.2017.02.006.
- [17] L.-L. Zhang, L.-J. Zhang, J. Ning, and S.-J. Na, "Effect of various combinations of Ti and Zr interlayers on the tensile properties of laser welded joints of molybdenum," *International Journal of Refractory Metals and Hard Materials*, vol. 101, 2021, doi: 10.1016/j.ijrmhm.2021.105662.
- [18] H. Walser and J. A. Shields, "Traditional and Emerging Applications of Molybdenum Metal and Its Alloys," ed: International Molybdenum Association, 2007.
- [19] *Standard Specification for Molybdenum and Molybdenum Alloy Plate, Sheet, Strip, Foil, and Ribbon*, B386/B386M-19e1, A. International, Metals Park, Ohio, 2019.
- [20] *Standard Specification for Molybdenum and Molybdenum Alloy Bar, Rod, and Wire*, B387-18, A. International, Metals Park, Ohio, 2018.

- [21] Rembar. "When To Use TZM Alloy Instead of Pure Molybdenum." Rembar Inc. <https://www.rembar.com/when-to-use-tzm-alloy-instead-of-pure-molybdenum/> (accessed 30-Apr-2023).
- [22] J. H. Bechtold and H. Scott, "Mechanical Properties of Arc-Cast and Powder Metallurgy Molybdenum," *Journal of the Electrochemical Society*, vol. 98, p. 11, 1951.
- [23] D. Scheiber, "Theoretical Study of Grain Boundaries in Tungsten and Molybdenum," Doctoral, Institute of Physics, Karl-Franzens University, Graz, Materials Center Leoben Forschung GmbH, 2016.
- [24] W. D. Callister Jr and D. G. Rethwish, *Materials Science and Engineering An Introduction*, 10th ed. John Wiley and Sons, 2018, p. 992.
- [25] J. F. Shackelford, *Introduction to Materials Science for Engineers*, 8 ed. Upper Saddle River, New Jersey: Pearson Higher Education, Inc., 2015, p. 687.
- [26] H. Zheng *et al.*, "Grain boundary properties of elemental metals," *Acta Materialia*, vol. 186, pp. 40-49, 2020, doi: 10.1016/j.actamat.2019.12.030.
- [27] D. Scheiber, R. Pippan, P. Puschnig, and L. Romaner, "Ab initio calculations of grain boundaries in bcc metals," *Modelling and Simulation in Materials Science and Engineering*, vol. 24, no. 3, 2016, doi: 10.1088/0965-0393/24/3/035013.
- [28] S. Tsurekawa, T. Tanaka, and H. Yoshinaga, "Grain boundary structure, energy and strength in molybdenum," *Materials Science and Engineering*, vol. A176, p. 8, 1994.
- [29] M. L. Jokl, V. Vitek, and C. J. McMahon Jr, "A microscopic theory of brittle fracture in deformable solids: A relation between ideal work to fracture and plastic work," *Acta Metallurgica*, vol. 28, p. 10, 1980.
- [30] C. J. McMahon Jr and V. Vitek, "The effects of segregated impurities on intergranular fracture energy," *Acta Metallurgica*, vol. 27, p. 7, 1978.
- [31] A. P. Sutton and R. W. Balluffi, *Interfaces in Crystalline Materials*. London: Oxford University Press, 2007, p. 856.
- [32] J. Pokluda and P. Šandera, "On the Intrinsic Ductility and Brittleness of Crystals," *Physica Status Solidi (b)*, vol. 167, no. 2, pp. 543-550, 1991, doi: 10.1002/pssb.2221670216.
- [33] J. B. Brosse, R. Fillit, and M. BISCONDI, "Intrinsic intergranular brittleness of molybdenum," *Scripta Metallurgica*, vol. 15, p. 5, 1981.

- [34] B. V. Cockeram, E. K. Ohriner, T. S. Byun, M. K. Miller, and L. L. Snead, "Weldable ductile molybdenum alloy development," *Journal of Nuclear Materials*, vol. 382, no. 2-3, pp. 229-241, 2008, doi: 10.1016/j.jnucmat.2008.08.021.
- [35] Y. Hiraoka, H. Kurishita, M. Narui, and H. Kayano, "Fracture and ductile-to-brittle transition characteristics of molybdenum by impact and static bend tests.," *Materials Transactions*, vol. 36, no. 4, p. 7, 1995.
- [36] R. Frauenfelder, "Permeation, Diffusion, and Solution of Nitrogen in Tungsten and Molybdenum," *The Journal of Chemical Physics*, vol. 48, no. 9, pp. 3966-3971, 2003, doi: 10.1063/1.1669721.
- [37] S. C. Srivastava and L. L. Seigle, "Solubility and thermodynamic properties of oxygen in solid molybdenum," *Metallurgical transactions*, vol. 5, no. 1, pp. 49-52, 1974/01/01 1974, doi: 10.1007/BF02642925.
- [38] D. E. Weaver, "The Diffusivity and Solubility of Nitrogen in Molybdenum and the Trapping of Nitrogen By Carbon in Molybdenum," Doctor of Philosophy, University of California, Livermore, California, UCRL-51182, 1972.
- [39] G. T. Hahn, A. Gilbert, and R. I. Jaffee, "The effects of solutes on the ductile-to-brittle transition of refractory," *DMIC Memorandum*, vol. 155, pp. 63-63, 1962.
- [40] D. McLean, *Grain boundaries in metals*, Oxford: Clarendon Press, 1957. [Online]. Available: <http://books.google.com/books?id=fkhRAAAAMAAJ>.
- [41] A. Kumar and B. L. Eyre, "Grain Boundary Segregation and Intergranular Fracture in Molybdenum," *Proceedings of the Royal Society A: Mathematical, Physical and Engineering Sciences*, vol. 370, no. 1743, pp. 431-458, 1980.
- [42] A. Drachinskiy, A. V. Kraynikov, and V. Slyunyaev, "Interrelation of impurity enrichment of grain boundaries and the cold shortness point during annealing of molybdenum," *Physics of Metals and Metallography*, vol. 66, no. 3, p. 9, 1988.
- [43] Z.-Q. Wang *et al.*, "Suppressing effect of carbon on oxygen-induced embrittlement in molybdenum grain boundary," *Computational Materials Science*, vol. 198, 2021, doi: 10.1016/j.commatsci.2021.110676.
- [44] Y. Hiraoka, M. Okada, and R. Watanabe, "Effect of aging after carbon doping on the ductility of molybdenum," *Journal of the Less Common Metals*, vol. 75, no. 1, pp. 31-42, 1980/11/01/ 1980, doi: [https://doi.org/10.1016/0022-5088\(80\)90366-5](https://doi.org/10.1016/0022-5088(80)90366-5).

- [45] T. Kadokura, Y. Hiraoka, Y. Yamamoto, and K. Okamoto, "Change of Mechanical Property and Fracture Mode of Molybdenum by Carbon Addition," *Materials Transactions*, vol. 51, no. 7, pp. 1296-1301, 2010, doi: 10.2320/matertrans.M2009377.
- [46] M. K. Miller and H. Kurishita, "APFIM Characterization of Grain Boundary Segregation in Titanium Carbide-Doped Molybdenum," *Le Journal de Physique IV*, vol. 06, no. C5, pp. C5-265-C5-270, 1996, doi: 10.1051/jp4:1996543.
- [47] M. K. Miller, E. A. Kenik, M. S. Mousa, K. F. Russell, and A. J. Bryhan, "Improvement in the ductility of molybdenum alloys due to grain boundary segregation," *Scripta Materialia*, vol. 46, no. 4, pp. 299-303, 2002/02/28/ 2002, doi: [https://doi.org/10.1016/S1359-6462\(01\)01242-8](https://doi.org/10.1016/S1359-6462(01)01242-8).
- [48] D. Scheiber, R. Pippan, P. Puschnig, and L. Romaner, "Ab initio search for cohesion-enhancing impurity elements at grain boundaries in molybdenum and tungsten," *Modelling and Simulation in Materials Science and Engineering*, vol. 24, no. 8, 2016, doi: 10.1088/0965-0393/24/8/085009.
- [49] A. V. Krajinikov, F. Morito, and V. N. Slyunyaev, "Impurity-induced embrittlement of heat-affected zone in welded Mo-based alloys," *International Journal of Refractory Metals and Hard Materials*, vol. 15, no. 5-6, p. 15, 1997.
- [50] E. A. Gulbransen, K. F. Andrew, and F. A. Brassart, "Oxidation of Molybdenum 550° to 1700°C," *Journal of The Electrochemical Society*, vol. 110, no. 9, p. 952, 1963/09/01 1963, doi: 10.1149/1.2425918.
- [51] G. R. Smolik, D. A. Petti, and S. T. Schuetz, "Oxidation and volatilization of TZM alloy in air," *Journal of Nuclear Materials*, vol. 283-287, pp. 1458-1462, 2000/12/01/ 2000, doi: [https://doi.org/10.1016/S0022-3115\(00\)00303-2](https://doi.org/10.1016/S0022-3115(00)00303-2).
- [52] F. Yang *et al.*, "La doping effect on TZM alloy oxidation behavior," *Journal of Alloys and Compounds*, vol. 593, pp. 196-201, 2014, doi: 10.1016/j.jallcom.2013.12.270.
- [53] S. P. Chakraborty, S. Banerjee, K. Singh, I. G. Sharma, A. K. Grover, and A. K. Suri, "Studies on the development of protective coating on TZM alloy and its subsequent characterization," *Journal of Materials Processing Technology*, vol. 207, no. 1-3, pp. 240-247, 2008, doi: 10.1016/j.jmatprotec.2007.12.075.
- [54] M. Bauccio, *ASM Metals Reference Book*. ASM International, 2003.

- [55] Y. Zhou, S. Wei, L. Xu, and X. Li, "Research on high-temperature properties of the molybdenum sheet doped with 1.0 wt%Al₂O₃ particles," *Journal of Alloys and Compounds*, vol. 769, pp. 340-346, 2018, doi: 10.1016/j.jallcom.2018.08.029.
- [56] P. M. Prasad, T. R. Mankhand, and A. J. K. Prasad, "Molybdenum extraction process: An overview," *NML Technical Journal*, vol. 39, no. 2, pp. 39-58, 1997.
- [57] G.-S. Kim, Y. J. Lee, D.-G. Kim, and Y. D. Kim, "Consolidation behavior of Mo powder fabricated from milled Mo oxide by hydrogen-reduction," *Journal of Alloys and Compounds*, vol. 454, no. 1-2, pp. 327-330, 2008, doi: 10.1016/j.jallcom.2006.12.039.
- [58] R. Morales, R. E. Aune, O. Grindler, and S. Seetharaman, "The powder metallurgy processing of refractory metals and alloys," *The journal of the minerals, metals and materials society (TMS)*, vol. 55, pp. 20-23, 2003, doi: 10.1007/s11837-003-0169-9.
- [59] R. M. German, "Powder Processing of Refractory Metals and Alloys," *MRS Online Proceedings Library*, vol. 322, no. 1, pp. 341-352, 1993/12/01 1993, doi: 10.1557/PROC-322-341.
- [60] J. L. Johnson, D. F. Heaney, and N. S. Myers, "Metal injection molding (MIM) of heavy alloys, refractory metals, and hardmetals," in *Handbook of Metal Injection Molding*, 2012, pp. 526-567.
- [61] D. M. Dimiduk and J. H. Perepezko, "Mo-Si-B Alloys: Developing a Revolutionary Turbine-Engine Material," *MRS Bulletin*, vol. 28, pp. 639-645, 2003, doi: 10.1557/mrs2003.191.
- [62] M. Konter and M. Thumann, "Materials and manufacturing of industrial gas turbine components," *Journal of Materials Processing Technology*, vol. 117, p. 5, 2001.
- [63] M. L. Hill, "Materials for structural use above 3000 °F," *Johns Hopkins APL Technical Digest*, vol. 3, no. 4, p. 12, 1964.
- [64] M. B. Uday, M. N. Ahmad-Fauzi, A. M. Noor, and S. Rajoo, "Current Issues and Problems in the Joining of Ceramic to Metal," in *Joining Technologies*, 2016, ch. Chapter 8.
- [65] Q. Group. "Typical high pressure turbine blade." Quaser Machine Tools Inc. <https://www.quaser.com/industries/detail-8> (accessed March 20, 2023).
- [66] "CuMoCu For Electronic Package And Heat Sink Manufacturers, Suppliers - Factory Direct Wholesale - Yuguang." Hebei Yuguang Welding Co.,Ltd.

- <https://www.ygmetal.com/clad-metals/clad-metal-for-coinage/cumocu-for-electronic-package-and-heat-sink.html> (accessed 2023).
- [67] V. V. Satya Prasad, R. G. Baligidad, and A. A. Gokhale, "Niobium and Other High Temperature Refractory Metals for Aerospace Applications," in *Aerospace Materials and Material Technologies*, vol. 1: Aerospace Materials, N. Eswara Prasad and R. J. H. Wanhill Eds., (Indian Institute of Metals Series: Springer, 2017).
- [68] *ISO/ASTM 52900:2021(en) Additive manufacturing — General principles — Fundamentals and vocabulary*, 01.040.25, 25.030, I. O. f. Standardization, 2021. [Online]. Available: <https://www.iso.org/obp/ui/#iso:std:iso-astm:52900:ed-2:v1:en>
- [69] E. R. Denlinger, M. Gouge, J. Irwin, and P. Michaleris, "Thermomechanical model development and in situ experimental validation of the Laser Powder-Bed Fusion process," *Additive Manufacturing*, vol. 16, pp. 73-80, 2017, doi: 10.1016/j.addma.2017.05.001.
- [70] R. Goodridge and S. Ziegelmeier, "Powder bed fusion of polymers," in *Laser Additive Manufacturing*, 2017, pp. 181-204.
- [71] S. Sun, M. Brandt, and M. Easton, "Powder bed fusion processes: an overview," in *Laser Additive Manufacturing*, 2017, pp. 55-77.
- [72] H. Chen, Q. Wei, Y. Zhang, F. Chen, Y. Shi, and W. Yan, "Powder-spreading mechanisms in powder-bed-based additive manufacturing: Experiments and computational modeling," *Acta Materialia*, vol. 179, pp. 158-171, 2019, doi: 10.1016/j.actamat.2019.08.030.
- [73] N. D. Dejene and H. G. Lemu, "Current Status and Challenges of Powder Bed Fusion-Based Metal Additive Manufacturing: Literature Review," *Metals*, vol. 13, no. 2, 2023, doi: 10.3390/met13020424.
- [74] M. Galati and L. Iuliano, "A literature review of powder-based electron beam melting focusing on numerical simulations," *Additive Manufacturing*, vol. 19, pp. 1-20, 2018, doi: 10.1016/j.addma.2017.11.001.
- [75] S. P. Narra, "Powder Bed Fusion – Metals," in *Encyclopedia of Materials: Metals and Alloys*, 2022, pp. 85-94.
- [76] S. M. Gaytan, L. E. Murr, F. Medina, E. Martinez, M. I. Lopez, and R. B. Wicker, "Advanced metal powder based manufacturing of complex components by electron beam melting," *Materials Technology*, vol. 24, no. 3, pp. 180-190, 2013, doi: 10.1179/106678509x12475882446133.

- [77] A. Garcia-Colomo, D. Wood, F. Martina, and S. W. Williams, "A comparison framework to support the selection of the best additive manufacturing process for specific aerospace applications," *International Journal of Rapid Manufacturing, Volume 9, Issue 2/3, 2020*, pp. 194 - 211, vol. 9, no. 2/3, p. 20, 2020, doi: DOI:10.1504/IJRAPIDM.2020.10019230.
- [78] Z. Y. Chua, I. H. Ahn, and S. K. Moon, "Process monitoring and inspection systems in metal additive manufacturing: Status and applications," *International Journal of Precision Engineering and Manufacturing-Green Technology*, vol. 4, no. 2, pp. 235-245, 2017, doi: 10.1007/s40684-017-0029-7.
- [79] M. Leary, M. Khorasani, A. Sarker, J. Tran, K. Fox, D. Downing, and A. Du Plessis, "Surface roughness," in *Fundamentals of Laser Powder Bed Fusion of Metals*, 2021, pp. 179-213.
- [80] R. Acharya, J. A. Sharon, and A. Staroselsky, "Prediction of microstructure in laser powder bed fusion process," *Acta Materialia*, vol. 124, pp. 360-371, 2017, doi: 10.1016/j.actamat.2016.11.018.
- [81] Z. Yan, W. Liu, Z. Tang, X. Liu, N. Zhang, M. Li, and H. Zhang, "Review on thermal analysis in laser-based additive manufacturing," *Optics & Laser Technology*, vol. 106, pp. 427-441, 2018, doi: 10.1016/j.optlastec.2018.04.034.
- [82] A. Khorasani, I. Gibson, J. K. Veetil, and A. H. Ghasemi, "A review of technological improvements in laser-based powder bed fusion of metal printers," *The International Journal of Advanced Manufacturing Technology*, vol. 108, no. 1-2, pp. 191-209, 2020, doi: 10.1007/s00170-020-05361-3.
- [83] I. Yadroitsev and I. Yadroitsava, "A step-by-step guide to the L-PBF process," in *Fundamentals of Laser Powder Bed Fusion of Metals*, 2021, pp. 39-77.
- [84] S. Chowdhury, N. Yadaiah, C. Prakash, S. Ramakrishna, S. Dixit, L. R. Gupta, and D. Buddhi, "Laser powder bed fusion: a state-of-the-art review of the technology, materials, properties & defects, and numerical modelling," *Journal of Materials Research and Technology*, vol. 20, pp. 2109-2172, 2022, doi: 10.1016/j.jmrt.2022.07.121.
- [85] C. Emmelmann, D. Herzog, and J. Kranz, "Design for laser additive manufacturing," in *Laser Additive Manufacturing*, 2017, pp. 259-279.

- [86] M. Mazur, M. Leary, M. McMillan, S. Sun, D. Shidid, and M. Brandt, "Mechanical properties of Ti6Al4V and AlSi12Mg lattice structures manufactured by Selective Laser Melting (SLM)," in *Laser Additive Manufacturing*, 2017, pp. 119-161.
- [87] M. J. Mirzaali, A. Azarniya, S. Sovizi, J. Zhou, and A. A. Zadpoor, "Lattice structures made by laser powder bed fusion," in *Fundamentals of Laser Powder Bed Fusion of Metals*, 2021, pp. 423-465.
- [88] M. Grasso, B. M. Colosimo, K. Slattery, and E. MacDonald, "Process monitoring of laser powder bed fusion," in *Fundamentals of Laser Powder Bed Fusion of Metals*, 2021, pp. 301-326.
- [89] W. E. King, A. T. Anderson, R. M. Ferencz, N. E. Hodge, C. Kamath, S. A. Khairallah, and A. M. Rubenchik, "Laser powder bed fusion additive manufacturing of metals; physics, computational, and materials challenges," *Applied Physics Reviews*, vol. 2, no. 4, 2015, doi: 10.1063/1.4937809.
- [90] T. Moges, G. Ameta, and P. Witherell, "A Review of Model Inaccuracy and Parameter Uncertainty in Laser Powder Bed Fusion Models and Simulations," *J Manuf Sci Eng*, vol. 141, 2019, doi: 10.1115/1.4042789.
- [91] P. Hanzl, M. Zetek, T. Bakša, and T. Kroupa, "The Influence of Processing Parameters on the Mechanical Properties of SLM Parts," *Procedia Engineering*, vol. 100, pp. 1405-1413, 2015, doi: 10.1016/j.proeng.2015.01.510.
- [92] T. M. Mower and M. J. Long, "Mechanical behavior of additive manufactured, powder-bed laser-fused materials," *Materials Science and Engineering: A*, vol. 651, pp. 198-213, 2016, doi: 10.1016/j.msea.2015.10.068.
- [93] O. Rehme and C. Emmelmann, "Reproducibility for properties of selective laser melting products," in *3rd International Conference; Lasers in manufacturing*, Stuttgart, Munich, Germany, 2005: AT-Verlag, pp. 227-232.
- [94] G. Yang, P. Yang, K. Yang, N. Liu, L. Jia, J. Wang, and H. Tang, "Effect of processing parameters on the density, microstructure and strength of pure tungsten fabricated by selective electron beam melting," *International Journal of Refractory Metals and Hard Materials*, vol. 84, 2019, doi: 10.1016/j.ijrmhm.2019.105040.
- [95] S. Z. Hussain *et al.*, "Feedback Control of Melt Pool Area in Selective Laser Melting Additive Manufacturing Process," *Processes*, vol. 9, no. 9, 2021, doi: 10.3390/pr9091547.

- [96] S. Cacace and Q. Semeraro, "About Fluence and Process Parameters on Maraging Steel Processed by Selective Laser Melting: Do They Convey the Same Information?," *International Journal of Precision Engineering and Manufacturing*, vol. 19, no. 12, pp. 1873-1884, 2018, doi: 10.1007/s12541-018-0204-y.
- [97] Y. Li and D. Gu, "Parametric analysis of thermal behavior during selective laser melting additive manufacturing of aluminum alloy powder," *Materials & Design*, vol. 63, pp. 856-867, 2014, doi: 10.1016/j.matdes.2014.07.006.
- [98] I. Yadroitsev, P. Krakhmalev, and I. Yadroitsava, "Selective laser melting of Ti6Al4V alloy for biomedical applications: Temperature monitoring and microstructural evolution," *Journal of Alloys and Compounds*, vol. 583, no. C, pp. 404-409, 2014, doi: 10.1016/j.jallcom.2013.08.183.
- [99] R. Li, Y. Shi, J. Liu, H. Yao, and W. Zhang, "Effects of processing parameters on the temperature field of selective laser melting metal powder," *Powder Metallurgy and Metal Ceramics*, vol. 48, no. 3-4, pp. 186-195, 2009, doi: 10.1007/s11106-009-9113-z.
- [100] I. Yadroitsev, A. Gusarov, I. Yadroitsava, and I. Smurov, "Single track formation in selective laser melting of metal powders," *Journal of Materials Processing Technology*, vol. 210, no. 12, pp. 1624-1631, 2010, doi: 10.1016/j.jmatprotec.2010.05.010.
- [101] W. J. Sames, F. A. List, S. Pannala, R. R. Dehoff, and S. S. Babu, "The metallurgy and processing science of metal additive manufacturing," *International Materials Reviews*, vol. 61, no. 5, pp. 315-360, 2016, doi: 10.1080/09506608.2015.1116649.
- [102] C. Zhao, Y. Bai, Y. Zhang, X. Wang, J. M. Xue, and H. Wang, "Influence of scanning strategy and building direction on microstructure and corrosion behaviour of selective laser melted 316L stainless steel," *Materials & Design*, vol. 209, 2021, doi: 10.1016/j.matdes.2021.109999.
- [103] L. Thijs, M. L. Montero Sistiaga, R. Wauthle, Q. Xie, J.-P. Kruth, and J. Van Humbeeck, "Strong morphological and crystallographic texture and resulting yield strength anisotropy in selective laser melted tantalum," *Acta Materialia*, vol. 61, no. 12, pp. 4657-4668, 2013, doi: 10.1016/j.actamat.2013.04.036.
- [104] S. Vock, B. Klöden, A. Kirchner, T. Weißgärber, and B. Kieback, "Powders for powder bed fusion: a review," *Progress in Additive Manufacturing*, vol. 4, no. 4, pp. 383-397, 2019, doi: 10.1007/s40964-019-00078-6.

- [105] D. Wang, C. Yu, J. Ma, W. Liu, and Z. Shen, "Densification and crack suppression in selective laser melting of pure molybdenum," *Materials & Design*, vol. 129, pp. 44-52, 2017, doi: 10.1016/j.matdes.2017.04.094.
- [106] H. W. Mindt, M. Megahed, N. P. Lavery, M. A. Holmes, and S. G. R. Brown, "Powder Bed Layer Characteristics: The Overseen First-Order Process Input," *Metallurgical and Materials Transactions A*, vol. 47, no. 8, pp. 3811-3822, 2016, doi: 10.1007/s11661-016-3470-2.
- [107] A. B. Spierings, M. Voegtlin, T. Bauer, and K. Wegener, "Powder flowability characterisation methodology for powder-bed-based metal additive manufacturing," *Progress in Additive Manufacturing*, vol. 1, no. 1-2, pp. 9-20, 2015, doi: 10.1007/s40964-015-0001-4.
- [108] J. Zielinski, S. Vervoort, H.-W. Mindt, and M. Megahed, "Influence of Powder Bed Characteristics on Material Quality in Additive Manufacturing," *BHM Berg- und Hüttenmännische Monatshefte*, vol. 162, no. 5, pp. 192-198, 2017, doi: 10.1007/s00501-017-0592-9.
- [109] A. V. Gusarov, "Radiative transfer, absorption, and reflection by metal powder beds in laser powder-bed processing," *Journal of Quantitative Spectroscopy and Radiative Transfer*, vol. 257, 2020, doi: 10.1016/j.jqsrt.2020.107366.
- [110] L. C. Wei, L. E. Ehrlich, M. J. Powell-Palm, C. Montgomery, J. Beuth, and J. A. Malen, "Thermal conductivity of metal powders for powder bed additive manufacturing," *Additive Manufacturing*, vol. 21, pp. 201-208, 2018, doi: 10.1016/j.addma.2018.02.002.
- [111] C. Meier, R. Weissbach, J. Weinberg, W. A. Wall, and A. J. Hart, "Critical influences of particle size and adhesion on the powder layer uniformity in metal additive manufacturing," *Journal of Materials Processing Technology*, vol. 266, pp. 484-501, 2019, doi: 10.1016/j.jmatprotec.2018.10.037.
- [112] X. Lu *et al.*, "Crack-free laser powder bed fusion by substrate design," *Additive Manufacturing*, vol. 59, 2022, doi: 10.1016/j.addma.2022.103149.
- [113] J.-P. Kruth, J. Deckers, E. Yasa, and R. Wauthlé, "Assessing and comparing influencing factors of residual stresses in selective laser melting using a novel analysis method," *Proceedings of the Institution of Mechanical Engineers, Part B: Journal of Engineering Manufacture*, vol. 226, no. 6, pp. 980-991, 2012, doi: 10.1177/0954405412437085.

- [114] A. v. Müller *et al.*, "Additive manufacturing of pure tungsten by means of selective laser beam melting with substrate preheating temperatures up to 1000 °C," *Nuclear Materials and Energy*, vol. 19, pp. 184-188, 2019, doi: 10.1016/j.nme.2019.02.034.
- [115] M. Saunders. "Gone with the wind - how gas flow governs LPBF performance." LinkedIn. (accessed 12-May-2023).
- [116] J. E. Ruiz, M. Cortina, J. I. Arrizubieta, and A. Lamikiz, "Study of the Influence of Shielding Gases on Laser Metal Deposition of Inconel 718 Superalloy," *Materials (Basel)*, vol. 11, no. 8, Aug 9 2018, doi: 10.3390/ma11081388.
- [117] S. Traore *et al.*, "Influence of gas atmosphere (Ar or He) on the laser powder bed fusion of a Ni-based alloy," *Journal of Materials Processing Technology*, vol. 288, 2021, doi: 10.1016/j.jmatprotec.2020.116851.
- [118] X. J. Wang, L. C. Zhang, M. H. Fang, and T. B. Sercombe, "The effect of atmosphere on the structure and properties of a selective laser melted Al–12Si alloy," *Materials Science and Engineering: A*, vol. 597, pp. 370-375, 2014, doi: 10.1016/j.msea.2014.01.012.
- [119] S. Roy, B. Silwal, A. Nycz, M. Noakes, E. Cakmak, P. Nandwana, and Y. Yamamoto, "Investigating the effect of different shielding gas mixtures on microstructure and mechanical properties of 410 stainless steel fabricated via large scale additive manufacturing," *Additive Manufacturing*, vol. 38, 2021, doi: 10.1016/j.addma.2020.101821.
- [120] B. Zhang, H. Liao, and C. Coddet, "Effects of processing parameters on properties of selective laser melting Mg–9%Al powder mixture," *Materials & Design*, vol. 34, pp. 753-758, 2012, doi: 10.1016/j.matdes.2011.06.061.
- [121] K. Kempen, B. Vrancken, S. Bols, L. Thijs, J. Van Humbeeck, and J.-P. Kruth, "Selective Laser Melting of Crack-Free High Density M2 High Speed Steel Parts by Baseplate Preheating," *Journal of Manufacturing Science and Engineering*, vol. 136, no. 6, 2014, doi: 10.1115/1.4028513.
- [122] C. Qiu, C. Panwisawas, M. Ward, H. C. Basoalto, J. W. Brooks, and M. M. Attallah, "On the role of melt flow into the surface structure and porosity development during selective laser melting," *Acta Materialia*, vol. 96, pp. 72-79, 2015, doi: 10.1016/j.actamat.2015.06.004.

- [123] M. Tang, P. C. Pistorius, and J. L. Beuth, "Prediction of lack-of-fusion porosity for powder bed fusion," *Additive Manufacturing*, vol. 14, pp. 39-48, 2017, doi: 10.1016/j.addma.2016.12.001.
- [124] T. DebRoy *et al.*, "Additive manufacturing of metallic components – Process, structure and properties," *Progress in Materials Science*, vol. 92, pp. 112-224, 2018, doi: 10.1016/j.pmatsci.2017.10.001.
- [125] R. Cunningham *et al.*, "Keyhole threshold and morphology in laser melting revealed by ultrahigh-speed x-ray imaging," *Science*, vol. 363, no. 6429, p. 4, 2019, doi: <https://doi.org/10.1126/science.aav4687>.
- [126] D. Faidel, D. Jonas, G. Natour, and W. Behr, "Investigation of the selective laser melting process with molybdenum powder," *Additive Manufacturing*, vol. 8, pp. 88-94, 2015, doi: 10.1016/j.addma.2015.09.002.
- [127] K. H. Leitz, P. Singer, A. Plankensteiner, B. Tabernig, H. Kestler, and L. S. Sigl, "Multi-physical simulation of selective laser melting," *Metal Powder Report*, vol. 72, no. 5, pp. 331-338, 2017, doi: 10.1016/j.mprp.2016.04.004.
- [128] K. H. Leitz, C. Grohs, P. Singer, B. Tabernig, A. Plankensteiner, H. Kestler, and L. S. Sigl, "Fundamental analysis of the influence of powder characteristics in Selective Laser Melting of molybdenum based on a multi-physical simulation model," *International Journal of Refractory Metals and Hard Materials*, vol. 72, pp. 1-8, 2018, doi: 10.1016/j.ijrmhm.2017.11.034.
- [129] J. Braun *et al.*, "Molybdenum and tungsten manufactured by selective laser melting: Analysis of defect structure and solidification mechanisms," *International Journal of Refractory Metals and Hard Materials*, vol. 84, 2019, doi: 10.1016/j.ijrmhm.2019.104999.
- [130] L. Kaserer *et al.*, "Fully dense and crack free molybdenum manufactured by Selective Laser Melting through alloying with carbon," *International Journal of Refractory Metals and Hard Materials*, vol. 84, 2019, doi: 10.1016/j.ijrmhm.2019.105000.
- [131] M. Higashi and T. Ozaki, "Selective laser melting of pure molybdenum: Evolution of defect and crystallographic texture with process parameters," *Materials & Design*, vol. 191, 2020, doi: 10.1016/j.matdes.2020.108588.
- [132] F. Oehlerking, M. T. Stawovy, S. Ohm, and A. Imandoust, "Microstructural characterization and mechanical properties of additively manufactured molybdenum and

- molybdenum alloys," *International Journal of Refractory Metals and Hard Materials*, vol. 109, 2022, doi: 10.1016/j.ijrmhm.2022.105971.
- [133] B. Guan *et al.*, "Strategies to reduce pores and cracks of molybdenum fabricated by selective laser melting," *International Journal of Refractory Metals and Hard Materials*, vol. 112, 2023, doi: 10.1016/j.ijrmhm.2023.106123.
- [134] L. Kaserer *et al.*, "Microstructure and mechanical properties of molybdenum-titanium-zirconium-carbon alloy TZM processed via laser powder-bed fusion," *International Journal of Refractory Metals and Hard Materials*, vol. 93, 2020, doi: 10.1016/j.ijrmhm.2020.105369.

Chapter 3 – Methods

3.1 Sample fabrication

3.1.1 Powder feedstock and its characterization

Gas-atomized Mo powders sourced from Tekna (Canada) and spray-dried pre-alloyed powders of TZM from American Elements (USA) were used in this study. Powder morphology was analyzed by Scanning Electron Microscopy (SEM) using a SU3500 (Hitachi, Japan) SEM. Figure 3.1 shows the SEM micrographs of the Mo and TZM powders. Particle size distribution (PSD) was measured by means of laser diffraction using an LA-920 laser particle size analyzer (Horiba, Japan). The flowability of the powders was tested using Hall and Carney funnel methods as per ASTM B213 and B964, respectively [1, 2]. The cohesiveness index of the powder at different rotational speeds was evaluated through the rotating drum technique using the GranuDrum® apparatus (Granutools, Belgium).

Table 3.1 shows the chemical composition of the powders used in this study, per the certificate of conformity.

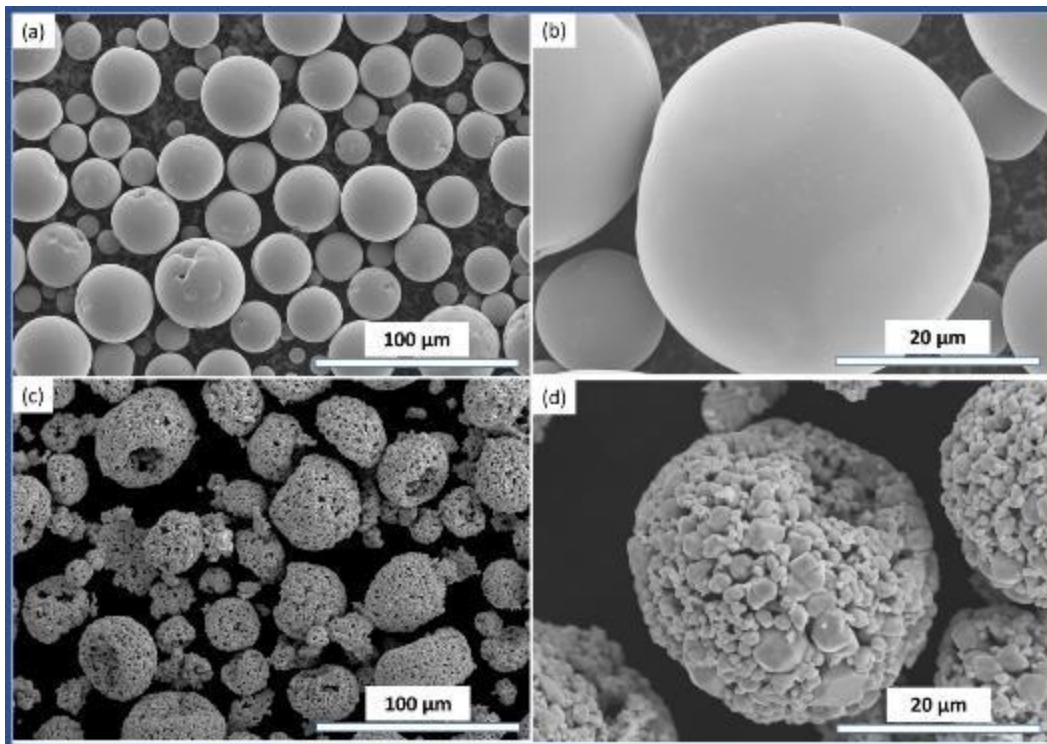


Figure 3.1 SEM micrographs of (a-b) Mo and (c-d) TZM powders used in this study

Table 3.1. Chemical composition (as per certificate of conformity) of powders used in this study.

Powder	Element	Mo	Ti	Zr	Fe	C	O	N	Others
Mo	wt.%	99.98	< 0.01	< 0.01	< 0.01	< 0.01	0.016	< 0.01	< 0.01
TZM	wt.%	99.38	0.49	0.09	< 0.01	0.029	< 0.01	< 0.01	< 0.01

3.1.2 LPBF AM

LPBF AM fabrication of the samples was performed using a Renishaw AM 400 (Renishaw, UK) LPBF machine with a reduced build volume (RBV) setup installed. The RBV setup allows for the fabrication of samples using a powder volume of up to 250 cm³. The machine is powered by a 400 W ytterbium fiber laser (wavelength, $\lambda = 1070$ nm) with a beam diameter of ~ 70 μm . Samples of various sizes were fabricated at room temperature. A bi-directional hatching pattern and 67° rotation between each layer were used as a scanning strategy. QuantAM build preparation software (Renishaw, UK) was utilized to prepare the build layout, assign the process parameters and process the CAD file into a machine-readable format. Figure 3.2 shows an image of the Renishaw AM400 LPBF machine and an example layout of the samples inside the QuantAM software. Mo (99.95% metal basis) plates of 2.5 mm thickness from Alfa Aesar (United States of America) were used as substrates.

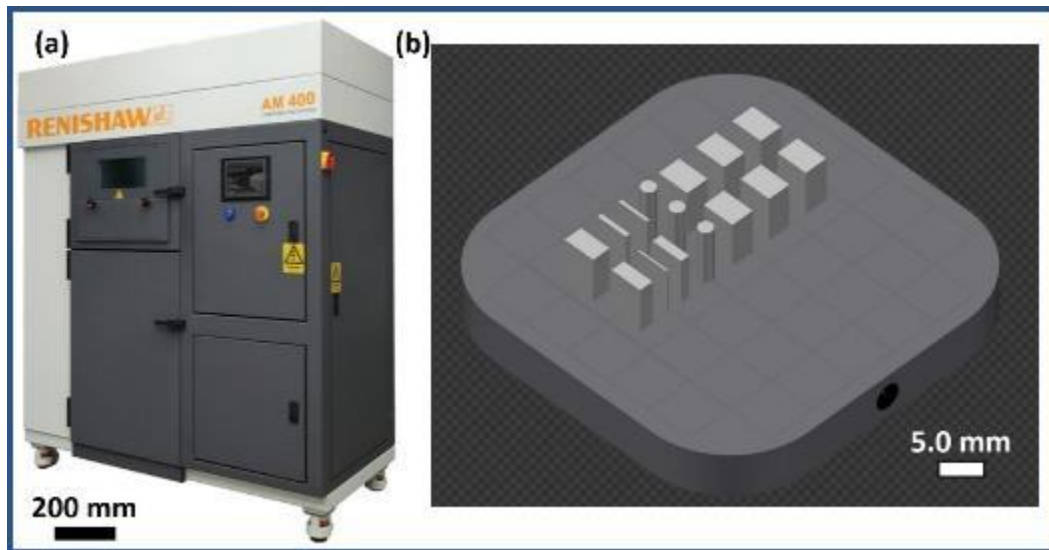


Figure 3.2. (a) Renishaw AM400 LPBF machine [3], and (b) Example image of a build layout on

3.1.3 Build atmosphere

Samples were fabricated under different atmospheres comprised of argon (Ar) and nitrogen (N₂) in varying combinations. Table 3.2 shows the details of the various gas combinations used in the studies detailed in this thesis. Gases with a purity of 4.8 HP (99.998% High Purity) were sourced from gas cylinders (Praxair, Canada). Oxygen was limited to less than 200 ppm (as reported by an integrated oxygen sensor) in the build atmosphere for all of the studies through the use of a semi-automated vacuum preparation cycle available in the Renishaw AM400 LPBF machine.

Table 3.2. Details of various gas combinations used in build atmosphere in this study.

Build Atmosphere (mol %)	N ₂ (%)	0	10	60	90	95	100
	Ar (%)	100	90	40	10	5	0
In thesis chapters		4, 5			5		4, 5, 6

3.2 Characterization

3.2.1 Sample preparation

The samples were separated from the build plate and then sectioned using an IsoMet™ Low-Speed precision cutter (Buehler, USA) for characterization. Samples for metallographic characterization were mounted in Technotherm 3000 warm embedding resin (Kulzer, Romania) using LaboPress-3 (Struers, USA) mounting equipment. Metallographic preparation was performed by an initial grinding of up to 800-grit SiC paper, then polishing with diamond suspensions of 9 μm, 3 μm, and 1 μm size particles, followed by 0.05 μm colloidal silica suspension on a LaboPol (Struers, USA) equipment.

3.2.2 Optical microscopy

Optical micrographs to characterize the as-built microstructure, density, and crack defect structure, were captured using a light optical microscope (Nikon, Japan) equipped with a Clemex Vision System (Clemex, Canada). The average crack length was calculated as the ratio of the cumulative crack length in a region of interest of size 1 mm² to the number of cracks. The optical micrographs

were used to characterize the as-built (AB) microstructure and determine the optical density. The cavity volume fraction was estimated from the optical micrographs using image analysis. Image analysis was performed using the Fiji distribution of ImageJ software [4].

3.2.3 Electron microscopy

The powder feedstock, the as-built parts and their cracking behaviour were characterized using a SU3500 (Hitachi, Japan) scanning electron microscope (SEM). Crystallographic texture and grain morphology were also studied using the SU3500 SEM equipped with an electron back-scattered diffraction (EBSD) detector (Oxford Instruments, UK). HKL Channel 5 software (Oxford Instruments, UK) was used for the analysis of the EBSD data. The alpha grain diameter was measured as equivalent circle diameter, and the local misorientation profile was evaluated using line maps of length equal to 80% grain diameter. A SU9000 (Hitachi, JAPAN) field emission scanning electron microscope (FE-SEM) equipped with an energy dispersive spectrometer (EDS) detector (Oxford Instruments, UK) was used for high magnification micrographs to characterize the precipitates in Chapter 4. The SU3500 SEM with an EDS detector (Oxford Instruments, UK) was used to characterize the wetting between the Cu and Mo regions in Chapter 6. From the EBSD analysis, the grains were classified as follows for recrystallization fraction analysis: grains with average misorientation exceeding 15° are classified as deformed, grains with average misorientation between 2 and 15° are considered sub-structured, and grains with misorientation below 2° are classified as recrystallized [5, 6].

3.2.4 X-ray diffraction

The phases were identified using X-ray diffraction (XRD) with the help of a D8 Discover diffractometer (Bruker, Germany) with a Cobalt (Co) anode ($K\alpha_1$ wavelength, $\lambda = 1.7890 \text{ \AA}$). Mounted and polished samples were used for the tests, and samples oscillated in X and Y directions with an amplitude of 0.75 mm during the exposure to X-rays. The diffraction data were acquired between 2θ values of 40° and 120° at a step size of 0.05° . Powder diffraction files (PDF) from the Crystallography Open Database (COD) were used to identify the constituent elements and phases. Full profile fitting analysis on the XRD data was performed using FullProf Suite [7].

3.2.5 Inert gas fusion

The N and O content of the powder feedstock and LPBF samples were measured using a LECO TC600 Nitrogen-Oxygen Determinator (LECO, USA). For the analysis, powder samples were collected from the containers under an inert atmosphere inside a glove box, while LPBF samples sectioned from the substrate immediately following fabrication were used.

3.2.6 Dilatometry

The CTE was measured between room temperature (RT) and 1073 K using a vertical DIL-L78-RITA dilatometer (Linseis, Germany) on samples of 10 mm (L) x 3 mm (B) x 3 mm (H). Type K thermocouples of 0.127 mm diameter were spot welded to the samples using a DCC Corp. Hotspot II TC welder. Samples were separated from the quartz rods of the dilatometer using a single sheet of mica, and measurements were performed in a flow of helium gas with a heating rate of 20 K/min up to the final temperature. The data collected were then corrected with the help of a Ni standard according to the ASTM A1033-10 standard [8].

3.2.7 Vickers microhardness

Vickers microhardness tests were performed using a Clark CM-100AT (Sun-tec, USA) automated microhardness equipment with 0.2 kgf load for a dwell time of 30 s, and measurements were reported as averages of 5 measurements. The samples were taken to microhardness tests in fully polished condition following the preparation indicated in section 3.2.1.

3.2.8 Laser flash analysis

In Chapter 6, laser flash analysis was used to measure thermal diffusivity. The test was performed using a LFA 427 laser flash analysis instrument (Netzsch, Germany) on control samples having a diameter of 12.7 mm and a thickness of 2.5 mm. Pure Cu reference samples The isothermal measurement conditions used single shots with a laser pulse voltage of 600 V and pulse width of 1 ms under flowing helium gas at 50 mL/min at 298 K (25 °C). Commercial laser flash analysis instruments, such as the Netzsch LFA 427, are typically limited to measuring cylindrical specimens with a diameter of 12.7 mm and a thickness of 2 to 3 mm due to the constraints of the

sample holder. On the other hand, heat sinks are cuboidal in shape, as seen from commercially available heat sink components. For this reason, an in-house custom-made laser flash analysis equipment was made in our facility.

The in-house custom-made laser flash analysis equipment was used to repeat the tests on the control samples and then used to test the samples from the study of size 10 mm (L) x 3 mm (B) x 10 mm (H). It used a NdYAG laser (1064 nm wavelength) shot of 10 W power and pulse width of 1 ms under flowing nitrogen at 50 mL/min at 298 K (25 °C). All samples were coated with graphite using a Cramolin (ITW Spraytec, Germany) colloidal-graphite spray. The measurements were performed through the thickness of the samples. Figure 3.3 shows the schematic of the custom-made laser flash analysis equipment with the different components. The setup used infrared (IR) detectors on one side of the sample to measure the change in temperature resulting from a laser shot hitting the other side of the sample, similar to how a typical laser flash analysis equipment works. The data were logged with timestamps at a rate of 1000 Hz. The chamber is connected to a vacuum pump and a nitrogen gas supply line. With the vacuum pump in operation, the chamber can maintain a vacuum of up to 500 mTorr. The chamber was prepared following three cycles of evacuation and purging of N₂, and then the gas was then allowed to flow to prevent any leaks into the chamber.

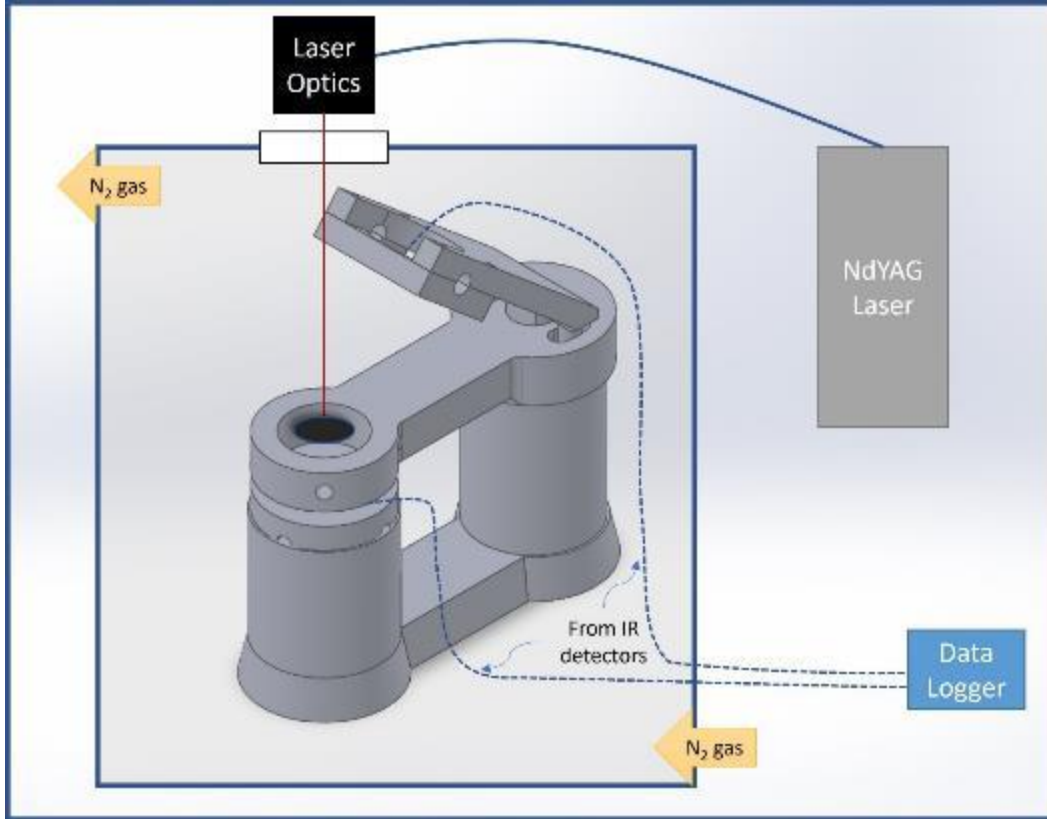


Figure 3.3. Schematic of the custom-made laser flash analysis equipment with the different components

Thermal diffusivity was calculated by measuring the time-linked temperature change using equation (3.1), where D is the thermal diffusivity (in $\text{m}^2 \cdot \text{s}^{-1}$), $t_{0.5}$ is the time (in s) needed to increase the temperature by 50%, and d is the thickness (in m) of the sample.

$$D = 0.1388 \frac{d^2}{t_{0.5}} \quad (3.1)$$

Following the calculation of thermal diffusivity, thermal conductivity was calculated using equation (3.2), where k is the thermal conductivity (in $\text{W} \cdot \text{m}^{-1} \cdot \text{K}^{-1}$), ρ is the density (in $\text{kg} \cdot \text{m}^{-3}$), and C_p is the specific heat capacity (in $\text{J} \cdot \text{kg}^{-1} \cdot \text{K}^{-1}$).

$$k = D \cdot \rho \cdot C_p \quad (3.2)$$

3.3 Phase diagram and paraequilibrium diagram calculations

The phase diagram and paraequilibrium diagram of the Mo-N system were calculated using FactSage thermochemical software [9]. The SpMTCBN thermochemical database reported by Frisk [10] was used for the calculations. Although the Gibbs energy of the HCP phase was estimated by Frisk [10] in the Mo-N system, this metastable phase was not considered in this study as there is no experimental evidence of its existence.

3.4 First-principles atomistic modelling and calculations

First-principles atomistic modelling and calculations based on Density Functional Theory (DFT) were performed to compute the interstitial formation energy and diffusion barrier energy for interstitials using the plane-wave basis set based Quantum Espresso package [11]. Ultrasoft pseudopotentials for modelling the interaction between ion cores and valence electrons and Perdew-Burke-Ernzerhof (PBE) functional of the Generalized Gradient Approximation (GGA) with non-linear core correction for treating exchange-correlation interactions were used [12]. Nudged elastic band (NEB) calculation, as implemented in the Quantum Espresso package, was used to compute diffusion barriers [13]. The theoretical background behind first-principles atomistic calculations is described below.

3.4.1 Schrödinger equation

The quantum mechanical wave function contains all the information about a system. Hence, a quantum-mechanical treatment can be used to understand different material properties. Such a system is described by the Schrödinger equation as depicted in equation (3.3), which is the fundamental equation of quantum mechanics formulated by Erwin Schrödinger [14]. It describes the behaviour of particles in terms of wave functions, which provide the probabilities of finding the particles in specific states. The equation represents a quantum system's time evolution, encapsulating wave and particle-like properties.

$$\hat{H}\Psi = E\Psi \quad (3.3)$$

In equation (3.3), \hat{H} is the Hamiltonian of the system, and E represents the system's energy. Here, Ψ is the many-body wave function of the system of nuclei and electrons and depends on the coordinates of all nuclei $\{R_i\}$ and electrons $\{r_j\}$, given by $\Psi(\{R_i\}, \{r_j\})$. While equation (3.3) is numerically solvable for simple systems with few electrons ($N < 10$), for larger systems, it becomes too complex. The Born-Oppenheimer (BO) approximation for the many-body electronic structure is a simplification for the analytical treatment of the Schrödinger equation and considers the nuclei and electrons separately [15]. The nuclei being much heavier than electrons, are approximated as fixed, generating an external potential V in which electrons move. In equation (3.4), \hat{T} is the kinetic energy, \hat{V} is the potential energy from the external field due to positively charged nuclei, and \hat{U} is the electron-electron interaction energy.

$$\hat{H} = \hat{T} + \hat{V} + \hat{U} \quad (3.4)$$

Despite the BO approximation, the complexity of solving the many-body wave function is still computationally prohibitive, and hence DFT with some further approximations is utilized.

3.4.2 Density functional theory

DFT is essentially based on the idea that a system defined by the wave function dependent on the coordinates of all electrons can also be defined by the electron density [16]. In DFT, the Kohn-Sham equation indicated in equation (3.5) describes the non-interacting Schrödinger-like equation of a system of one-particles (electrons) under an effective potential that generates the same density as any given system of interacting particles [17]. In equation (3.5) with eigenstates $\varphi_i(r)$ and eigenvalues ε_i , $v_{eff}(r)$ is the effective Kohn-Sham potential which includes the external potential and the Coulomb interactions between electrons.

$$\left(-\frac{1}{2}\nabla^2 + v_{eff}(r) \right) \varphi_i(r) = \varepsilon_i \varphi_i(r) \quad (3.5)$$

The Kohn-Sham equations are solved self-consistently, starting with an assumed electron density and iterating until convergence. By using the converged ground-state electron density, the ground-

state energy and other properties can be computed using equation (3.6). A critical aspect of the Kohn-Sham equation is the exchange-correlation (xc) functional which incorporates the exchange interaction between electrons and the electron-electron correlation effects. The exchange term accounts for the Pauli exclusion principle, whereas the correlation term captures the electron-electron interactions beyond the mean-field approximation.

$$E = \sum_i^N \epsilon_i + E_{xc}[n(r)] - \int v_{xc}(r) n(r) dr - \frac{1}{2} \int \frac{n(r)n(r')}{|r-r'|} dr dr' \quad (3.6)$$

The exchange-correlation functional is the most challenging aspect of DFT since its exact form is unknown; hence, approximations are used. Different exchange-correlation approximations, such as the local density approximation (LDA) and the generalized gradient approximation (GGA), are available, which balance the accuracy of the calculations and computational efficiency. LDA assumes that the energy density is the same everywhere, leading to errors in the estimation of exchange energy and correlation energy. GGA improves on this by accounting for the non-homogeneity of the true electron density.

3.4.3 Generalized-gradient approximation

The GGA describes the gradient of the density to account for the non-homogeneity of the true electron density and reduces the errors in estimating the exchange interactions and correlation energies. Equation (3.7) describes the xc -energy for GGA, F_{xc} is an enhancement factor, ϵ_{xc}^{unif} is the xc -energy per electron of the uniform electron gas with density $n(r)$. In this study, the PBE implementation of the GGA has been used [18].

$$E_{xc}^{GGA}[n(r)] = \int n(r) \epsilon_{xc}^{unif}(n(r)) F_{xc}(n(r), |\nabla n(r)|) dr \quad (3.7)$$

3.4.4 Atomistic modelling using Quantum Espresso

A cubic 3 x 3 x 3 supercell of the bcc lattice was used. The supercell was structurally relaxed by first-principles DFT calculations for total energies, forces, and stresses, using the GGA-PBE functional for exchange-correlation. All DFT calculations were done with the PWscf code of the Quantum Espresso software package [11]. The wave functions of the valence electrons are represented by a plane-waves basis set with a cutoff energy of 816 eV (60 Ry), and the electron density and effective Kohn–Sham potential by discrete Fourier series with a cutoff energy of 8163 eV (600 Ry). The interactions of valence electrons with the atomic nuclei and core electrons are described by ultrasoft pseudopotentials. Brillouin-zone integrals are evaluated on a Monkhorst–Pack mesh of 6 x 6 x 6 k-points with Gaussian smearing of 0.02 eV. The convergence criteria were set to 1.0×10^{-8} eV for the total energy and to 1.0×10^{-5} eV·Å⁻¹ for the forces on atoms. All thermodynamic quantities were calculated following the ab initio thermodynamics formalism at zero pressure and temperature.

The solution energy of an atom X (X = N or O) at an interstitial site in the supercell of the metal (M) bcc crystal is calculated using equation (3.8). Here, $E_I(X_i)$ is the interstitial incorporation energy for interstitial i , at interstitial position I , in a lattice of metal M . $E(M + X_i)$ is the total energy of the metal lattice with the interstitial, $E(M)$ is the total energy of the pure metal lattice, and $E(X)$ is the total energy of an isolated atom (calculated as half the energy of the molecule for O and N) that forms the interstitial. The lattice constants were kept fixed during total energy calculations of point defects. The chemical potentials with respect to the N and O atoms were calculated as half of the binding energies of the N₂ and O₂ molecules. Convergence tests were performed with various k-point sampling and cut-off energies before choosing the settings for further computations. Using 6 x 6 x 6 k-point mesh with cut-off energy of 60 Ry, the Mo lattice parameter was computed to 3.130 Å, which corresponds closely to the theoretical value of 3.147 Å [19]. The energy calculations described by equation (3.8) can be used to arrive at various properties for material systems, including those discussed earlier in Section 2.3.1.1.

$$E_I(X_i) = E(M + X_i) - (E(M) + E(X)) \quad (3.8)$$

3.5 Finite element analysis

3.5.1 Governing Equations

Three-dimensional (3D) coupled temperature-displacement thermo-mechanical models were used for thermo-mechanical analysis. A thermo-mechanical analysis essentially involves a nonlinear calculation in which the displacements and temperatures are simultaneously solved. This allows for handling the reciprocal action of the temperature on the displacements and the displacements on the temperature. Equation (3.9) depicts the heat conduction equation used in the thermo-mechanical analysis, where T is the temperature, k is the thermal conductivity, Q represents the internal heat generation, ρ is the density of the material, C_P is the specific heat capacity, and t is the time [20].

$$\rho C_P \left(\frac{\partial T}{\partial t} \right) = \nabla \cdot (k \nabla T) + Q \quad (3.9)$$

The mechanical behaviour of the system, as defined by the strain due to thermal constraints, is depicted in equation (3.10) for the strain vector u . Here, ε is the strain tensor. Then, the mechanical equilibrium is defined as in equation (3.11), where σ is the stress tensor, and F represents the body force density vector.

$$\varepsilon = \nabla u + (\nabla u)^T \quad (3.10)$$

$$\nabla \cdot \sigma + F = 0 \quad (3.11)$$

The nonlinear system is linearized within each step of the iteration and solved with a full Newton-Raphson iteration scheme. Equation (3.12) shows the exact implementation of Newton's method for fully coupled temperature-displacement analysis. Here, Δu and $\Delta \theta$ are the corrections to the incremental displacement and temperature, K_{ij} represents the tangent stiffness matrix, and R_u and R_θ are the mechanical and thermal residue vectors, respectively [21]. Equation (3.13) defines the stiffness matrix, where $[B]$ contains the spatial derivatives of the element shape functions $[N]$, and

$[J]$ is the material Jacobian matrix [21].

$$\begin{bmatrix} K_{uu} & K_{u\theta} \\ K_{\theta u} & K_{\theta\theta} \end{bmatrix} \begin{Bmatrix} \Delta u \\ \Delta \theta \end{Bmatrix} = \begin{Bmatrix} R_u \\ R_\theta \end{Bmatrix} \quad (3.12)$$

$$[K^{t+\Delta t}] = \int_V [B]^T [J] [B] dV \quad (3.13)$$

3.5.2 FEM using ABAQUS

The 3D computer-aided design (CAD) models were developed using 3DEXPERIENCE® SOLIDWORKS (Dassault Systèmes, USA). Three-dimensional coupled temperature-displacement thermo-mechanical models were prepared with the commercial finite element analysis (FEA) software Abaqus/CAE 2021 (Dassault Systèmes Simulia Corp, USA). The models were built with the C3D4T (coupled temperature displacement tetragonal) mesh, and a mesh sensitivity analysis was performed. A surface heat load of $5 \times 10^6 \text{ W}\cdot\text{m}^{-2}$ was imposed on the semiconductor. The exposed surfaces of the heat sink had a boundary condition of radiation and natural convection to an ambient sink temperature of 298 K (25 °C). The free surface of the semiconductor was encastered as a mechanical boundary condition for the calculation.

3.6 References

- [1] *Standard Test Methods for Flow Rate of Metal Powders Using the Hall Flowmeter Funnel*, A. International, 2020.
- [2] *Standard Test Methods for Flow Rate of Metal Powders Using the Carney Funnel*, A. International, 2023.
- [3] Renishaw. "Renishaw AM 400 additive manufacturing system." Renishaw Plc. <https://www.renishaw.com/resourcecentre/en/details?data=101092&lang=gen> (accessed 28-May-2023).
- [4] J. Schindelin *et al.*, "Fiji: an open-source platform for biological-image analysis," *Nat Methods*, vol. 9, no. 7, pp. 676-82, Jun 28 2012, doi: 10.1038/nmeth.2019.

- [5] H. E. Sabzi, N. T. Aboulkhair, X. Liang, X.-H. Li, M. Simonelli, H. Fu, and P. E. J. Rivera-Díaz-del-Castillo, "Grain refinement in laser powder bed fusion: The influence of dynamic recrystallization and recovery," *Materials & Design*, vol. 196, 2020, doi: 10.1016/j.matdes.2020.109181.
- [6] S. E. Atabay, O. Sanchez-Mata, J. A. Muñoz-Lerma, and M. Brochu, "Effect of heat treatment on the microstructure and elevated temperature tensile properties of Rene 41 alloy produced by laser powder bed fusion," *Journal of Alloys and Compounds*, vol. 858, p. 157645, 2021/03/25/ 2021, doi: <https://doi.org/10.1016/j.jallcom.2020.157645>.
- [7] J. Rodríguez-Carvajal, "Recent advances in magnetic structure determination by neutron powder diffraction," *Physica B: Condensed Matter*, vol. 192, no. 1, pp. 55-69, 1993/10/01/ 1993, doi: [https://doi.org/10.1016/0921-4526\(93\)90108-I](https://doi.org/10.1016/0921-4526(93)90108-I).
- [8] *Standard Practice for Quantitative Measurement and Reporting of Hypoeutectoid Carbon and Low-Alloy Steel Phase Transformations*, A. International, West Conshohoken, PA, 2010.
- [9] C. W. Bale *et al.*, "FactSage thermochemical software and databases, 2010–2016," *Calphad*, vol. 54, pp. 35-53, 2016/09/01/ 2016, doi: <https://doi.org/10.1016/j.calphad.2016.05.002>.
- [10] K. Frisk, "A thermodynamic evaluation of the Cr-N, Fe-N, Mo-N and Cr-Mo-N systems," *Calphad*, vol. 15, no. 1, pp. 79-106, 1991/01/01/ 1991, doi: [https://doi.org/10.1016/0364-5916\(91\)90028-I](https://doi.org/10.1016/0364-5916(91)90028-I).
- [11] P. Giannozzi *et al.*, "QUANTUM ESPRESSO: a modular and open-source software project for quantum simulations of materials," *Journal of Physics: Condensed Matter*, vol. 21, no. 39, p. 395502, 2009/09/01 2009, doi: 10.1088/0953-8984/21/39/395502.
- [12] J. P. Perdew, K. Burke, and M. Ernzerhof, "Generalized Gradient Approximation Made Simple," *Physical Review Letters*, vol. 77, no. 18, pp. 3865-3868, 10/28/ 1996, doi: 10.1103/PhysRevLett.77.3865.
- [13] P. Giannozzi *et al.*, "Advanced capabilities for materials modelling with Quantum ESPRESSO," *Journal of Physics: Condensed Matter*, vol. 29, no. 46, p. 465901, 2017/10/24 2017, doi: 10.1088/1361-648X/aa8f79.
- [14] E. Schrödinger, "An undulatory theory of the mechanics of atoms and molecules," *Physical Review*, vol. 28, no. 6, pp. 1049-1070, 1926, doi: 10.1103/PhysRev.28.1049.

- [15] M. Born and R. Oppenheimer, "Zur Quantentheorie der Molekeln," *Annalen der Physik*, vol. 389, no. 20, pp. 457-484, 1927, doi: <https://doi.org/10.1002/andp.19273892002>.
- [16] P. Hohenberg and W. Kohn, "Inhomogeneous Electron Gas," *Physical Review*, vol. 136, no. 3B, pp. B864-B871, 11/09/ 1964, doi: 10.1103/PhysRev.136.B864.
- [17] W. Kohn and L. J. Sham, "Self-Consistent Equations Including Exchange and Correlation Effects," *Physical Review*, vol. 140, no. 4A, pp. A1133-A1138, 11/15/ 1965, doi: 10.1103/PhysRev.140.A1133.
- [18] J. P. Perdew, K. Burke, and M. Ernzerhof, "Generalized gradient approximation made simple," *Physical review letters*, vol. 77, no. 18, p. 3865, 1996. [Online]. Available: <https://journals.aps.org/prl/abstract/10.1103/PhysRevLett.77.3865>.
- [19] C. L. Fu and K. M. Ho, "First-principles calculation of the equilibrium ground-state properties of transition metals: Applications to Nb and Mo," *Physical Review B*, vol. 28, no. 10, pp. 5480-5486, 11/15/ 1983, doi: 10.1103/PhysRevB.28.5480.
- [20] S. V. Patankar, *Numerical heat transfer and fluid flow* (Series in computational methods in mechanics and thermal sciences). New York: Hemisphere Pub. Corp. ; McGraw-Hill (in English), 1980.
- [21] M. Smith, *ABAQUS/Standard User's Manual, Version 6.9*. Dassault Systèmes Simulia Corp (in English).

Chapter 4 – Laser powder bed fusion additive manufacturing of molybdenum using a nitrogen build atmosphere

In Chapter 2, the literature review established that the key challenge in the LPBF processing of Mo is the cracking due to GB embrittlement from O. Another significant learning from the literature review was the relative influence of other interstitials on GB cohesion in Mo and the competition between them. With this understanding, LPBF-AM processing of Mo under N₂ build atmosphere was proposed to introduce N into Mo. This chapter discusses the use of N₂ build atmosphere instead of argon as a process control in LPBF processing of Mo and investigates the microstructure and mechanical properties of the fabricated crack-free samples of Mo. A comparison with samples prepared under an Ar atmosphere is also performed. Fracture surface investigations are performed to study the influence of N on the formation of oxides in the samples. DFT modelling was performed to study the diffusion barrier of O in a pure Mo lattice and Mo with N.

This chapter has been submitted to the International Journal of Refractory Metals and Hard Materials with manuscript reference number: IJRMHM-D-23-00860 as: *T. Ramakrishnan*, E. R. L. Espiritu, S. Kwon, M. K. Keshavarz, J. A. Muniz Lerma, R. Gauvin and M. Brochu, “Laser powder bed fusion additive manufacturing of molybdenum using a nitrogen build atmosphere”.

4.1 Abstract

A method was developed to suppress the crack formation during laser powder bed fusion (LPBF) of molybdenum (Mo). The method uses a nitrogen (N₂) atmosphere to fabricate crack-free samples without any additional processing. To compare with the effect of the N₂ atmosphere, samples were prepared under an argon (Ar) atmosphere as well with the same process parameters. The microstructure analyses by optical and high-resolution electron microscopy revealed that crack-free samples were produced under this condition, whereas grain boundary cracks were observed throughout the sample fabricated in Ar atmosphere. To understand the mechanism of crack prevention by nitrogen (N), the energetics of solute components in the BCC-Mo structure were studied by Density Functional Theory (DFT). The theoretical calculations showed that the introduction of N into the BCC-Mo hinders oxygen (O) diffusion, causing O entrapment in the lattice at interstitial positions. As a result, reduced oxides within grains and at grain boundaries (GB) were observed. The results are consistent with the experimental observation made from the fracture surface investigation. The reduced embrittlement of GB from the reduced GB oxide formation is believed to suppress GB cracking.

4.2 Introduction

Molybdenum (Mo) is a refractory metal with a high melting point (2896 K), high mechanical properties (yield strength of 400 MPa) and high thermal conductivity ($138 \text{ Wm}^{-1}\text{K}^{-1}$) [1]. Mo alloys are among the refractory materials with increasing interest in high-temperature applications such as aviation and nuclear power generation industries [2]. Despite these advantages, Mo has not been widely employed in these industries due to its susceptibility to cracking and inherent brittleness at room temperature [3], leading to difficulties in fabricating complex parts using conventional casting and subtractive manufacturing processes. Laser powder bed fusion (LPBF) additive manufacturing is a process that can overcome this limitation.

LPBF is an emerging material fabrication technology that facilitates the creation of net shape complex parts beyond the limitations of conventional manufacturing processes without a significant need for machining [4–6]. During LPBF, powder particles are spread onto a substrate, and then a laser beam is rastered on the spread powder layer, causing the particles to melt and

solidify with the previous layers. This process is repeated in a layer-by-layer approach to build a part [7–9]. To date, LPBF of various materials, including aluminum [5, 10, 11], copper [12], CoCrMo [13, 14], nickel [15, 16], steel [17, 18], and titanium alloys [19, 20] have been widely studied.

To better understand the LPBF processing feasibility of Mo and the associated metallurgy challenges, the following considerations must be accounted. Mo is sensitive to intergranular cracking, which predominantly occurs due to the lack of ductility in the material when a thermal cycle around the ductile-to-brittle transition temperature (DBTT) is imposed [21–23]. At commercial purity levels, the DBTT range of Mo is reported between 323 K to 373 K (50 °C to 100 °C) [24, 25] and is altered by impurity levels, grain size and dislocation density [25]. Among these factors, the interstitial impurity content remains the most dominant factor. Literature shows that the presence of interstitial elements increases the DBTT of Mo, with oxygen (O) showing the greatest embrittling effect through diffusion to, and weakening of, grain boundary regions [26–30]. The solubility of O in Mo drastically decreases with temperature, from about 400 ppm close to the melting point to less than 50 ppm at RT [31, 32]. Any O that has dissolved in Mo during processing must diffuse out of Mo as it cools down, and they often end up at the GB. Researchers have shown that among various elements, O has the highest embrittling effect on Mo GB [33, 34] and that the GB oxides are the major factor causing GB cracking in Mo [23, 28]. In the LPBF-AM process, O is inevitably introduced from the residual content in powder feedstock and the build atmosphere [35].

Despite the challenges in processing Mo, the following pioneer studies on LPBF documenting the issues involved in its processing via this route, are available in the literature. Faidel et al. [36] was among the pioneering studies where they discussed the strategies employed to reduce porosity defects by melt-pool overlap control via manipulation of the point distance and hatch distance. The study reported that densification to only 82.5% of the theoretical density (TD) was achieved and that higher energy inputs caused thermal deformation in the parts prepared. Leitz et al. [37] conducted simulations, evaluated the influence of powder bed characteristics, and suggested that the high melting point of Mo presents small melt pools. The small melt-pool size causes the process

to be sensitive to the morphological characteristics of the powder bed and hinders densification efforts involving melt-pool overlap control strategies. D. Wang et al. [38] studied the use of the dry granulation process and plasma spheroidization of Mo powders and reported densities up to 99.1%. Using support structures that can maintain a higher build temperature (reported above 200 °C, which is higher than DBTT of Mo) and lower the cooling rate, they claimed crack suppression in Mo parts. Braun and Kaserer et al. [35] ascribed the crack formation in pure Mo to the O content coming from contamination on the powder surface and pick up during processing, which led to segregated oxygen at the grain boundaries that caused embrittlement.

Researchers have employed various strategies to reduce GB brittleness and improve the ductility of Mo processed by various techniques early on. Nagae et al. [39] employed nitriding on pure and low-alloyed Mo samples processed through the powder metallurgy route and reported that the yield strength and ductility of the samples improved. They also reported that DBTT could be lowered well below RT (up to 130 K) and that recrystallization resistance could be increased. Olds et al. [40] studied the effects of O, N and C interstitials on the ductility of Mo by studying the DBTT of samples with varying interstitial content and concluded that O had the highest detrimental effect, with N and C showing lower effects. Their study concluded that the effects of O and N are not additive, with indications that N may have the ability to offset the embrittlement caused by O. Kurishita et al. [41] doped N into Mo bi-crystals with weak $\langle 110 \rangle$ symmetric tilt boundary and showed that presence of N within the lattice improved the ductility of Mo, reducing the DBTT. From their studies, samples with N content above 55 ppm showed good ductility even at liquid N₂ temperatures and exhibited transgranular fracture indicating improved GB cohesion. Literature also showed that compared to Mo samples with O as interstitial, Mo with simultaneous N and O interstitials possessed a lower DBTT, suggesting an impact of N on O solubility and diffusion [42].

This work investigated the use of a nitrogen gas (N₂) build atmosphere to induce N pick-up at the melt interface to reduce GB embrittlement and annihilate cracking of Mo parts fabricated using LPBF. Optical and electron microscopy were used to analyze the resulting microstructure of the fabricated samples. Grain size and morphology, along with interstitial impurity content, as the major factor annihilating the cracking tendency, was investigated.

4.3 Experimental methods

Gas atomized Mo powders with chemical composition shown in Table 4.1, were procured from Tekna (Canada) and used in this study. Powder morphology was analyzed by Scanning Electron Microscopy (SEM) using a SU3500 (Hitachi, Japan) SEM. Particle size distribution (PSD) was measured by means of laser diffraction using an LA-920 laser particle size analyzer (Horiba, Japan). Each of these tests was conducted three times to provide statistical significance of the reported values. Flowability of the powders was tested using Hall and Carney funnel methods as per ASTM B213 and B964, respectively. The rotating drum technique was used to evaluate the cohesive index of the powder using the GranuDrum® apparatus (Granutools, Belgium).

Table 4.1 Composition of Mo powders used in this study as per the certificate of conformity

Element	Mo	Cr	Fe	Ni	C	O	N	H	Others
Wt.%	99.98	< 0.01	< 0.01	< 0.01	< 0.005	0.016	< 0.01	< 0.002	< 0.01

LPBF was performed on an AM400 LPBF machine equipped with a reduced build volume (Renishaw, UK). Samples with a size of 10 mm x 5 mm x 5 mm (L x W x H) were fabricated at room temperature using identical laser parameters under two different atmospheres: argon (Ar) and nitrogen (N₂), both with a purity of 4.8 HP (99.998% High Purity, Praxair, Canada). A bi-directional hatching pattern and 67° rotation between each layer were used as a scanning strategy. Oxygen was limited to less than 200 ppm in either build atmosphere. Mo (99.95% metal basis) plates of 2.5 mm thickness from Alfa Aesar (USA) were used as substrates.

Samples were sectioned for characterization using an IsoMet™ Low Speed Precision Cutter (Buehler, USA). Metallographic preparation was performed by grinding up to 800-grit SiC paper, then polishing with diamond suspensions of 9 µm, 3 µm, and 1 µm size particles, followed by 0.05 µm colloidal silica suspension on a Labopol (Struers, USA) equipment. Optical micrographs to characterize the as-built microstructure, density, and crack defect structure, were captured using a light optical microscope (Nikon, Japan) equipped with a Clemex Vision System (Clemex, Canada). Average crack length was calculated as the ratio of the cumulative crack length in a region of

interest to the number of cracks, and crack density was calculated as the ratio of the cumulative crack length within a 1 mm^2 area divided by the average crack length calculated earlier using Fiji distribution of ImageJ software [43].

Crystallographic texture and grain morphology were studied using a SU3500 SEM equipped with an electron back-scattered diffraction (EBSD) detector (Oxford Instruments, UK). HKL Channel 5 software (Oxford Instruments, UK) was used for the analysis of the EBSD data. The alpha grain diameter was measured as equivalent circle diameter, and the local misorientation profile was evaluated using line maps of length equal to 80% grain diameter. A SU9000 (Hitachi, Japan) field emission scanning electron microscope (FE-SEM) equipped with an energy dispersive spectrometer (EDS) detector (Oxford Instruments, UK) was used for high magnification micrographs to characterize the precipitates.

Vickers microhardness tests were performed using a Clark CM-100AT (Sun-tec, USA) automated microhardness equipment with 0.2 kgf load for a dwell time of 30 s, and measurements are reported as averages of 5 measurements. N and O content of the powder feedstock and LPBF samples were measured using a LECO TC600 Nitrogen-Oxygen Determinator (LECO, USA).

4.4 Computational methods

The phase diagram and paraequilibrium diagram of the Mo-N system were calculated using FactSage thermochemical software [44]. The SpMCBN thermochemical database reported by Frisk [45] was used for the calculations. Although the Gibbs-energy of the HCP phase was estimated by Frisk [45] in the Mo-N system, this metastable phase was not considered in this study as there is no experimental evidence of its existence.

Density Functional Theory (DFT) calculations were performed using the plane-wave basis set based Quantum Espresso package [46, 47]. Ultrasoft pseudopotentials for modelling the interaction between ion cores and valence electrons and Perdew-Burke-Ernzerhof (PBE) functional of the Generalized Gradient Approximation (GGA) with non-linear core correction for treating exchange-correlation interactions were used [48]. Nudged elastic band (NEB) calculation, as implemented in Quantum Espresso package, was used to compute diffusion barriers.

4.5 Results and Discussion

4.5.1 Powder Characterization

The SEM micrographs of the Mo powder used in this study are shown in Figure 4.1a-b. The powders are spherical in nature, without any satellites or agglomeration. The results of Hall and Carney flow tests showed flow times of 13.26 ± 0.1 s (per 50 g) and 6.2 ± 0.0 s (per 150 g), respectively, indicating high flowability of the powder. The apparent density was measured to be 57 ± 1 %. The powders showed a narrow PSD, as depicted in Figure 4.1c, with D_{10} , D_{50} and D_{90} values of 20 ± 2 μm , 29 ± 2 μm , and 43 ± 3 μm , respectively. Figure 4.1d shows a representative result of the rotating drum experiment, plotting the relationship of the cohesiveness index with respect to rotational speed. The cohesiveness index values are well below the critical value of 24, suggesting easy spreading during recoating; thus, regular recoating speed could be used [49].

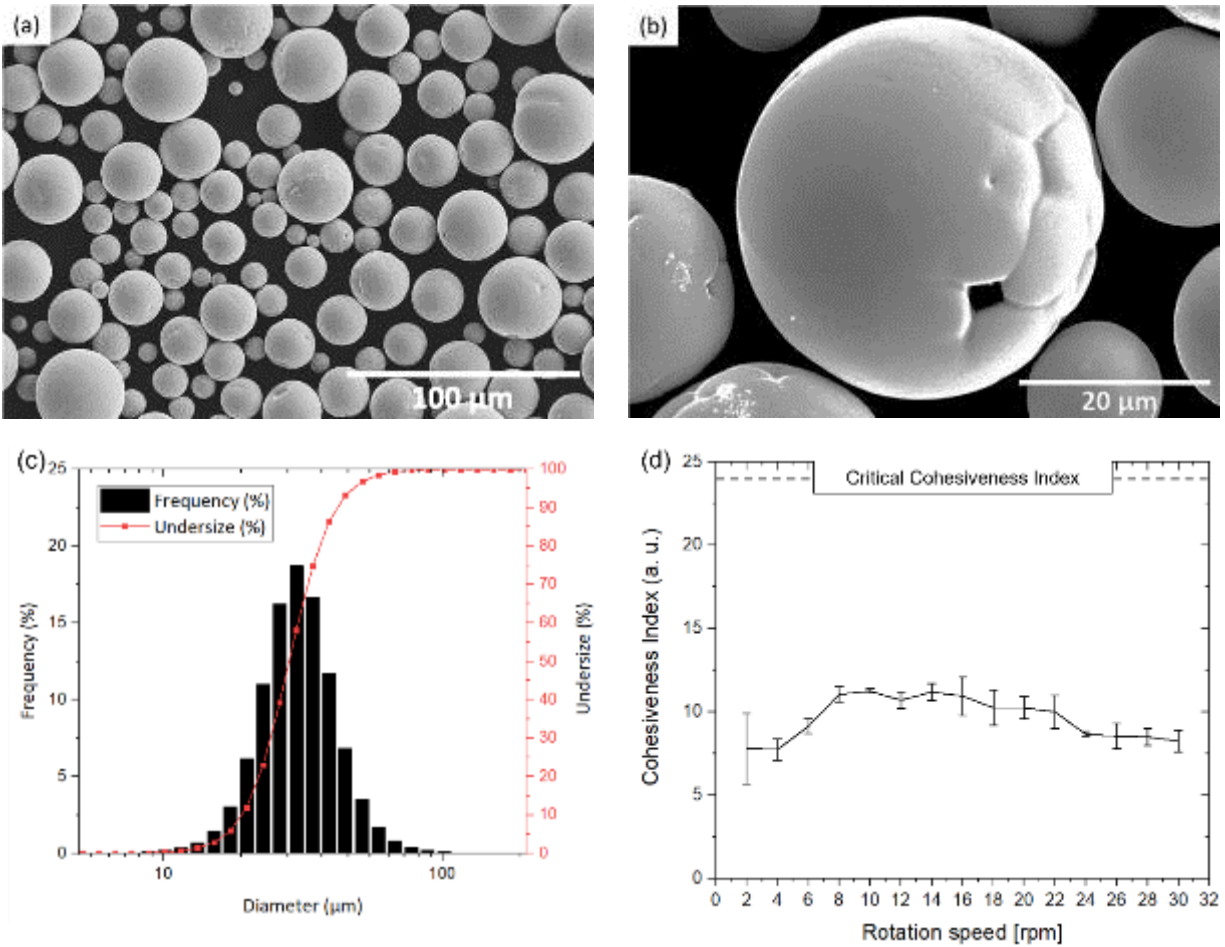


Figure 4.1 (a,b) SEM images of Mo powders showing size and morphology of the particles. (c) Particle size distribution, and (d) cohesiveness index wrt rotation speed, for Mo powder.

4.5.2 Sample Characterization

4.5.2.1 Microstructure and grain size

Optical and EBSD micrographs of the cross-section of a sample fabricated under an Ar atmosphere (Mo-Ar) are shown in Figure 4.2a and Figure 4.2b, respectively. The optically measured density of the sample was 98.7 ± 0.4 %. The micrographs indicated a strong columnar growth structure, as expected in the solidification of a pure element, despite the 67° rotation scanning strategy. The partial re-melting of the previous layer in LPBF eliminates the nucleation barrier and provides a base for the epitaxial growth of grains. Being a pure metal, there is no hindrance to grain growth other than the competition between different orientations [38, 50]. Figure 4.2c shows the optimization of part density and cracking characteristics against volumetric energy density for

parts fabricated via LPBF-AM. Square symbols indicate density (with corresponding error bars) for various samples, with red representing cracked samples. Higher volumetric energy density from the laser scan strategy was required to achieve higher densities. The average crack length (in μm) is shown in the figure using colormap regions (legend in table).

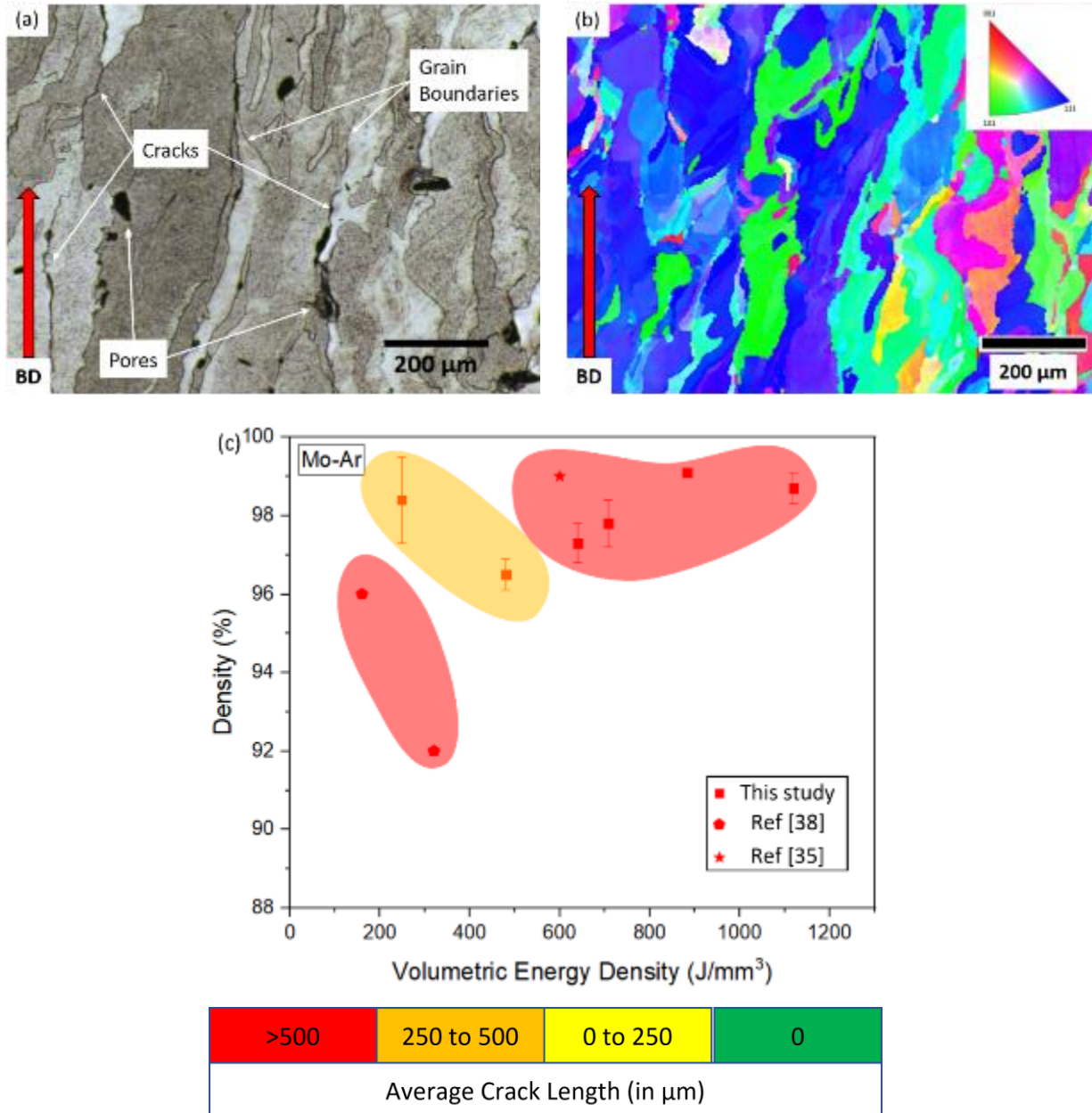


Figure 4.2 (a) Optical, and (b) EBSD micrograph of Mo-Ar sample. BD indicates the build direction of the samples. (c) Optimization results showing part density against volumetric energy density with average crack length of the samples

The Mo-Ar sample showed a grain structure with vertically elongated grains (from the columnar epitaxial growth) having an aspect ratio (L/W) ranging between 3.2 and 4.1. The grain size distribution showed numerous grains with diameters between 11 to 40 μm and some grains with diameters between 40 to 180 μm . Cracks were observed along the grain boundaries and mostly aligned with the build direction. The Mo-Ar sample showed an average crack length of 632 ± 41 μm , with a crack density of 4.8 ± 0.3 cracks per mm^2 with very few cracks with lengths above 1 mm. Cracks were reported in previous studies in the literature [35, 38], but no quantification in terms of crack density nor crack length was discussed. Using the provided literature micrographs, a crack density of 7 cracks per mm^2 and a crack length of 550 ± 80 μm could be estimated from the work by Wang et al [38]. Similarly extracted from Braun et al. [35], values of 16 cracks per mm^2 and 870 ± 70 μm were discerned. The quantified crack properties from the literature [35], [38] are in good agreement with this study. Majority of the grains investigated in Mo-Ar indicated a misorientation angle of about $27.9 \pm 2.5^\circ$.

Figure 4.3a and Figure 4.3b show the optical and EBSD micrographs of a representative sample fabricated under the N_2 atmosphere (Mo-N). In contrast to the Mo-Ar samples, Mo-N samples that did not show any evident cracking could be produced. The optically measured density of the Mo-N sample was 99.1 ± 0.1 %. In the Mo-N sample, the grain structure shows limited columnar nature, and along the build direction, grains are disrupted by melt-pool-like boundaries. Except for some grains with large columnar structures, the majority of the grains are larger in width than their length, with an aspect ratio (H/W) ranging between 0.8 and 1.3. Most of the grains showed a grain diameter between 6 to 20 μm , with a few grains of larger grain diameter between 20 and 140 μm . The misorientation angle for Mo grain boundaries in the Mo-N sample was measured at $30.1 \pm 2.1^\circ$, while there were many grains which showed a higher misorientation value of $48.3 \pm 3.7^\circ$. Figure 4.3c shows the part density and cracking characteristics optimization against volumetric energy density, indicating the ideal range for achieving crack-free high-density parts using LPBF-AM under an N_2 atmosphere. Square symbols indicate density (with corresponding error bars) for various samples, with red and green squares representing samples with and without cracks, respectively. Average crack length (in μm) is shown in the figure using colormap regions, with the table indicating the legend for the same.

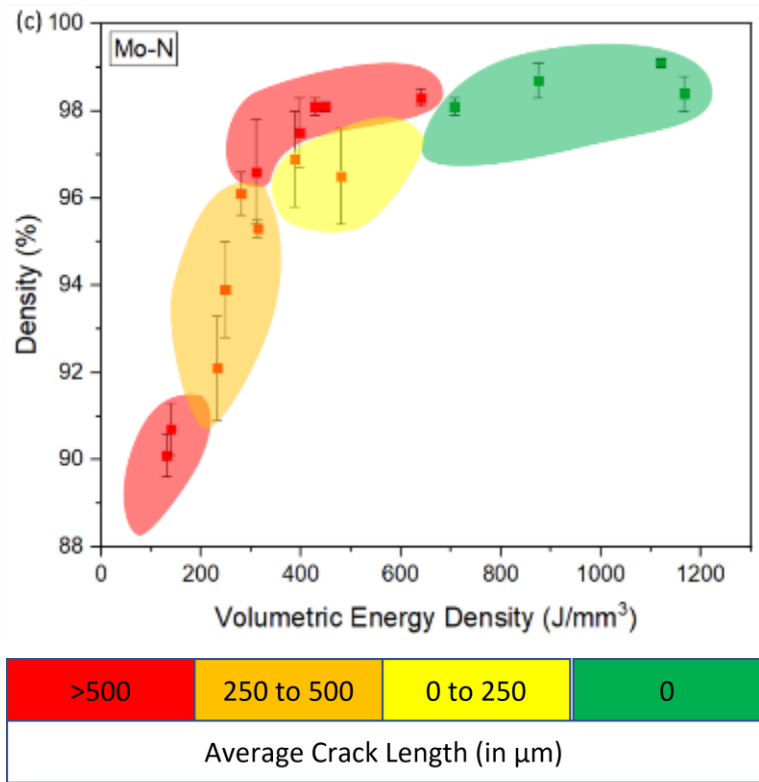
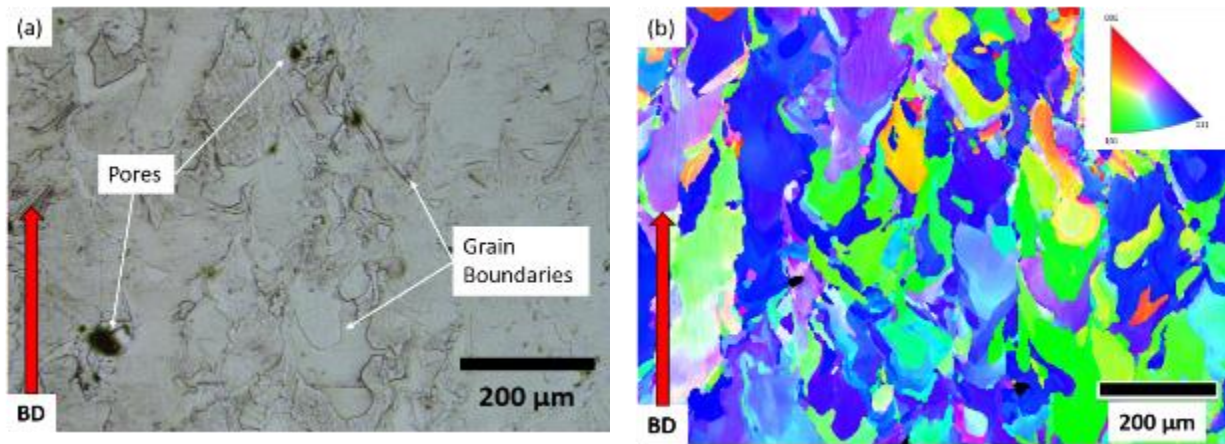


Figure 4.3 (a) Optical, and (b) EBSD micrograph of a representative crack-free Mo-N sample. (c) Optimization results showing part density against volumetric energy density with average crack length of the samples

4.5.2.2 Grain and precipitates characterization

High-resolution microscopy was used to better understand the mechanisms driving the grain structure and annihilating the cracking in Mo. Figure 4.4a depicts a representative back-scattered electron (BSE) micrograph of Mo-N sample. Two types of grains are visible – alpha-Mo grains

and grains with distinct precipitates. The ratio of precipitate-free grains to grains with precipitates is about 2:3. Figure 4.4b shows a higher magnification micrograph obtained from the location marked in Figure 4.4a. The high magnification image indicates that some of the precipitates are also present along the grain boundaries (as identified by BSE contrast). It is interesting to note that the precipitate-bearing grains showed the higher misorientation value discussed in section 4.5.2.1.

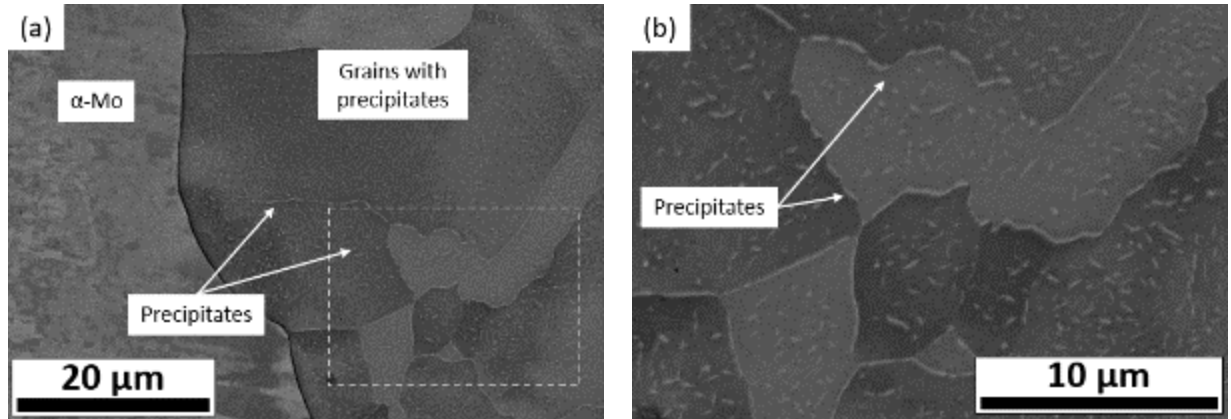


Figure 4.4 (a, b) BSE micrograph of Mo-N grains showing precipitates

Figure 4.5a and Figure 4.5b show the precipitates through micrographs captured using scanning transmission electron microscopy (STEM). The precipitates have a needle-like morphology. They were 464 ± 117 nm long and less than 30 nm wide, yielding an aspect ratio of approximately 15:1. They were uniformly distributed within smaller grains and formed approximately 0.8 % area fraction of the grains. Figure 4.5c presents the results of an EDS line-scan analysis of 200 nm taken from point A to B as indicated through a round precipitate and the needle-like precipitate. The EDS results indicate the needle-shaped precipitates to be rich in N, suggesting a molybdenum nitride phase. The round precipitates contained higher O, suggesting a molybdenum oxide phase. A quantification of oxide particles for Mo-Ar and Mo-N was performed using microstructural analysis.

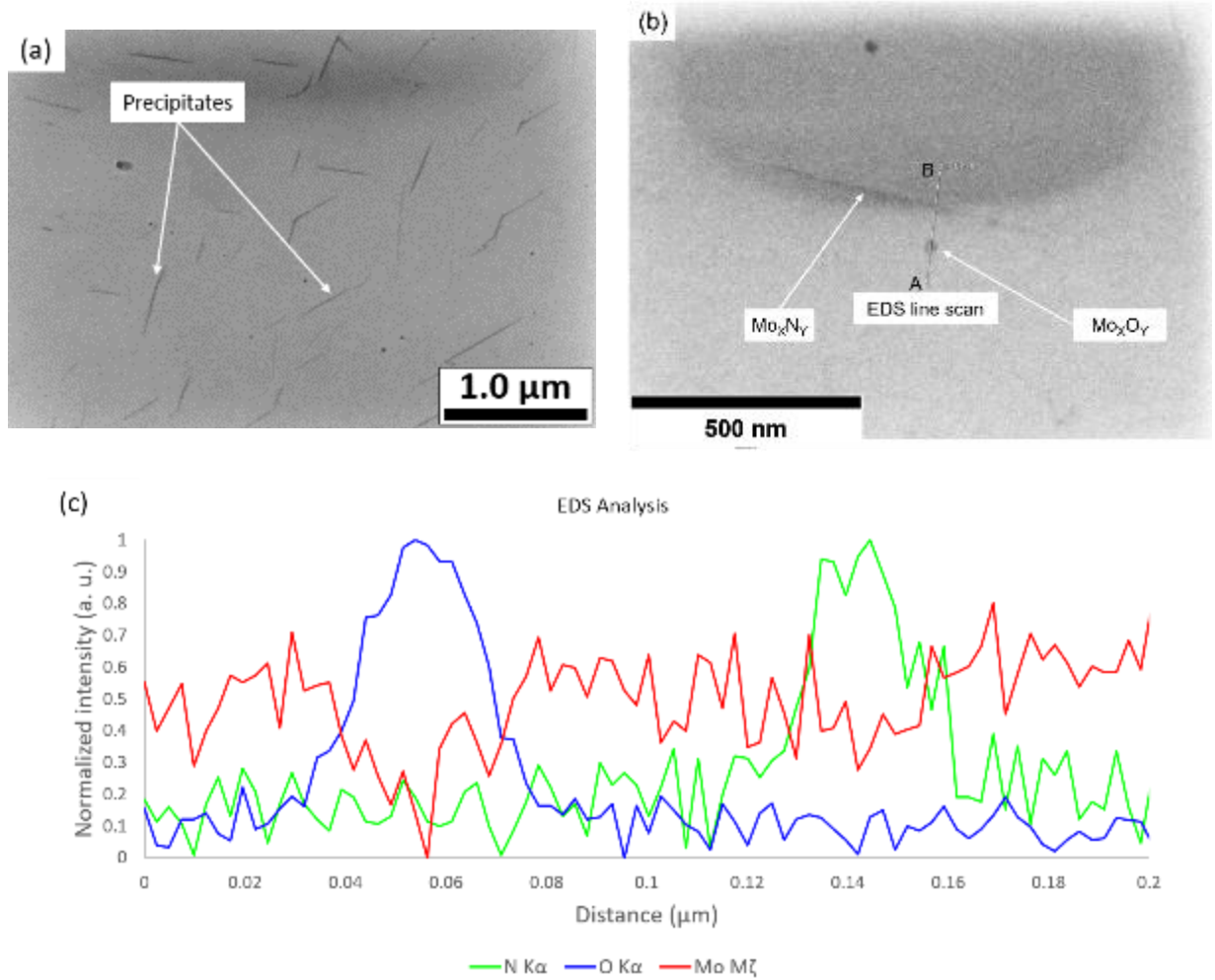


Figure 4.5 (a, b) High magnification STEM showing the precipitates, and (c) EDS line scan analysis of the precipitates as shown in Figure 4.5b.

Representative SEM micrographs of Mo-Ar and Mo-N samples are depicted in Figure 4.6a and Figure 4.6b, respectively, showing the presence of oxide particles as dark round artifacts. The Mo-Ar sample presents an area fraction of oxides at 0.35%, with an average diameter of $0.152 \pm 0.024 \mu\text{m}$, while the Mo-N sample showed an area fraction of 0.12% with an average diameter of $0.082 \pm 0.017 \mu\text{m}$, indicating a much smaller number of oxides (in size and number density) within the grain in Mo-N.

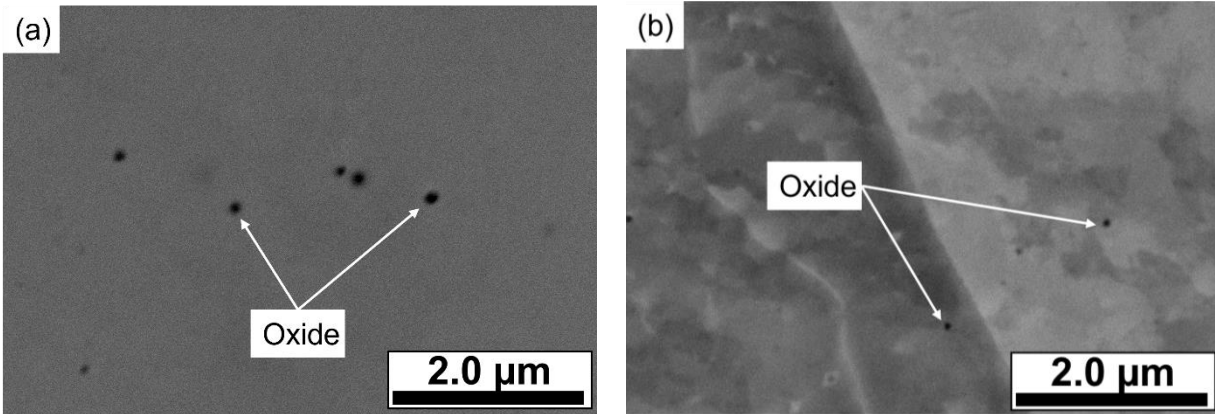


Figure 4.6 SEM micrographs showing oxide particles in (a) Mo-Ar, and (b) Mo-N.

4.5.2.3 Formation of Mo₂N precipitates

Early studies in the literature on Mo suggest very low solubility for N in Mo [51]. But, researchers in the field of welding have suggested that the increased gas fugacity from the dissociation of diatomic gas molecules in the plasma arc can lead to increased dissolution of N and formation of nitrides in the weld metal [52]. Additional studies on laser nitriding indicated a similar increased solubility behaviour through plasma-enhanced N activity [53]. Such an increased solubility of N was also observed in refractory metals. Bandopadhyay et al [54] reported that the plasma-enhanced activity of N was 10.15 ± 0.65 times that of diatomic N₂ gas over niobium and tantalum samples, and the corresponding solubility was three times the equilibrium solubility in these materials. Furthermore, researchers have reported that metal vapours and plasma above the melt pool are prevalent during the LPBF of metals due to the high laser energy conditions [55], [56].

Figure 4.7 shows the phase diagram of the Mo-N system in solid black lines. Three solution phases (i.e., Liquid, BCC-Mo, FCC-Mo₂N) appear to be stable in equilibrium. The temperature of the eutectic reaction (Liquid → BCC-Mo + FCC-Mo₂N) is at 2172 K (1899 °C). The maximum solubility of nitrogen in BCC-Mo at this temperature is 1.32 at% N. The solid red lines are the paraequilibrium diagram (T₀ lines) calculated with the assumption of no elemental diffusion between phases. The paraequilibrium diagram often represents the theoretical limit of eutectic growth under rapid solidification conditions [57, 58]. In the composition range between 0 and 36.7 at% N, the lowest temperature that the liquid phase that can exist during rapid solidification is at 1822 K (1549 °C). The theoretical limit of nitrogen solubility in BCC-Mo at this condition is 12

at%. In practice, eutectic growth occurs between these two regimes [57, 58]. As such, the initial grain of BCC-Mo during rapid solidification conditions can have a high content of nitrogen and precipitate Mo_2N within the grain after the grain growth.

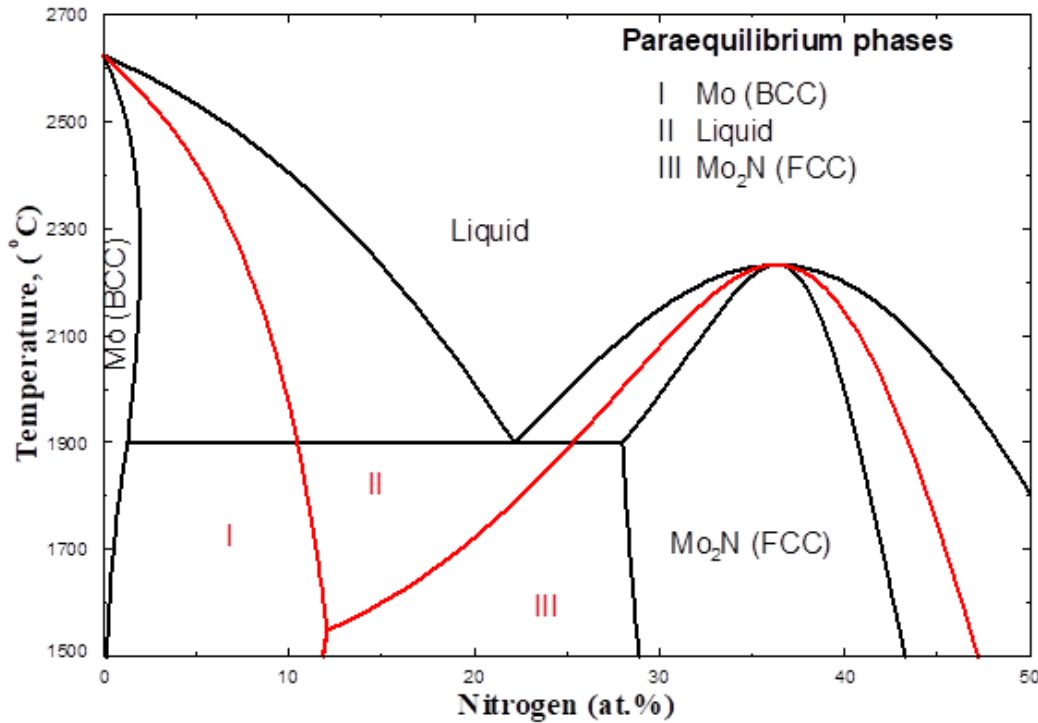


Figure 4.7 Calculated paraequilibrium line in Mo-N phase diagram.

From laser welding studies, Liang-Liang Zhang et al. [59] reported the formation of Mo_2N precipitates in Mo alloy under the influence of N_2 within the welding atmosphere, with the precipitate morphology matching very closely to what we have observed in this study. The authors reported that within the fusion zone, Mo_2N precipitates were observed within the grains and at the grain boundaries, similar to that reported in Section 4.5.2.2. Using a simple dislocation model described by Zenk et al [60], they proposed that there exists a coherent or semi-coherent interface between the $\{111\}$ planes of Mo_2N and $\{110\}$ planes of Mo with about 8.6% mismatch. According to Zenk et al. [60], misfits below 15 % can result in the formation of coherent interfaces with reasonably high bonding, which could be possible in this case.

4.5.2.4 Microhardness measurements

Microhardness measurements of the two types of grains were carried out to study the impact of N content and Mo₂N precipitates in the fabricated samples. As a comparison for this work, the hardness of electron-beam welded Mo reported by Kolarikova et. al. [61], showed fusion zone values between 170 to 200 HV. The hardness values measured for the Mo-Ar sample were 205 ± 12 HV, which corresponds to the upper range of the fusion weld values. On the other hand, the precipitate-free grains for the Mo-N sample showed a hardness value of 249 ± 11 HV. This hardening indirectly indicates the significant presence of interstitial trapped in the lattice. In comparison, the precipitate-containing grains in the Mo-N sample showed a hardness of 213 ± 12 HV. The hardness for the precipitate-containing grains can be treated as in a composite material where the Mo₂N is acting as the second phase. Koshy et al [62] reported a value of 2200 HV for the hardness of Mo₂N phase, while Bouaouina et al. [63] reported a value of 1400 HV. Applying the rule of mixtures, considering the hardness of precipitate-free and interstitial-free grains from Mo-Ar as the basis (205 HV) and hardness of secondary phase (i.e., Mo₂N) the values reported in [62] and [63], a precipitate containing grain is expected to have a hardness between 214 to 221 HV, which is close to the measured value. This suggests that in the grains with precipitates, most of the N content is present as precipitates and only a negligible amount is retained in the lattice.

4.5.2.5 Fracture surface analysis

Fracture surface SEM micrographs obtained from uncontrolled cracking of the samples are shown in Figure 4.8a and Figure 4.8b for the Mo-Ar sample. The fracture surface features suggest crack propagation at the grain boundaries in Mo-Ar samples. Higher magnification micrograph, as seen in Figure 4.8b, indicated the presence of a large number of irregular oxide particles at most of the grain boundaries in the sample. Liang-Liang Zhang et al. [64] reported similar observations of oxide particles at fracture surfaces in laser welding of Mo. Mallett [65] observed that with increasing oxygen content, the shape of precipitates at the grain boundaries changes from discrete precipitates to continuous film. In the present study, the oxygen level was not high enough to yield a continuous film, but a transition toward such a formation could be observed in certain regions. The surface is indicative of a grain morphology, as it was earlier seen in EBSD analysis. Figure 4.8c and Figure 4.8d, respectively show the fracture surface micrographs of the Mo-N sample. In stark contrast to Mo-Ar samples, Mo-N indicated fewer and smaller round precipitates at very few

locations on the fracture surface. It is interesting to report that an extensive grain boundary search was needed in the Mo-N sample to identify some or any oxide particles. This is in line with the results in Section 4.5.2.2 above, where in comparison to Mo-Ar, there was a drastically reduced amount of oxide particles within the grains in Mo-N.

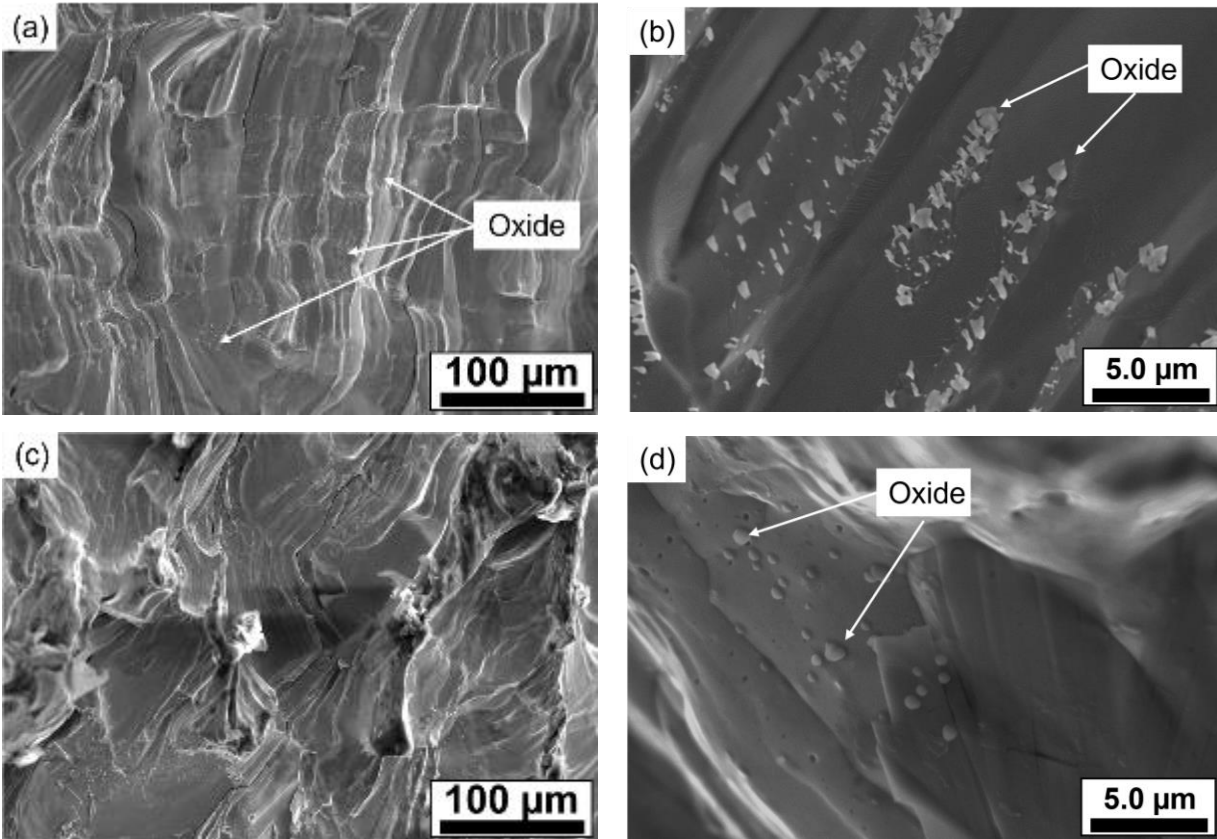


Figure 4.8 SEM fractographs (a, b) Mo-Ar, and (c, d) Mo-N, showing oxide particles.

4.5.2.6 N and O content analysis

Table 4.2 below provides the results of the N and O content analysis performed on the samples. Mo powder showed an O content of 320 ppm and a N content of less than 5 ppm. Mo-Ar and Mo-N samples showed statistically similar O content to the starting powder. This is interesting to note considering the earlier observations of a reduced amount of oxide particles observed in the Mo-N microstructure within the grains and at the fracture surface. The N content in Mo-Ar was 16 ± 2.9 ppm, while in Mo-N showed a 3600% increase to 590 ± 110 ppm.

Table 4.2. N and O content in Mo powder, Mo-Ar and Mo-N samples (values in ppm)

Sample	O content (ppm)	N content (ppm)
Mo powder	320 ± 52	<5
Mo-Ar	400 ± 65	16 ± 2.9
Mo-N	330 ± 54	590 ± 110

4.5.3 DFT calculations

4.5.3.1 Interstitial incorporation energy

DFT calculations were performed to better understand the incorporation energy for O and N interstitials in bcc Mo. Additional details of the DFT calculations and the results of the convergence test are provided in the Supplementary Material section. Interstitial incorporation energy, $E_I(X_i)$ is defined as per Equation (4.1), where $E_I(X_i)$ is the interstitial incorporation energy for interstitial i , at interstitial position I , in a lattice of metal M . $E(M + X_i)$ is the total energy of the metal lattice with the interstitial, $E(M)$ is the total energy of the pure metal lattice, and $E(X)$ is the total energy of an isolated atom (calculated as half the energy of the molecule for O and N) that forms the interstitial.

$$E_I(X_i) = E(M + X_i) - (E(M) + E(X)) \quad (4.1)$$

In order to validate our calculations, the energy difference for the tetrahedral lattice position with respect to octahedral lattice position for O and N in Mo was computed and compared to the literature. For physical relevance, energy differences rather than absolute energies are used here, as is commonly practiced in DFT studies, since the latter is dependent on the type of pseudopotentials used [66].

Table 4.3 shows the energy difference for O and N interstitials in Mo. A negative value indicates an energetically favourable difference ($E_{Tet}(X_i) - E_{Oct}(X_i)$), and suggests that the tetrahedral position is more favoured for O, while a positive value, such as in the case of N, indicates that the octahedral position is more favoured for N. This is in good agreement with results reported for various bcc metals by previous researchers [67, 68].

Table 4.3 Interstitial incorporation energies for O and N in Mo.

Material	$E_{tet}(O_i) - E_{oct}(O_i)$	$E_{tet}(N_i) - E_{oct}(N_i)$	Remarks
Mo	-0.28 eV/atom	0.76 eV/atom	[68], [69]
	-0.17 eV/atom	0.69 eV/atom	This study

4.5.3.2 Diffusion barrier

NEB calculations were performed to compute the diffusion barrier for interstitial O in pure bcc Mo, and Mo with N interstitial. Figure 4.9a and Figure 4.9b indicate the minimal energy path (MEP) for both conditions (O diffusion in pure bcc cell and O diffusion in bcc cell with N interstitial). In bcc Mo, as in those produced under Ar atmosphere in LPBF, the diffusion barrier for O is low with an activation energy of around 0.16 eV, resulting in easy O lattice diffusion to GBs. The MEP suggests that the diffusion barrier for O in bcc Mo with interstitial N is much higher than that for O in pure bcc Mo. This suggests that with N interstitial presence, O's diffusion towards GB will be reduced.

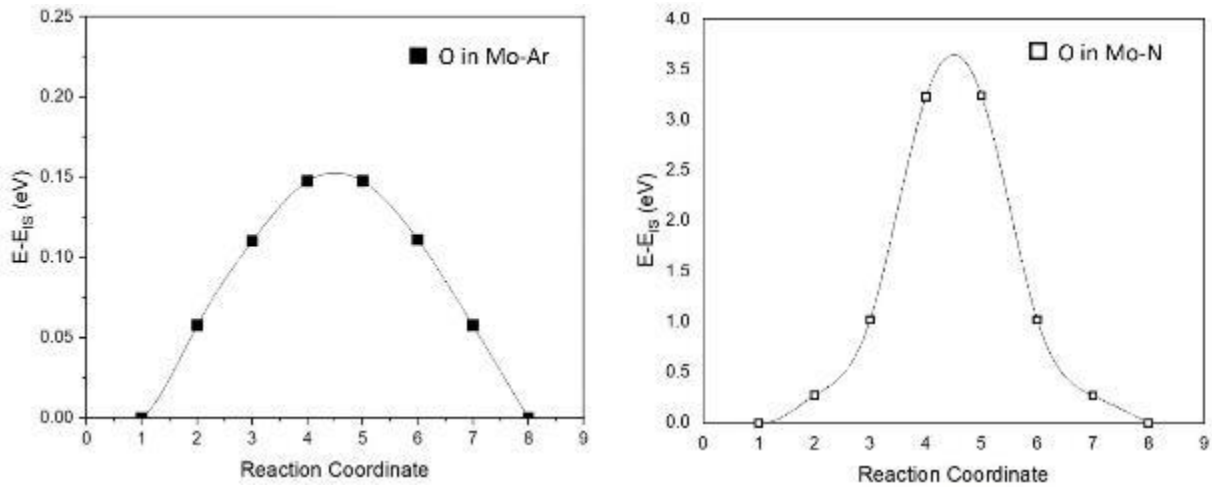


Figure 4.9 Diffusion barrier for (a) O in bcc Mo, and (b) O in bcc Mo with N interstitial

4.5.4 Effect of nitrogen

From the DFT calculations above, we propose that N introduced into the Mo lattice incorporates at the octahedral interstitial positions, while O prefers tetrahedral interstitial positions. The presence of N in the lattice raises the diffusion barrier for O and prevents its diffusion in Mo lattice. The reduced diffusion results in much lower oxide particles within the grain and at GBs as

observed above in Section 4.5.2.2 with Figure 4.6 and in Section 4.5.2.5 with Figure 4.8. GB oxides are known to be the major contributor to GB embrittlement in Mo [27, 28, 30, 34]. This reduction of GB oxides is proposed as a major factor in the suppression of cracking in LPBF processed Mo presented in this study. Additionally, while earlier studies have reported that interstitial elements can have a detrimental effect on GB cohesion energy, N was reported to have a lower or negligible effect in comparison to O [34, 70, 71]. More recently, D. Scheiber et al. [27] have reported that N improves the GB cohesion in Mo based on DFT studies on GB cohesion energy computed for various impurities in Mo. The presence of Mo₂N results in increased misorientation, and micron-sized sub-grains within the sample, as discussed in Section 4.5.2.1, possibly contributing to their hardening. Also, L-L. Zhang et al. [59] discussed that there is a coherent interface between {111} of Mo₂N and {110} of Mo, leading to a strengthening effect from the increased driving force for crack propagation.

4.6 Conclusion

Pure molybdenum was processed by LPBF-AM under Ar and N₂ atmospheres. While samples processed under Ar showed cracking, crack-free samples were fabricated under an N₂ atmosphere. Under the N₂ atmosphere, N was introduced into the Mo part. This increases the energy barrier for O diffusion, which traps O within the lattice at interstitial positions, resulting in reduced oxide formation within the grain and at grain boundaries, leading to a reduction in GB embrittlement. GB cracking, which was inevitable in typical LPBF processing of Mo, is eliminated without significantly affecting the purity of the LPBF part. Plasma-enhanced fugacity of nitrogen resulted in increased nitrogen content in the LPBF part, showing that nitrogen doping and even in-situ nitriding are feasible during LPBF. Using grain boundary engineering via N₂ atmosphere in LPBF, the suppression of grain boundary cracking in Mo fabricated through LPBF-AM was successfully demonstrated.

4.7 Supplementary Material

In order to compute the interstitial formation energies and migration barriers of interstitial atoms, a cubic 3 x 3 x 3 supercell of the bcc lattice was used. The supercell was structurally relaxed by first-principles DFT calculations for total energies, forces, and stresses, using the GGA-PBE

functional for exchange–correlation. All DFT calculations were done with the PWscf code of the Quantum Espresso software package. The wave-functions of the valence electrons are represented by a plane-waves basis set with a cutoff energy of 816 eV (60 Ry), and the electron density and effective Kohn–Sham potential by discrete Fourier series with a cutoff energy of 8163 eV (600 Ry). The interactions of valence electrons with the atomic nuclei and core electrons are described by ultrasoft pseudopotentials. Brillouin-zone integrals are evaluated on a Monkhorst–Pack mesh of $6 \times 6 \times 6$ k-points with a Gaussian smearing of 0.02 eV. The convergence criteria were set to 1.0×10^{-8} eV for the total energy and to 1.0×10^{-5} eV·Å⁻¹ for the forces on atoms. All thermodynamic quantities were calculated following the ab initio thermodynamics formalism at zero pressure and temperature. The solution energy of an atom X (X = N or O) at an interstitial site i in the supercell of the metal (M) bcc crystal is calculated as below. The lattice constants were kept fixed during total energy calculations of point-defects. The chemical potentials with respect to the N and O atoms were calculated as half of the binding energies of the N₂ and O₂ molecules.

Convergence tests were performed with various k-point sampling and cut-off energies before choosing the settings for further computations as shown in Figure 4.10 below. Using $6 \times 6 \times 6$ k-point mesh, with cut-off energy of 60 Ry, Mo lattice parameter was computed to 3.130 Å, which corresponds closely to theoretical value of 3.147 Å.

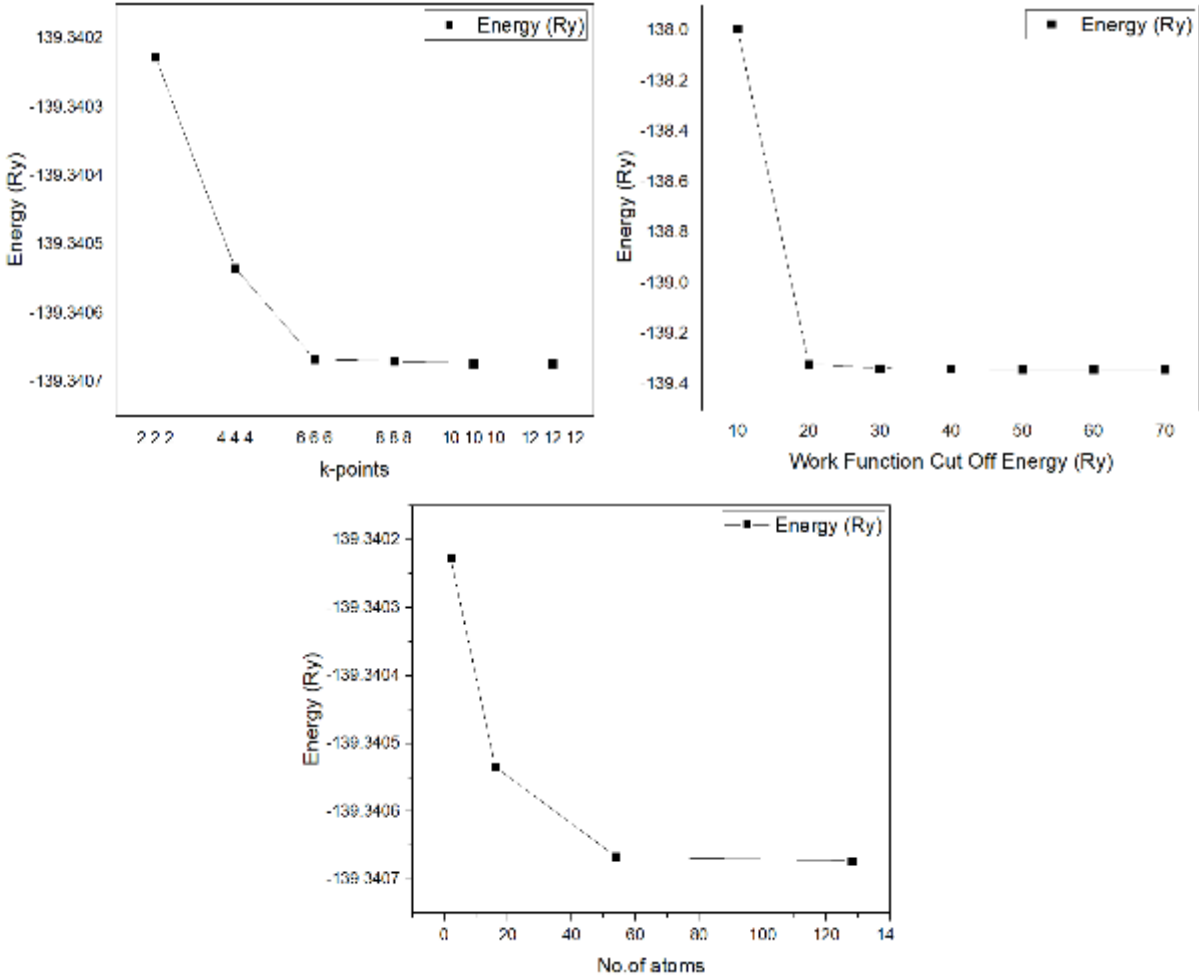


Figure 4.10 Convergence tests (a) Brillouin-zone sampling, (b) Work function cut-off energy, and (c) No. of atoms in supercell.

4.8 Acknowledgement

The authors would like to thank the generous research support provided by the Natural Sciences and Engineering Research Council (NSERC) of Canada (NSERC Project Number: NETGP 494158–16). The authors would also like to acknowledge the McGill Engineering Doctoral Award (MEDA) granted to Tejas Ramakrishnan. We also thank Nicolas Brodusch in the Mining and Materials Engineering Department of McGill University for help in STEM operation and data collection.

4.9 References

- [1] R. Syre, “Niobium, Molybdenum, Tantalum, and Tungsten - A summary of their properties with recommendations for research and development,” *NATO Advisory Group for Aeronautical Research and Development*, vol. VII, no. AGARDograph 50, p. 152, 1961.
- [2] B. Tabernig and N. Reheis, “Joining of molybdenum and its application,” *International Journal of Refractory Metals and Hard Materials*, vol. 28, no. 6, pp. 728–733, 2010, doi: 10.1016/j.ijrmhm.2010.06.008.
- [3] C. L. Briant, “New Applications and Novel Processing of Refractory Metal Alloys,” *15th International Plansee Seminar*, vol. 1, pp. 389–403, 2001.
- [4] M. Letenneur, A. Kreitchberg, and V. Brailovski, “Optimization of Laser Powder Bed Fusion Processing Using a Combination of Melt Pool Modeling and Design of Experiment Approaches : Density Control,” 2019, doi: 10.3390/jmmp3010021.
- [5] C. August and M. Engineering, “Evaluation of Laser Powder Bed Fusion (LPBF) Fabricated A356 (Al7SiMg) Components through Finite Element Analysis,” vol. 356, no. August, 2018.
- [6] A. J. Dunbar and A. J. Dunbar, “Analysis of the Laser Powder Bed Fusion Additive Manufacturing Process Through Experimental Measurement and Finite Element Modeling,” *Thesis*, no. May, 2016.
- [7] G. Jacob, C. U. Brown, and A. Donmez, “The Influence of Spreading Metal Powders with Different Particle Size Distributions on the Powder Bed Density in Laser-Based Powder Bed Fusion Processes”.
- [8] M. Gouge and P. Michaleris, *An Introduction to Additive Manufacturing Processes and Their Modeling Challenges*, 1st ed. Elsevier Inc., 2018. doi: 10.1016/B978-0-12-811820-7.00002-1.
- [9] M. Caelers, “Study of in-situ monitoring methods to create a robust SLM process,” 2017.
- [10] J. Muñoz-Lerma, A. Nommeots-Nomm, K. Waters, and M. Brochu, “A Comprehensive Approach to Powder Feedstock Characterization for Powder Bed Fusion Additive Manufacturing: A Case Study on AlSi7Mg,” *Materials*, vol. 11, no. 12, p. 2386, 2018, doi: 10.3390/ma11122386.

- [11] S. C. Chou, M. Trask, J. Danovitch, X. L. Wang, J. P. Choi, and M. Brochu, "Pulsed laser powder bed fusion additive manufacturing of A356," *Materials Characterization*, vol. 143, no. January, pp. 27–33, 2018, doi: 10.1016/j.matchar.2018.02.004.
- [12] D. Heuben, "Additive manufacture of highly conductive copper by LPBF," *Fraunhofer Institute for Laser T*, 2018.
- [13] K. Darvish, Z. W. Chen, and T. Pasang, "Reducing lack of fusion during selective laser melting of CoCrMo alloy: Effect of laser power on geometrical features of tracks," *Materials and Design*, vol. 112, pp. 357–366, 2016, doi: 10.1016/j.matdes.2016.09.086.
- [14] B. Qian, K. Saeidi, L. Kvetková, F. Lofaj, C. Xiao, and Z. Shen, "Defects-tolerant Co-Cr-Mo dental alloys prepared by selective laser melting," *Dental Materials*, vol. 31, no. 12, pp. 1435–1444, 2015, doi: 10.1016/j.dental.2015.09.003.
- [15] R. Engeli, T. Etter, S. Hövel, and K. Wegener, "Processability of different IN738LC powder batches by selective laser melting," *Journal of Materials Processing Technology*, vol. 229, pp. 484–491, 2016, doi: 10.1016/j.jmatprotec.2015.09.046.
- [16] O. Sanchez-Mata, X. Wang, J. A. Muñoz-Lerma, M. A. Shandiz, R. Gauvin, and M. Brochu, "Fabrication of crack-free nickel-based superalloy considered non-weldable during laser powder bed fusion," *Materials*, vol. 11, no. 8, pp. 1–9, 2018, doi: 10.3390/ma11081288.
- [17] J.-P. Choi *et al.*, "Densification Behavior of 316L Stainless Steel Parts Fabricated by Selective Laser Melting by Variation in Laser Energy Density," *Materials Transactions*, vol. 57, no. 11, pp. 1952–1959, 2016, doi: 10.2320/matertrans.M2016284.
- [18] X. Wang *et al.*, "Characterization of single crystalline austenitic stainless steel thin struts processed by laser powder bed fusion," *Scr Mater*, vol. 163, pp. 51–56, 2019, doi: 10.1016/j.scriptamat.2018.12.032.
- [19] M. K. Keshavarz, F. Sikan, C. E. Boutet, J. Milligan, A. Bois-Brochu, and M. Brochu, "Impact properties of half stress-relieved and hot isostatic pressed Ti–6Al–4V components fabricated by laser powder bed fusion," *Materials Science and Engineering A*, vol. 760, no. May, pp. 481–488, 2019, doi: 10.1016/j.msea.2019.05.035.
- [20] M. Mazur, M. Leary, M. McMillan, S. Sun, D. Shidid, and M. Brandt, *Mechanical properties of Ti6Al4V and AlSi12Mg lattice structures manufactured by Selective Laser Melting (SLM)*. Elsevier Ltd, 2016. doi: 10.1016/B978-0-08-100433-3.00005-1.

- [21] A. Kumar and B. L. Eyre, “Grain Boundary Segregation and Intergranular Fracture in Molybdenum,” *Proceedings of the Royal Society A: Mathematical, Physical and Engineering Sciences*, vol. 370, no. 1743, pp. 431–458, 1980, doi: 10.1098/rspa.1980.0043.
- [22] K. Leitner *et al.*, “How grain boundary chemistry controls the fracture mode of molybdenum,” *Materials and Design*, vol. 142, pp. 36–43, 2018, doi: 10.1016/j.matdes.2018.01.012.
- [23] K. Leitner (née Babinsky) *et al.*, “On grain boundary segregation in molybdenum materials,” *Materials and Design*, vol. 135, pp. 204–212, 2017, doi: 10.1016/j.matdes.2017.09.019.
- [24] E. Pink and R. Eck, “Refractory Metals and Their Alloys,” in *Materials Science and Technology*, 2006. doi: 10.1002/9783527603978.mst0088.
- [25] E. Pink and R. W. Armstrong, “Total material variables influencing DBTT for Molybdenum,” *Technical Report to Office of Naval Research*, vol. NR031-739, no. I, 1970.
- [26] A. Kumar and B. L. Eyre, “Grain Boundary Segregation and Intergranular Fracture in Molybdenum,” *Proceedings of the Royal Society A: Mathematical, Physical and Engineering Sciences*, vol. 370, no. 1743, pp. 431–458, 1980, doi: 10.1098/rspa.1980.0043.
- [27] D. Scheiber, R. Pippan, P. Puschnig, and L. Romaner, “Ab initio search for cohesion-enhancing impurity elements at grain boundaries in molybdenum and tungsten,” *Modelling and Simulation in Materials Science and Engineering*, vol. 24, no. 8, p. 85009, 2016, doi: 10.1088/0965-0393/24/8/085009.
- [28] K. Leitner *et al.*, “How grain boundary chemistry controls the fracture mode of molybdenum,” *Materials and Design*, vol. 142, pp. 36–43, 2018, doi: 10.1016/j.matdes.2018.01.012.
- [29] K. Leitner (née Babinsky) *et al.*, “Grain boundary segregation engineering in as-sintered molybdenum for improved ductility,” *Scripta Materialia*, vol. 156, pp. 60–63, 2018, doi: 10.1016/j.scriptamat.2018.07.008.
- [30] K. Leitner (née Babinsky) *et al.*, “On grain boundary segregation in molybdenum materials,” *Materials and Design*, vol. 135, pp. 204–212, 2017, doi: 10.1016/j.matdes.2017.09.019.
- [31] W. E. Few and G. K. Manning, “Solubility of Carbon and Oxygen in Molybdenum,” *Jom*, vol. 4, no. 3, pp. 271–274, 2017, doi: 10.1007/bf03397689.

- [32] B. A. Gnesin, V. V Kireiko, and A. P. Zuev, "Oxygen concentration and defect structure in molybdenum and tungsten," *15th International Plansee Seminar*, vol. 3, no. 15, pp. 161–170, 2001, doi: 10.1016/s0026-0657(02)80434-9.
- [33] G. L. Krasko, "Effect of impurities on the electronic structure of grain boundaries and intergranular cohesion in tungsten," *Materials Research Society Symposium Proceedings*, vol. 291, pp. 109–114, 1993, doi: 10.1557/proc-291-109.
- [34] Daniel Scheiber, "Theoretical Study of Grain Boundaries in Tungsten and Molybdenum.," p. 160, 2016.
- [35] J. Braun *et al.*, "Molybdenum and tungsten manufactured by selective laser melting: Analysis of defect structure and solidification mechanisms," *Int J Refract Metals Hard Mater*, vol. 84, no. June, p. 104999, 2019, doi: 10.1016/j.ijrmhm.2019.104999.
- [36] D. Faidel, D. Jonas, G. Natour, and W. Behr, "Investigation of the selective laser melting process with molybdenum powder," *Additive Manufacturing*, vol. 8, pp. 88–94, 2015, doi: 10.1016/j.addma.2015.09.002.
- [37] K. H. Leitz *et al.*, "Fundamental analysis of the influence of powder characteristics in Selective Laser Melting of molybdenum based on a multi-physical simulation model," *International Journal of Refractory Metals and Hard Materials*, vol. 72, no. November 2017, pp. 1–8, 2018, doi: 10.1016/j.ijrmhm.2017.11.034.
- [38] D. Wang, C. Yu, J. Ma, W. Liu, and Z. Shen, "Densification and crack suppression in selective laser melting of pure molybdenum," *Materials and Design*, vol. 129, no. March, pp. 44–52, 2017, doi: 10.1016/j.matdes.2017.04.094.
- [39] M. Nagae, T. Yoshio, J. Takada, and Y. Hiraoka, "Improvement in Recrystallization Temperature and Mechanical Properties of a Commercial TZM Alloy through Microstructure Control by Multi-Step Internal Nitriding," *Materials Transactions*, vol. 46, no. 10, pp. 2129–2134, 2005, doi: 10.2320/matertrans.46.2129.
- [40] L. E. Olds and G. W. P. Rengstorff, "Effects of Oxygen, Nitrogen, and Carbon on The Ductility of Cast Molybdenum," *Jom*, vol. 8, no. 2, pp. 150–155, 1956, doi: 10.1007/bf03377662.
- [41] H. Kurishita, O. Tokunaga, and H. Yoshinaga, "Effect of Nitrogen on the Intergranular Brittleness in Molybdenum," *Materials Transactions, JIM*, vol. 31, no. 3. pp. 190–194, 1990. doi: 10.2320/matertrans1989.31.190.

- [42] G. T. Hahn, A. Gilbert, and R. I. Jaffee, “The effects of solutes on the ductile-to-brittle transition of refractory,” *DMIC Memorandum*, vol. 155, p. 63, 1962.
- [43] J. Schindelin, I. Arganda-Carreras, and E. Frise, “Fiji - an Open Source platform for biological image analysis,” *Nat Methods*, vol. 9, no. 7, pp. 676–682, 2012, doi: 10.1038/nmeth.2019.Fiji.
- [44] C. W. Bale *et al.*, “Reprint of: FactSage thermochemical software and databases, 2010–2016,” *Calphad: Computer Coupling of Phase Diagrams and Thermochemistry*, vol. 55, pp. 1–19, 2016, doi: 10.1016/j.calphad.2016.07.004.
- [45] K. Frisk, “A thermodynamic evaluation of the Cr-N, Fe-N, Mo-N and Cr-Mo-N systems,” *Calphad*, vol. 15, no. 1, pp. 79–106, 1991, doi: 10.1016/0364-5916(91)90028-I.
- [46] P. Giannozzi *et al.*, “QUANTUM ESPRESSO: A modular and open-source software project for quantum simulations of materials,” *Journal of Physics Condensed Matter*, vol. 21, no. 39, 2009, doi: 10.1088/0953-8984/21/39/395502.
- [47] P. Giannozzi *et al.*, “Advanced capabilities for materials modelling with Quantum ESPRESSO,” *Journal of Physics Condensed Matter*, vol. 29, no. 46, 2017, doi: 10.1088/1361-648X/aa8f79.
- [48] J. P. Perdew, K. Burke, and M. Ernzerhof, “Generalized gradient approximation made simple,” *Physical Review Letters*, vol. 77, no. 18, pp. 3865–3868, 1996, doi: 10.1103/PhysRevLett.77.3865.
- [49] G. Yablokova *et al.*, “Rheological behavior of β -Ti and NiTi powders produced by atomization for SLM production of open porous orthopedic implants,” *Powder Technology*, vol. 283, pp. 199–209, 2015, doi: 10.1016/j.powtec.2015.05.015.
- [50] L. Thijs, M. L. Montero Sistiaga, R. Wauthle, Q. Xie, J. P. Kruth, and J. Van Humbeeck, “Strong morphological and crystallographic texture and resulting yield strength anisotropy in selective laser melted tantalum,” *Acta Materialia*, vol. 61, no. 12, pp. 4657–4668, 2013, doi: 10.1016/j.actamat.2013.04.036.
- [51] D. E. Weaver, “The diffusivity and solubility of nitrogen in molybdenum and the trapping of nitrogen by carbon in molybdenum,” *University of California, Ph.D. Thesis*, p. 84, 1972.
- [52] K. Mundra and T. Debroy, “A general model for partitioning of gases between a metal and its plasma environment,” *Metallurgical and Materials Transactions B*, vol. 26, no. 1, pp. 149–157, 1995, doi: 10.1007/BF02648987.

- [53] P. Schaaf, "Laser nitriding of metals," *Progress in Materials Science*, vol. 47, pp. 1–161, 2002.
- [54] A. Bandopadhyay, A. Banerjee, and T. Debroy, "Nitrogen activity determination in plasmas," *Metallurgical Transactions B*, vol. 23, no. 2, pp. 207–214, 1992, doi: 10.1007/BF02651855.
- [55] P. Bidare, I. Bitharas, R. M. Ward, M. M. Attallah, and A. J. Moore, "Laser powder bed fusion at sub-atmospheric pressures," *International Journal of Machine Tools and Manufacture*, vol. 130–131, no. April, pp. 65–72, 2018, doi: 10.1016/j.ijmachtools.2018.03.007.
- [56] Q. Guo *et al.*, "Transient dynamics of powder spattering in laser powder bed fusion additive manufacturing process revealed by in-situ high-speed high-energy x-ray imaging," *Acta Materialia*, vol. 151, pp. 169–180, 2018, doi: 10.1016/j.actamat.2018.03.036.
- [57] W. Kurz, B. Giovanola, and R. Trivedi, "Theory of microstructural development during rapid solidification," *Acta Metallurgica*, vol. 34, no. 5, pp. 823–830, 1986, doi: 10.1016/0001-6160(86)90056-8.
- [58] W. Kurz and D. J. Fisher, "Fundamentals of Solidification, Fourth revised edition," 1998.
- [59] L. L. Zhang, L. J. Zhang, J. Ning, Y. J. Sun, W. I. Cho, and S. J. Na, "On the laser gas (N₂) alloying in the welding of molybdenum alloy," *Journal of Materials Processing Technology*, vol. 296, no. April, p. 117184, 2021, doi: 10.1016/j.jmatprotec.2021.117184.
- [60] C. H. Zenk, A. Bauer, P. Goik, S. Neumeier, H. J. Stone, and M. Göken, "Microstructure, Lattice Misfit, and High-Temperature Strength of γ' -Strengthened Co-Al-W-Ge Model Superalloys," *Metallurgical and Materials Transactions A: Physical Metallurgy and Materials Science*, vol. 47, no. 5, pp. 2141–2149, 2016, doi: 10.1007/s11661-016-3408-8.
- [61] M. Kolarikova, L. Kolarik, and P. Vondrous, "Welding of thin molybdenum sheets by EBW and GTAW," *23rd DAAAM International Symposium on Intelligent Manufacturing and Automation 2012*, vol. 2, no. 1, pp. 1005–1008, 2012.
- [62] R. A. Koshy, M. E. Graham, and L. D. Marks, "Synthesis and characterization of CrN/Mo₂N multilayers and phases of Molybdenum nitride," *Surface and Coatings Technology*, vol. 202, no. 4–7, pp. 1123–1128, 2007, doi: 10.1016/j.surfcoat.2007.07.090.
- [63] B. Bouaouina, A. Besnard, S. E. Abaidia, and F. Haid, "Residual stress, mechanical and microstructure properties of multilayer Mo₂N/CrN coating produced by R.F Magnetron

- discharge,” *Applied Surface Science*, vol. 395, pp. 117–121, 2017, doi: 10.1016/j.apsusc.2016.04.024.
- [64] L. L. Zhang, L. J. Zhang, J. Long, J. Ning, J. X. Zhang, and S. J. Na, “Effects of titanium on grain boundary strength in molybdenum laser weld bead and formation and strengthening mechanisms of brazing layer,” *Materials and Design*, vol. 169, p. 107681, 2019, doi: 10.1016/j.matdes.2019.107681.
- [65] M. W. Mallett, “The determination of interstitial elements in the refractory metals,” *Talanta*, vol. 9, no. 2, pp. 133–144, 1962, doi: 10.1016/0039-9140(62)80036-8.
- [66] W. E. Pickett, “Pseudopotential methods in condensed matter applications,” *Computer Physics Reports*, vol. 9, no. 3, pp. 115–197, 1989, doi: 10.1016/0167-7977(89)90002-6.
- [67] Y. W. You *et al.*, “Interaction of carbon, nitrogen and oxygen with vacancies and solutes in tungsten,” *RSC Advances*, vol. 5, no. 30, pp. 23261–23270, 2015, doi: 10.1039/c4ra13854f.
- [68] D. Nguyen-Manh, “Ab-Initio Modelling of Point Defect-Impurity Interaction in Tungsten and other BCC Transition Metals,” *Adv Mat Res*, vol. 59, pp. 253–256, 2008, doi: 10.4028/www.scientific.net/amr.59.253.
- [69] Y. Liu and Z. Dai, “Role of vacancy in trapping impurity of nitrogen in molybdenum,” *Xiyou Jinshu Cailiao Yu Gongcheng/Rare Metal Materials and Engineering*, vol. 45, no. 8, pp. 1973–1977, 2016.
- [70] T. Frolov, Q. Zhu, T. Ooppelstrup, J. Marian, and R. E. Rudd, “Structures and transitions in bcc tungsten grain boundaries and their role in the absorption of point defects,” *Acta Materialia*, vol. 159, pp. 123–134, 2018, doi: 10.1016/j.actamat.2018.07.051.
- [71] G. L. Krasko, “Effect of impurities on the electronic structure of grain boundaries and intergranular cohesion in tungsten,” *International Journal of Refractory Metals and Hard Materials*, vol. 12, no. 5, pp. 251–260, 1993, doi: 10.1016/0263-4368(93)90033-C.

Chapter 5 – Laser powder bed fusion of molybdenum under various Ar-N₂ mixture build atmospheres

Chapter 4 demonstrated that while samples processed under Ar showed cracking, crack-free samples could be fabricated under an N₂ atmosphere. Under the N₂ atmosphere, N was introduced into the Mo part beyond the equilibrium solid solubility of N in Mo. The presence of N raised the energy barrier for O diffusion, which trapped O within the lattice at interstitial positions. The formation of oxides within the grain and at grain boundaries was reduced, leading to a reduction in GB embrittlement. The results in Chapter 4 showed that nitrogen doping and even in-situ nitriding were feasible through LPBF. Chapter 4 also highlighted the influence of N content on the grain structure in LPBF-processed Mo. The results raised the question of the influence of N partial pressure on N content and grain structure in LPBF processed Mo. This chapter explores the use of nitrogen-argon gas mixtures as build atmospheres and their influences on the LPBF processing of Mo parts. Various combinations of Ar-N₂ were chosen for this purpose, and samples were fabricated. Microstructural characterization was performed, and mechanical properties were evaluated.

This chapter has been submitted to the International Journal of Refractory Metals and Hard Materials with manuscript reference number: IJRMHM-D-23-00861 as: *T. Ramakrishnan*, S. Kwon, and M. Brochu, “Laser powder bed fusion of molybdenum under various Ar-N₂ mixture build atmospheres”.

5.1 Abstract

Laser powder bed fusion (LPBF) is a promising technology for the processing of refractory metals like molybdenum (Mo). Unfortunately, LPBF-processed Mo exhibits cracking when processed under typical conditions, limiting the application of the process. The influence of N content in a gas mixture used as the build atmosphere on the cracking tendency of LPBF processed Mo was studied. The effect of N partial pressure on grain structure, cracking characteristics and mechanical properties was evaluated under varying Ar-N₂ gas mixtures. The microstructure analysis revealed that the increasing content of N in the build atmosphere caused a shift from columnar grain structure which is expected for pure metals fabricated under LPBF, to irregular grain structure. Also, a decrease in average crack length was observed with the increase in nitrogen content in the samples. A linked trend of decreasing oxide content was observed at grain boundaries from fracture surface investigation. The reduced embrittlement of GB from the suppression of GB oxide formation is believed to hinder GB cracking in LPBF processed Mo. While cracks were observed in some samples, crack-free samples could be fabricated under high N partial pressure conditions, resulting in N content equal to or higher than 580 ppm.

5.2 Introduction

Laser powder bed fusion additive manufacturing (LPBF-AM) is an emerging technology which employs a layer-by-layer laser-enabled fusion of powder particles into parts [1–4]. For each layer, powder particles are spread over a substrate, or the previously processed layer and, using a laser, are selectively melted following a defined pattern of the part to be fabricated. LPBF-AM enables the possibility of fabricating complex parts with intricate features, unlike other processes. LPBF-AM protocols have been studied for various metals and their alloys, including aluminum [5, 6], iron [7, 8], nickel [9, 10], and titanium [11, 12].

Molybdenum (Mo) refractory metal is characterized by a high melting point, good mechanical strength, a low coefficient of thermal expansion, high electrical and thermal conductivities, and high corrosion resistance against many molten metals [13, 14]. This unique combination of properties elevates Mo as a potential candidate for a wide range of applications in aerospace, electronics, and nuclear applications [15]. Widespread application of Mo refractory metal has been

limited, in part, from the limitations of conventional manufacturing processes. Cracking and porosity are major issues found in fusion welding [16–18], as well as laser powder bed fusion additive manufacturing (LPBF-AM) [19–21]. The main cause of cracking in LPBF-AM processed Mo is the lack of ductility close to room temperature due to the ductile-to-brittle transition (DBT) phenomena shown by Mo, like most bcc refractory metals [22]. This is worsened by the reduction of grain boundary (GB) cohesion from the increasing presence of impurities like oxygen (O) [23], [24]. Researchers have shown that among various elements, O has the highest embrittling effect on Mo GB [25, 26], and that the GB oxides are the major factor explaining GB cracking [26–30]. In the LPBF-AM process, O is inevitably introduced from its residual content in the powder feedstock and from the build atmosphere [20]. Braun et al. [20] studied LPBF AM processing of Mo under various conditions, including those with process O as high as 800 ppmv (part per million by volume) and reported that O content in Mo from the powder surface and picked up during the processing, diffuses to the grain boundaries and form GB oxides causing embrittlement.

In an earlier study by the same authors, crack suppression in LPBF-AM processed Mo was shown using a pure N₂ build atmosphere. The results showed that during the LPBF process, N is introduced into the melt pool from the build atmosphere, and its presence in interstitial sites introduces a barrier for O diffusion, which prevents diffusion to the GBs. This was modelled using Density Functional Theory simulations. Cracking was suppressed by limiting the amount of GB oxides (as evidenced by a reduced amount of GB oxides on the fracture surfaces).

In this study, we investigated the use of a gas-mixture (Ar-N₂) build atmosphere to study the influence of the N partial pressure on N pick-up at the melt interface during LPBF-AM of Mo and delineate critical N content to avoid cracking. Optical and electron microscopy were used to analyze the resulting microstructure of the fabricated samples. The influence of N content on the grain size and morphology and on the cracking tendency was investigated. Fracture surface investigations were used to review the GB conditions, especially of GB oxide content. Microhardness analysis was performed to evaluate the influence of N pick-up on the mechanical properties, and LECO analysis was performed to quantify the content of interstitial elements from pick-up by the various gas mixtures used. The study identifies a threshold value of N content required to limit GB oxide that is related to crack suppression in LPBF AM.

5.3 Experimental methods

The gas-atomized Mo powders (chemical composition in Table 5.1) used in this study were procured from Tekna (Canada). The powder morphology was analyzed by Scanning Electron Microscopy (SEM) using a SU3500 (Hitachi, Japan) SEM. The particle size distribution (PSD) was evaluated via laser diffraction using an LA-920 laser particle size analyzer (Horiba, Japan). Powder flowability was tested using the Hall funnel test as per ASTM B213 standard. The cohesiveness index of the powder at different rotational speeds was evaluated through the rotating drum technique using GranuDrum® apparatus (Granutools, Belgium). These tests were performed at least thrice to provide statistical significance for the reported values.

Table 5.1 Chemical composition of Mo powders used as per the certificate of conformity

Element	Mo	Cr	Fe	Ni	C	O	N	H	Others
Wt.%	99.98	< 0.01	< 0.01	< 0.01	< 0.005	0.016	< 0.01	< 0.002	< 0.01

LPBF constructs were prepared using a Renishaw AM400 LPBF machine equipped with a reduced build volume (Renishaw, UK). Samples of various sizes (as shown in Figure 5.1) were fabricated using identical laser parameters under different atmospheres, as indicated in Table 5.2. The Table also indicates identification notes (ID) for the different samples to be used therein. The scan strategy comprised of a simple hatching pattern with 67° rotation between each layer. Oxygen content was limited to below 200 ppm in the build atmosphere for each build. Pure Mo (99.95% metal basis) plates of 2.5 mm thickness from Alfa Aesar (United States of America) were used as substrates for LPBF fabrication.

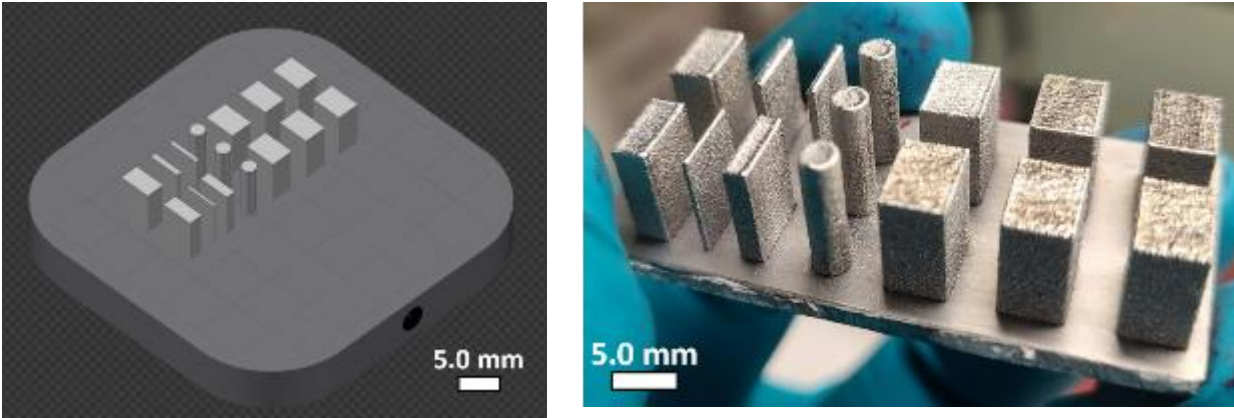


Figure 5.1 (a) Design layout of the build plate, (b) Representative image of a build plate.

Table 5.2 Build atmospheres used for the LPBF process, with sample IDs

Sample ID		MoAr	Mo10N	Mo60N	Mo90N	Mo95N	MoN
Build Atmosphere (mol %)	N ₂ (%)	0	10	60	90	95	100
	Ar (%)	100	90	40	10	5	0

The samples for characterization were sectioned using an IsoMet™ Low Speed Precision Cutter (Buehler, USA). Metallographic preparation involved grinding of the samples up to 800-grit SiC paper, then polishing with diamond suspensions of 9 μm, 3 μm, and 1 μm, followed by 0.05 μm colloidal silica suspension on a Labopol (Struers, USA) equipment.

Optical micrographs were captured using a light optical microscope (Nikon, Japan) equipped with a Clemex Vision System (Clemex, Canada) to characterize the build microstructure, density, and crack defect structure. The average crack length was calculated as the ratio of the cumulative crack length in a region of interest to the number of cracks using the Fiji distribution of ImageJ software [31].

Grain morphology and crystallographic texture were studied using a SU3500 SEM equipped with an electron back-scattered diffraction (EBSD) detector (Oxford Instruments, UK). EBSD data was analyzed using HKL Channel 5 software (Oxford Instruments, UK). Fracture surface analysis was performed using the SU3500 SEM on samples exposed to drop impact fracture. X-ray diffraction (XRD) studies were conducted on the sample using a D8 Discover diffractometer (Bruker,

Germany) with a Cobalt (Co) anode ($K\alpha_1$ with wavelength, $\lambda = 1.7890 \text{ \AA}$). Data was collected between 2θ values of 40° and 120° with a step size of 0.05° . Full profile fitting analysis on the XRD data was performed using FullProf Suite [32].

Vickers microhardness tests were performed using a Clark CM-100AT (Sun-tec, USA) unit with 0.2 kgf load for a dwell time of 30 s. The measurements are reported as averages of 5 measurements. LECO TC600 Nitrogen-Oxygen Determinator (LECO, USA) was used to measure the N and O content of the LPBF samples.

5.4 Results and Discussion

5.4.1 Powder Characterization

Figure 5.2a and Figure 5.2b show the SEM micrographs of the Mo powder used in this study. The powders are smooth and spherical in nature, without any satellites or agglomeration. The powders showed a narrow PSD with D_{10} , D_{50} and D_{90} values of $20 \pm 2 \text{ \mu m}$, $29 \pm 2 \text{ \mu m}$, and $43 \pm 3 \text{ \mu m}$, respectively. The measured cohesiveness index values for different rotating speeds varied between 5 to 12 and are well below the critical value of 24, suggesting that regular recoating speeds can be used [33]. The powders exhibited flow times of $13.3 \pm 0.1 \text{ s}$ (per 50 g) under Hall flow tests indicating high flowability. The apparent density was measured to be $57 \pm 1 \%$.

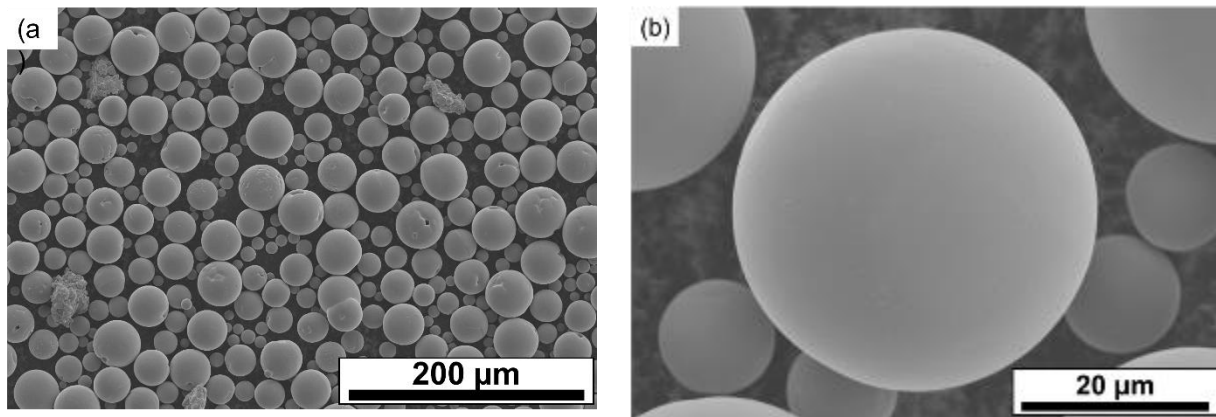


Figure 5.2 (a, b) SEM micrographs showing morphology of the Mo powders.

5.4.2 Sample Characterization

5.4.2.1 Microstructure and cracking

Optical micrographs of the MoAr, Mo10N, Mo60N, Mo90N, Mo95N, and MoN samples are shown in Figure 5.3a-f. The optical micrographs were acquired from cross-sections along the build direction (BD), and the BD is referenced in the Figures. With the increasing content of N₂ gas in the build atmosphere, a significant change in the cracking characteristics of the samples was observed. Samples MoAr, Mo10N, Mo60N and Mo90N exhibited cracking, with the extent of cracking decreasing with an increase in the N content in the build atmosphere. Almost all cracks were observed to be aligned along the build direction. The Mo95N and MoN samples did not exhibit any observable cracking. All the samples exhibited porosity, with MoN sample showing the least porosity.

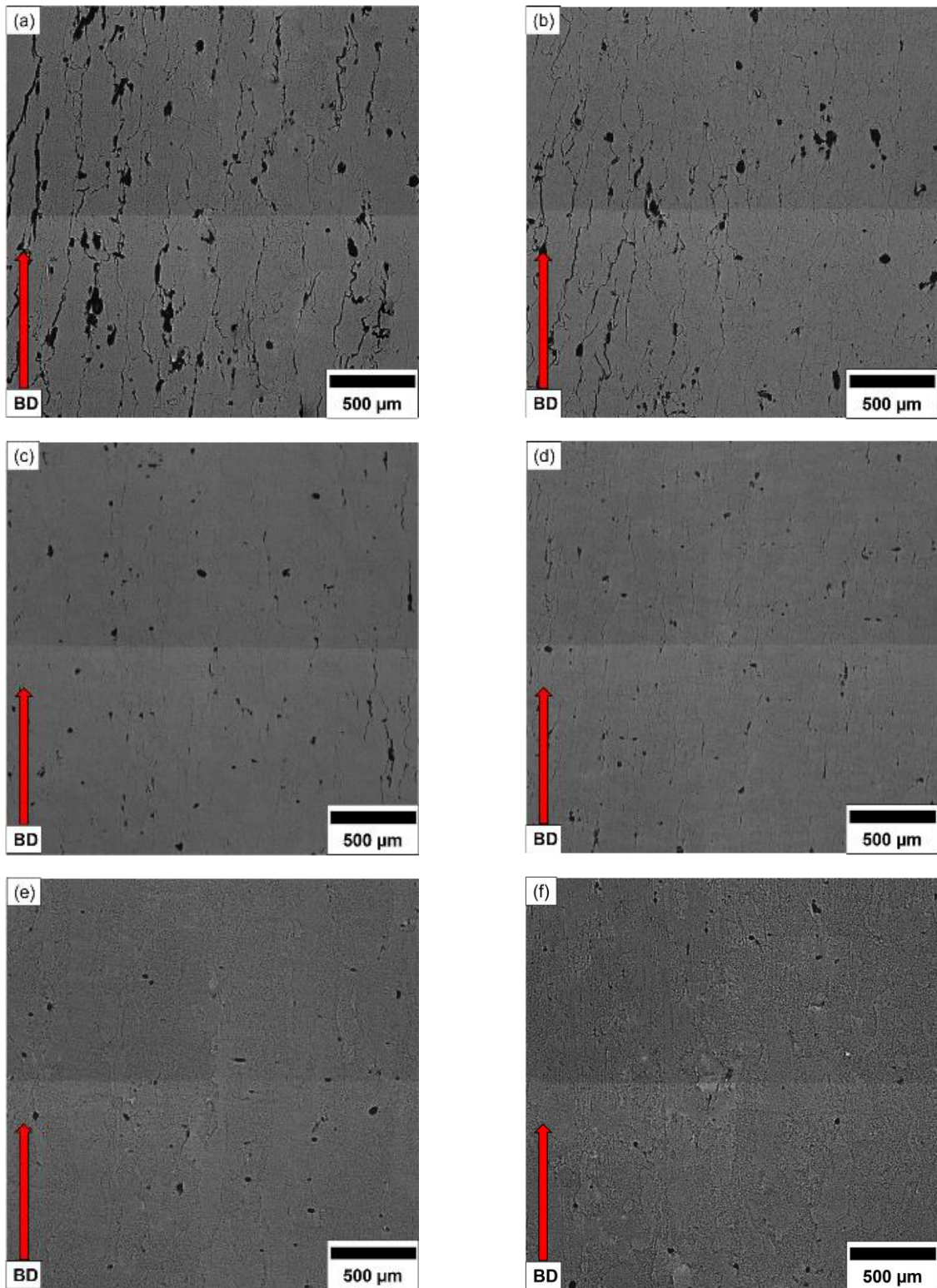


Figure 5.3 (a-f) Optical micrographs of samples MoAr, Mo10N, Mo60N, Mo90N, Mo95N, and MoN, respectively.

Figure 5.4 plots the average crack length (in μm) and porosity (in %) vs N_2 gas content in the build atmosphere for the different samples processed. Average crack length decreased from values around $640 \pm 40 \mu\text{m}$ for samples built under an atmosphere with less than 10% N_2 content to no cracking in samples built under an atmosphere containing 95% or more N_2 content. Unlike the effect on average crack length, there was no observable correlation between the N_2 content in the build atmosphere and the overall porosity in the samples. While all samples exhibited porosity to some extent, MoN samples showed the least porosity at $0.9 \pm 0.1 \%$.

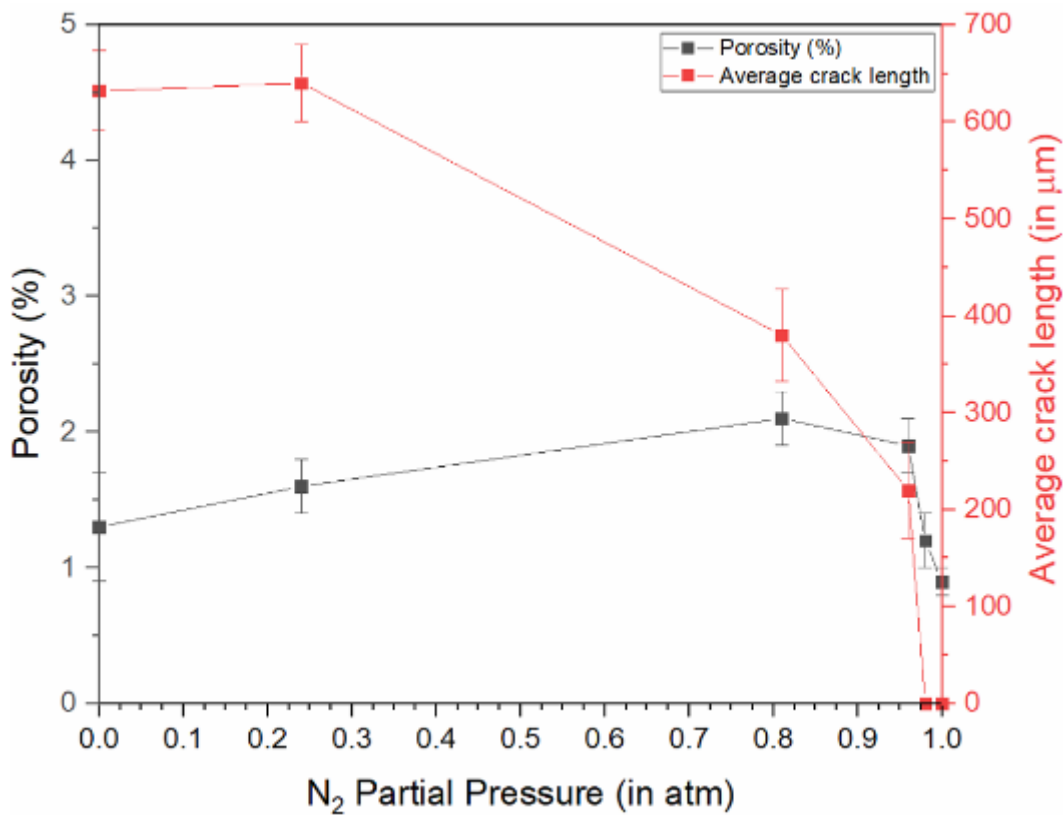


Figure 5.4 Average crack length, and porosity, vs N_2 gas content in the build atmosphere, respectively.

5.4.2.2 Grain structure and texture

In order to identify the influence of the N_2 gas on the grain structure and understand its impact on the cracking characteristics, IPF maps were generated from EBSD scans. Figure 5.5a-f depicts the IPF maps for all samples. The MoAr sample showed large columnar grains with GB aligned along the build direction. Despite the 67° rotation scanning strategy employed in the laser processing between each layer, the pure nature of the material and the partial remelting of the previous layer

during LPBF provides the base for this epitaxial growth. This is typical of LPBF-processed Mo samples, as reported by various researchers in the literature [34, 35]. With the increased content of N₂ gas in the build atmosphere, a gradual change in the grain structure can be observed. The aspect ratio of the columnar grain structure changes from 5.6~9.7 for the MoAr sample to 0.7~2.1 for those of the MoN sample. The columnar grains, which dominated the MoAr microstructure, are replaced by an increasing fraction of irregular grains with GBs no longer aligned to build direction. A greater degree of colour change in the IPF maps is observed within the grains, which does not correspond to high-angle grain boundaries, suggesting that sub-grain structures are also present in the microstructure [36].

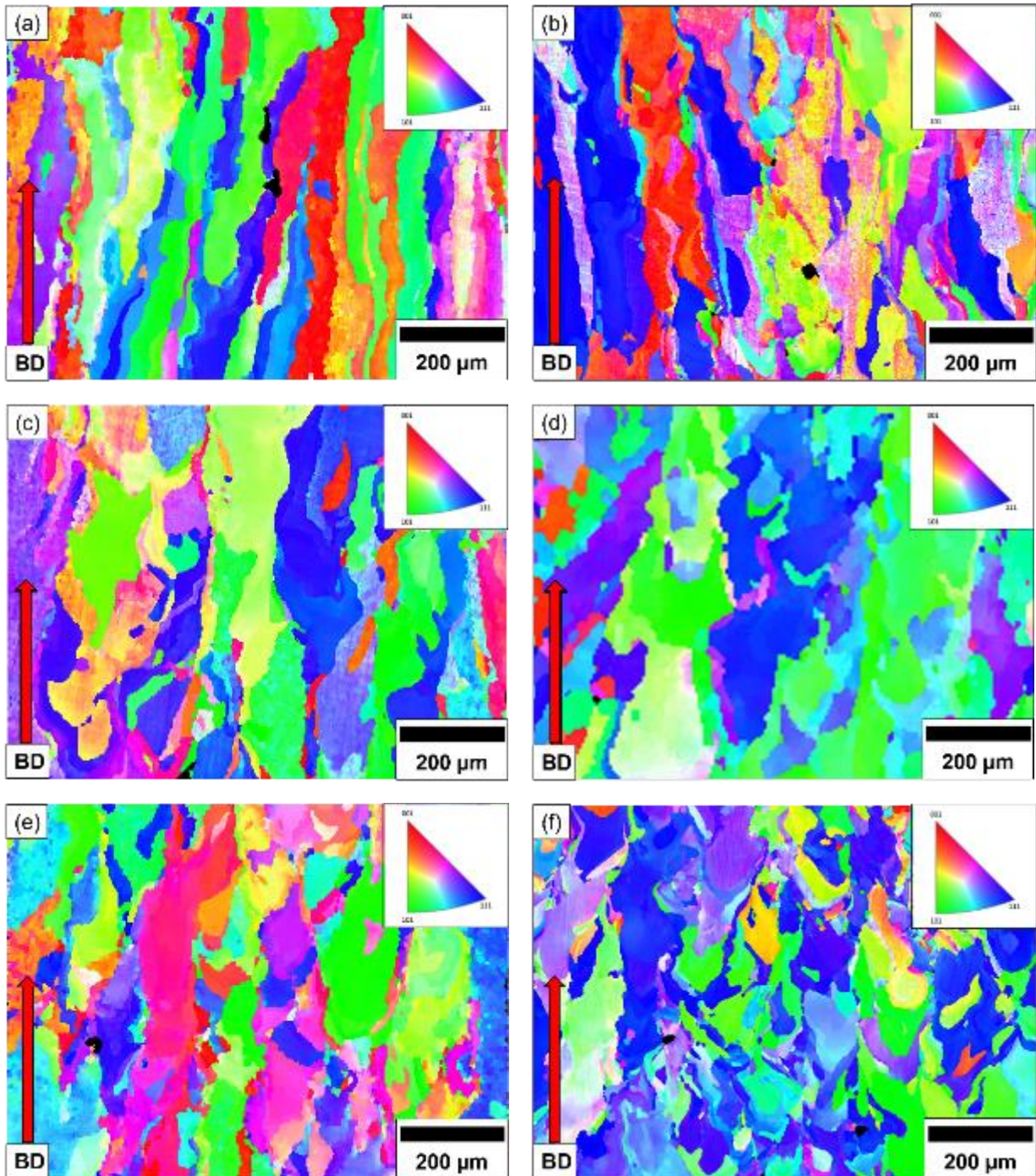


Figure 5.5 IPF maps from EBSD analysis of (a) MoAr, (b) Mo10N, (c) Mo60N, (d) Mo90N, (e) Mo95N, and (f) Mo-N sample.

Literature reports that cracking in LPBF-processed Mo is mostly intergranular and predominantly occurs along high-angle grain boundaries (HAGBs) aligned with the build direction [21, 36, 37].

As the irregular grain structure introduces deflections along the GBs for the cracks, this partially explains the reduction in average cracking length observed here, but these deflections do not affect crack initiation [38]. Also, interestingly most of the cracked samples showed GB misorientation angle values between 29° and 32° exclusively, while crack-free samples had a significant number of GBs with misorientation angles close to 48° . Figure 5.6a shows representative GB misorientation maps from the crack-free Mo-N sample. The misorientation profiles across the GBs for 3 locations are shown in Figure 5.6b through Figure 5.6d, showing the presence of GBs with high misorientation angles. Researchers have shown that the local grain misorientation is typically indicative of the state of local strain or deformation in the material and that residual stress or externally introduced stress, as in cases of plastic deformation, can cause an increase in this misorientation [39]. Figure 5.6e plots the local grain misorientation for cracked (MoAr) and crack-free (MoN) samples. In the case of crack-free samples, the misorientation was higher, indicating that the samples were able to accommodate a greater amount of deformation within the material when processed under a build atmosphere containing N_2 . In order to understand the primary mechanism contributing to crack reduction and elimination in these samples, a fracture surface investigation was performed.

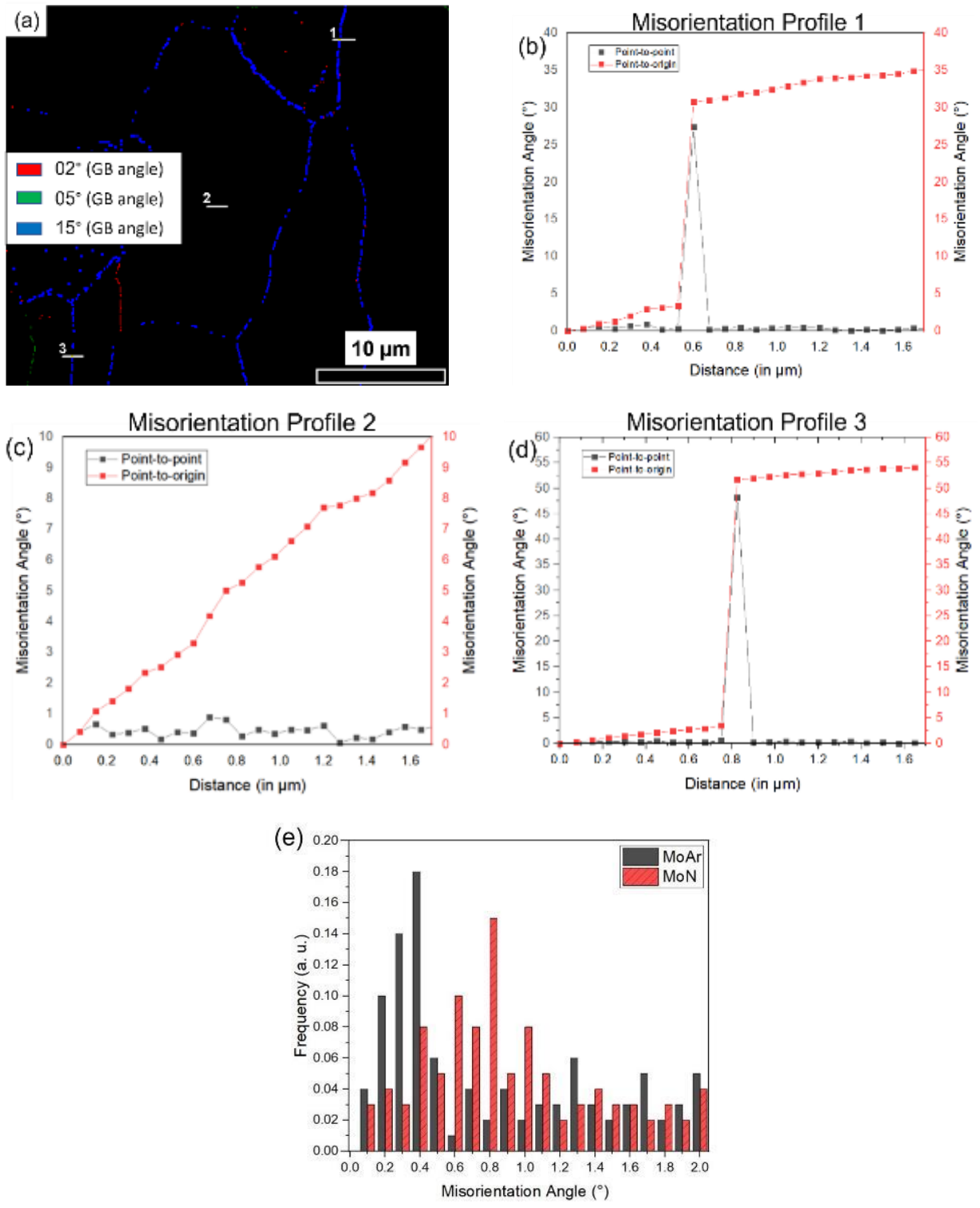


Figure 5.6 (a) Representative grain boundaries with high misorientation angles in MoN, (b-d) misorientation angle plots for 3 locations in Figure 5.6a, and (e) within grain misorientation for MoAr and MoN.

5.4.2.3 Fracture surface characterization

Representative SEM micrographs of the fracture surfaces of the samples are depicted in Figure 5.7a-f. The smooth surfaces indicate that these fractures have remained predominantly intergranular and show the presence of oxide particles to various extent in different forms [40]. A clear trend of reduced GB oxides with increasing N content in the build atmosphere is observed. Additionally, samples prone to cracking indicated a higher amount of oxides than the crack-free samples. L. L. Zhang et al. [17] studied laser welding of Mo under different gas mixtures and reported similar observations of oxide particles on fracture surfaces. In samples MoAr and Mo10N produced under no or low N₂ content in the gas mixture, thick oxide films can be observed in multiple locations, as shown in Figure 5.7a and Figure 5.7b. Mallett [41] observed that the shape of the oxide precipitates at the grain boundaries could change from discrete particles to continuous film with increasing O content. The LPBF processing literature reports that the presence of O in the build atmosphere inevitably results in GB oxides and that the resulting embrittlement is the major factor contributing to cracking in LPBF-processed Mo. Braun et al. [36] studied LPBF processing of Mo with different O content in the process and proposed that as O solubility is low in Mo, O enriches the primary liquid during the precipitation of the primary α -Mo phase. The solidification of this O-rich primary liquid could form oxide films if O is present in sufficient quantities. When a lower amount of O, and thereby, oxides are present, the liquid constricts into small droplets according to Plateau Rayleigh stability [42].

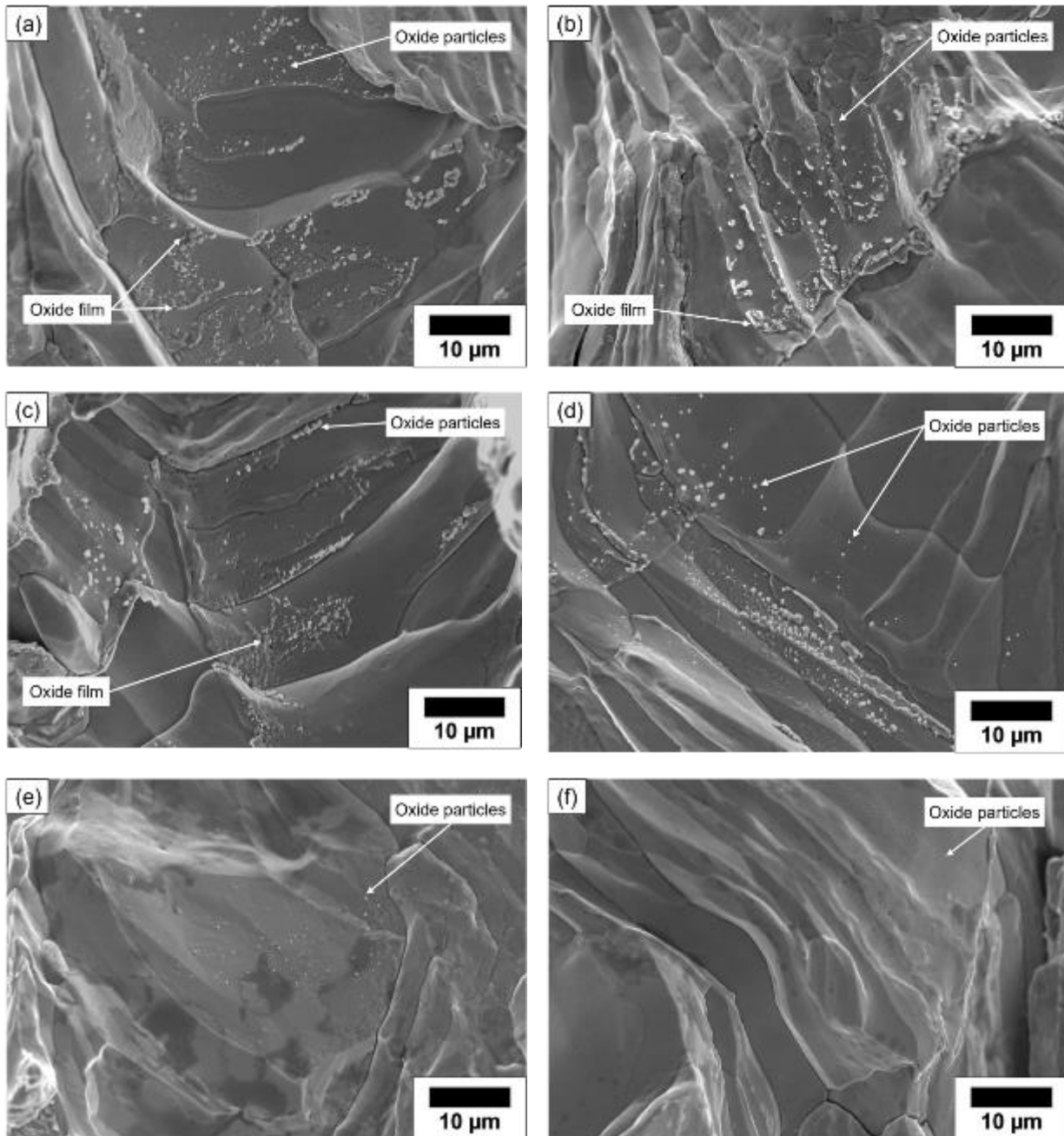


Figure 5.7 Fracture surface micrographs showing oxide particles in (a) MoAr, (b) Mo10N, (c) Mo60N, (d) Mo90N, (e) Mo95N, and (f) MoN.

5.4.2.4 Nitrogen and Oxygen

Table 5.3 provides the results of the N and O content analysis performed on the powder feedstock and the LPBF processed Mo samples. The Mo powder showed an O content of 320 ppm, and a N content of less than 5 ppm. As shown, most of the samples showed statistically similar O content. This observation is interesting, considering the earlier observations of reducing the amount of

oxide particles on the fracture surface observed with increasing N content in the build atmosphere. The N content in MoAr sample was 16 ± 3 ppm and increased to 590 ± 110 ppm for the MoN sample, following a trend similar to that reported in the literature by researchers for N content in bcc-iron (Fe) vs partial pressure of N in welding gas [43].

Table 5.3. N and O content in the samples (values in ppm)

Sample	O content (ppm)	N content (ppm)
Mo powder	320 ± 52	<5
MoAr	400 ± 65	16 ± 3
Mo10N	290 ± 59	140 ± 12
Mo60N	350 ± 5	430 ± 17
Mo90N	220 ± 5	520 ± 17
Mo95N	260 ± 11	580 ± 29
MoN	330 ± 54	590 ± 110

Literature suggests very low solubility for either O or N in Mo [44–48]. D. E. Weaver measured the N solubility in Mo under different N_2 partial pressure and reported that the results follow Sievert’s Law [48]. The data is plotted in Figure 5.8, along with the results from our study. LPBF samples produced under increasing N_2 partial pressure follow a similar trend at lower partial pressures, but the value is beyond Sievert’s law at higher partial pressures. Researchers in the field of welding have reported that under the plasma arc, the dissociation of diatomic gas molecules occurs, and an increased gas fugacity can lead to increased dissolution of N in the weld metal [43, 49]. Other studies on nitriding under a laser beam have indicated a similarly increased solubility through plasma-enhanced N activity, including in the case of refractory metals. Bandopadhyay et al. [49] reported that the plasma-enhanced activity of N was 10.15 ± 0.65 times that of diatomic N_2 gas over niobium and tantalum samples, and the corresponding solubility was three times the equilibrium solubility in these materials. L. L. Zhang et al. [17] also reported increased solubility of N in Mo during laser welding under gas atmospheres containing N. Furthermore, researchers have reported that metal vapours and plasma above the melt pool are prevalent due to the high laser energy conditions during the LPBF processing of metals [51].

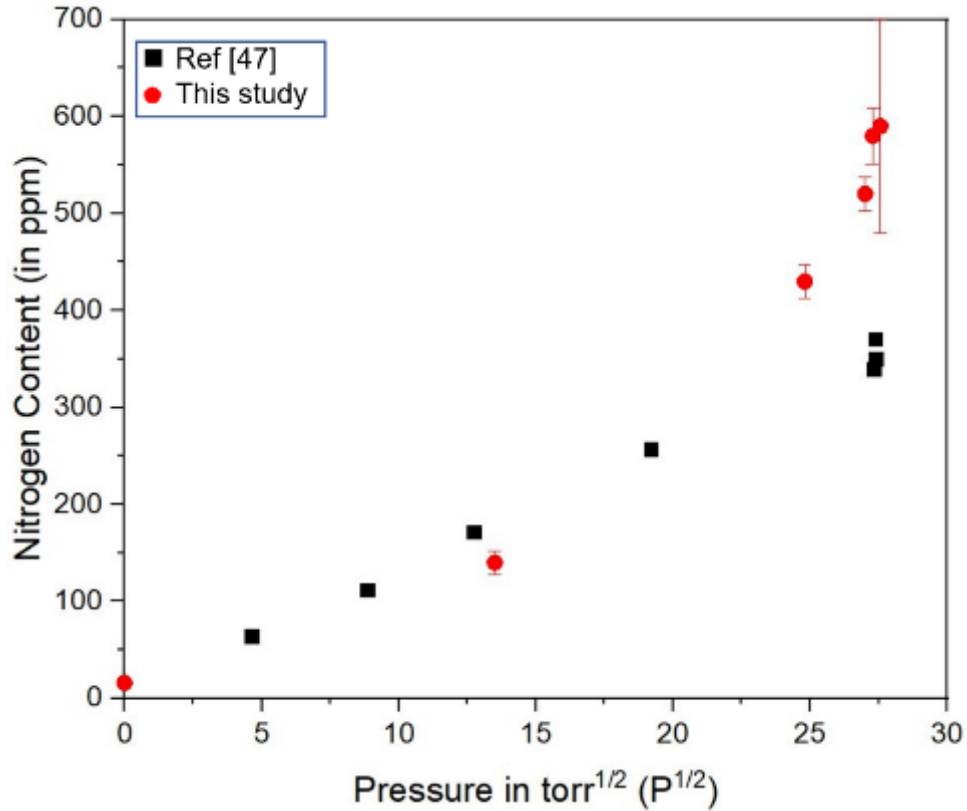


Figure 5.8 N content in Mo vs N₂ partial pressure.

Under the influence of laser and N in the build atmosphere, it is hypothesized that an increased dissolution and retention of N in the Mo is occurring. It is proposed that the presence of N creates a stronger barrier for diffusion for O in the Mo lattice. This has been indicated from DFT simulations performed in our earlier study [as in Chapter 4]. A greater diffusion barrier traps O in the Mo lattice and reduces the amount of GB oxides, improving GB cohesion in Mo. This reduction of GB embrittlement is proposed as the major factor in eliminating cracking in the crack-free samples produced in this study. All the samples produced under some level of N₂ gas in build atmosphere showed N content above 140 ppm, but only samples with N above 580 ppm were crack-free, indicating that there is a critical N content to ensure crack elimination at these O concentrations. The study by Kurishita et al. [52] indicated that ductility improved (as evidenced by a 500% increase in fracture stress) for Mo samples with 55 ppm N content when compared to samples with lower N content (20 ppm). While their results indicated that a further increase in N content to 88 ppm caused a loss of some of this ductility, the fracture stress was still higher compared to samples with low or no N content. Their study did not consider samples with N above

88 ppm and had very low O content at less than 10 ppm for all samples. With the understanding of O embrittlement of GBs [27, 28, 53], we propose that for O levels observed in LPBF processed samples, the threshold value of 550 ppm N content is required to ensure that samples fabricated are crack-free.

5.4.2.5 XRD analysis

Figure 5.9 shows the results of the X-ray diffraction analysis performed on the samples. Table 5.4 summarizes the results of the full profile fitting analysis performed on the XRD data. With increasing the partial pressure of N₂ gas in the build atmosphere, an increase in lattice parameter is observed in the samples. Such an observation is possibly linked to the increased N content in the lattice. The deviation from the theoretical lattice constant accompanied by the rapid solidification conditions may also contribute a hindrance to the epitaxial growth of columnar grains which was observed in section 5.4.2.2 above. Researchers have described deviations from epitaxial growth in materials due to deviations from lattice parameter from studies on semiconductor materials [54, 55] and in materials with strained structures [56, 57]. Matsunaka et al. [58] studied the epitaxial growth of silver (Ag) on a strained Ag (111) surface and proposed that a reduction in surface diffusion due to the strain causes an increase in island density. This may hinder the epitaxial growth and result in the grain structure observed in section 5.4.2.2 [58].

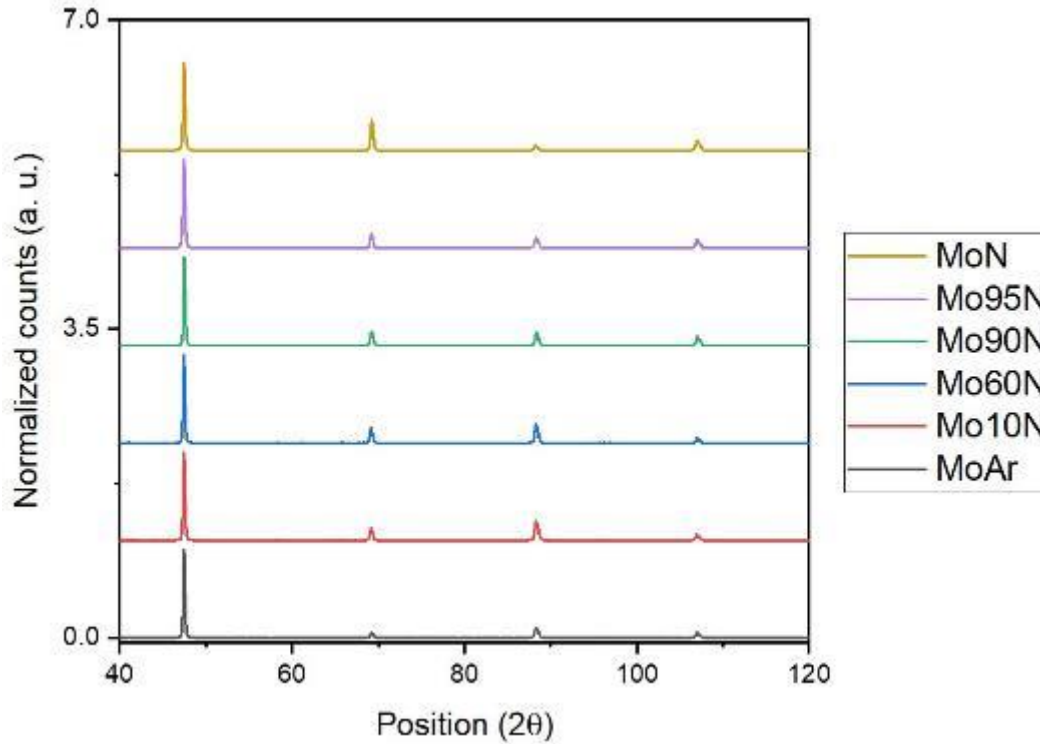


Figure 5.9 XRD analysis plots for the samples

Table 5.4. Lattice parameters for different samples estimated from XRD analysis

Sample	Lattice parameter (Å)	Difference (%)
Mo (theoretical)	3.14700	-
MoAr	3.14670	-0.01
Mo10N	3.14738	0.01
Mo60N	3.14768	0.02
Mo90N	3.14782	0.03
Mo95N	3.15201	0.16
MoN	3.15240	0.17

5.4.2.6 Microhardness measurements

Microhardness, measurements of the samples were performed to evaluate the influence of N content in the fabricated samples. Figure 5.10 plots the N content and hardness for the different samples against N₂ gas content in the build atmosphere. The MoAr sample showed a hardness of

205 ± 12 HV, which is slightly higher but comparable to hardness values reported by Kolarikova et al [59]. from the fusion zone for electron-beam welded Mo. The hardness increased following a linear trend from Mo10N through samples Mo60N and Mo90N, with Mo90N sample showing a hardness of 262 ± 11 HV. The increase in hardness for Mo10N, Mo60N and Mo90N is attributed to the increased interstitial N content in the Mo lattice for these samples. Mo95N and MoN samples showed that within the standard deviation, statistically similar hardness values of 254 ± 9 HV and 249 ± 11 HV were obtained. In the case of Mo95N and MoN, we also observe grains with precipitates identified as nitrides, as described in greater detail in an earlier study (in Chapter 4). L. L. Zhang et al. [17], reported similar nitrides under laser gas welding of Mo and proposed that the semi-coherent interface exists between the nitrides and Mo grains.

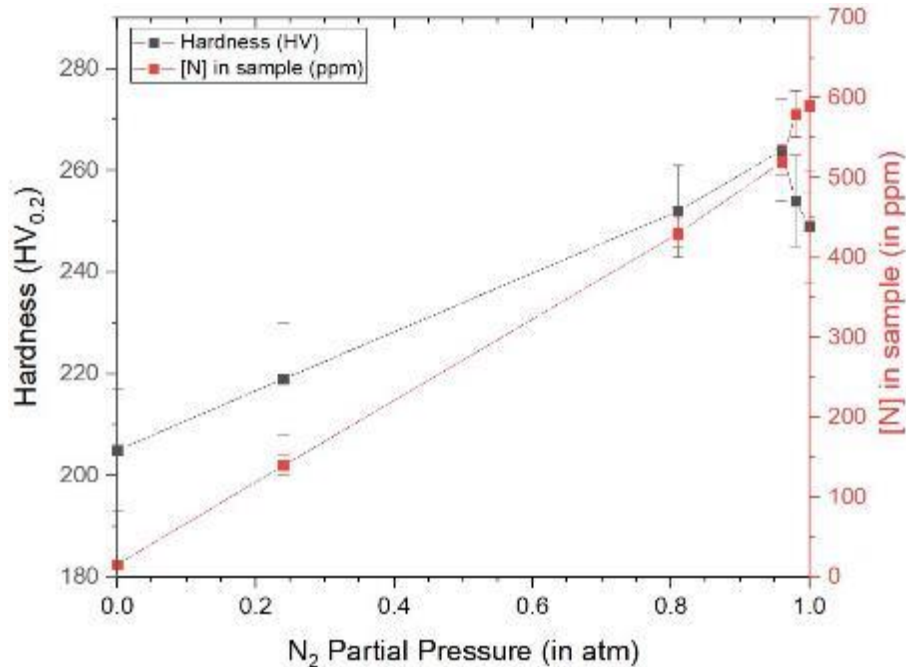


Figure 5.10 Microhardness and N content in samples vs N₂ partial pressure in the build atmosphere

5.5 Conclusion

Pure molybdenum was processed by LPBF-AM under different Ar-N₂ gas-mixture atmospheres. While most of the samples processed exhibited cracking, crack-free samples were fabricated under 5% Ar-95% N₂ and 100% N₂ atmosphere. Under the influence of laser in the N₂ atmosphere, N was introduced into the Mo part in varying quantities. Cracking was not observed in samples with N content above 580 ppm, suggesting a threshold value which is required to ensure the characteristic

microstructure and GB oxide levels to prevent cracking. The introduction of N into the lattice increases the barrier for O diffusion, which traps O within the lattice at interstitial positions, resulting in reduced oxide formation at grain boundaries, leading to a reduction in GB embrittlement. Our work suggests that N content beyond Sievert's value is attainable in LPBF-processed Mo.

5.6 Acknowledgement

The authors would like to thank the generous research support provided by the Natural Sciences and Engineering Research Council (NSERC) of Canada (NSERC Project Number: NETGP 494158–16). The authors would also like to acknowledge the McGill Engineering Doctoral Award (MEDA) granted to Tejas Ramakrishnan.

5.7 References

- [1] H. Yeung, B. Lane, F. Kim, J. Heigel, J. Fox, and J. Neira, "Continuous Laser Scan Strategy for Faster Build Speeds in Laser Powder Bed Fusion System," *Solid Freeform Fabrication Symposium*, pp. 1423–1431, 2017.
- [2] F. Caltanissetta, M. Grasso, S. Petró, and B. M. Colosimo, "Characterization of in-situ measurements based on layerwise imaging in laser powder bed fusion," *Additive Manufacturing*, vol. 24, no. August, pp. 183–199, 2018, doi: 10.1016/j.addma.2018.09.017.
- [3] A. G. Fallis, "Laser powder-bed fusion AM," *Journal of Chemical Information and Modeling*, vol. 53, no. 9, pp. 1689–1699, 2013, doi: 10.1017/CBO9781107415324.004.
- [4] W. E. King *et al.*, "Laser powder-bed fusion additive manufacturing of metals; physics, computational, and materials challenges," *Additive Manufacturing Handbook: Product Development for the Defense Industry*, vol. 041304, no. 2015, pp. 461–506, 2017, doi: 10.1201/9781315119106.
- [5] S. C. Chou, M. Trask, J. Danovitch, X. L. Wang, J. P. Choi, and M. Brochu, "Pulsed laser powder bed fusion additive manufacturing of A356," *Mater Charact*, vol. 143, no. January, pp. 27–33, 2018, doi: 10.1016/j.matchar.2018.02.004.

- [6] A. Aversa *et al.*, “Single scan track analyses on aluminium based powders,” *Journal of Materials Processing Technology*, vol. 255, no. December 2017, pp. 17–25, 2018, doi: 10.1016/j.jmatprotec.2017.11.055.
- [7] X. Wang, J. A. Muñoz-Lerma, O. Sánchez-Mata, M. Attarian Shandiz, and M. Brochu, “Microstructure and mechanical properties of stainless steel 316L vertical struts manufactured by laser powder bed fusion process,” *Materials Science and Engineering A*, vol. 736, no. July, pp. 27–40, 2018, doi: 10.1016/j.msea.2018.08.069.
- [8] F. Caltanissetta, M. Grasso, S. Petró, and B. M. Colosimo, “Characterization of in-situ measurements based on layerwise imaging in laser powder bed fusion,” *Additive Manufacturing*, vol. 24, no. August, pp. 183–199, 2018, doi: 10.1016/j.addma.2018.09.017.
- [9] S. J. Davies, S. P. Jeffs, M. P. Coleman, and R. J. Lancaster, “Effects of heat treatment on microstructure and creep properties of a laser powder bed fused nickel superalloy,” *Materials and Design*, vol. 159, pp. 39–46, 2018, doi: 10.1016/j.matdes.2018.08.039.
- [10] O. Sanchez-Mata, X. Wang, J. A. Muñoz-Lerma, M. A. Shandiz, R. Gauvin, and M. Brochu, “Fabrication of crack-free nickel-based superalloy considered non-weldable during laser powder bed fusion,” *Materials*, vol. 11, no. 8, pp. 1–9, 2018, doi: 10.3390/ma11081288.
- [11] C. Xu *et al.*, “Microstructure and mechanical behavior of as-built and heat-treated Ti–6Al–7Nb produced by laser powder bed fusion,” *Materials Science and Engineering A*, vol. 793, no. January, 2020, doi: 10.1016/j.msea.2020.139978.
- [12] L. Caprio, G. Chiari, A. G. Demir, and B. Previtali, “Development of novel high temperature laser powder bed fusion system for the processing of crack-susceptible alloys,” *Solid Freeform Fabrication 2018: Proceedings of the 29th Annual International Solid Freeform Fabrication Symposium – An Additive Manufacturing Conference*, pp. 2275–2285, 2018.
- [13] R. W. Burman, “Molybdenum—a super superalloy,” *Jom*, vol. 29, no. 12, pp. 12–17, 2014, doi: 10.1007/bf03354338.
- [14] H. Walser, W. Knabl, and S. McCrossan, “Traditional and new applications of Molybdenum metal and alloys,” *Proceedings of the 8th International Conference on Tungsten, Refractory and Hardmaterials*, vol. 108, no. July, pp. 81–811, 2011.

- [15] B. Tabernig and N. Reheis, "Joining of molybdenum and its application," *International Journal of Refractory Metals and Hard Materials*, vol. 28, no. 6, pp. 728–733, 2010, doi: 10.1016/j.ijrmhm.2010.06.008.
- [16] G. Chen, J. Liu, X. Shu, B. Zhang, and J. Feng, "Study on microstructure and performance of molybdenum joint welded by electron beam," *Vacuum*, vol. 154, no. December 2017, pp. 1–5, 2018, doi: 10.1016/j.vacuum.2018.04.031.
- [17] L. L. Zhang, L. J. Zhang, J. Ning, Y. J. Sun, W. I. Cho, and S. J. Na, "On the laser gas (N₂) alloying in the welding of molybdenum alloy," *Journal of Materials Processing Technology*, vol. 296, no. March, p. 117184, 2021, doi: 10.1016/j.jmatprotec.2021.117184.
- [18] J. Wang, J. Wang, Y. Li, and D. Zheng, "Progress of research on welding for molybdenum alloys," *High Temperature Materials and Processes*, vol. 33, no. 3, pp. 193–200, 2014, doi: 10.1515/htmp-2013-0037.
- [19] D. Wang, C. Yu, J. Ma, W. Liu, and Z. Shen, "Densification and crack suppression in selective laser melting of pure molybdenum," *Mater Des*, vol. 129, no. March, pp. 44–52, 2017, doi: 10.1016/j.matdes.2017.04.094.
- [20] J. Braun *et al.*, "Molybdenum and tungsten manufactured by selective laser melting: Analysis of defect structure and solidification mechanisms," *Int J Refract Metals Hard Mater*, vol. 84, no. June, p. 104999, 2019, doi: 10.1016/j.ijrmhm.2019.104999.
- [21] D. Faidel, D. Jonas, G. Natour, and W. Behr, "Investigation of the selective laser melting process with molybdenum powder," *Additive Manufacturing*, vol. 8, pp. 88–94, 2015, doi: 10.1016/j.addma.2015.09.002.
- [22] E. Pink and R. W. Armstrong, "Total material variables influencing DBTT for Molybdenum," *Technical Report to Office of Naval Research*, vol. NR031-739, no. I, 1970.
- [23] K. Leitner *et al.*, "How grain boundary chemistry controls the fracture mode of molybdenum," *Mater Des*, vol. 142, pp. 36–43, 2018, doi: 10.1016/j.matdes.2018.01.012.
- [24] A. Kumar and B. L. Eyre, "Grain Boundary Segregation and Intergranular Fracture in Molybdenum," *Proceedings of the Royal Society A: Mathematical, Physical and Engineering Sciences*, vol. 370, no. 1743, pp. 431–458, 1980, doi: 10.1098/rspa.1980.0043.
- [25] G. L. Krasko, "Effect of impurities on the electronic structure of grain boundaries and intergranular cohesion in tungsten," *Materials Research Society Symposium Proceedings*, vol. 291, pp. 109–114, 1993, doi: 10.1557/proc-291-109.

- [26] Daniel Scheiber, “Theoretical Study of Grain Boundaries in Tungsten and Molybdenum.,” p. 160, 2016.
- [27] D. Scheiber, R. Pippan, P. Puschnig, A. Ruban, and L. Romaner, “Ab-initio search for cohesion-enhancing solute elements at grain boundaries in molybdenum and tungsten,” *International Journal of Refractory Metals and Hard Materials*, vol. 60, pp. 75–81, 2016, doi: 10.1016/j.ijrmhm.2016.07.003.
- [28] K. Leitner *et al.*, “How grain boundary chemistry controls the fracture mode of molybdenum,” *Mater Des*, vol. 142, pp. 36–43, 2018, doi: 10.1016/j.matdes.2018.01.012.
- [29] K. Leitner (née Babinsky) *et al.*, “On grain boundary segregation in molybdenum materials,” *Mater Des*, vol. 135, pp. 204–212, 2017, doi: 10.1016/j.matdes.2017.09.019.
- [30] D. Scheiber, R. Pippan, P. Puschnig, and L. Romaner, “Ab initio search for cohesion-enhancing impurity elements at grain boundaries in molybdenum and tungsten,” *Model Simul Mat Sci Eng*, vol. 24, no. 8, p. 85009, 2016, doi: 10.1088/0965-0393/24/8/085009.
- [31] J. Schindelin, I. Arganda-Carreras, and E. Frise, “Fiji - an Open Source platform for biological image analysis,” *Nat Methods*, vol. 9, no. 7, pp. 676–682, 2012, doi: 10.1038/nmeth.2019.Fiji.
- [32] J. Rodriguez-Carvajal, “Recent advances in magnetic structure determination by neutron powder diffraction,” *Physica B*, vol. 192, pp. 55–69, 1993.
- [33] G. Yablokova *et al.*, “Rheological behavior of β -Ti and NiTi powders produced by atomization for SLM production of open porous orthopedic implants,” *Powder Technology*, vol. 283, pp. 199–209, 2015, doi: 10.1016/j.powtec.2015.05.015.
- [34] D. Wang, C. Yu, X. Zhou, J. Ma, W. Liu, and Z. Shen, “Dense Pure Tungsten Fabricated by Selective Laser Melting,” *Applied Sciences*, vol. 7, no. 4, p. 430, 2017, doi: 10.3390/app7040430.
- [35] L. Thijs, M. L. Montero Sistiaga, R. Wauthle, Q. Xie, J. P. Kruth, and J. Van Humbeeck, “Strong morphological and crystallographic texture and resulting yield strength anisotropy in selective laser melted tantalum,” *Acta Mater*, vol. 61, no. 12, pp. 4657–4668, 2013, doi: 10.1016/j.actamat.2013.04.036.
- [36] J. Braun *et al.*, “Molybdenum and tungsten manufactured by Selective Laser Melting - Analysis of defect structure and solidification mechanism,” *Int J Refract Metals Hard*

- Mater.*, vol. 84, no. SI: Additive Manufacturing, p. 104999, 2019, doi: 10.1016/j.ijrmhm.2019.104999.
- [37] D. Wang, Z. Wang, K. Li, J. Ma, W. Liu, and Z. Shen, “Cracking in laser additively manufactured W: Initiation mechanism and a suppression approach by alloying,” *Materials and Design*, vol. 162, pp. 384–393, 2019, doi: 10.1016/j.matdes.2018.12.010.
- [38] J. A. Lemberg, M. R. Middlemas, T. Weingärtner, B. Gludovatz, J. K. Cochran, and R. O. Ritchie, “On the fracture toughness of fine-grained Mo-3Si-1B (wt.%) alloys at ambient to elevated (1300 °C) temperatures,” *Intermetallics*, vol. 20, no. 1, pp. 141–154, 2012, doi: 10.1016/j.intermet.2011.09.003.
- [39] C. Fressengeas *et al.*, “On the evaluation of dislocation densities in pure tantalum from EBSD orientation data,” *Materiaux et Techniques*, vol. 106, no. 6, 2018, doi: 10.1051/mattech/2018058.
- [40] T. Wang, Y. Zhang, S. Jiang, X. Li, B. Zhang, and J. Feng, “Stress relief and purification mechanisms for grain boundaries of electron beam welded TZM alloy joint with zirconium addition,” *Journal of Materials Processing Technology*, vol. 251, no. August 2017, pp. 168–174, 2018, doi: 10.1016/j.jmatprotec.2017.08.031.
- [41] M. W. Mallett, “The determination of interstitial elements in the refractory metals,” *Talanta*, vol. 9, no. 2, pp. 133–144, 1962, doi: 10.1016/0039-9140(62)80036-8.
- [42] R. Krechetnikov, “Stability of liquid sheet edges,” *Physics of Fluids*, vol. 22, no. 9, 2010, doi: 10.1063/1.3474640.
- [43] W. Dong, H. Kokawa, Y. S. Sato, and S. Tsukamoto, “Nitrogen absorption by iron and stainless steels during CO₂ laser welding,” *Metallurgical and Materials Transactions B: Process Metallurgy and Materials Processing Science*, vol. 34, no. 1, pp. 75–82, 2003, doi: 10.1007/s11663-003-0057-2.
- [44] S. C. Srivastava and L. L. Seigle, “Solubility and thermodynamic properties of oxygen in solid molybdenum,” *Metallurgical Transactions*, vol. 5, no. 1, pp. 49–52, 1974, doi: 10.1007/BF02642925.
- [45] A. Kumar and B. L. Eyre, “Grain Boundary Segregation and Intergranular Fracture in Molybdenum,” *Proceedings of the Royal Society A: Mathematical, Physical and Engineering Sciences*, vol. 370, no. 1743, pp. 431–458, 1980, doi: 10.1098/rspa.1980.0043.

- [46] R. Frauenfelder, “Permeation, Diffusion, and Solution of Nitrogen in Tungsten and Molybdenum,” *The Journal of Chemical Physics*, vol. 48, no. 9, pp. 3966–3971, 1968, doi: 10.1063/1.1669721.
- [47] H. Domke and M. G. Froberg, “Solubility of nitrogen in liquid molybdenum,” *Scripta Metallurgica*, vol. 8, pp. 289–292, 1974.
- [48] D. E. Weaver, “The diffusivity and solubility of nitrogen in molybdenum and the trapping of nitrogen by carbon in molybdenum,” *University of California, Ph.D. Thesis*, p. 84, 1972.
- [49] K. Sugiura, S. Kodama, Y. Tsujimura, A. B. Murphy, and M. Tanaka, “Numerical modeling of nitrogen absorption during gas tungsten arc welding,” *Yosetsu Gakkai Ronbunshu/Quarterly Journal of the Japan Welding Society*, vol. 31, no. 4, pp. 1–4, 2013, doi: 10.2207/qjjws.31.14s.
- [50] A. Bandopadhyay, A. Banerjee, and T. Debroy, “Nitrogen activity determination in plasmas,” *Metallurgical Transactions B*, vol. 23, no. 2, pp. 207–214, 1992, doi: 10.1007/BF02651855.
- [51] P. Bidare, I. Bitharas, R. M. Ward, M. M. Attallah, and A. J. Moore, “Fluid and particle dynamics in laser powder bed fusion,” *Acta Materialia*, vol. 142, pp. 107–120, 2018, doi: 10.1016/j.actamat.2017.09.051.
- [52] H. Kurishita, O. Tokunaga, and H. Yoshinaga, “Effect of Nitrogen on the Intergranular Brittleness in Molybdenum,” *Materials Transactions, JIM*, vol. 31, no. 3, pp. 190–194, 1990. doi: 10.2320/matertrans1989.31.190.
- [53] K. Leitner (née Babinsky) *et al.*, “On grain boundary segregation in molybdenum materials,” *Mater Des*, vol. 135, pp. 204–212, 2017, doi: 10.1016/j.matdes.2017.09.019.
- [54] F. Arciprete, J. E. Boschker, S. Cecchi, E. Zallo, V. Bragaglia, and R. Calarco, “Hints for a General Understanding of the Epitaxial Rules for van der Waals Epitaxy from Ge-Sb-Te Alloys,” *Advanced Materials Interfaces*, vol. 9, no. 9, 2022, doi: 10.1002/admi.202101556.
- [55] J. Faugier-Tovar, F. Lazar, C. Marichy, and C. Brylinski, “Influence of the lattice mismatch on the atomic ordering of zno grown by atomic layer deposition onto single crystal surfaces with variable mismatch (InP, GaAs, GaN, SiC),” *Condensed Matter*, vol. 2, no. 1, pp. 1–8, 2017, doi: 10.3390/condmat2010003.

- [56] D. Matsunaka, D. O. I. Yoshiharu, and Y. Shibutani, “Effects of substrate strain on epitaxial growth by kinetic Monte Carlo method,” *Zairyo/Journal of the Society of Materials Science, Japan*, vol. 59, no. 8, pp. 610–615, 2010, doi: 10.2472/jsms.59.610.
- [57] H. Yamada, M. Kawasaki, and Y. Tokura, “Epitaxial growth and valence control of strained perovskite SrFeO₃ films,” *Applied Physics Letters*, vol. 80, no. 4, pp. 622–624, 2002, doi: 10.1063/1.1445805.
- [58] S. Liu, L. Bönig, and H. Metiu, “The effect of island coalescence on island density during epitaxial growth,” *Surface Science*, vol. 392, no. 1–3, 1997, doi: 10.1016/S0039-6028(97)00707-3.
- [59] M. Kolarikova, L. Kolarik, and P. Vondrous, “Welding of thin molybdenum sheets by EBW and GTAW,” *23rd DAAAM International Symposium on Intelligent Manufacturing and Automation 2012*, vol. 2, no. 1, pp. 1005–1008, 2012.

Chapter 6 – Laser powder bed fusion additive manufacturing of Mo and TZM exoskeleton with Cu infiltration for new heat sinks configuration

Chapters 4 and 5 developed a deep understanding of the influence of N₂ build atmosphere on LPBF-processed parts, their microstructure, mechanical properties and cracking behaviour. The understanding required to prepare crack-free dense Mo parts using the LPBF process was achieved. A practical application was devised to leverage this learning to fabricate Mo parts with intricate features. A power electronics heat sink was chosen to demonstrate the practical application of LPBF-processed parts of this nature. Mo and TZM (an alloy of Mo) parts with thin walls and honeycomb cavity structures were devised as an exoskeleton to be fabricated using the LPBF process. Cu infiltration would be performed on these to prepare heat sinks with similar Cu content to match commercial laminate heat sinks. Microstructural and mechanical characterization of the as-built parts was planned. Similar characterization following Cu infiltration was planned to study the influence of the process. Thermal diffusivity measurements and FEM modelling to evaluate the performance of the fabricated heat sinks against commercial heat sink was devised.

This chapter has been submitted to the Advanced Materials Technologies with manuscript reference number: admt.202301328 as: *T. Ramakrishnan*, A. Kumar, P. Hudon, and M. Brochu, “Laser powder bed fusion additive manufacturing of Mo and TZM exoskeleton with Cu infiltration for new heat sinks configuration”.

6.1 Abstract

This study reports the fabrication and characterization of Mo and TZM exoskeletons with honeycomb cavity structures that are infiltrated with oxygen-free high conductivity (OHFC) Cu under an inert atmosphere as a potential replacement for Cu-Mo-Cu laminate in heat sink applications. The thermal expansion behaviour, particularly the influence of the high coefficient of thermal expansion (CTE) of copper, and the thermal loading of the Mo and TZM structures and Cu-infiltrated parts are evaluated. Mo and TZM structures with high density (>99 %) and Mo-based heat sinks with improved CTE ($6.6 \times 10^{-6} \text{ K}^{-1}$) were fabricated. Compared to conventional Cu-Mo-Cu laminated heat sinks (CTE = $7.6 \times 10^{-6} \text{ K}^{-1}$), Mo and TZM structures promise superior performance due to their closer CTE to that of GaAs and similar semiconductors (CTE = $5.7 \times 10^{-6} \text{ K}^{-1}$). Exposure to temperatures up to 1073 K did not affect the Mo microstructure due to the inherent resistance to recrystallization, while exposure to 1373 K did reduce hardness. In contrast, TZM exoskeletons showed resistance to recrystallization even at 1373 K. The fabricated composite heat sinks showed thermal diffusivity ($\sim 61 \times 10^6 \text{ m}^2 \cdot \text{s}^{-1}$) that is within the upper limits of those reported for commercial laminated heat sinks.

6.2 Introduction

Molybdenum (Mo) is a refractory metal with good mechanical and thermal properties, such as a high melting point (2896 K) and thermal conductivity ($134 \text{ W} \cdot \text{m}^{-1} \cdot \text{K}^{-1}$) [1,2]. Mo and its alloys are among the materials being explored for use under high operating temperatures in power electronics, aviation engines and nuclear power generation applications [3–5]. TZM is a Mo alloy which nominally contains 0.5 wt. % titanium, 0.08 wt. % zirconium, and between 0.01 to 0.04 wt. % carbon [6]. Although more expensive than pure Mo, TZM has a higher recrystallization temperature (1673 K) and offers improved strength at elevated temperatures (>300 MPa even at 1473 K) from the development of Mo and Ti carbides and Zr and Ti oxides precipitates strengthening grain boundaries [7-9]. Due to their refractory nature, Mo and TZM are mainly processed via the powder metallurgy (PM) route [10].

Despite the advantages listed above, Mo or TZM have yet to find wide adoption in high-temperature applications because of the limitations in manufacturing complex parts using

conventional processes [4,6]. For example, improved heat sinks for power electronic semiconductors could be possible if complex parts could be fabricated with these materials. Copper is an ideal heat sink material due to its excellent thermal diffusivity ($\sim 115 \times 10^6 \text{ m}^2 \cdot \text{s}^{-1}$), but the significant difference in the coefficient of thermal expansion (CTE) between Cu ($17.0 \times 10^{-6} \text{ K}^{-1}$) and semiconductors (5.7 to $7.0 \times 10^{-6} \text{ K}^{-1}$) presents a disadvantage for its use as a heat sink [11–13]. High junction temperature and interfacial stresses generated by the mismatch in the thermal expansion between Cu and the semiconductors result in debonding issues [14]. Currently, as a compromise, laminated Mo-Cu or Cu-Mo-Cu heat sinks with good thermal diffusivity (~ 45 to $62 \times 10^6 \text{ m}^2 \cdot \text{s}^{-1}$) and acceptable CTE values (7.6 to $9.1 \times 10^{-6} \text{ K}^{-1}$) are used as they were proven to reduce the risk of debonding between the semiconductor and the heat sink [12,14]. A more significant optimization could be achieved with heat sinks offering closer CTE while having high thermal diffusivity. Table 6.1 lists the typical thermal properties of materials used in such applications, and the difference in CTE between the semi-conductor and Cu-Mo-Cu heat sink indicates the need for customized heat sinks with lower CTE values (~ 6.0 to $7.0 \times 10^{-6} \text{ K}^{-1}$) and good thermal diffusivity (~ 50 to $60 \times 10^6 \text{ m}^2 \cdot \text{s}^{-1}$). Heat sinks with good thermal diffusivity, and tailored CTE could be manufactured if more complex designs than laminates could be fabricated.

Table 6.1 Thermal properties of power electronics semiconductors and possible heat sink materials.

Material	CTE (10^{-6} K^{-1})	CTE _{MAT} - CTE _{GaAs} (10^{-6} K^{-1})	Thermal diffusivity ($10^6 \text{ m}^2 \cdot \text{s}^{-1}$)	Reference
GaAs	5.8	-	31	[13,15]
Cu	17	11.3	115	[16,17]
Mo	4.9 to 5.2	-0.7	55	[18]
TZM	5.2	-0.1	50	[18]
Cu-Mo-Cu	7.6 to 9.1	-3.4 to -1.9	45 to 65	[19]

Honeycomb-structured systems have great potential for developing compact heat sinks [20,21]. One such product could be made of Mo/TZM exoskeletons with integral honeycomb cavity structures (HCS) that would be filled with Cu. The exoskeletons will dictate the CTE in this

configuration, while the Cu infill will increase the thermal diffusivity. Unfortunately, conventional methods cannot yet fabricate such structures cost-effectively. However, laser powder bed fusion (LPBF) additive manufacturing (AM) is an alternative process that can eliminate this constraint since it allows the fabrication of parts with complex and intricate geometries, such as honeycomb-based heat sinks [22].

During the LPBF process, powder particles are spread into a thin layer on a substrate. Then, a laser beam is projected onto the powder layer causing the particles to melt, solidify, and bond with the substrate or previous layers. This process is repeated in a layer-by-layer sequence to build a part [23–25]. Aluminum [26,27], copper [28], nickel [29,30], steel [31,32], and titanium [33,34] alloys are some of the materials that have been extensively employed with LPBF. Various LPBF studies have shown the feasibility of fabricating thin walls (sizes from 0.25 mm to 1.00 mm) and parts with thin features [35–37]. Interestingly, the LPBF fabrication of AlSi10Mg and Cu parts with lattice structures for heat sink applications has already been reported [38,39].

The literature on LPBF of pure refractory materials and their alloys, especially Mo and TZM, is very limited. As for that of LPBF-processed Mo and TZM parts with thin features or lattice structures for heat sink applications, literature is lacking. The work of Faidel et al. [40] on the LPBF of Mo are among the pioneer studies that showed densification to about 82.5% of the theoretical density (TD) of Mo. Wang et al. [41] achieved Mo densification up to 99.1% and crack suppression using support-like elements that reduce cooling rates and maintain fabrication temperatures above the ductile-to-brittle transition temperature. Very high densification was obtained by Kaserer et al. [42], who reported LPBF-fabricated TZM parts with a density of 99.7% TD. In that study, a crack-free microstructure was produced by heating the substrate to 1073 K and then by cooling it at 100 K per hour [42]. Note that in all the studies mentioned above, only cuboidal samples with dimensions of 10 mm (L) x 10 mm (B) x 5 mm (H) or larger were produced.

The present study reports the development of heat sinks from Mo-HCS and TZM-HCS through the LPBF process. First, a Mo-HCS exoskeleton was fabricated by LPBF, and Cu infiltration was performed to produce a complex heat sink. The heat sink produced was then characterized by evaluating the microstructure, CTE, and microhardness. The same procedure was then repeated

with TZM-HCS and Cu, and the characterization data of the heat sink were compared to the ones obtained with Mo-HCS for resistance to recrystallization during the infiltration process. Thermal diffusivity was then measured to benchmark for heat sink application, and finite element method (FEM) modelling was performed to compare their performance with conventional Cu-Mo-Cu laminated heat sinks.

6.3 Material and methods

6.3.1 LPBF fabrication of HCS

The powders employed were made of gas-atomized powders of Mo and spray-dried pre-alloyed powders of TZM sourced from Tekna (Canada) and American Elements (USA), respectively. Samples of 10 mm (L) x 3 mm (B) x 10 mm (H) and 0.5 mm wall thickness were fabricated using LPBF. The size of the internal honeycomb cavity was chosen to achieve a volumetric cavity fraction of 40 vol. %. The dimensions were selected to tailor the CTE using the rule of mixtures. Equation (6.1) shows the modified rule of mixtures as described by Schapery [43,44]. Here, $\bar{\alpha}$ is the CTE (in K^{-1}) of the system, E_i is the modulus (in Pa), α_i the CTE, and V_i is the volume fraction of the individual components. Section 6.A1 of the Supplementary Information provides additional details on the CTE calculations.

$$\bar{\alpha} = \frac{E_1 \cdot \alpha_1 \cdot v_1 + E_2 \cdot \alpha_2 \cdot v_2}{E_1 \cdot v_1 + E_2 \cdot v_2} \quad (6.1)$$

The samples were fabricated with a AM400 LPBF machine (Renishaw, UK) equipped with a reduced build volume unit using a bi-directional scanning pattern and 67° rotation between each layer. Molybdenum plates (99.95% metal basis) of 2.5 mm thickness from Alfa Aesar (USA) were used as the substrate. The oxygen was limited to below 300 ppm throughout the build process. Figure 6.1a and 1b show model views of the HCS.

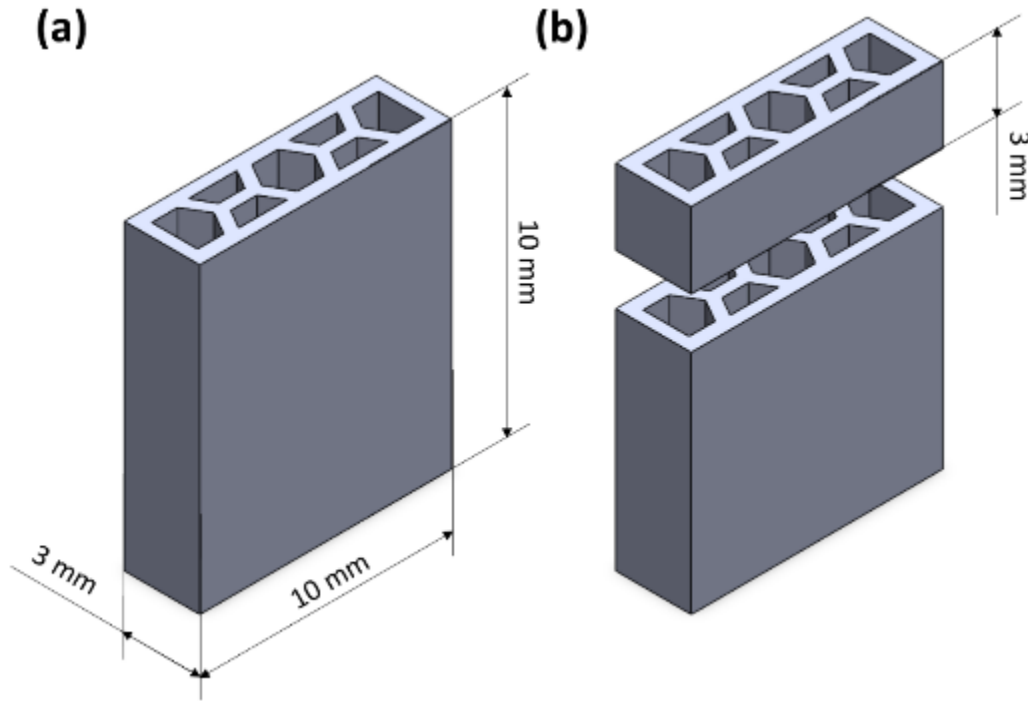


Figure 6.1 (a) Model view of the HCS with dimensions and (b) view of the section prepared for CTE and microstructural analysis.

6.3.2 Cu infiltration into HCS

Oxygen-free high conductivity (OFHC) Cu was infiltrated into the Mo-HCS and TZM-HCS honeycomb cavities. The infiltration was performed in a F21100 tube furnace (Thermo Scientific, USA) that was previously calibrated using the melting points of indium (429.6 K), silver (1235 K), and gold (1337 K), ensuring temperature precision to ± 2 K. Before heating, the samples were put at the hot spot of the furnace, and titanium sponges were placed around them to scavenge oxygen. The furnace was then sealed, filled with flowing N_2 gas at room temperature for about 120 min, and then brought to 1373 K (1100 °C) at 10 K/min in the same flowing inert atmosphere. Figure 6.2 shows the temperature profile used during the infiltration. The temperature was measured using a Type K thermocouple placed inside the tube just above the samples to be infiltrated. Once the infiltration was completed, the samples were left to cool down in the furnace and removed from the tube when the temperature was below 323 K (50 °C).

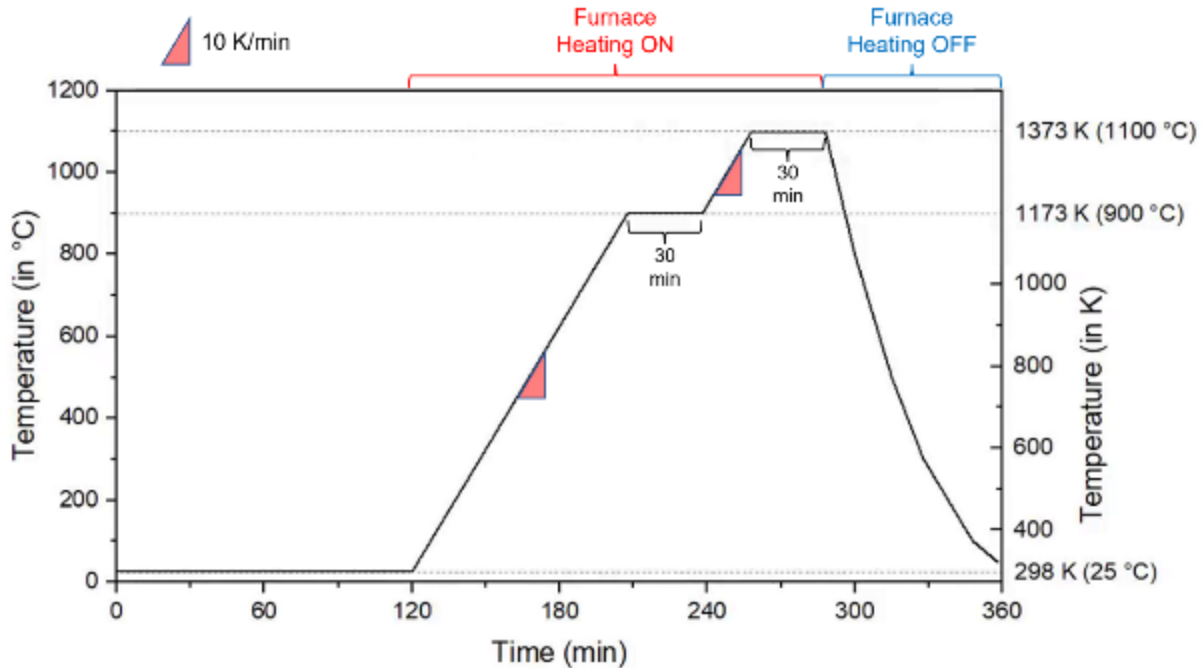


Figure 6.2 Temperature profile of the Cu infiltration process.

6.3.3 Sample preparation and characterization

The samples were separated from the build plate and then sectioned using an IsoMet™ Low-Speed precision cutter (Buehler, USA) for characterization. Metallographic preparation was achieved by an initial grinding up to 800 grit SiC paper, followed by polishing on a Labopol (Struers, USA) equipment with diamond suspensions of 9 μm , 3 μm , and 1 μm . A final polishing step using 0.05 μm colloidal silica suspension was then performed.

Optical micrographs were captured using an optical microscope (Nikon, Japan) equipped with a Clemex Vision System (Clemex, Canada) to characterize the as-built (AB) microstructure and determine the optical density. The cavity volume fraction was estimated from the optical micrographs using image analysis with the ImageJ software [45]. Crystallographic texture and grain morphology were studied using a SU3500 SEM (Hitachi, Japan) equipped with energy dispersive spectroscopy (EDS) and electron back-scattered diffraction (EBSD) detectors (Oxford Instruments, UK). Figure 3 shows in a red box where the EDS maps were taken. EBSD data were analyzed using HKL Channel 5 software (Oxford Instruments, UK). The grains were classified as follows for recrystallization fraction analysis: grains with average internal misorientation

exceeding 15° are classified as deformed, grains with average internal misorientation between 2 and 15° are considered sub-structured, and grains with misorientation below 2° are classified as recrystallized [46,47].

Phases were identified using X-ray diffraction (XRD) using a D8 Discover diffractometer (Bruker, Germany) with a Cobalt (Co) anode ($K\alpha_1$ wavelength, $\lambda = 1.7890 \text{ \AA}$). The diffraction data were acquired between 2θ values of 40° and 120° at a step size of 0.05°. Powder diffraction files (PDF) from the Crystallography Open Database (COD) were used to identify the constituent elements and phases. Full profile fitting analysis on the XRD data was performed using FullProf Suite [48].

Vickers microhardness measurements were performed using a Clark CM-100AT (Sun-Tec, USA) automated microhardness equipment with a 0.1 kgf load and a dwell time of 10 s; the reported measurements are an average of 5 indents. In addition to the measurements carried out on AB samples, microhardness measurements were repeated for each sample after CTE measurement and Cu infiltration. Figure 6.3 shows the schematic of the locations (blue “+” symbols) and the line corresponding to the microhardness profile analysis (blue dashed line) performed on Cu-infiltrated Mo-HCS and TZM-HCS samples. The CTE was measured between room temperature (RT) and 1073 K using a vertical DIL-L78-RITA dilatometer (Linseis, Germany) on samples of 10 mm (L) x 3 mm (B) x 3 mm (H). Type K thermocouples of 0.127 mm in diameter were spot welded to the samples using a DCC Corp. Hotspot II TC welder. Samples were separated from the quartz rods of the dilatometer using a single sheet of mica, and measurements were performed in a flow of helium with a heating rate of 20 K/min up to the final temperature. The data collected were then corrected using a Ni standard according to the ASTM A1033-10 standard [49].

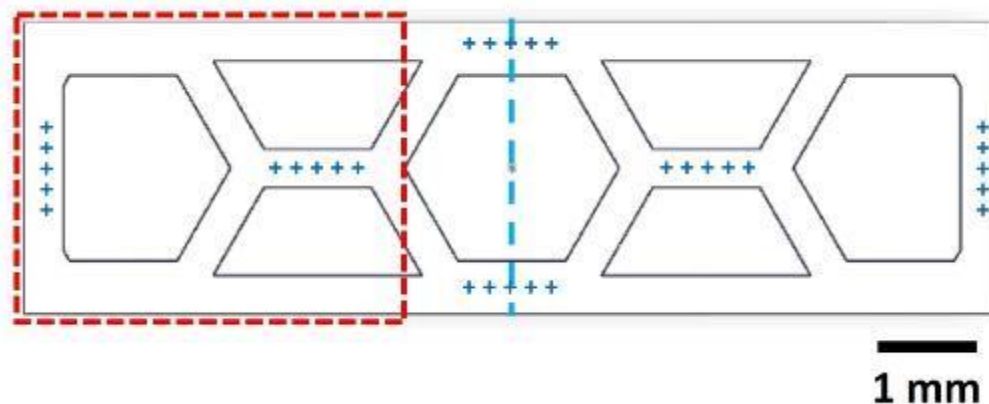


Figure 6.3 Location of EDS map (marked in red) and those for microhardness analysis (marked in blue) performed on the HCS sample.

6.3.4 Thermal diffusivity setup and measurements

Thermal diffusivity measurements were performed using a LFA 427 laser flash analysis instrument (Netzsch, Germany) on control samples having a diameter of 12.7 mm and a thickness of 2.5 mm. The isothermal measurement conditions used single shots with a laser pulse voltage of 600 V and pulse width of 1 ms under flowing helium at 50 mL/min at 298 K (25 °C). An in-house custom-made laser flash analysis equipment was also used to repeat the tests on the control samples and to test the Cu-infiltrated HCS samples of 10 mm (L) x 3 mm (B) x 10 mm (H). This unit used a NdYAG laser (1064 nm wavelength) shot of 10 W power and pulse width of 1 ms under flowing nitrogen at 50 mL/min at 298 K (25 °C). All samples were coated with graphite using a Cramolin (ITW Spraytec, Germany) colloidal-graphite spray. The measurements were performed through the thickness of the samples. Section 6.A2 of the Supplementary Information provides additional details about the LFA equipment and measurements.

Thermal diffusivity was calculated by measuring the time-linked temperature change using equation (6.2), where D is the thermal diffusivity (in $\text{m}^2 \cdot \text{s}^{-1}$), $t_{0.5}$ is the time (in s) needed to increase the temperature by 50%, and d is the thickness (in m) of the sample.

$$D = 0.1388 \frac{d^2}{t_{0.5}} \quad (6.2)$$

Following the calculation of thermal diffusivity, thermal conductivity was calculated using equation (6.3), where k is the thermal conductivity (in $\text{W}\cdot\text{m}^{-1}\cdot\text{K}^{-1}$), ρ is the density (in kg m^{-3}), and C_p is the specific heat capacity (in $\text{J}\cdot\text{kg}^{-1}\cdot\text{K}^{-1}$).

$$k = D \cdot \rho \cdot C_p \quad (6.3)$$

6.3.5 FEM simulation of Cu-Mo-Cu vs Mo-HCS

Three-dimensional (3D) models were developed using 3DEXPERIENCE® SOLIDWORKS (Dassault Systèmes, USA). FEM simulation was performed on the proposed Cu-infiltrated Mo-HCS (hereafter referred to as Mo-HCS+Cu) heat sink and a commercially available Cu-Mo-Cu conventional laminate heat sink with similar Cu content. Three-dimensional coupled temperature-displacement thermo-mechanical models were prepared with the commercial finite element analysis (FEA) software Abaqus/CAE 2021 (Dassault Systèmes Simulia Corp, USA). Figure 6.4a and Figure 6.4b show the model layout of both Mo-HCS+Cu and Cu-Mo-Cu heat sinks respectively, with a GaAs semiconductor on top. A simplified construction was chosen to compare the heat sink behaviour; hence, the semiconductor was directly used instead of an integrated chip with all its components. Similar simplification for FEM simulation has been previously employed for heat sink performance evaluation [12]. Both models were built with the C3D4T (coupled temperature displacement tetragonal) mesh, and a mesh sensitivity analysis was run. As a result of the analysis, mesh sizes of 200 μm and 12.5 μm were assigned for the heat sink and GaAs, respectively. Table 2 shows the selected thermomechanical properties of the materials used in the simulations. A surface heat load of $5 \times 10^6 \text{ W}\cdot\text{m}^{-2}$ was imposed on the GaAs semiconductor. The exposed surfaces of the heat sink had a boundary condition of radiation and natural convection to an ambient sink temperature of 298 K (25 °C). The free surface of the GaAs was encastered as a mechanical boundary condition for the calculation. Additional details of the FEM simulation are provided in Section A3 of the Supplementary Information.

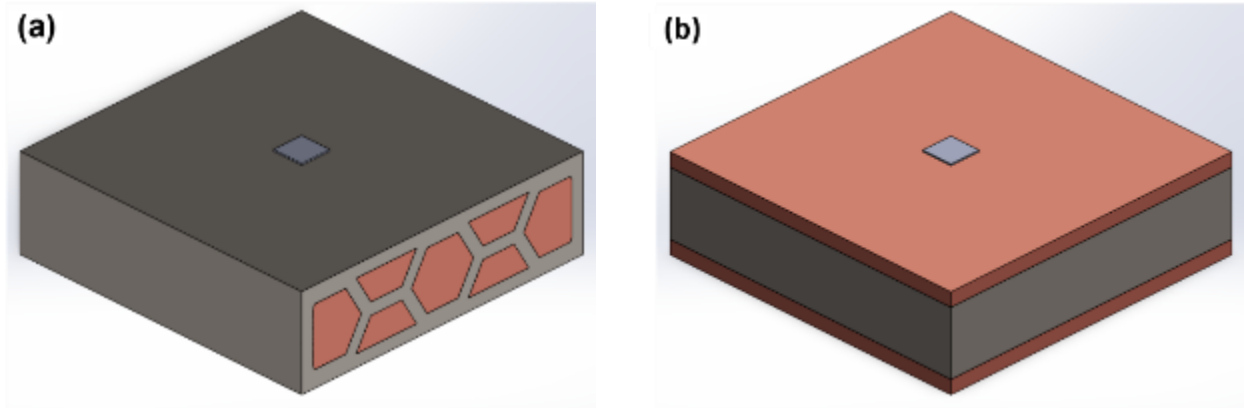


Figure 6.4 Three-dimensional models of (a) GaAs-Mo-HCS+Cu and (b) GaAs-CuMoCu, respectively.

Table 6.2 Selected thermomechanical properties used for FEM simulations.

Property	Unit	Cu	Mo	GaAs
Thermal conductivity, k	$\text{W}\cdot\text{m}^{-1}\cdot\text{K}^{-1}$	400	138	55
Density, ρ	$\text{kg}\cdot\text{m}^{-3}$	8960	10280	5320
Thermal diffusivity, α	$\text{m}^2\cdot\text{s}^{-1}$	115	55	31
Specific heat capacity, C_P	$\text{J}\cdot\text{kg}^{-1}\cdot\text{K}^{-1}$	385	250	330
CTE	$\times 10^6 \text{K}^{-1}$	17.0	5.1	5.8
Young's modulus, E	GPa	120	330	86
Poisson's ratio, η		0.35	0.33	0.35

As a mark of performance, the conduction resistance was computed using equation (6.4) from the output data of the simulation. In equation (6.4), R_{COND} is the conduction resistance (in K/W), ΔT is the temperature difference (in K) between the interface/junction and the outside of the heat sink, and q is the heat flow (in W).

$$R_{COND} = \Delta T/q \quad (6.4)$$

6.4 Results and Discussion

6.4.1 Fabrication and characterization of Mo-HCS

Figure 6.5a shows an SEM micrograph of a Mo-HCS part fabricated for this study, while Figure 6.5b and Figure 6.5c show magnified SEM micrographs of a thin wall and a cavity, respectively. Wall thicknesses of 0.61 ± 0.06 mm were measured for the sample, which is slightly larger than the design dimension of 0.5 mm, but these were considered acceptable for the study. The cavities are unobstructed with a volume fraction of 34 %. Figure 6.5d shows an optical micrograph of the cross-section of a thin wall. The sample had some porosity, but no sign of cracking was observed. The porosity analysis showed that Mo samples with densities of 99.0 ± 0.1 % were produced. Figure 6.5e shows a representative EBSD inverse pole figure (IPF) map of the thin wall feature, indicating an irregular grain structure with grains of length (along the build direction) less than 0.3 mm. This microstructure is different from the large columnar grain structure in LPBF of pure Mo reported by Wang et al. [41], where grains as long as 2 mm were observed. Braun et al. [50] also reported a columnar grain structure but with grains 0.6 mm in length.

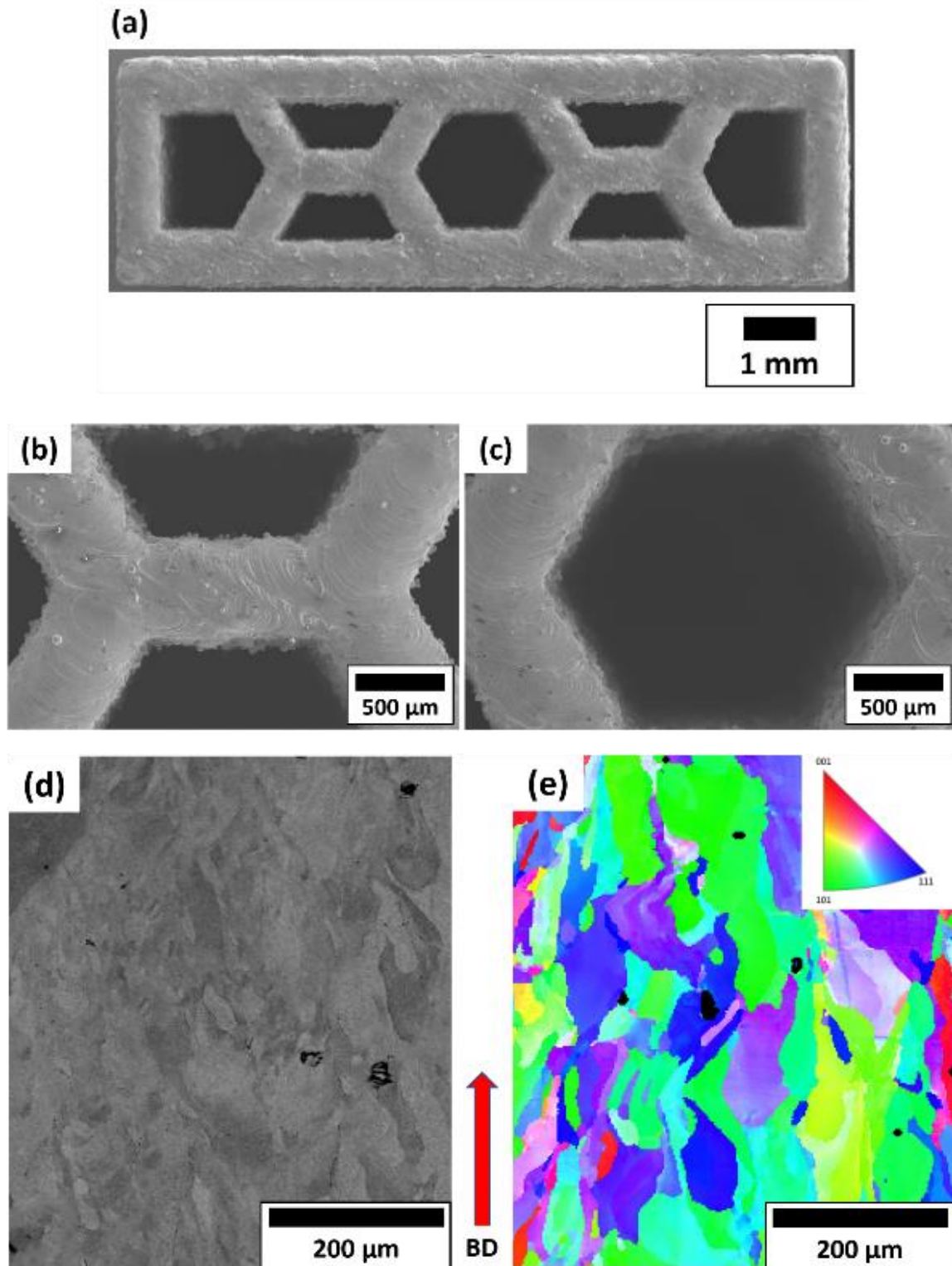


Figure 6.5 (a) LPBF-AM of a Mo-HCS sample with honeycomb structure, (b, c) SEM micrographs detailing the thin walls and cavity features, (d) optical micrograph, and (e) EBSD micrograph of a thin wall.

The Mo-HCS sample showed statistically similar hardness values of $\sim 210 \pm 12$ HV. The current results also match the hardness value (208 ± 4 HV₁₀) previously reported for pure Mo processed with LPBF-AM [51]. The CTE of the Mo-HCS sample was measured to be $5.3 \pm 0.1 \times 10^{-6} \text{ K}^{-1}$, which is comparable to the values reported in the literature for pure Mo (4.9 to $5.2 \times 10^{-6} \text{ K}^{-1}$) [4,5]. Since the CTE measurement exposed the sample to a temperature of 1073 K, the microhardness analysis was repeated to verify if this heat cycle affected the sample properties. A similar hardness value (211 ± 10 HV) to the AB condition was measured, suggesting that the brief exposure to 1073 K (800 °C) did not affect the microstructure.

6.4.2 Cu-infiltrated Mo-HCS

Figure 6.6a and Figure 6.6b show representative optical micrographs of the Mo-HCS after Cu infiltration (Mo-HCS+Cu). The micrographs suggest proper infiltration and excellent wetting at the interface between the Cu infill and the Mo exoskeleton. Figure 6.6c and Figure 6.6d show the results of EDS maps of Mo and Cu for the region marked by the red dashed rectangle in Figure 6.3. There are no regions of overlap between the Mo and Cu regions and no evidence of dissolution of Cu in the Mo or vice-versa. The possible interactions were further investigated using XRD analysis. Figure 6.6e shows the result of the XRD study and indicates peaks matching the PDF files COD#9008543 and COD#4105681 for Mo and Cu, respectively. There is no indication of the formation of other phases. Full profile fitting analysis of the peaks indicated lattice parameter values of 0.315217 nm and 0.362109 nm for Mo and Cu, respectively. The values are within 0.16 % and 0.17 % of theoretical values, respectively.

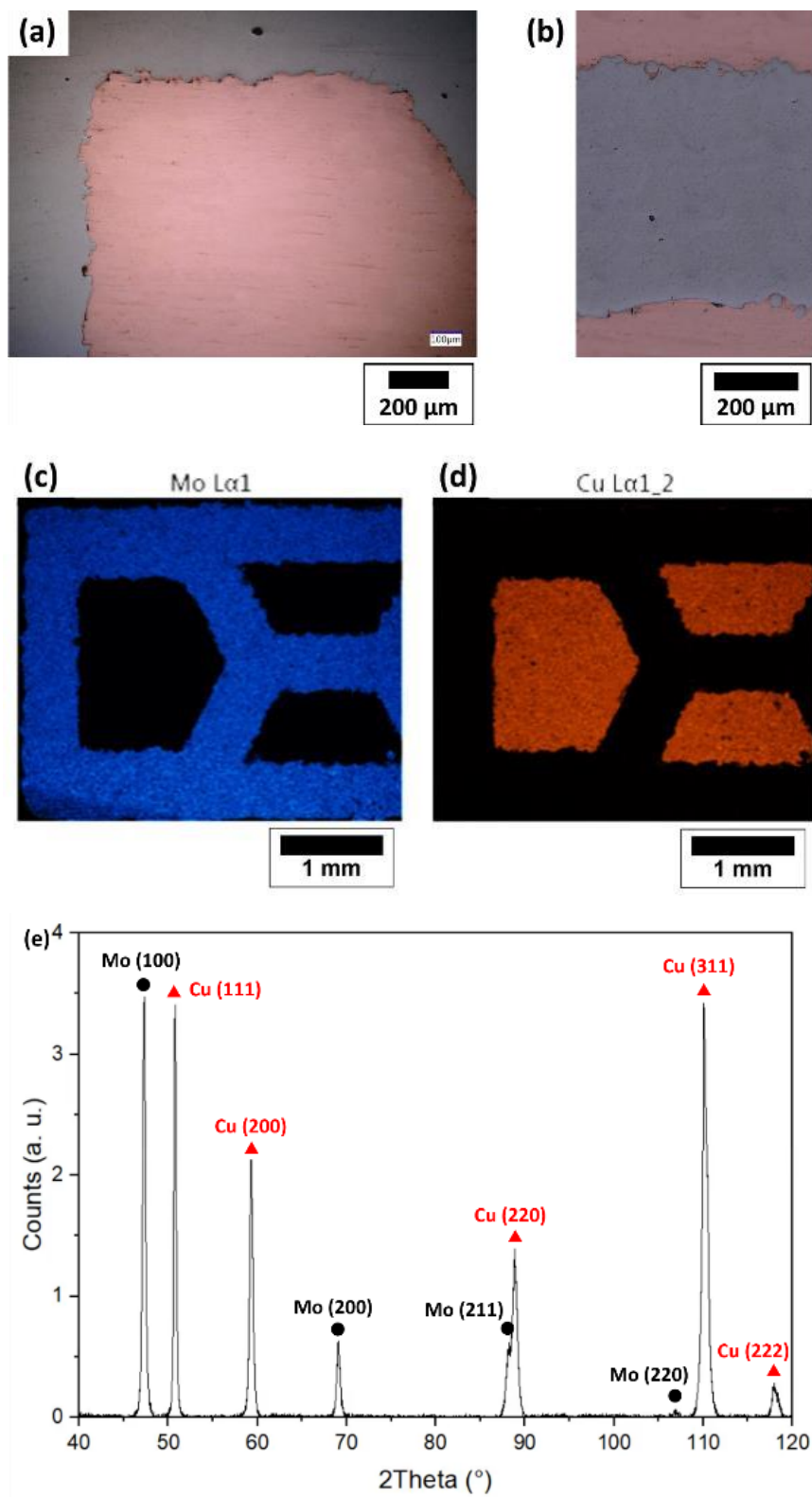


Figure 6.6 Mo and Cu regions shown in (a, b) optical micrographs, and (c, d) EDS maps; (e) XRD spectrum showing Mo and Cu phases.

Following Cu infiltration into the Mo cavities, the CTE of Mo-HCS+Cu was measured to be $6.5 \times 10^{-6} \text{ K}^{-1}$, which is higher than the CTE of Mo-HCS ($5.3 \pm 0.1 \times 10^{-6} \text{ K}^{-1}$). This increase was expected due to the contribution of the Cu phase, which has a higher CTE ($\sim 17 \times 10^{-6} \text{ K}^{-1}$). Interestingly, our measured CTE is similar to the $6.6 \times 10^{-6} \text{ K}^{-1}$ CTE calculated for Mo-HCS (using actual dimensions) using Equation (2). Our measured CTE is lower than the ones (7.6 to $9.1 \times 10^{-6} \text{ K}^{-1}$) reported for commercial Cu-Mo-Cu laminated heat sinks with similar Cu content (30 wt.%) and closer ($5.8 \times 10^{-6} \text{ K}^{-1}$) to the CTE of GaAs semiconductors [52,53].

Figure 6.7a shows the results of the recrystallized fraction analysis performed on Mo-HCS samples in three conditions: AB, exposed to 1073 K (following CTE measurements), and exposed to 1373 K (after Cu infiltration). Figure 6.7b-d show representative maps for the three conditions. No statistically significant difference was observed between the recrystallized fractions in AB Mo-HCS and after exposure to 1073 K (800 °C). These results suggest that no microstructural changes occur even after exposure to 1073 K (800 °C). On the other hand, exposure to 1373 K (1100 °C) has caused an increase in the recrystallized fraction (from 3 % to 12 %). This is in agreement with Primig et al. [54], who reported that pure Mo sheets, with some stored strain energy from deformation, showed clear signs of recrystallization when exposed to a temperature of 1373 K (1100 °C) for 1 hour.

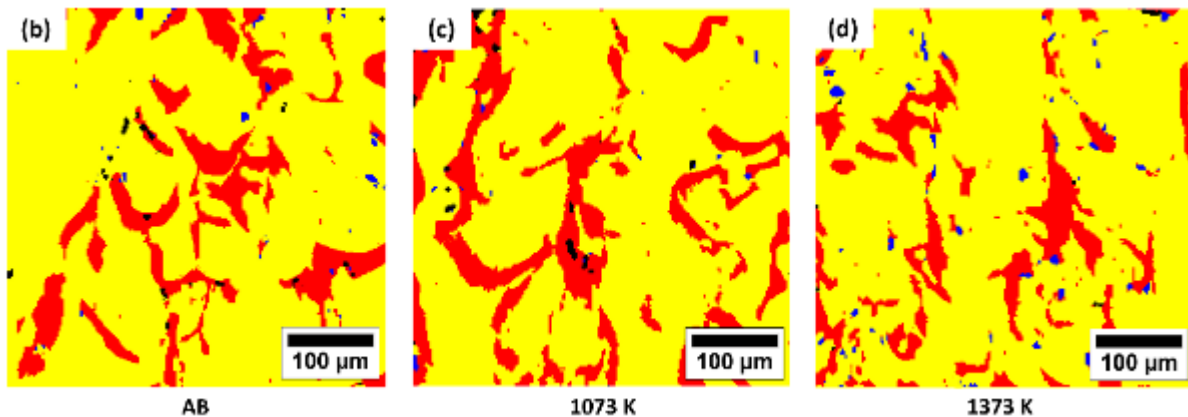
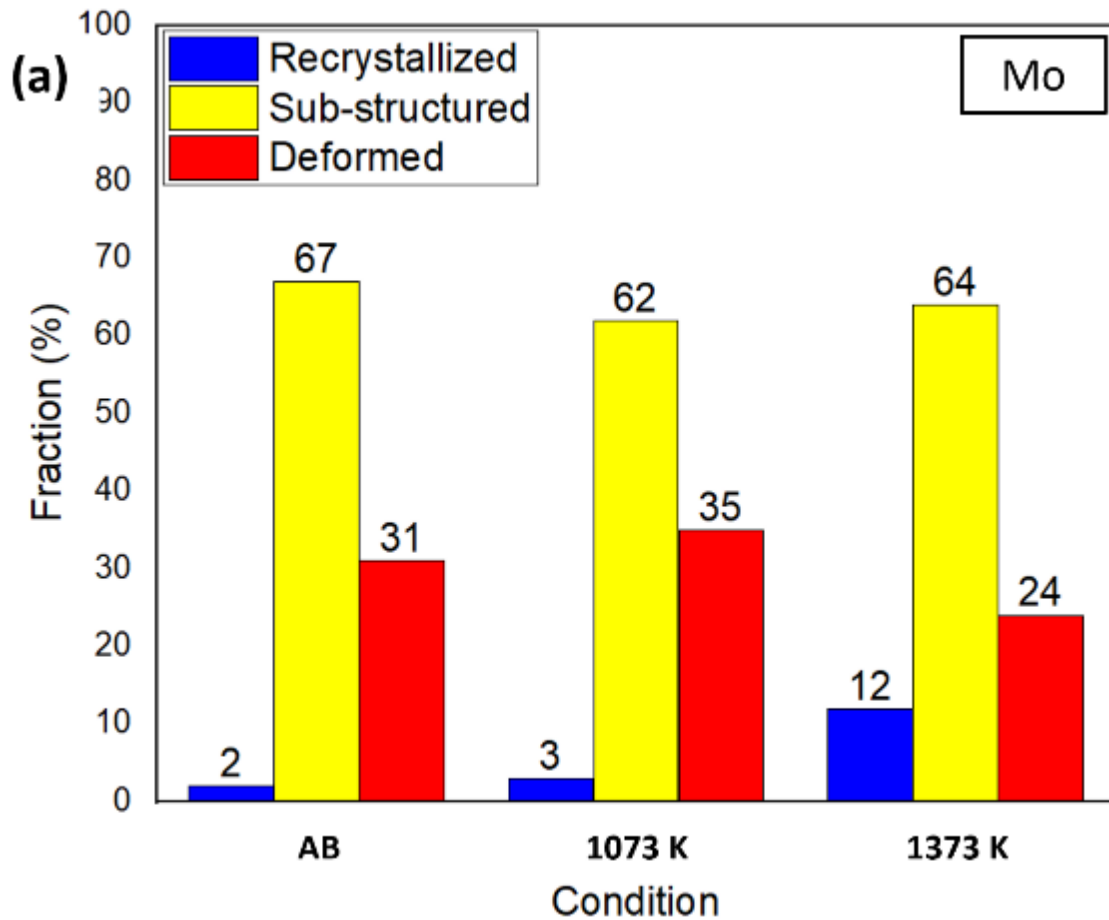


Figure 6.7 (a) Recrystallization fraction analysis from EBSD for Mo and representative maps for (b) AB, (c) 1073 K, and (d) 1373 K conditions.

Microhardness measurements were performed following infiltration of Cu into Mo-HCS and a reduction to 179 ± 13 HV (compared to $\sim 210 \pm 12$ HV for Mo-HCS alone) was observed which

may be attributed to heating above the recrystallization onset temperature of Mo [54–56]. The result matches the observed increase in recrystallized fraction shown in Figure 6.7. Primig et al. [54] have observed a similar response for microhardness in Mo that has been exposed to a temperature of 1373 K (1100 °C).

6.4.3 TZM vs Mo as exoskeleton in HCS

To circumvent the loss in hardness, Mo was substituted by TZM, which is known to have a recrystallization temperature of 1673 K (1400 °C) [57]. TZM-HCS was fabricated, matching the dimensions of the Mo-HCS. Wall thicknesses of 0.59 ± 0.11 mm were measured for the sample, with a cavity fraction of ~36%, comparable to that observed for Mo-HCS. Figure 8a shows the optical micrograph of the TZM-HCS exoskeleton. The microstructural analysis showed that walls with a 99.1 ± 0.3 % density were fabricated. While some porosity was observed, no cracking was evident in the microstructure. Figure 8b shows a representative IPF map from the EBSD analysis of the wall structure. The TZM-HCS sample showed an irregular grain structure comparable to that of Mo-HCS, indicating that the grain macrostructure was agnostic of the light alloying present in TZM-HCS. A similar grain structure has been reported by Kaserer et al. [58] on TZM processed by LPBF. In TZM-HCS, grains of length (along the build direction) less than 0.2 mm were observed, which is smaller than the grains found in Mo-HCS. This is attributed to the grain refining effects of Ti and Zr precipitates present in TZM. The aspect ratios of the grains here matched that of Mo-HCS samples.

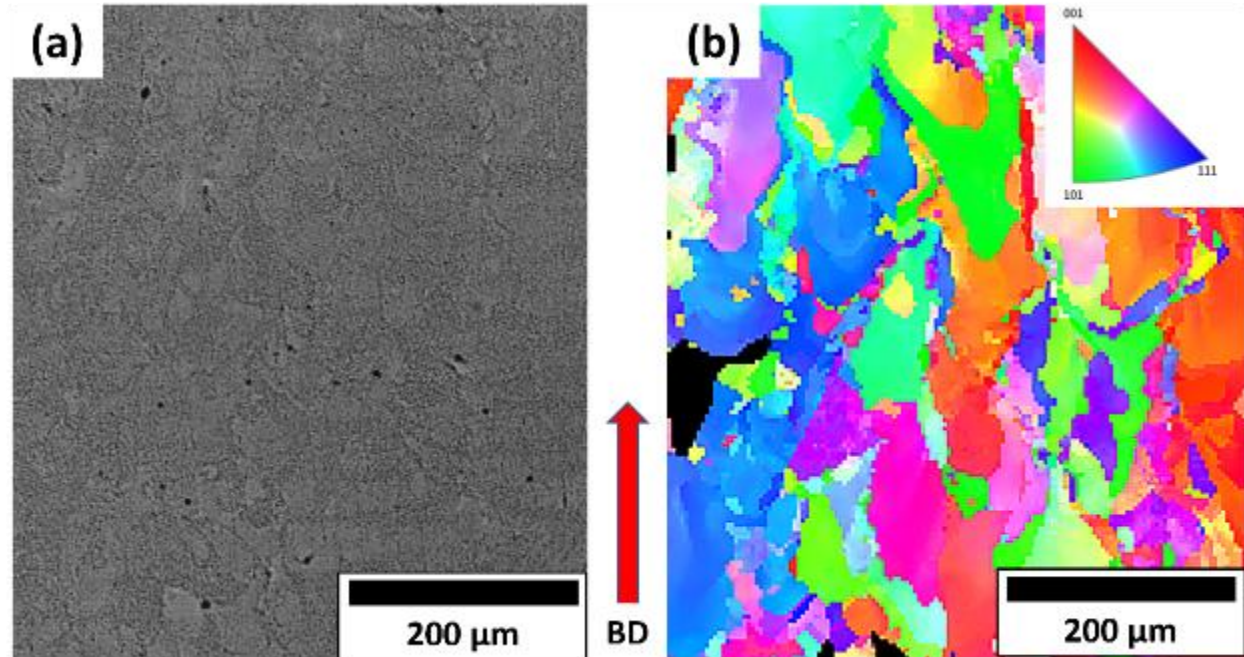


Figure 6.8 (a) Optical micrograph and (b) IPF map from EBSD analysis of a wall in TZM-HCS.

TZM-HCS showed the same CTE as Mo-HCS at $5.3 \times 10^{-6} \text{ K}^{-1}$, indicating that the alloying elements do not influence the CTE of LPBF-processed TZM. The CTE of conventionally processed TZM ($5.2 \times 10^{-6} \text{ K}^{-1}$) is also similar [18]. Following Cu infiltration, the measured CTE of the TZM-HCS+Cu sample showed an increase to $6.6 \times 10^{-6} \text{ K}^{-1}$, which is similar to the one measured for Mo-HCS+Cu ($6.5 \times 10^{-6} \text{ K}^{-1}$). It is also close to the CTE ($6.8 \times 10^{-6} \text{ K}^{-1}$) calculated for TZM-HCS using Equation (2), and the higher estimation of CTE for TZM is attributed to the higher Young's modulus value for TZM. Figure 6.9 shows the results of the recrystallization fraction analysis and representative maps of TZM-HCS samples under the three conditions: AB, exposed to 1073 K (800 °C) (following CTE measurements), and exposed to 1373 K (1100 °C) (after Cu infiltration). The TZM-HCS samples for all three conditions showed similar fractions of recrystallized grains, indicating that none of the conditions affected the microstructural aspects of the material, unlike that for Mo.

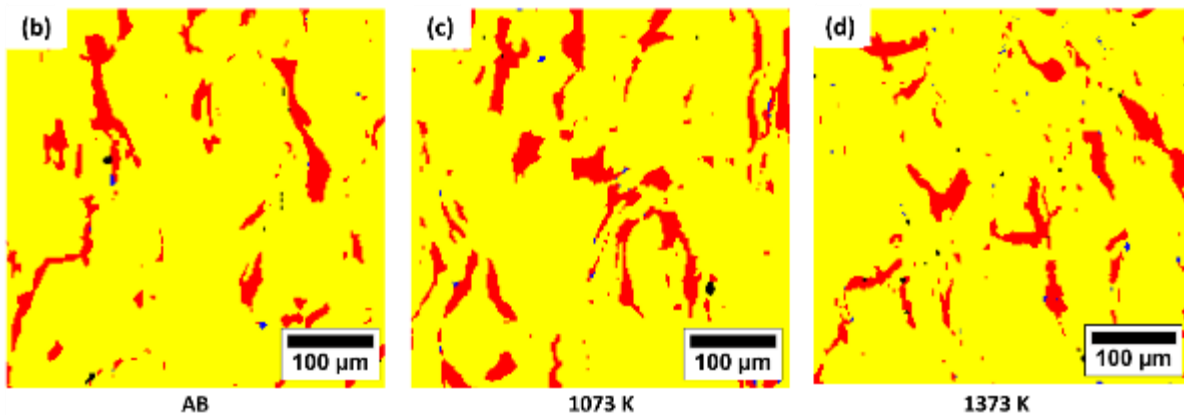
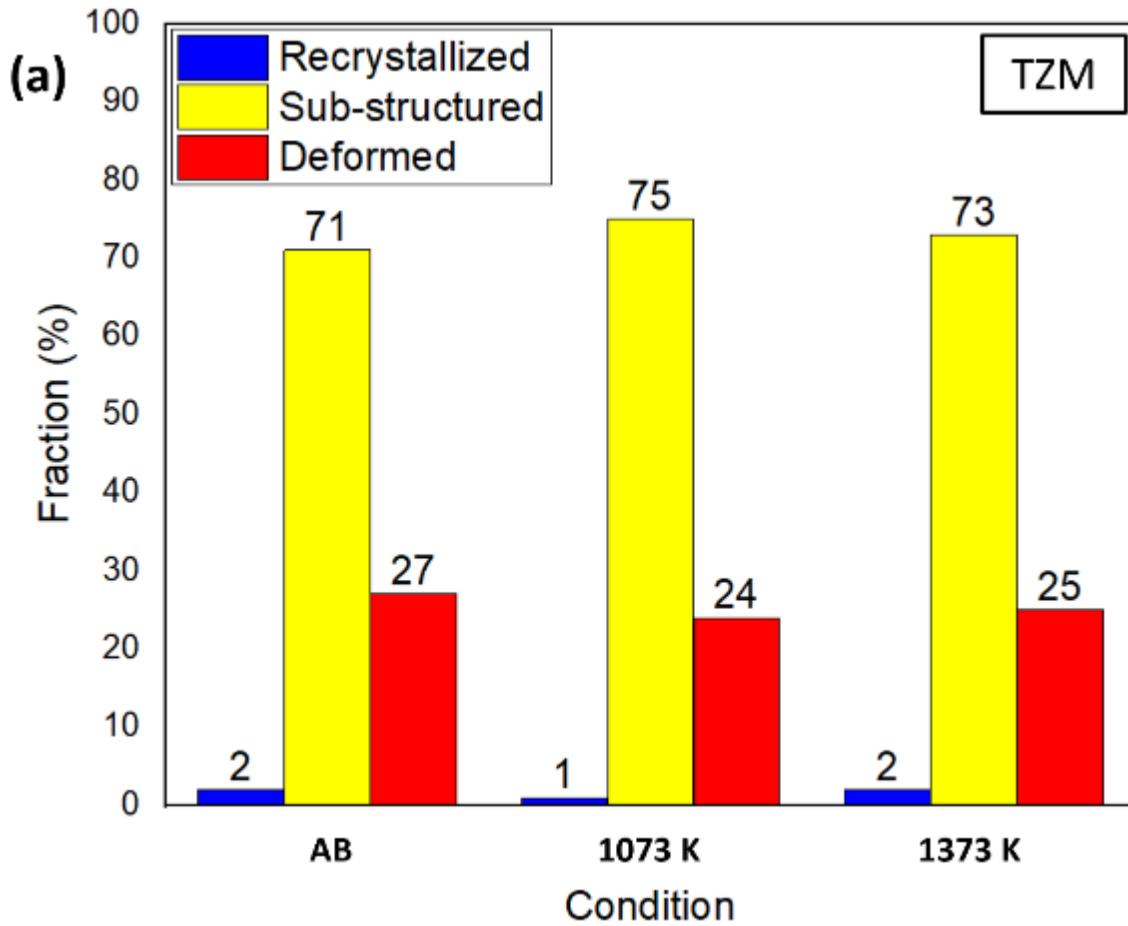


Figure 6.9 (a) Recrystallization fraction analysis from EBSD for TZM and representative maps for (b) AB, (c) 1073 K, and (d) 1373 K conditions.

Figure 6.10 shows the microhardness profile results of Mo-HCS+Cu and TZM-HCS+Cu collected across the samples according to the line in Figure 6.3. The results of AB Mo-HCS and AB TZM-

HCS are added for comparison. As expected, TZM-HCS and TZM-HCS+Cu samples have a much higher hardness (272 ± 7 HV) compared to Mo-HCS (210 ± 12 HV) due to the contribution of alloying elements in TZM. The hardness of TZM-HCS is comparable to the 264 ± 19 HV value reported by Braun et al. [42] for LPBF-processed bulk TZM samples. In the case of TZM-HCS samples, the hardness is similar in AB condition and after Cu infiltration. This is expected because the samples were not exposed to the recrystallization temperature of TZM even after Cu infiltration at 1373 K (1100 °C) [57]. The microhardness responses are in good agreement with the results of recrystallized fraction analysis.

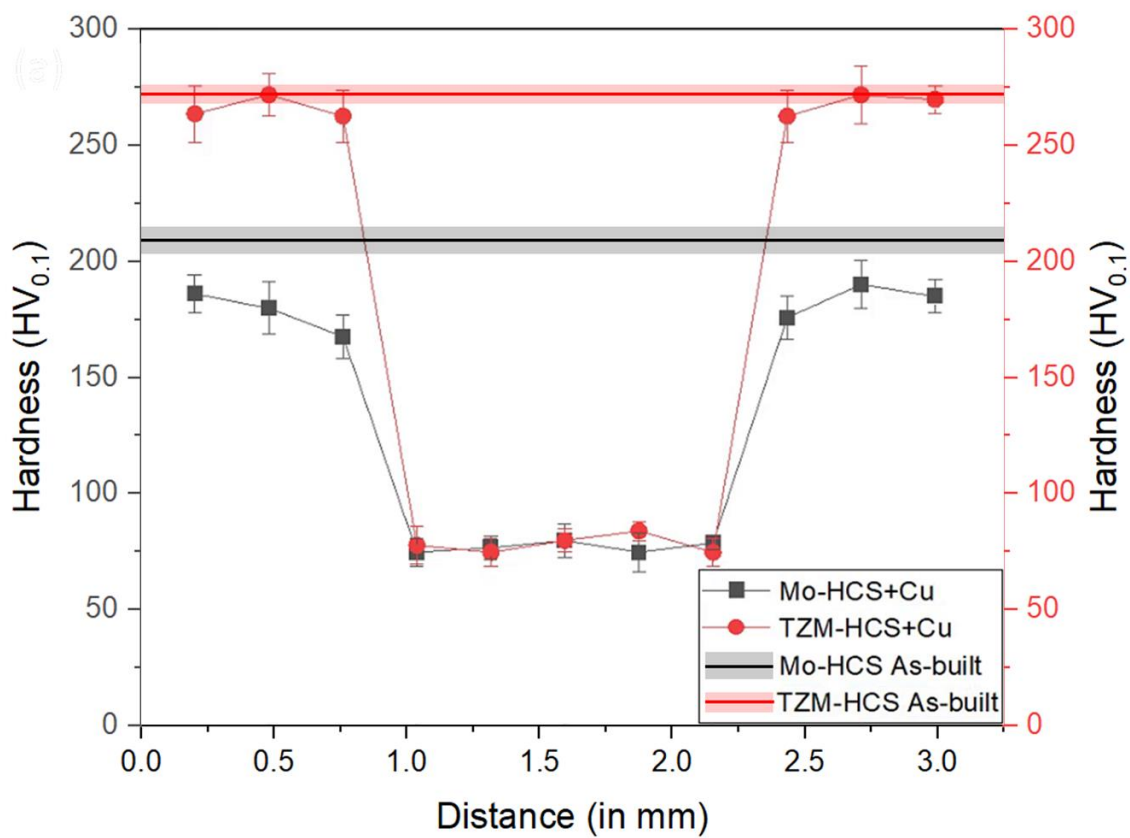


Figure 6.10 Microhardness values of AB Mo-HCS and AB TZM-HCS along with the microhardness profile across the breadth of Mo-HCS+Cu and TZM-HCS+Cu.

6.4.4 Thermal diffusivity measurements

Table 6.3 lists the thermal diffusivity and thermal conductivity results of the Mo-HCS+Cu and TZM-HCS+Cu samples calculated using Equations (2) and (3) (see details in Section A2 of

Supplementary Information). Mo-HCS+Cu has a thermal diffusivity of $61.7 \pm 0.8 \times 10^6 \text{ m}^2 \cdot \text{s}^{-1}$ which is similar to the value of $60.3 \pm 1.0 \times 10^6 \text{ m}^2 \cdot \text{s}^{-1}$ measured for TZM-HCS+Cu. The thermal diffusivities of both samples are within the upper limits of those reported for laminated heat sinks by manufacturers (45 to $65 \times 10^6 \text{ m}^2 \cdot \text{s}^{-1}$) [19]. The thermal diffusivities suggest that Mo-HCS+Cu and TZM-HCS+Cu would be excellent replacements for Cu-Mo-Cu in heat sink applications owing to the former structures' similar thermal diffusivity but superior thermal expansion. In order to evaluate the superior performance of HCS structures compared to laminates, FEM simulations were performed.

Table 6.3 Thermal diffusivity and thermal conductivity at 298 K (25 °C) for the samples.

Sample	Thermal diffusivity ($10^6 \text{ m}^2 \cdot \text{s}^{-1}$)	Thermal conductivity ($\text{W} \cdot \text{m}^{-1} \cdot \text{K}^{-1}$)
Mo-HCS+Cu	61.7 ± 0.8	158.6 ± 2.0
TZM-HCS+Cu	60.3 ± 1.0	154.2 ± 2.6

6.4.5 FEM simulation of Cu-Mo-Cu vs Mo/TZM-HCS

Figure 6.11a shows the modelled temperature profiles along the depth of the heat sinks starting from the interface between the GaAs semiconductor and the heat sinks. T_J marks the junction temperature followed by T_1 through T_5 within the heat sink, and T_O marks the temperature at the outer surface of the heat sinks. For the same heat flux, the Cu-Mo-Cu heat sink produced an R_{COND} value of 8.8 K/W, while the Mo-HCS+Cu heat sink gave a similar value of 8.4 K/W. This indicates that conduction resistance is very similar for both heat sinks despite Mo replacing Cu as a contact material in the proposed Mo-HCS system. This opens the opportunity to make the HCS more complex by introducing, for example, integrated fins to improve the performance of the heat sink. Figure 6.11b and Figure 6.11c illustrate the stress field on the GaAs heat sink interface/surface. For the GaAs-Cu-Mo-Cu laminate setup, the thermal stresses near the interface peak at about 188 MPa for a T_J of 527 K (254 °C). In comparison, for a similar T_J of 513 K (240 °C), the GaAs Mo-HCS+Cu heat sink shows a stress value of only 95 MPa at the interface, which is linked with the lower CTE of the engineered Mo-HCS+Cu heat sink. With the closely matching CTE and excellent heat conduction performance, the thermal stresses in the system can be reduced. Fang et al. [9] showed comparable performance improvement for Mo-Cu heat sinks with a two-phase heat

transport system in comparison to pure Cu heat sinks. This study reaches similar outputs with a more straightforward heat sink construction.

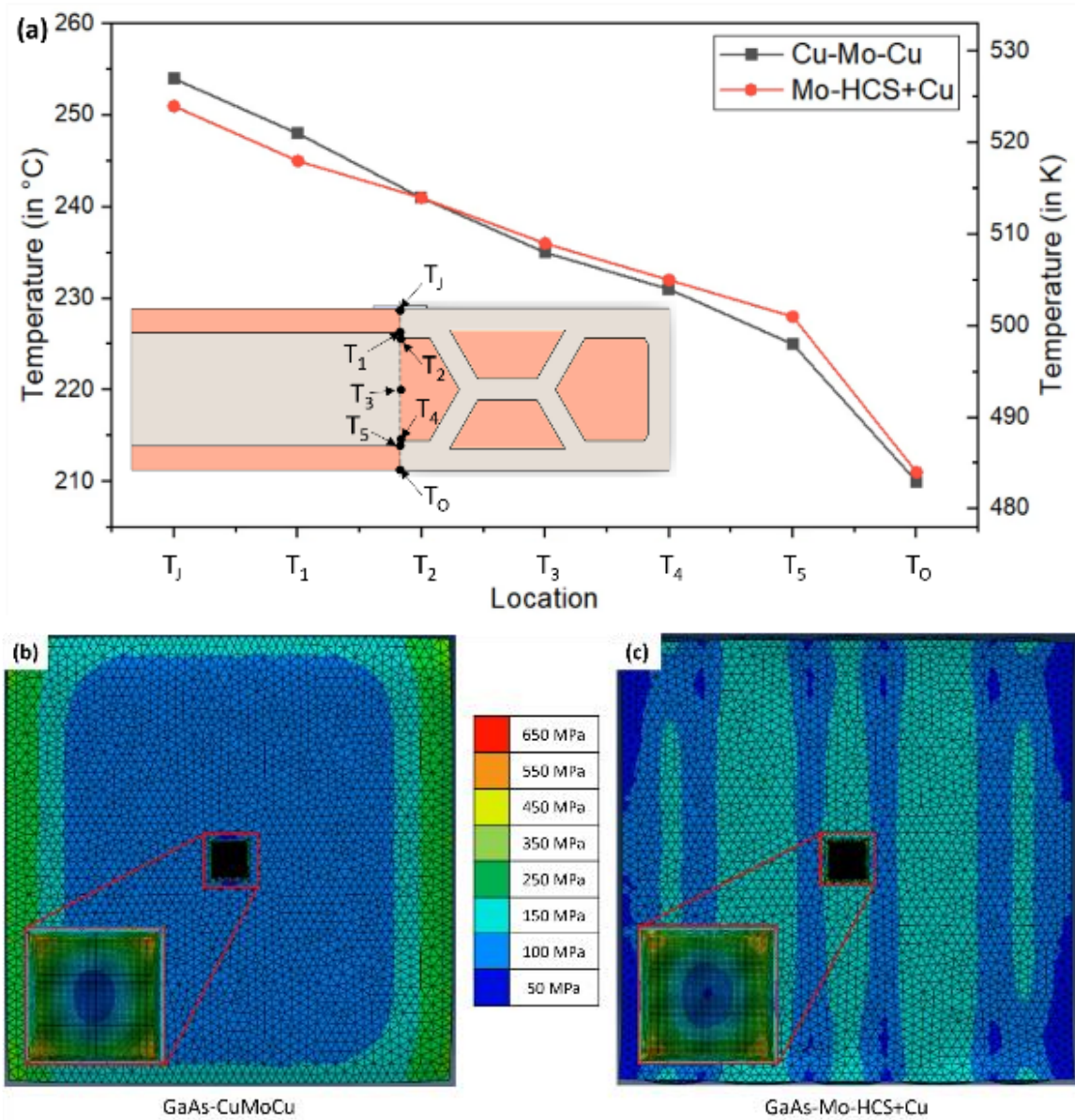


Figure 6.11 (a) Temperature profile along the depth of the heat sink. Stress maps for (b) GaAs-CuMoCu and (c) GaAs-Mo-HCS+Cu setups, respectively.

6.5 Conclusion

Mo and TZM exoskeletons with thin honeycomb cavity structures were successfully manufactured

via LPBF. Mo and TZM samples show good mechanical and thermal properties. Exposure to 1073 K did not influence the samples' properties, indicating that their suitability for application within that temperature range could be possible. Copper infiltration into the cavities was successfully performed, and the produced parts show good wetting and bonding between the Cu infill and the Mo or TZM exoskeletons. The introduction of high CTE Cu increased the overall thermal expansion of the structure to $6.6 \times 10^{-6} \text{ K}^{-1}$. The Mo and TZM exoskeletons with Cu filling showed lower CTE values than commercial Cu-Mo-Cu laminated heatsinks ($7.6 \times 10^{-6} \text{ K}^{-1}$), indicating that these could be excellent replacements in such applications. Moreover, the CTE of Mo and TZM exoskeletons with Cu filling being close to the CTE of GaAs semiconductors ($5.7 \times 10^{-6} \text{ K}^{-1}$), the risk of delamination due to thermal stresses would be potentially lowered. FEM simulation confirms that Mo-HCS shows lower stress and delamination risk to the GaAs heat sink interface for a comparable heat extraction capability.

6.6 Supplementary Material

6.6.1 CTE calculations from simple and modified rules of mixtures

Equations 6.5 and 6.6 show the simple and modified rules of mixtures for the calculation of the CTE for composite structures. Various dimensions of Mo-HCS were devised to match commercial combinations of Mo-Cu laminates in terms of Cu content and thermal diffusivity. The modified rule of mixtures by Schapery has been discussed by Hahnlen et al. [59] for composites of isotropic metals and alloys. Here, $\bar{\alpha}$ is the CTE (in K^{-1}) of the system, E_i is the modulus (in Pa), α_i the CTE, and V_i is the volume fraction of the individual components. Table 6.4 shows the calculations of CTE using simple and modified rules of mixtures.

$$\bar{\alpha} = \sum \alpha_i \cdot V_i \quad (6.5)$$

$$\bar{\alpha} = \frac{E_1 \cdot \alpha_1 \cdot v_1 + E_2 \cdot \alpha_2 \cdot v_2}{E_1 \cdot v_1 + E_2 \cdot v_2} \quad (6.6)$$

Table 6.4 Calculations of CTE (in $10^{-6} K^{-1}$) using simple and modified rules of mixtures.

Sample		Fraction		CTE contribution		CTE by simple rule	CTE by modified rule
		Mo	Cu	Mo	Cu		
Design	Mo-HCS	0.59	0.41	2.97	6.91	9.88	7.39
Actual dimensions	Mo-HCS	0.70	0.30	3.52	5.04	8.56	6.60
	TZM-HCS	0.70	0.30	3.66	5.04	8.70	6.77

6.6.2. In-house custom-made laser flash analysis equipment and measurements

Commercial laser flash analysis instruments, such as the Netzsch LFA 427, are typically limited to measuring cylindrical specimens with a diameter of 12.7 mm and a thickness of 2 to 3 mm due to the constraints of the sample holder. On the other hand, heat sinks are cuboidal in shape, as seen from commercially available heat sink components. For this reason, an in-house custom-made laser flash analysis equipment was made in our facility. The setup used infrared (IR) detectors to measure on one side of the sample the change in temperature resulting from a laser shot hitting the other side of the sample, similar to how a typical laser flash analysis equipment works.

Figure 6.12a shows the schematic of the custom-made laser flash analysis equipment with the different components. Figure 6.12b shows a picture of the custom-made setup, which used fused deposition modelling printed polylactic acid (PLA) parts and commercially available IR detectors. The data were logged to a commercial prototyping board with timestamps at a rate of 1000 Hz. Figure 6.12c shows the setup inside the chamber with a glass window and the optics of the NdYAG laser above. The chamber is connected to a vacuum pump and an nitrogen gas supply line. With the vacuum pump in operation, the chamber can maintain a vacuum of up to 500 mTorr. The chamber was prepared following three cycles of evacuation and purging of N_2 . The gas was then allowed to flow through the chamber at 50 mL/min to prevent any leaks into the chamber.

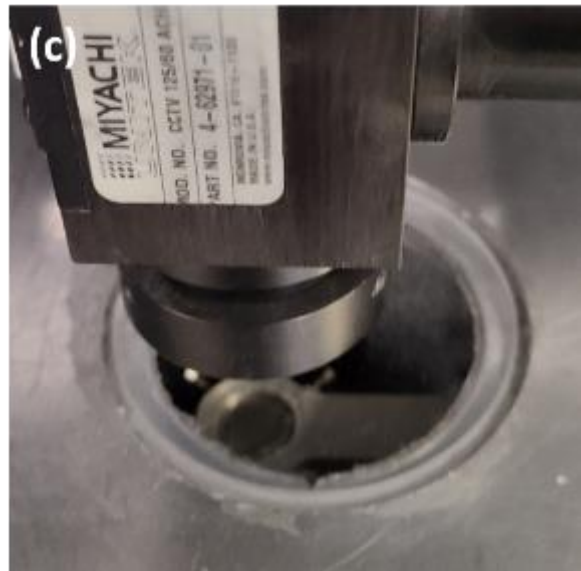
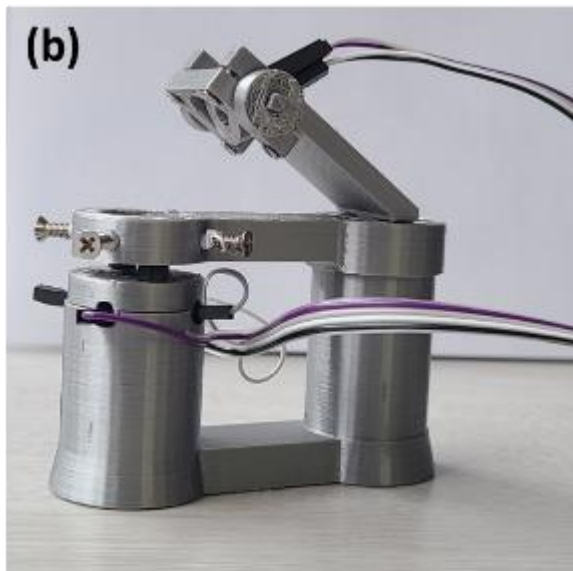
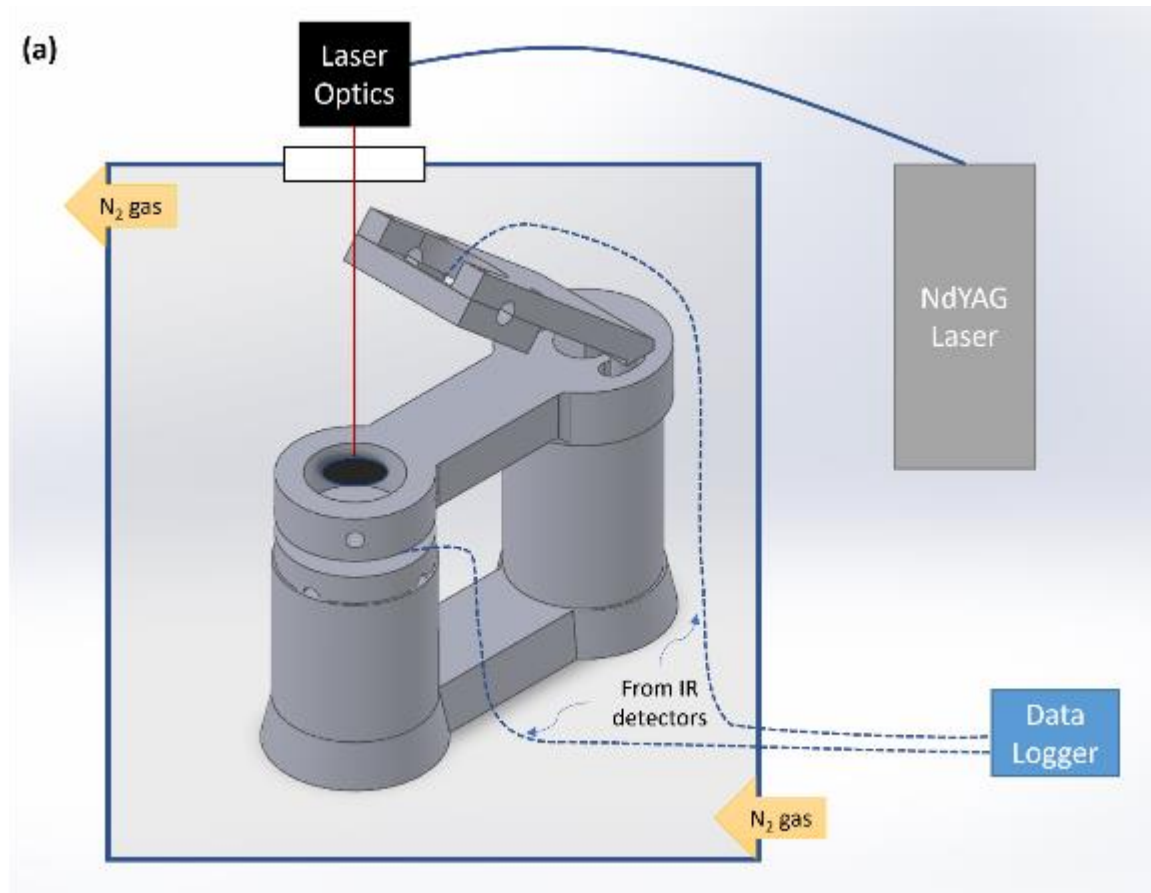


Figure 6.12 (a) Schematic of the custom-made laser flash analysis equipment with the different components; (b) view of the sample stage with integrated IR detectors; (c) the sample stage inside the chamber seen through the glass window with the laser optics above it.

In commercial instruments like the Netzsch LFA 427, the InSb sensor is cooled with liquid N₂ and very sensitive to short, low-energy pulses and a wide range of sample temperatures. For consumer IR detectors, the sensitivity is different, although for room temperature measurements, it is observed that they are acceptable. In this setup, we use two detectors; one facing the side where the laser is impinging and the other placed below, facing the side opposite where the laser is impinging. The first IR detector starts to log the signal and sets the start time $t = 0$, while the second measures the change in temperature of the sample from the conduction through the thickness. Figure 6.13 shows representative responses from the Netzsch LFA and the custom-made setup.

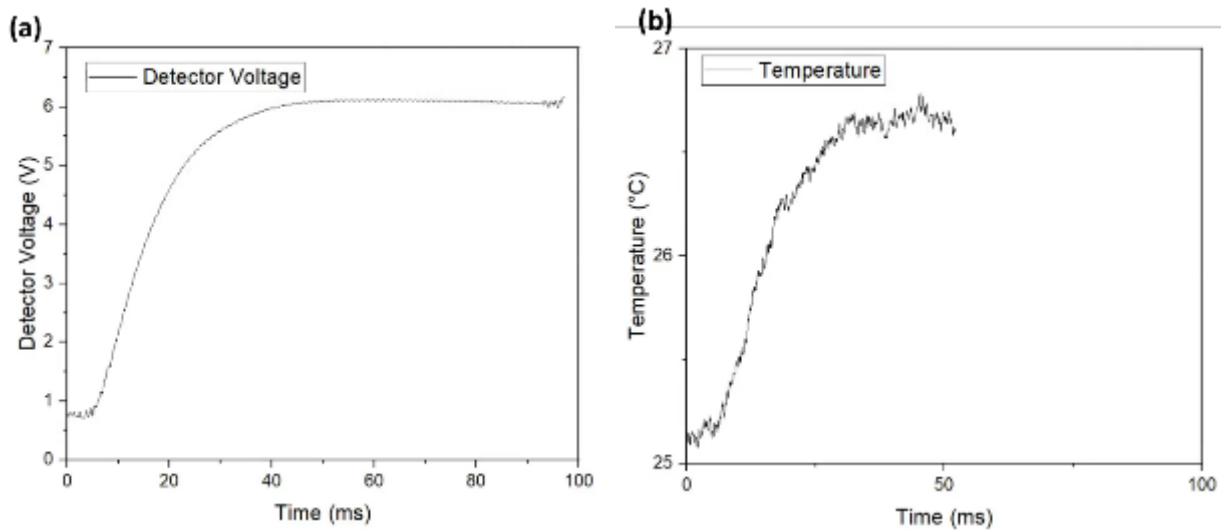


Figure 6.13 Representative response signals from (a) Netzsch LFA 427 and (b) custom-made laser flash analysis equipment.

Table 6.5 provides the collected measurements and calculated values for different parameters for the control samples. Pure Cu reference from Netzsch and pure Mo (prepared from a 99.998% purity Mo plate) samples were tested on the LFA equipment, and their thermal diffusivity values were found to be comparable to those of the literature [16,17,60].

Table 6.5 Thermal diffusivity and thermal conductivity at 25 °C of the samples.

Sample ID	Thermal diffusivity ($\times 10^6 \text{ m}^2 \cdot \text{s}^{-1}$)	Thermal conductivity (in $\text{W} \cdot \text{m}^{-1} \cdot \text{K}^{-1}$)	Measurement equipment	Reference
Pure Cu	113.5 ± 0.4	391.4 ± 1.4	Netzsch LFA 427	Netzsch Reference sample # 29000
Pure Mo	52.5 ± 0.5	133.3 ± 1.1	Netzsch LFA 427	Alfa Aesar (99.998% purity)
Pure Cu	113.1 ± 1.7	390.1 ± 5.7	Custom-made equipment	Reference sample # 29000
Pure Mo	52.2 ± 0.6	134.1 ± 1.5	Custom-made equipment	Alfa Aesar (99.998% purity)
Mo-HCS+Cu	61.7 ± 0.8	158.6 ± 2.0	Custom-made equipment	This study
TZM-HCS+Cu	60.3 ± 1.1	154.2 ± 2.6	Custom-made equipment	This study
Cu	115	396~401		[16,17]
Mo	55	138~139		
TZM	50	126		[60]

Table 6.6 and Table 6.7 provide the calculations performed for the Mo, Cu, Mo-HCS+Cu and TZM-HCS+Cu samples. The difference in the estimated thermal diffusivity (α) and thermal conductivity (k) for the control samples between the laser flash analysis equipment was about 6.0 to 8.0 %; a correction factor was used to arrive at *α -corrected* and *k -corrected values*. This correction factor was also applied for all subsequent measurements and in the data reported in Table 6.3.

Table 6.6 Collected measurements and calculated values from LFA for control samples.

	Mo			Cu		
	1	2	3	1	2	3
Sample thickness, d (mm)	2.305	2.305	2.305	2.541	2.541	2.541
Time, $t_{0.5}$ (s)	0.0148	0.0152	0.0151	0.0083	0.0086	0.0084
D ($10^6 \text{ m}^2 \cdot \text{s}^{-1}$)	49.82756	48.51631	48.83761	107.9744	104.2078	106.689
k ($\text{W} \cdot \text{m}^{-1} \cdot \text{K}^{-1}$)	128.0568	124.6869	125.5127	372.4684	359.4753	368.0343
D corrected ($10^6 \text{ m}^2 \cdot \text{s}^{-1}$)	53.00804	51.61309	51.9549	114.8664	110.8594	113.4989
k corrected ($\text{W} \cdot \text{m}^{-1} \cdot \text{K}^{-1}$)	136.2307	132.6456	133.5241	396.243	382.4206	391.5258

Table 6.7 Collected measurements and calculated values from LFA for Mo and TZM-HCS+Cu.

	Mo-HCS+Cu			TZM-HCS+Cu		
	1	2	3	1	2	3
Sample thickness, d (mm)	3.096	3.096	3.096	3.081	3.081	3.081
Time, $t_{0.5}$ (s)	0.0229	0.0226	0.0233	0.0238	0.0229	0.023
D ($10^6 \text{ m}^2 \cdot \text{s}^{-1}$)	58.09729	58.86849	57.09991	55.35998	57.5357	57.28554
k ($\text{W} \cdot \text{m}^{-1} \cdot \text{K}^{-1}$)	149.31	151.292	146.7468	141.4447	147.0037	146.3646
D corrected ($10^6 \text{ m}^2 \cdot \text{s}^{-1}$)	61.80563	62.62606	60.74459	58.89359	61.20819	60.94207
k corrected ($\text{W} \cdot \text{m}^{-1} \cdot \text{K}^{-1}$)	158.8405	160.949	156.1136	150.4731	156.3869	155.707

6.6.3 FEM simulations

FEM simulations were performed to evaluate the performance of the commercial Cu-Mo-Cu laminated heat sink and the Mo-HCS+Cu heat sink. Figure 6.14a and Figure 6.14b show the 3D coupled temperature-displacement thermo-mechanical models of commercial CuMoCu laminated heat sink and the proposed Mo-HCS+Cu heat sink, respectively, with a GaAs semiconductor on

top, inside the Abaqus/CAE interface. Figure 6.14c and Figure 6.14d show the meshed part of the respective models.

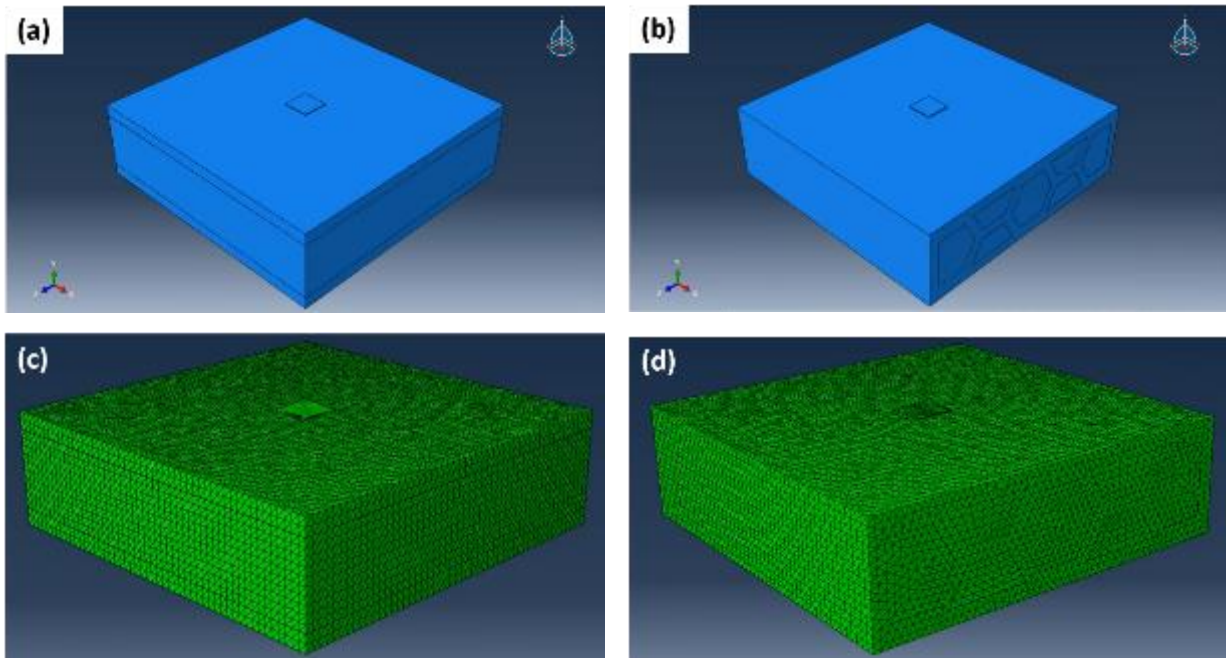


Figure 6.14 Coupled temperature-displacement thermo-mechanical models and mesh structure for the heat sinks of (a, c) GaAs-CuMoCu and (b, d) GaAs-MoHCS+Cu, respectively.

6.7 Acknowledgement

The authors would like to thank the research support provided by the Natural Sciences and Engineering Research Council (NSERC) of Canada (NSERC Project Number: NETGP 494158–16) and Mrs. Angelica Ivonne Valencia Ruiz for her support with the sample fabrication. The authors would also like to acknowledge the McGill Engineering Doctoral Award (MEDA) granted to Tejas Ramakrishnan.

6.8 References

- [1] G.M. Ault, A decade of progress in refractory metals, NASA Tech Memo. TM X-52135 (1965).
- [2] Machlin. I, R.T. Begley, E.D. Weisert, Refractory Metal Alloys - Metallurgy and Technology, Plenum Press, 1968.

- [3] B. Tabernig, N. Reheis, Joining of molybdenum and its application, *Int J Refract Metals Hard Mater.* 28 (2010) 728–733. <https://doi.org/10.1016/j.ijrmhm.2010.06.008>.
- [4] J. Shields, *Applications of Mo Metal and Its Alloys*, 1995. http://www.imoa.info/download_files/molybdenum/Applications_Mo_Metal.pdf.
- [5] ASM Handbook Committee, ed., *ASM Handbook Volume 2: Properties and Selection: Nonferrous Alloys and Special-Purpose Materials*, ASM International, 1990. <https://doi.org/10.31399/asm.hb.v02.9781627081627>.
- [6] E. Pink, R. Eck, *Refractory Metals and Their Alloys*, in: *Materials Science and Technology*, 2006. <https://doi.org/10.1002/9783527603978.mst0088>.
- [7] C.L. Briant, *Refractory Metals and Alloys*, *Encyclopedia of Materials: Science and Technology*. 1 (2004) 8088–8095. <https://doi.org/10.1016/b0-08-043152-6/01453-4>.
- [8] C.T. Liu, H. Inouye, *Internal Oxidation and Mechanical Properties of TZM-Mo Alloy.*, *Metallurgical Transactions*. 5 (1974) 2515–2525. <https://doi.org/10.1007/BF02643872>.
- [9] L.L. Zhang, L.J. Zhang, J. Ning, S.J. Na, *Effect of various combinations of Ti and Zr interlayers on the tensile properties of laser welded joints of molybdenum*, *Int J Refract Metals Hard Mater.* 101 (2021) 105662. <https://doi.org/10.1016/j.ijrmhm.2021.105662>.
- [10] D.F. Heaney, *Sintering of advanced materials - Vacu*, in: *Sintering of Advanced Materials - Fundamentals and Processes*, 2010: pp. 189–221. <https://doi.org/10.1533/9781845699949.2.189>.
- [11] I. Firkowska, A. Boden, B. Boerner, S. Reich, *The Origin of High Thermal Conductivity and Ultralow Thermal Expansion in Copper-Graphite Composites*, *Nano Lett.* 15 (2015) 4745–4751. <https://doi.org/10.1021/acs.nanolett.5b01664>.
- [12] C. Fang, F. Zheng, B. Chu, W. Cheng, H. Guo, H. Chen, R. Wang, C. Song, P. Tao, W. Shang, B. Fu, T. Deng, *Molybdenum copper based ultrathin two-phase heat transport system for high power-density gallium nitride chips*, *Appl Therm Eng.* 211 (2022) 118458. <https://doi.org/10.1016/j.applthermaleng.2022.118458>.
- [13] V.K. Yang, M. Groenert, C.W. Leitz, A.J. Pitera, M.T. Currie, E.A. Fitzgerald, *Crack formation in GaAs heteroepitaxial films on Si and SiGe virtual substrates*, *J Appl Phys.* 93 (2003) 3859–3865. <https://doi.org/10.1063/1.1558963>.

- [14] J.E. Park, I. Jasiuk, A. Zubelewicz, Stresses and fracture at the chip/underfill interface in flip-chip assemblies, *Journal of Electronic Packaging*, Transactions of the ASME. 125 (2003) 44–52. <https://doi.org/10.1115/1.1527656>.
- [15] J.A. Shields, *Applications of Molybdenum Metal and its Alloys*, 2013. http://www.imoa.info/download_files/molybdenum/Applications_Mo_Metal.pdf.
- [16] K.C. Mills, Cu Pure Copper, in: *Recommended Values of Thermophysical Properties for Selected Commercial Alloys*, 2002: pp. 89–97. <https://doi.org/10.1533/9781845690144.89>.
- [17] K.F. Shackelford, W. Alexander, eds., *Materials Science and Engineering Handbook*, 3rd ed., CRC Press, Boca Raton, Florida, 2001. <https://doi.org/10.1126/science.232.4757.1485>.
- [18] Ed Fagan Inc, *Molybdenum TZM Properties*, Ed Fagan Inc. (n.d.) 1–4. <https://www.edfagan.com/refractory-metal-supplier/molybdenum-tzm/molybdenum-tzm-properties/> (accessed April 24, 2023).
- [19] D. Metals, *Molybdenum Copper*, Edgetech Industries. (n.d.) 2.
- [20] Y. Zhang, Y. Xu, S. Liu, A fast numerical method for the analysis of the heat transfer performance of graded metallic honeycomb materials, *Int J Heat Mass Transf.* 79 (2014) 507–517. <https://doi.org/10.1016/j.ijheatmasstransfer.2014.08.036>.
- [21] M. Khalil, M.I. Hassan Ali, K.A. Khan, R. Abu Al-Rub, Forced convection heat transfer in heat sinks with topologies based on triply periodic minimal surfaces, *Case Studies in Thermal Engineering.* 38 (2022) 102313. <https://doi.org/10.1016/j.csite.2022.102313>.
- [22] S. Chowdhury, N. Yadaiah, C. Prakash, S. Ramakrishna, S. Dixit, L.R. Gupta, D. Buddhi, Laser powder bed fusion: a state-of-the-art review of the technology, materials, properties & defects, and numerical modelling, *Journal of Materials Research and Technology.* 20 (2022) 2109–2172. <https://doi.org/10.1016/j.jmrt.2022.07.121>.
- [23] R.J. Hebert, Metallurgical aspects of powder bed metal additive manufacturing, *J Mater Sci.* 51 (2016) 1165–1175. <https://doi.org/10.1007/s10853-015-9479-x>.
- [24] J.J. Lewandowski, M. Seifi, *Metal Additive Manufacturing: A Review of Mechanical Properties*, *Annu Rev Mater Res.* 46 (2016) 151–186. <https://doi.org/10.1146/annurev-matsci-070115-032024>.
- [25] M. Gouge, P. Michaleris, *An Introduction to Additive Manufacturing Processes and Their Modeling Challenges*, 1st ed., Elsevier Inc., 2018. <https://doi.org/10.1016/B978-0-12-811820-7.00002-1>.

- [26] J. Muñiz-Lerma, A. Nommeots-Nomm, K. Waters, M. Brochu, A Comprehensive Approach to Powder Feedstock Characterization for Powder Bed Fusion Additive Manufacturing: A Case Study on AlSi7Mg, *Materials*. 11 (2018) 2386. <https://doi.org/10.3390/ma11122386>.
- [27] A. Aversa, M. Moshiri, E. Librera, M. Hadi, G. Marchese, D. Manfredi, M. Lorusso, F. Calignano, S. Biamino, M. Lombardi, M. Pavese, Single scan track analyses on aluminium based powders, *J Mater Process Technol*. 255 (2018) 17–25. <https://doi.org/10.1016/j.jmatprotec.2017.11.055>.
- [28] D. Heuben, Additive manufacture of highly conductive copper by LPBF, Fraunhofer Institute for Laser T. (2018).
- [29] F. Zhang, L.E. Levine, A.J. Allen, C.E. Campbell, E.A. Lass, S. Cheruvathur, M.R. Stoudt, M.E. Williams, Y. Idell, Homogenization kinetics of a nickel-based superalloy produced by powder bed fusion laser sintering, *Scr Mater*. 131 (2017) 98–102. <https://doi.org/10.1016/j.scriptamat.2016.12.037>.
- [30] A. Basak, S. Das, Microstructure of nickel-base superalloy MAR-M247 additively manufactured through scanning laser epitaxy (SLE), *J Alloys Compd*. 705 (2017) 806–816. <https://doi.org/10.1016/j.jallcom.2017.02.013>.
- [31] F. Gürtler, M. Karg, K. Leitz, M. Schmidt, Simulation of laser beam melting of steel powders using the three-dimensional volume of fluid method, *Phys Procedia*. 41 (2013) 881–886. <https://doi.org/10.1016/j.phpro.2013.03.162>.
- [32] Y.J. Yin, J.Q. Sun, J. Guo, X.F. Kan, D.C. Yang, Mechanism of high yield strength and yield ratio of 316 L stainless steel by additive manufacturing, *Materials Science and Engineering A*. 744 (2019) 773–777. <https://doi.org/10.1016/j.msea.2018.12.092>.
- [33] L.-C. Zhang, H. Attar, M. Calin, J. Eckert, Review on manufacture by selective laser melting and properties of titanium based materials for biomedical applications, *Materials Technology*. 31 (2016) 66–76. <https://doi.org/10.1179/1753555715Y.0000000076>.
- [34] Y. Li, D. Gu, Thermal behavior during selective laser melting of commercially pure titanium powder: Numerical simulation and experimental study, *Addit Manuf*. 1 (2014) 99–109. <https://doi.org/10.1016/j.addma.2014.09.001>.

- [35] J. S, R. M, S.P. AVS, N. B K, C. U, Study of residual stresses and distortions from the Ti6Al4V based thin-walled geometries built using LPBF process, *Defence Technology*. (2023) 1–9. <https://doi.org/10.1016/j.dt.2023.01.002>.
- [36] S.I. Shahabad, U. Ali, Z. Zhang, A. Keshavarzkermani, R. Esmailizadeh, A. Bonakdar, E. Toyserkani, On the effect of thin-wall thickness on melt pool dimensions in laser powder-bed fusion of Hastelloy X: Numerical modeling and experimental validation, *J Manuf Process*. 75 (2022) 435–449. <https://doi.org/10.1016/j.jmapro.2022.01.029>.
- [37] X. Wang, J.A. Muñiz-Lerma, O. Sanchez-Mata, M. Attarian Shandiz, N. Brodusch, R. Gauvin, M. Brochu, Characterization of single crystalline austenitic stainless steel thin struts processed by laser powder bed fusion, *Scr Mater*. 163 (2019) 51–56. <https://doi.org/10.1016/j.scriptamat.2018.12.032>.
- [38] D. Kong, E. Jung, Y. Kim, V.V. Manepalli, K.J. Rah, H.S. Kim, Y. Hong, H.G. Choi, D. Agonafer, H. Lee, An additively manufactured manifold-microchannel heat sink for high-heat flux cooling, *Int J Mech Sci*. 248 (2023) 108228. <https://doi.org/10.1016/j.ijmecsci.2023.108228>.
- [39] G. Sciacca, M. Sinico, G. Cogo, D. Bigolaro, A. Pepato, J. Esposito, Experimental and numerical characterization of pure copper heat sinks produced by laser powder bed fusion, *Mater Des*. 214 (2022) 110415. <https://doi.org/10.1016/j.matdes.2022.110415>.
- [40] D. Faidel, D. Jonas, G. Natour, W. Behr, Investigation of the selective laser melting process with molybdenum powder, *Addit Manuf*. 8 (2015) 88–94. <https://doi.org/10.1016/j.addma.2015.09.002>.
- [41] D. Wang, C. Yu, J. Ma, W. Liu, Z. Shen, Densification and crack suppression in selective laser melting of pure molybdenum, *Mater Des*. 129 (2017) 44–52. <https://doi.org/10.1016/j.matdes.2017.04.094>.
- [42] L. Kaserer, J. Braun, J. Stajkovic, K.H. Leitz, P. Singer, I. Letofsky-Papst, H. Kestler, G. Leichtfried, Microstructure and mechanical properties of molybdenum-titanium-zirconium-carbon alloy TZM processed via laser powder-bed fusion, *Int J Refract Metals Hard Mater*. 93 (2020) 105369. <https://doi.org/10.1016/j.ijrmhm.2020.105369>.
- [43] Y. Zhou, C. Zhou, Z. Wang, Y. Wu, Q. Zhang, J. Qiao, G. Wu, The effect of interface reaction on the thermal and mechanical properties of Mn_{3.2}Zn_{0.5}Sn_{0.3}N/Al composites, *Ceram Int*. 48 (2022) 25826–25832. <https://doi.org/10.1016/j.ceramint.2022.05.257>.

- [44] R.A. Schapery, Thermal expansion coefficients of composite materials based on energy principles, *J Compos Mater.* 2 (1968) 380–404.
- [45] J. Schindelin, I. Arganda-Carreras, E. Frise, Fiji - an Open Source platform for biological image analysis, *Nat Methods.* 9 (2012) 676–682. <https://doi.org/10.1038/nmeth.2019.Fiji>.
- [46] H.E. Sabzi, N.T. Aboulkhair, X. Liang, X.H. Li, M. Simonelli, H. Fu, P.E.J. Rivera-Díaz-del-Castillo, Grain refinement in laser powder bed fusion: The influence of dynamic recrystallization and recovery, *Mater Des.* 196 (2020). <https://doi.org/10.1016/j.matdes.2020.109181>.
- [47] S.E. Atabay, O. Sanchez-Mata, J.A. Muñiz-Lerma, M. Brochu, Effect of heat treatment on the microstructure and elevated temperature tensile properties of Rene 41 alloy produced by laser powder bed fusion, *J Alloys Compd.* 858 (2021). <https://doi.org/10.1016/j.jallcom.2020.157645>.
- [48] J. Rodriguez-Carvajal, Recent advances in magnetic structure determination by neutron powder diffraction, *Physica B.* 192 (1993) 55–69.
- [49] ASTM A01.13 subcommittee, ASTM A1033: Standard Practice for Quantitative Measurement and Reporting of Hypoeutectoid Carbon and Low-Alloy Steel Phase Transformations, *Book of Standards Volume 01.03.* (2010). <https://doi.org/10.1520/A1033-10>.
- [50] J. Braun, L. Kaserer, J. Stajkovic, K.-H. Leitz, B. Tabernig, P. Singer, P. Leibenguth, C. Gspan, H. Kestler, G. Leichtfried, Molybdenum and tungsten manufactured by selective laser melting: Analysis of defect structure and solidification mechanisms, *Int J Refract Metals Hard Mater.* 84 (2019) 104999. <https://doi.org/10.1016/j.ijrmhm.2019.104999>.
- [51] L. Kaserer, J. Braun, J. Stajkovic, K.-H. Leitz, B. Tabernig, P. Singer, I. Letofsky-Papst, H. Kestler, G. Leichtfried, Fully dense and crack free molybdenum manufactured by Selective Laser Melting through alloying with carbon, *Int J Refract Metals Hard Mater.* 84 (2019) 105000. <https://doi.org/10.1016/j.ijrmhm.2019.105000>.
- [52] S. Primig, H. Leitner, H. Clemens, A. Lorich, W. Knabl, R. Stickler, On the recrystallization behavior of technically pure molybdenum, *Int J Refract Metals Hard Mater.* 28 (2010) 703–708. <https://doi.org/10.1016/j.ijrmhm.2010.03.006>.
- [53] M.L. Lobanov, S. V. Danilov, V.I. Pastukhov, S.A. Averin, Y.Y. Khrunyk, A.A. Popov, The crystallographic relationship of molybdenum textures after hot rolling and

- recrystallization, *Mater Des.* 109 (2016) 251–255. <https://doi.org/10.1016/j.matdes.2016.06.103>.
- [54] P.G. V Estulin, Recrystallization of Molybdenum, *Heat-Resistant Steels and Alloys*. (2000) 5–7.
- [55] C. Fang, F. Zheng, B. Chu, W. Cheng, H. Guo, H. Chen, R. Wang, C. Song, P. Tao, W. Shang, B. Fu, T. Deng, Molybdenum copper based ultrathin two-phase heat transport system for high power-density gallium nitride chips, *Appl Therm Eng.* 211 (2022) 118458. <https://doi.org/10.1016/j.applthermaleng.2022.118458>.
- [56] V.M. Glazov, A.S. Pashinkin, Thermal expansion and heat capacity of GaAs and InAs, *Inorganic Materials*. 36 (2000) 225–231. <https://doi.org/10.1007/BF02757926>.
- [57] T. Mrotzek, A. Hoffmann, U. Martin, Hardening mechanisms and recrystallization behaviour of several molybdenum alloys, *Int J Refract Metals Hard Mater.* 24 (2006) 298–305. <https://doi.org/10.1016/j.ijrmhm.2005.10.003>.
- [58] L. Kaserer, J. Braun, J. Stajkovic, K.H. Leitz, P. Singer, I. Letofsky-Papst, H. Kestler, G. Leichtfried, Microstructure and mechanical properties of molybdenum-titanium-zirconium-carbon alloy TZM processed via laser powder-bed fusion, *Int J Refract Metals Hard Mater.* 93 (2020) 105369. <https://doi.org/10.1016/j.ijrmhm.2020.105369>.
- [59] R. Hahnen, J.L. Morris, M.J. Dapino, *Ultrasonic Additive Manufacturing of Metal-Matrix Shape Memory Composites*, Elsevier Ltd., 2021. <https://doi.org/10.1016/B978-0-12-819726-4.00134-4>.
- [60] *Advanced Refractory Metals, TZM Molybdenum Alloy*, Refractory Metal Org. (n.d.). <https://www.refractorymetal.org/tzm-alloy-tzm-molybdenum/> (accessed April 16, 2023).

Chapter 7 – Discussion

7.1 Introduction

Refractory metals offer various benefits like high melting point, good resistance to electrochemical corrosion, high-temperature strength and hardness, excellent thermal conductivity, and low CTE [1, 2]. Among them, Mo metal and its TZM alloy are ideal candidates for various high-temperature applications, including in the aerospace, automotive and power electronics industries [3, 4]. The conventional processing of Mo and TZM parts is limited to simple geometries due to the nature of these materials. The brittleness of these materials and their susceptibility to GB cracking present challenges in their processing and application [5]. Another major factor is the high melting point of Mo and TZM at around 2,896 K (2,623 °C). This makes it challenging to form Mo or TZM into shapes or conventionally cast into various products. Another factor is the high strength and hardness of these materials, making their machining and shaping costly and cumbersome. Unlike most metals, Mo and TZM retain their strength at higher temperatures, presenting challenges in their high-temperature processing as well [6].

LPBF AM process is a layer-by-layer manufacturing process in which metal powders are fused together using the selective scanning of a laser beam. The LPBF AM offers great design freedom and enables the fabrication of parts with near-net complex forms with intricate features [7]. Literature reveals that the LPBF processing of Mo results in cracking defects in the parts produced [8-11]. This is attributed to the inherent brittleness of Mo, which is worsened by the presence of O interstitial [5]. O is an unavoidable impurity in the LPBF process and enters the process from the powder feedstock and the build atmosphere. Under the action of a laser, when powder melts and forms a melt pool, O dissolves into it in significant amounts. Upon solidification and cooling, O is forced out of the lattice due to its low solid solubility in Mo at lower temperatures. O segregates to free surfaces and GBs, and the formation of oxides at the GBs leads to its embrittlement [12]. The residual stresses in the parts generated by the cyclic heating and cooling in the LPBF process are usually relieved by some deformation. The presence of embrittled GBs leads to cracking as the major mechanism for releasing residual stresses. The literature evidences that the optimization of LPBF process parameters has yielded a reduction in cracking behaviour,

but it has proved insufficient to eliminate cracking completely. Researchers have used alloying and substrate heating to suppress cracking in LPBF-processed Mo with success, but such approaches present limitations in the form of material specifications and design limitations, and the literature lacks a protocol which doesn't present such limitations [13, 14].

7.2 Mo and TZM powders for LPBF

The powder feedstock is one of the most important components in the LPBF process. The influence of powder feedstock characteristics on the LPBF processing of materials has been discussed in section 2.6.3 earlier. In this study, gas-atomized pure Mo powders and spray-dried TZM powders were used. The Mo powder particles are spherical and smooth in nature and do not show any satellite or agglomeration, while on the other hand, TZM powder particles seem to be rough spheroidized aggregates of varying spheroidicity and density formed from finer particles. The Mo powder showed flow times of 13.2 ± 0.1 s (per 50 g) and 6.2 ± 0.0 s (per 150 g) under Hall and Carney funnel flow tests respectively, suggesting a high powder flowability. TZM powders did not exhibit flow under either of the funnel flow tests, which is attributed to the increased possibility of mechanical locking of the powder particles owing to their morphology. The apparent density of the Mo and TZM powders were measured to be 57 ± 1 % and 30 ± 1 % of theoretical density, respectively. The apparent density calculation considered $10280 \text{ kg}\cdot\text{m}^{-3}$ for Mo and $10220 \text{ kg}\cdot\text{m}^{-3}$ for TZM as the full dense value.

Additional characterization was performed to study the spreading behaviour of the powders through rotating drum experiments. The results of the rotating drum apparatus for both powders provided further clarity on the behaviour of the powders. The mechanical locking tendency of the TZM particle morphology was evidenced by the higher values of the angle of repose observed for TZM in comparison to Mo powders. Mo powders showed low values of the cohesiveness index at all speeds indicating that higher recoating speeds could be used to reduce process time. TZM powders, on the other hand, indicated higher values of cohesiveness index along with some shear-thickening behaviour suggesting that higher recoating speeds may affect powder spreadability. Hence the default recoating speed was used for both powders, and the powder bed was visually

observed to be without defects and suitable for LPBF processing. In conclusion, both powders could be suitably used for the LPBF processing of these materials.

7.3 Crack-free Mo via LPBF

The study evaluated the feasibility of fabricating crack-free Mo samples through the LPBF process using the N₂ build atmosphere. As a comparative study, samples were initially fabricated through the LPBF process under the Ar build atmosphere since this was the default atmosphere reported in the literature [10, 14]. Microstructural characterization of the control samples produced under an inert Ar atmosphere (Mo-Ar) evidenced a typical columnar grain structure, with grains aligned with build direction. The columnar grain structure is attributed to the epitaxial growth of grains where the previous layers are used as a substrate by the grains growing within the melt pool [14]. In LPBF, the partial re-melting of the previous layer eliminates the nucleation barrier and provides a base for the epitaxial growth of grains. In a pure metal like Mo, grain growth has no hindrance beyond the competition between the different orientations. The O level in the build chamber was reduced to <200 ppm using vacuum cycles, but the results of the inert gas fusion analysis showed that the fabricated samples showed an O content of ~400 ppm. This is attributed to the O contamination in the powder feedstock in addition to the O level in the build chamber. This value of O content in LPBF processed Mo is similar to other studies reported in the literature [10].

An investigation of the fracture surface showed a large amount of oxides, validating the segregation tendency of O to GB, its detrimental effect on GB cohesion and causing GB cracking. Literature abounds with similar observations in LPBF processed Mo [8-10, 14, 15]. The residual stresses from the cyclic heating and cooling in the LPBF process resulted in the cracking of the embrittled GBs in these Mo-Ar samples. The microstructural characterization revealed that large cracks aligned along the build direction were present. EBSD analysis showed that these cracks were formed at GBs. Optimization of the process parameters to study the influence of ED on porosity and cracking tendency was performed. The results showed that by controlling the ED, porosity could be reduced, and samples with densities around 99% could be fabricated. It was noticed that for achieving higher densities, higher ED was required. On the other hand, the cracking

behaviour did not show any discernible trend with ED, and large cracks along the GB were observed for most samples. An average crack length above 500 μm could be measured for most Mo-Ar samples produced in this study. This is comparable to the results reported in the literature for LPBF processed Mo under an Ar atmosphere [10].

In contrast, samples produced under an N_2 build atmosphere (Mo-N) were found to be crack-free. Samples with densities up to 99.1% could be fabricated by optimizing the process parameters. Unlike the inert Ar atmosphere, the N_2 atmosphere introduced N content into the LPBF processed parts close to ~ 600 ppm. The presence of N also affected the grain structure in LPBF-processed Mo. The aspect ratio of grains in Mo-N samples was closer to 1, in contrast to the vertically elongated grains with aspect ratios of ~ 2 to 4 observed in Mo-Ar. The Mo-N samples showed a similar level of O as Mo-Ar, but the GBs and fracture surfaces were cleaner, with scarcely any oxides. Within the grains, the Mo-Ar sample presents an area fraction of oxides at 0.35%, with an average diameter of $0.152 \pm 0.024 \mu\text{m}$, while the Mo-N sample showed an area fraction of 0.12% with an average diameter of $0.082 \pm 0.017 \mu\text{m}$, indicating a much smaller number of oxides (in size and number density) within the grain in Mo-N. This suggests that oxides were prevented from forming within the grains and at the GBs. The results of the optimization study showed a similar response as that of Mo-Ar samples in terms of porosity. At higher ED values, for example, above $\sim 700 \text{ J}\cdot\text{mm}^{-3}$, samples with very low porosity could be fabricated. Samples with densities around 99.1% were fabricated in this study. In contrast to the Mo-Ar samples, cracking also could be eliminated in these samples. The study successfully showed that by employing an N_2 build atmosphere and optimizing LPBF process parameters, crack-free and dense LPBF-processed Mo samples could be fabricated.

7.4 Influence of N_2 on LPBF-processed Mo

The use of an N_2 build atmosphere introduces N into the melt pool in LPBF processing. This has been reported in the welding literature in laser welding of Mo [16]. The introduction of N influenced the O diffusion characteristics in Mo. With first-principles atomistic modelling via DFT, using the nudged elastic band (NEB) method, the diffusion barrier for O in pure Mo lattice

and Mo lattice with N was computed. The diffusion barrier was higher for the case with N in the Mo lattice. Similar results have been reported in the literature for the O-C combination in Mo, where C raised the diffusion barrier for O [17]. Under rapid solidification conditions similar to that observed in the LPBF process, the raising of the diffusion barrier forces the O to be trapped within the lattice beyond the limits of equilibrium solid solubility. It hinders O segregation to free surfaces and GBs in quantities sufficient to form oxides and essentially results in a purification of the GBs. SEM analysis confirmed that O segregation to the GBs was limited, and oxide formation was negligible in the samples prepared under the N₂ atmosphere in comparison to those prepared under the Ar atmosphere.

Using different Ar+N₂ gas mixtures in the build chamber allows for the fabrication of LPBF-processed parts under different N partial pressure and provides a control on the amount of N introduced in the sample. In Mo, Sievert's law follows that the N content will increase with N partial pressure [18]. By varying N₂ gas content from 0% to 100% in the build atmosphere, N content in the LPBF-processed samples could be changed within a range of ~16 ppm to ~600 ppm. The N content followed Sievert's law at lower partial pressure levels but deviated at higher values, and N content beyond the equilibrium solid solubility was measured in the samples. Similar results have been reported and attributed to the plasma-enhanced fugacity of N in the welding literature [19].

The amount of N in the sample influenced the solidification and growth of Mo grains, leading to changes in the grain structure. Microstructural analysis revealed that samples with an N content of less than or equal to 520 ppm showed predominantly columnar grains with high aspect ratios (2 to 4), with some amount of irregularly shaped grains with a low aspect ratio (~1). The study showed that the grain structure transitioned from columnar to irregular, the irregularity increasing with N content. The results of the full profile fitting analysis in Chapter 4 showed that the trapping of N and O strains the Mo lattice. The results discussed in Chapter 5 further validated this and evidenced that the lattice strain increased with increasing N content, and an increase of lattice strain up to ~0.2% was observed. The strain in the lattice disrupted the epitaxial growth of grains in the samples, leading to an increase in the irregularity of grain structure that was observed from microstructural characterization. With N content above the threshold level of ~580 ppm, the grain

structure was observed to be fully irregular. In literature, a similar influence of lattice strain on the grain structure has been observed with the epitaxial growth of silver (Ag) on a strained Ag (111) surface, and it was suggested that a reduction in surface diffusion due to the strain leads to an increase in island density and disrupts the epitaxial growth [20]. The microstructural characterization also evidenced a decrease in the average crack length with this change in grain structure. As the N content increased and the aspect ratio of grains lowered, the crack lengths decreased from $640 \pm 40 \mu\text{m}$ in samples prepared under pure Ar atmosphere through to $220 \pm 50 \mu\text{m}$ for samples with ~ 520 ppm N. The irregularity in the grain structure presented a hindrance to crack growth in these samples. At a threshold N level in the samples (~ 580 ppm), the grain structure was observed to be fully irregular without any evidence of GB cracking.

Fracture surface investigations were performed, which revealed the influence of N on the extent of GB oxide segregation. With increasing N content, there was a decrease in GB oxides, and beyond the threshold N level, GB oxides were scarce. The purification of the GB oxides, in this manner, is the most significant factor for the elimination of cracking in LPBF-processed Mo parts manufactured in this study. The microhardness measurements revealed a generally increasing trend of hardness with N content. This was consistent with the increase in lattice strain in the samples. At high N partial pressures, the samples showed grains with significant differences in hardness values (~ 210 HV and 250 HV). This was due to the presence of two distinct types of grains in the samples; grains with sub-micron molybdenum nitride precipitates and grains without precipitates. The precipitate containing grains' microhardness could be explained through a composite analysis of the precipitate and hardness of Mo grains without precipitates or interstitials.

7.5 Microstructure of Mo and TZM parts with thin wall features

Leveraging the understanding gained from the previous LPBF study, Mo and TZM samples with thin wall features were fabricated under an N_2 atmosphere. Thin walls of 0.4 mm, 0.7 mm and 1.1 mm thickness were fabricated with density values around 99%. Both the Mo and TZM fabricated samples showed an irregular grain structure similar to that observed in bulk Mo samples discussed earlier. Despite the presence of carbide and oxide forming Ti, Zr and C alloying elements in TZM, no discernible change was observed in the microstructure. The grain structure matched that reported for LPBF-processed TZM samples in the literature [21]. This suggests that the influence

of N on the grain structure in LPBF-processed Mo could be analogous to that of the alloying elements in TZM. The samples were also observed to be devoid of any cracking, and GBs were observed to be clean of any oxide presence, unlike Mo and TZM samples fabricated under an Ar atmosphere. The results of microstructural characterization showed that the grain structure was very similar for all the samples indicating that the part dimension did not affect the grain structure.

7.6 Cu infiltrated Mo and TZM structures with tailored CTE

Using the knowledge developed to fabricate crack-free Mo and TZM parts and parts with thin wall features using the LPBF process, a practical application was sought. A power electronics heat sink was chosen to demonstrate a practical application of LPBF-processed parts of this nature. The parts were designed to be built out of Mo and TZM for their very low CTE and good thermal diffusivity, while the cavity will be infiltrated with Cu for its high thermal diffusivity. The use of the low CTE and high strength Mo and TZM exoskeleton will also resist the thermal expansion of the high CTE Cu region. Such a heat sink would offer a good overall thermal diffusivity while limiting the thermal expansion to match that of power electronics semiconductors. A closer matching of CTE to the semiconductors will allow for improved performance since commercially available Cu-Mo-Cu laminate heat sinks show delamination failure due to a CTE mismatch. Additionally, LPBF offers the benefits of creating complex heat sink structures, including integral fins, for greater performance.

Using the LPBF process, Mo and TZM parts with thin walls and honeycomb cavity structures (HCS) were fabricated under an N₂ atmosphere. The Mo and TZM samples showed the characteristic irregular grain structure described earlier, which was resistant to cracking. The samples showed no evidence of cracking and achieved a density of 99.1%. Dilatometric measurements provided CTE values of $\sim 5.3 \times 10^{-6} \text{ K}^{-1}$ for both Mo and TZM samples fabricated in the study. The CTE values are comparable to those reported in the literature [22]. Exposure to a temperature of 1073 K (800 °C) did not bring any material change to the Mo or TZM parts. The results of hardness measurements and microstructural characterization provided evidence for this.

Cu infiltration was successfully performed into both Mo and TZM HCS by melting OFHC Cu above the samples at 1373 K (1100 °C). The microstructural characterization using optical

micrography showed excellent wetting between the Mo HCS and Cu infill. EDS maps generated from SEM analysis affirmed this finding. Mo and Cu are immiscible, and XRD analysis did not evidence the formation of any new phases. The exposure to 1373 K (1100 °C) during Cu infiltration resulted in partial recrystallization of Mo microstructure, as evidenced by an increase in the recrystallized fraction under EBSD analysis. A decrease in hardness value by 12% was also noted, in agreement with this observation. This was expected due to the recrystallization start temperature for Mo being ~ 1173 K (900 °C). On the other hand, TZM samples did not show any reduction in hardness or change in recrystallized fraction due to their increased resistance to recrystallization. The presence of precipitates of Mo and Ti carbides and Zr and Ti oxides in TZM provide GB pinning support and resists recrystallization. The AB TZM samples and those exposed to 1373 K (1100 °C) showed a hardness value of 272 ± 7 HV.

Cu infiltration increased the CTE of the samples to $\sim 6.6 \times 10^{-6} \text{ K}^{-1}$, which matched the estimated CTE values through calculations using the modified rule of mixtures by Schapery [23]. Commercial laminate Cu-Mo-Cu heat sinks reported CTE values of 7.6 to $9.0 \times 10^{-6} \text{ K}^{-1}$ for similar Cu content. The thermal diffusivity of Mo and TZM HCS with Cu infill was measured at $61.7 \pm 0.8 \times 10^6 \text{ m}^2 \cdot \text{s}^{-1}$ and $60.3 \pm 1.0 \times 10^6 \text{ m}^2 \cdot \text{s}^{-1}$, respectively. This value matched the upper bound values for commercial laminate Cu-Mo-Cu heat sinks with similar Cu content (30 wt.%). The CTE and thermal diffusivity values show that the proposed heat sinks could be a drop-in replacement.

FEM modelling was performed to compare the performance of Mo-HCS+Cu and Cu-Mo-Cu heat sinks. The conduction resistance was computed for both structures (Mo-HCS+Cu and Cu-Mo-Cu) in this study and found to be similar at $\sim 8.6 \text{ K/W}$. The reduced CTE of the Mo-HCS+Cu ($\sim 6.6 \times 10^{-6} \text{ K}^{-1}$) in comparison to Cu-Mo-Cu ($7.6 \times 10^{-6} \text{ K}^{-1}$), which is closer to the values for power electronics semiconductors ($5.7 \times 10^{-6} \text{ K}^{-1}$), suggests that the delamination risk due to thermal stresses will be lower, allowing for higher junction temperatures in the operation of the heat sink. FEM modelling showed that for a similar junction temperature of $\sim 513 \text{ K}$ (240 °C), the Mo-HCS+Cu showed lower interface stress at 95 MPa in comparison to the 188 MPa shown by the Cu-Mo-Cu laminate heat sink. A lower value of interface stress translates to lower stresses on the mating surfaces and the thermal pastes used between the surfaces. This lowers the risk of delamination between the LPBF fabricated heat sink and the semiconductor. The similarity in the

thermal diffusivity and conduction resistance, along with the reduced thermal stresses evidenced from modelling, validate that the fabricated component could be a suitable replacement for laminate Cu-Mo-Cu heat sinks. The study successfully fabricated Mo and TZM parts with thin walls and honeycomb cavity structures and demonstrated the successful Cu infiltration of such structures for creating components with a tailored coefficient of thermal expansion.

7.7 References

- [1] E. Pink and R. Eck, "Refractory Metals and Their Alloys," in *Materials Science and Engineering*: Wiley-VCH Verlag GmbH, 2006, ch. 10.
- [2] C. L. Briant, "Refractory Metals and Alloys," in *Encyclopedia of Materials: Science and Technology*, K. H. J. Buschow, R. W. Cahn, M. C. Flemings, E. J. Kramer, B. Ilchner, S. Mahajan, and P. Veyssi re Eds.: Elsevier Science Ltd, 2001, pp. 8088-8095.
- [3] N. R. Philips, M. Carl, and N. J. Cunningham, "New Opportunities in Refractory Alloys," *Metallurgical and Materials Transactions A*, vol. 51, no. 7, pp. 3299-3310, 2020, doi: 10.1007/s11661-020-05803-3.
- [4] V. V. Satya Prasad, R. G. Baligidad, and A. A. Gokhale, "Niobium and Other High Temperature Refractory Metals for Aerospace Applications," in *Aerospace Materials and Material Technologies*, vol. 1: Aerospace Materials, N. Eswara Prasad and R. J. H. Wanhill Eds., (Indian Institute of Metals Series: Springer, 2017.
- [5] J. B. Brosse, R. Fillit, and M. BISCONDI, "Intrinsic intergranular brittleness of molybdenum," *Scripta Metallurgica*, vol. 15, p. 5, 1981.
- [6] J. H. Bechtold and H. Scott, "Mechanical Properties of Arc-Cast and Powder Metallurgy Molybdenum," *Journal of the Electrochemical Society*, vol. 98, p. 11, 1951.
- [7] R. Morales, R. E. Aune, O. Grinder, and S. Seetharaman, "The powder metallurgy processing of refractory metals and alloys," *The journal of the minerals, metals and materials society (TMS)*, vol. 55, pp. 20-23, 2003, doi: 10.1007/s11837-003-0169-9.
- [8] B. Guan *et al.*, "Strategies to reduce pores and cracks of molybdenum fabricated by selective laser melting," *International Journal of Refractory Metals and Hard Materials*, vol. 112, 2023, doi: 10.1016/j.ijrmhm.2023.106123.

- [9] M. Higashi and T. Ozaki, "Selective laser melting of pure molybdenum: Evolution of defect and crystallographic texture with process parameters," *Materials & Design*, vol. 191, 2020, doi: 10.1016/j.matdes.2020.108588.
- [10] J. Braun *et al.*, "Molybdenum and tungsten manufactured by selective laser melting: Analysis of defect structure and solidification mechanisms," *International Journal of Refractory Metals and Hard Materials*, vol. 84, 2019, doi: 10.1016/j.ijrmhm.2019.104999.
- [11] D. Faidel, D. Jonas, G. Natour, and W. Behr, "Investigation of the selective laser melting process with molybdenum powder," *Additive Manufacturing*, vol. 8, pp. 88-94, 2015, doi: 10.1016/j.addma.2015.09.002.
- [12] K. Leitner *et al.*, "On grain boundary segregation in molybdenum materials," *Materials & Design*, vol. 135, pp. 204-212, 2017, doi: 10.1016/j.matdes.2017.09.019.
- [13] L. Kaserer *et al.*, "Fully dense and crack free molybdenum manufactured by Selective Laser Melting through alloying with carbon," *International Journal of Refractory Metals and Hard Materials*, vol. 84, 2019, doi: 10.1016/j.ijrmhm.2019.105000.
- [14] D. Wang, C. Yu, J. Ma, W. Liu, and Z. Shen, "Densification and crack suppression in selective laser melting of pure molybdenum," *Materials & Design*, vol. 129, pp. 44-52, 2017, doi: 10.1016/j.matdes.2017.04.094.
- [15] F. Oehlerking, M. T. Stawovy, S. Ohm, and A. Imandoust, "Microstructural characterization and mechanical properties of additively manufactured molybdenum and molybdenum alloys," *International Journal of Refractory Metals and Hard Materials*, vol. 109, 2022, doi: 10.1016/j.ijrmhm.2022.105971.
- [16] L.-L. Zhang, L.-J. Zhang, J. Ning, Y.-J. Sun, W.-I. Cho, and S.-J. Na, "On the laser gas (N₂) alloying in the welding of molybdenum alloy," *Journal of Materials Processing Technology*, vol. 296, 2021, doi: 10.1016/j.jmatprotec.2021.117184.
- [17] Z.-Q. Wang *et al.*, "Suppressing effect of carbon on oxygen-induced embrittlement in molybdenum grain boundary," *Computational Materials Science*, vol. 198, 2021, doi: 10.1016/j.commatsci.2021.110676.
- [18] D. E. Weaver, "The Diffusivity and Solubility of Nitrogen in Molybdenum and the Trapping of Nitrogen By Carbon in Molybdenum," Doctor of Philosophy, University of California, Livermore, California, UCRL-51182, 1972.

- [19] A. Bandopadhyay, A. Banerjee, and T. Debroy, "Nitrogen activity determination in plasmas," *Metallurgical Transactions B*, vol. 23B, p. 207, 1992.
- [20] D. Matsunaka and Y. Shibutani, "Effects of tensile strain on Ag(111) epitaxial growth by kinetic Monte Carlo simulations," *J Phys Condens Matter*, vol. 23, no. 26, p. 265008, Jul 6 2011, doi: 10.1088/0953-8984/23/26/265008.
- [21] L. Kaserer *et al.*, "Microstructure and mechanical properties of molybdenum-titanium-zirconium-carbon alloy TZM processed via laser powder-bed fusion," *International Journal of Refractory Metals and Hard Materials*, vol. 93, 2020, doi: 10.1016/j.ijrmhm.2020.105369.
- [22] M. Baucchio, *ASM Metals Reference Book*. ASM International, 2003.
- [23] R. A. Schapery, "Thermal expansion coefficients of composite materials based on energy principles," *Journal of Composite Materials*, vol. 2, no. 3, p. 25, 1968.

Chapter 8 – Conclusion

This study systematically investigated and successfully demonstrated the fabrication of crack-free Mo parts using the LPBF AM process. Crack-free parts could be fabricated without the need for pre-alloying and substrate heating. The study investigated the influence of N₂ gas in the build atmosphere of the LPBF process. Mo and TZM parts with thin features and honeycomb cavity structures were successfully fabricated in this study, and Cu infiltration was performed into the cavities to create replacements for commercial laminate heat sinks. As an example application, the study successfully demonstrated the benefits of LPBF-processed parts as replacements for commercial components used in power electronics applications. The significant conclusions drawn from the study are summarized as follows:

- Under Ar atmosphere, LPBF-processed parts exhibit columnar grain structures with a high aspect ratio along the build direction, which were prone to GB cracking. Using an N₂ build atmosphere, the grain structure achieved was irregular, with a much lower aspect ratio. The N₂ build atmosphere introduces N into LPBF-processed Mo parts, restricting O segregation. Measurements showed that despite similar O content, samples processed under N₂ build atmosphere exhibited lower amounts of oxides within the grains and at GBs, compared to samples processed under Ar. DFT simulations indicated that the presence of N raises the diffusion barrier energy for O in Mo lattice. Samples produced under the N₂ atmosphere achieved a higher microhardness value than those produced under Ar. Fabricating crack-free Mo samples with excellent mechanical properties through the LPBF process is feasible using an N₂ build atmosphere.
- The use of different Ar+N₂ gas mixtures allows for the fabrication of LPBF-processed parts under different N partial pressure. The N content introduced in the sample increased with an increase in N partial pressure. The study demonstrated the ability to perform in-situ nitriding in LPBF-processed AM samples with a nitrogen content ranging from 100 to 600 ppm through the variation of partial pressure inside the build chamber. The amount of N in the sample influenced the solidification and growth of Mo grains, leading to changes in the grain structure. Samples with a N content of less than or equal to 520 ppm N content showed predominantly columnar grains. The grain structure transitioned from columnar to irregular as the N content increased. The irregularity in the grain structure presented a

hindrance to crack growth in these samples. With increasing N content, where the columnar structure was increasingly disturbed, a concurrent decrease in average crack length in the sample was observed. Average crack lengths decreased from $640 \pm 40 \mu\text{m}$ in samples without significant N, through $220 \pm 50 \mu\text{m}$ for samples with ~ 400 ppm N, to no cracks in samples with N content greater than or equal to 580 ppm. Full profile fitting analysis of XRD data showed that the lattice strain increased with increasing N content, and a similar trend was observed for the microhardness results.

- Mo and TZM parts with thin walls and honeycomb cavity structures could be fabricated under an N_2 atmosphere to achieve a similar grain structure as the bulk samples. The samples showed no evidence of cracking and achieved a density of 99.1%. The CTE of both Mo and TZM samples were similar at $\sim 5.3 \times 10^{-6} \text{ K}^{-1}$ and is comparable to values reported in the literature. Cu infiltration was successfully performed into both Mo and TZM HCS, as evidenced by the excellent wetting shown under microstructural characterization. Exposure to 1373 K (1100 °C) during Cu infiltration resulted in partial recrystallization of Mo samples, as evidenced by a decrease in microhardness and an increase in a recrystallized fraction under EBSD analysis. This was expected due to the recrystallization start temperature for Mo being close to 1173 K (900 °C). TZM samples showed no reduction in hardness or change in recrystallized fraction due to its increased resistance to recrystallization from the Ti and Zr precipitates in the sample. Cu infiltration increased the CTE of the samples to $\sim 6.6 \times 10^{-6} \text{ K}^{-1}$ as estimated through calculations using the modified rule of mixtures by Schapery. Both Mo and TZM HCS with Cu showed improved thermal diffusivity of $\sim 61 \times 10^6 \text{ m}^2 \cdot \text{s}^{-1}$, matching the upper bound values for commercial laminate Cu-Mo-Cu with similar Cu content. Similar conduction resistance as to that of Cu-Mo-Cu was computed for the samples in this study, using FEM modelling. The similarity in thermal diffusivity and conduction resistance shows that the fabricated component could be a suitable replacement. The reduced CTE of the HCS, which is closer to the values for power electronics semiconductors ($5.7 \times 10^{-6} \text{ K}^{-1}$) in comparison to Cu-Mo-Cu ($7.6 \times 10^{-6} \text{ K}^{-1}$), indicates that the delamination risk due to thermal stresses will be lower, allowing for higher junction temperatures in the operation of the heat sink. The study successfully fabricated Mo and TZM parts with thin walls and honeycomb cavity structures and

demonstrated the successful Cu infiltration of such structures for creating components with a tailored coefficient of thermal expansion.